THE UNIVERSITY *of* EDINBURGH

A behavioural framework for studying visually-directed reaching in the mouse

Matt Colligan

Doctor of Philosophy
Centre for Discovery Brain Sciences
Deanery of Biomedical Sciences
The University of Edinburgh
2024

Abstract

Reaching and grasping are fundamental behaviours that humans and other mammalian species depend on to perform useful interactions with our environment. To execute this behaviour, forelimb movements require to be accurately targeted based on the egocentric spatial position of objects of interest. As we navigate our environment, we first visually identify the location of nearby objects, then use this information to compute necessary movement trajectories. Decades of primate research has successfully utilised reaching tasks to identify and characterise a number of brain areas involved in visually-directed movement. Mice display a somewhat similar behavioural repertoire to humans, including the ability to reach and grasp, and can therefore be used as a model system to investigate neural control of movement. The improved genetic tractability of mice has expanded our ability to delineate cell type- and pathway-specific functionality in the brain, and such research benefits from higher throughput and lower financial cost. However, due to the lack of a suitable behavioural task, to date there has been a distinct lack of research using mice to study visually-directed reaching. To address this problem, I aimed to design a novel task for mice that researchers can use to study this critical behaviour.

First, I designed and implemented a task in which freely moving mice learned to perform visually-directed reaches. During the task, one of two reach targets was illuminated and mice learned to reach and grasp the illuminated target to receive a water reward. Once trained, mice would perform an initial reach to the visual stimulus followed by up to 10 repetitive, self-initiated reaches. Expert mice had a high success rate and performed an average of 120 cued reaches per 30-minute session after 4 weeks of training.

Next, to take full advantage of the kinematic richness of the behaviour by enabling the task to be combined with high temporal resolution extracellular recordings, I developed a user-friendly data processing and analysis pipeline for electrophysiological data collected using Neuropixels silicone probes. The pipeline, named `pixels` and open-sourced at https://github.com/DuguidLab/pixels, provides a simple Python API that

enables visualisation and statistical testing of neuron population extracellular activity recorded during trial-based behavioural tasks. To enable high resolution examination of the spatiotemporally detailed movements performed during the task and how they relate to neural activity, `pixels` integrates closely with the DeepLabCut motion tracking toolbox (Mathis et al., 2018).

Lastly, as a proof-of-concept demonstrating the utility of the visually-directed reaching task, I performed extracellular recordings in expert mice and used `pixels` to examine neural correlates of behaviour. Using chronically-implanted Neuropixels silicone probes, I recorded population activity in posterior secondary motor cortex (pM2) and dorsomedial striatum (DMS), brain areas implicated in visuomotor control (Hwang et al., 2019; Itokazu et al., 2018) and goal-directed behaviour (Hwang et al., 2019; Wang et al., 2013), respectively. In deep layers of pM2, over half of pM2 neurons exhibited reproducible firing rate changes as mice initiated and executed visually-directed reaches. During a 300 ms pre-reach window, a small proportion of pM2 neurons displayed activity changes, suggestive of a role in movement preparation or initiation. During reach execution, reduced firing rates dominated pM2 population activity in both pyramidal cells and interneurons, while a small subset of pyramidal cells became more active. Two competing models may explain this finding. The small excitatory component may convey motor signals, with widespread inhibition possibly serving to improve the signal-to-noise ratio in recipient areas. Alternatively, movement-related information may be conveyed directly by the firing rate decreases, complementing the excitatory signals to provide bidirectional modulation of recipient areas. Only approximately half of pM2 neurons active during cued reaches remained active during repetitive reaches, suggestive of distinct motor pathways underlying these types of behaviours. Activity profiles in DMS mirrored those in pM2, indicative of a close functional relationship between the two areas. A quarter of DMS neurons active during cued reaches were also active during repetitive reaches. As repetitive reaches had lower average peak velocities, this finding is consistent with DMS regulating movement vigour according to expected reward value (Wang et al., 2013). By identifying novel correlates between activity in these brain areas and visually-directed reaching, this experiment demonstrates how the newly developed task can yield new insights into the neural dynamics underlying this behaviour.

In addition, I utilised `pixels` to analyse silicone probe recordings as part of collaborative projects to investigate the neural underpinnings of forelimb motor control in mice performing object manipulation tasks (Currie et al., 2022; Dacre et al., 2021). We found that cerebellar-thalamocortical signals are required to shape motor cortical activity and trigger movement in a behavioural context-dependent manner (Dacre et al., 2021). Next, we examined how motor cortex encodes movement when mice perform two distinct movements. We found that while movement-invariant responses dominated layer 5B projection neurons, movement-specific activity is displayed by a small, distributed population of layer 5B neurons and differentially between projection neuron classes (Currie et al., 2022).

Lay Summary

Whether it is picking up our morning cup of coffee or returning serve in a game of tennis, the interactions we make with objects in our environment critically depend on visual information for guidance. Using our sense of sight, we first collect information about the identity and location of nearby objects, then we use this information to compute the trajectory of subsequent limb movements. This process recruits brain areas concerned with vision and motor control, which coordinate to generate motor commands that are sent to the spinal cord and muscles. Over the past few decades, research using non-human primates has revealed a number of brain areas whose activity relates to visually-directed reaching as well as how these areas interact. This research has illuminated our understanding of how the brain is able to generate movements guided by vision, our most vital behaviour, but using primates to probe the causal roles of specific neuron pathways in detail is difficult and costly.

In recent years, mice have become increasingly popular as model systems in biological research due to the similarities between the mouse and human brain. Their relative affordability has improved the throughput of experimental work and facilitated the development of procedures that enable neuroscientists to answer more specific questions about the brain. Despite these advantages, mice have yet to be exploited to further our understanding of how the brain controls visually-directed reaching. To begin to take advantage of this opportunity, the neuroscience community needs an accessible visually-directed reaching task for mice that can be used alongside common laboratory techniques used for probing brain function.

To address this, I first designed and implemented a behavioural task during which mice learned to perform visually-directed reaches. During the task, one of two reach targets was illuminated and mice learned to reach and grasp the illuminated target to receive a water reward. Expert mice typically followed cued reaches with a series of repetitive, self-initiated reaches, likely to collect any remnants of water left on the target. By training mice to perform high numbers of visually-directed reaches, the task can be

employed by researchers to study how the brain controls this behaviour while benefiting from the advantages of the mouse model.

Silicone probes are implantable devices that are often used to record the activity of populations of cells in the brain with high temporal resolution, which is critical for understanding how this activity relates to complex movements, such as reaches. To take full advantage of cutting-edge silicone probes called *Neuropixels*, I developed a data processing and analysis pipeline referred to as `pixels`. `pixels` forms a user-friendly library that can be used in scripts written in Python, one of the most commonly used scientific programming languages. The library has in-built integration with software for tracking complex movements during behavioural experiments and can be used with other trial-based behavioural tasks to improve the ease and speed of data analysis.

Lastly, as an example experiment to demonstrate how the task facilitates research into the brain's control of visually-directed reaching, I investigated how brain activity correlates with the behaviour. I examined activity in two brain areas: posterior secondary motor cortex (pM2), which is involved in visual behaviours, and dorsomedial striatum (DMS), which supports decision making. Once mice had become expert in the task, I implanted *Neuropixels* probes such that I could simultaneously record activity from populations of cells in both areas. After recording from these cells as mice engaged in the task, I used `pixels` to assess how changes in their activity related to the time course of reaches. Over half of pM2 cells changed their activity as mice performed visually-directed reaches: some cells displayed heightened or reduced activity from before movement, while throughout movement the proportion of cells that had reduced activity grew, suggestive of a potential role for pM2 in initiating and performing reaches. The increases and decreases in activity may complement each other to signal movement-related information to other brain areas, or alternatively, a signal may be sent by the small group of cells that were more active, with the widespread reduction in activity serving to improve the clarity of the signal. A smaller proportion of DMS cells appeared to be involved in the task, though movement-related DMS cells followed similar activity patterns to pM2 cells. In both pM2 and DMS, only a subset of movement-related cells continued to be display activity changes during repetitive reaches, suggesting that the brain controls cued and repetitive reaches differently. This may be due to cued reaches being more 'goal-directed', or alternatively, the differences in

activity may reflect differences in expected reward (i.e. water volume) or reach velocity, which was lower during repetitive reaches.

In addition, I also contributed to collaborative projects investigating how the brain controls limb movement by examining activity in key movement-related brain areas in mice performing cued pushing and pulling of a lever (Currie et al., 2022; Dacre et al., 2021). For these projects, I employed `pixels` to characterise movement-related activity in cells in a brain region called motor cortex. First, we showed that a pathway from cerebellum, through thalamus, to motor cortex is required for performing learned lever pushes, and artificially stimulating parts of this pathway led to initiation of movement. Next, we explored how two distinct movements were encoded by the activity of cells in motor cortex and found that only a small proportion of cells active during movement displayed activity that was different between the two movements, indicating that movement non-specific activity dominates this population of cells.

Acknowledgements

The last few years have been an incredible journey of fun, learning, and growth, and it has been a great privilege to share it with so many talented scientists.

I would first like to thank Ian for his endlessly supportive supervision and for pushing me to become the best that I could be. I am profoundly grateful to have received such wise and thoughtful guidance throughout my project and to have had the opportunity to carry out my project in the highly collaborative lab environment that Ian has carefully crafted.

I would also like to thank the members of my committee, Dr Gülşen Sürmeli, Dr Matthias Hennig, and Prof Mike Ludwig for their insightful and enthusiastic discussions. For a stimulating yet challenging discussion during my viva, I thank Prof Emma Wood and Dr Andrew Peters.

My fellow lab mates have truly made the past few years an absolute joy and made every day an adventure (for better or for worse). I thank Julian, Stephen, Julia, and Josh, who taught me so much and inspired me with their curiosity and drive. I also thank my fellow students Constantinos, Victor, Tom, Arthur, and Marie, with whom I shared much of this experience and who kept me going through thick and thin.

I especially thank Michelle for the love, support, and inspiration throughout my project.

Carrying out this project has been an unforgettable experience that would not have been the same without all of you.

Declaration

I declare that this thesis was composed by myself, that the work contained herein is my own except where explicitly stated otherwise in the text, and that this work has not been submitted for any other degree or professional qualification except as specified.

Matt Colligan

30th June 2023

Table of Contents

List of Abbreviations

Abbreviation	Definition
ANOVA	Analysis of variance
AP	Action potential
API	Application programming interface
CFA	Caudal forelimb area
CI	Confidence interval
DAQ	Data acquisition
DLS	Dorsolateral striatum
DMS	Dorsomedial striatum
DN/IPN	Dentate/interpositus cerebellar nuclei
GABA	γ-Aminobutyric acid
GPIO	General purpose input/output
GRIN	Gradient index
ICMS	Intra-cortical microstimulation
IN	Interneuron
IT	Intratelencephalic
ITI	Inter-trial interval
L1	Cortical layer 1
L2/3	Cortical layer 2/3
L5	Cortical layer 5
L6	Cortical layer 6
LFP	Local field potential
M1	Primary motor cortex

Abbreviation	Definition
M2	Secondary motor cortex
MSN	Medium spiny neuron
PC	Pyramidal cell
PM	Premotor cortex
PMd	Dorsal premotor cortex
PMv	Ventral premotor cortex
pM2	Posterior secondary motor cortex
PPC	Posterior parietal cortex
PT	Pyramidal tract
RFA	Rostral forelimb area
SD	Standard deviation
SSE	Sum of squared errors
V1	Primary visual cortex

Chapter 1

Introduction

Reaching and grasping is a vitally important ability that we and many other animal species use to interact with our environment, from picking up food and drinks to skilfully performing fast-paced actions like catching a basketball. The competitive advantages that these behaviours provide have resulted in the evolution of increasingly complex neural mechanisms to facilitate them. To perform these movements, we first use visual information to identify an object of interest and its egocentric spatial position. Next, we make the decision to move. Finally, motor control brain areas output the motor command to the brain stem and spinal cord to engage the muscles and initiate the movement. These processes require a complex interplay between brain areas concerned with visual perception and decision making, and motor areas that drive movement execution.

Primate research has revealed much about how the brain directs reaches to visual targets, but the specific cellular and circuit mechanisms that underlie this process remain unresolved. Using the mouse as a tractable model system with which to interrogate circuit function, in this thesis, I will describe the design, implementation, and validation of a novel visually-directed reaching task for mice and some of the neural dynamics underlying this essential behaviour.

1.1 Studying reaching behaviours in humans, non-human primates, and rodents

Reaching represents one of the primary interfaces through which we interact with our environment and has consequently been the subject of intense study by neuroscientists seeking to understand the neural underpinnings of human and animal behaviour. To

study the behaviour, researchers have performed experiments using human subjects and a range of animal models, including non-human primates, cats, and rodents.

Monkeys have proven to be an invaluable model system for studying visually-directed reaching. Several task designs have been published which typically involve head-fixation of the monkey to facilitate convenient access to the brain during invasive experiments. For example, Mountcastle et al. (1975) implemented a task that allowed positioning of the visual target anywhere along a horizontal rail in front of the animal (Figure 1.1, left). Later tasks trained monkeys to reach to visual targets whose spatial positions spanned all 3 dimensions, enabling researchers to probe how 3D space is represented in the brain (Figure 1.1, right) (Caminiti et al., 1996; Johnson et al., 1996). Similarly, human subjects have been trained in reaching tasks (Figure 1.1, bottom). These behavioural tasks have been pivotal for identifying primate brain areas whose activities correlate to features of the movement or are required to perform reaches.

Mountcastle et al., 1975

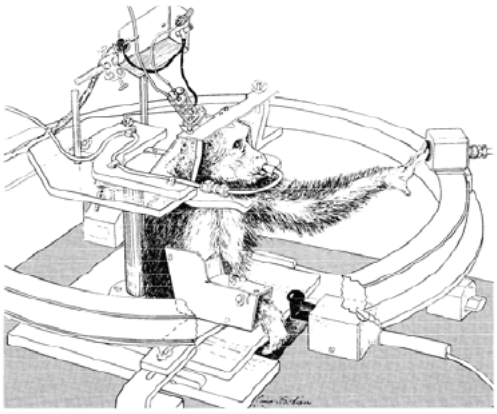

Johnson et al., 1996

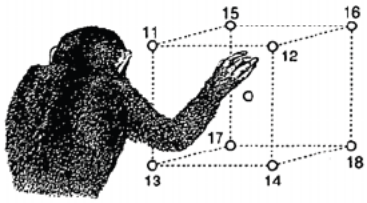

Bonnefoi-Kyriacou et al., 1998

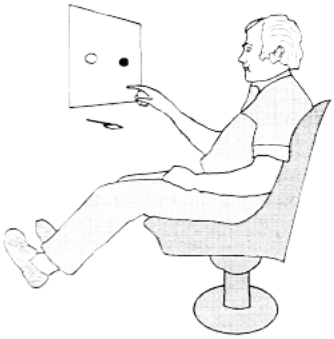

Figure 1.1: Visually-directed reaching tasks for primates and humans.
Example task designs for monkeys (top) and humans (bottom) involve the stationary subject reaching to visual targets in 1, 2 or 3 dimensions.

Research into the neural control of reaching requires a characterisation of the biomechanics of the behaviour. By using high frame rate cameras to record humans performing reaches of different distances, Jeannerod (1984) investigated how extension of the limb and shaping of the grasping hand align during reaching. Reaches were described as having two phases, a high-velocity phase involving movement of the limb and a low-velocity grip shaping phase, which consistently encompassed approximately 75% and 25% of the reach duration, respectively, regardless of distance or duration (Jeannerod, 1984). Using electromyography to record muscle activation patterns in humans and non-human primates performing reaches to visual targets, researchers have thoroughly characterised how upper body muscles engage and disengage in concert to extend the limb (Gielen et al., 1984; W.J et al., 1979). In brief, muscles in the chest and shoulder engage to initiate the movement and lift the limb (Gabriel, 1997), while the biceps and triceps act as agonist and antagonist muscle pairs, performing complementary contractions and relaxations to accelerate and then decelerate the limb towards the target (Gabriel, 1997; Gielen et al., 1984; W.J et al., 1979). Muscles in the wrist and hand coordinate to shape the hand into an appropriate configuration for grasping, after which the reach is complete.

To learn how activity in the brain relates to reaching movement and muscle activation patterns, studies employed electrophysiological recordings in monkeys trained in reaching tasks (Mountcastle et al., 1975; Schwartz et al., 1988). By correlating neuron spike patterns to task or movement variables, neural recordings have provided much insight into how different areas of the brain are involved in reaching. To probe causal involvement of specific brain areas in the behaviour, researchers began using manipulation methods such as lesions (Savidan et al., 2017), injections of muscimol (a GABA-A receptor agonist) (Mason et al., 1998), and cortical cooling (Cooke et al., 2015; Takei et al., 2021) to disrupt normal brain function. Combined with anatomical tracing studies (Bakola et al., 2013; Galea and Dariansmith, 1994; Gerbella et al., 2011; Gharbawie et al., 2010) and observations in human patients with localised brain lesions (Gréa et al., 2002; Pisella et al., 2000), these experimental approaches have been instrumental in clarifying the neural substrates of reaching.

Human and non-human primate research has been complemented by studies using rodent model systems, such as the rat and mouse, which take advantage of the behavioural and physiological similarities they share with humans. Rodents display a somewhat similar behavioural repertoire to humans, including comparable reach and grasp movements (Figure 1.2) (Sacrey et al., 2009), and with the use of food and water control procedures can be quickly and easily trained to perform behavioural tasks, providing high experimental throughput with relatively low financial cost. The improved genetic tractability of rodents has expanded our ability to delineate cell type- and pathway-specific functionality in the brain (Luo et al., 2008; Navabpour et al., 2020). This genetic access, when combined with sophisticated technologies such as optogenetic manipulation methods (Chen et al., 2018; Zhang et al., 2007) and optical imaging (Peron et al., 2015), allows researchers to ask highly specific questions about the rodent brain. For these reasons, rodents have proved extremely valuable as model systems for investigating the neural control of movement (Klein et al., 2012; Nicola et al., 2022; Ölveczky, 2011). Rodents have also been instrumental for modelling disease states and their effects on the ability to perform reaches (Diep et al., 2012; Klein et al., 2012), facilitated by the relative ease and speed of developing disease models (Vandamme, 2014).

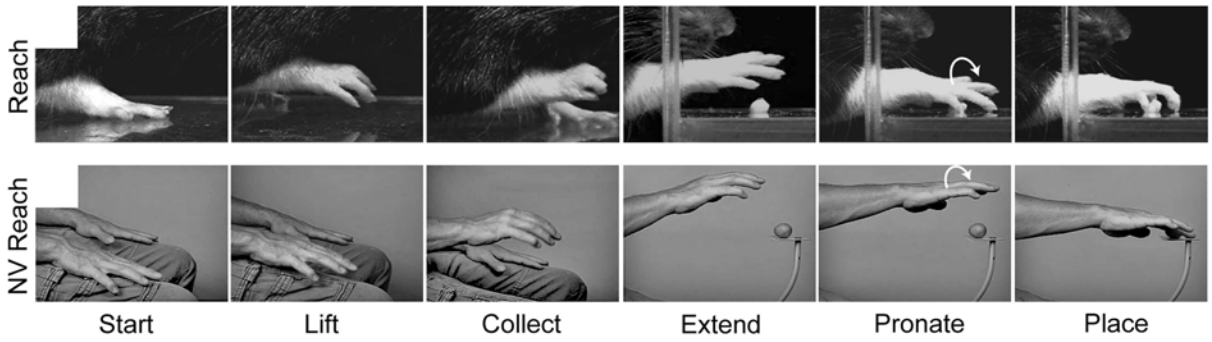

Figure 1.2: Conserved reach and grasp movements between humans and rodents.
Images illustrating the kinematic structure of reaching and grasping in a rat and a human, demonstrating homology between the species. In both cases, the hand is lifted, the digits collect, the arm is extended towards the target, the hand pronates, and is lastly placed upon the target. Adapted from Karl and Whishaw (2013).

As with primates, rodents have been used in reaching task experiments to understand how the brain generates these movements (Figure 1.3) (Guo et al., 2014a; Montoya et al.,

1991; Nicola et al., 2022). A variety of task designs have been published using both freely moving and head restrained animals to study reaching behaviours. Freely moving reaching tasks can be categorised into two groupings: the 'staircase test', where rodents reach for food pellets down small steps (Figure 1.3, top left) (Baird et al., 2001; Montoya et al., 1991), and designs where the animal reaches through one or more slits in the wall of a chamber to retrieve a reward (Figure 1.3, top right) (Hurd et al., 2013; Li and Hollis, 2021; Whishaw and Tomie, 1989). Tasks using head restraint have also been published (Figure 1.3, bottom), in which mice reach for food pellets (Levy et al., 2020), water droplets (Galiñanes et al., 2018), or agar cubes (Manita et al., 2022). In most reaching tasks, animals learn to direct their movement towards the target by following directional sensory information such as from olfaction or tactile sensation (Figure 1.3, top). Other tasks instead aim for mice to learn to associate an arbitrary auditory (Hasegawa et al., 2017) or vibrotactile (Galiñanes et al., 2018) stimulus to a learned movement (Figure 1.3, bottom), and thus do not require that the animal use spatial information from the target to control the movement. Directed movement, as performed during primate visual reaching tasks, requires that brain areas that process target spatial information influence motor control areas. While existing rodent task designs have been used effectively to further our understanding of motor control, so far no published task exists in which mice learn to perform visually-directed reaching.

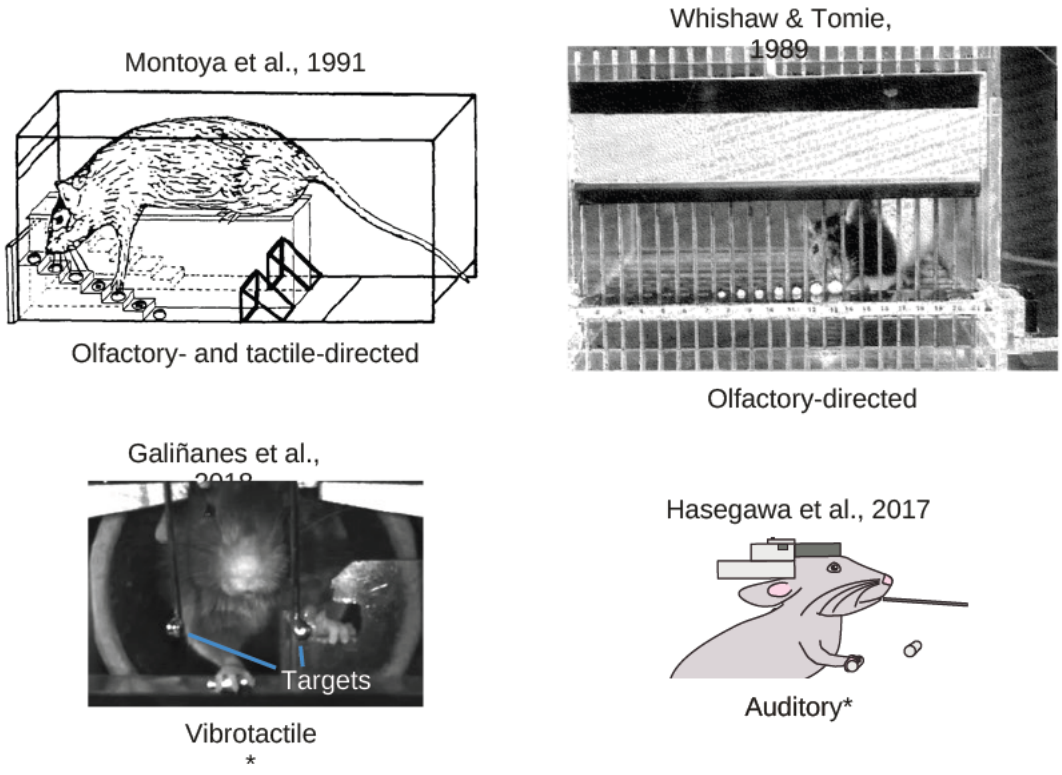

Figure 1.3: Reaching tasks for rodents.
Example task designs for rodents show a diversity of features including unrestricted movement (top) or head fixation (bottom). Tasks that associate an arbitrary sensory stimulus to a learned movement rather than requiring that the animal use spatial information to direct movement are indicated by *.

The lack of a mouse visually-directed reach task represents a missed opportunity to extend the numerous scientific advantages of the mouse as a model system to interrogate circuit function. While mice do have inferior vision when compared to primates, they are capable of traversing virtual reality environments using visual landmarks (Harvey et al., 2009; Leinweber et al., 2017), and when attempting to approach and capture prey, visual perception is critical for success (Hoy et al., 2016). Therefore, development of a visually-directed reaching task for mice will enable researchers to ask highly specific questions about how visual brain areas interact with motor control areas to direct movement.

1.2 Neural control of visually-directed reaching in primates

By combining behavioural tasks with in vivo neural recording and manipulation techniques, and analysing neuroanatomy, researchers have identified a number of key brain areas required for visually-directed reaching and what roles they may serve.

Motor cortex is the seat of motor execution and has therefore been the subject of intense study. Primate motor cortex is composed of several subregions including the primary motor cortex (M1), premotor cortex (PM), and supplementary motor area. The primary function of M1 is to generate motor commands and output them via pyramidal tract neurons, which target the brainstem and spinal cord (Dum and Strick, 2002; Galea and Darian-smith, 1994), ultimately leading to engagement of the muscles and the initiation of movement (Fogassi et al., 2001; Schaffelhofer and Scherberger, 2016; Umilta et al., 2007). During movement execution, neural activity in M1 correlates with a range of movement parameters, including speed (Churchland et al., 2006), direction (Schwartz et al., 1988), and force (Evarts, 1968). Neural activity has also been found to correlate to more complex features of movement. For example, when monkeys reach and grasp an object, neurons in M1 display activity that is selective for the reach and grasp components (Vaidya et al., 2015). Similar observations have led to recent models

positing that M1 organisation aligns with ethological categories of behaviours such as hand-to-mouth, defensive, or reaching movements (Graziano, 2006). Activity within these subregions is required for specific movements, as exemplified by the finding that inactivating thumb- or index finger-related regions with muscimol disrupts grasping (Brochier et al., 1999). The importance of this activity is underlined by experiments that showed electrical microstimulation of motor cortex can elicit complex, multi-joint arm movements, indicating that motor cortical output is sufficient to command movements (Graziano et al., 2005).

Premotor cortex is further subdivided into dorsal PM (PMd) and ventral PM (PMv), which are believed to support decision making and preparatory functions (Boussaoud and Wise, 1993; Cisek and Kalaska, 2005; Lara et al., 2018). Inactivating PMv, whose activity reflects the grip posture required for grasping observed objects (Murata et al., 1997; Umilta et al., 2007), results in failure to perform visually-directed grasping (Fogassi et al., 2001). While PMd displays activity related to both reaching and grasping (Cisek and Kalaska, 2005; Grol et al., 2007), electrical microstimulation of subregions across PM can induce reaching or grasping specifically (Gharbawie et al., 2011; Graziano et al., 2005; Kaas et al., 2013), suggesting parallel pathways may control these components. In addition to outputting from M1, corticospinal projections also arise from premotor cortex to exert direct control over computations in the spinal cord (Dum and Strick, 2002; Geyer et al., 2000).

Motor cortical activity is shaped by a number of subcortical areas. Activity in the cerebellum has been found to represent movement parameters during reaching such as direction, position, and speed (Casabona et al., 2010), and disrupting this activity induces inaccuracies in reaching and grasping movements (Bonnefoi-Kyriacou et al., 1998; Goodkin and Thach, 2003; Mason et al., 1998; Monzee et al., 2004). The cerebellum modulates activity in motor cortex via the thalamic ventral lateral nucleus (Geyer et al., 2000; Ilinsky and Kultas-Ilinsky, 2002; Nashef et al., 2019), which is thought to integrate motivational and proprioceptive information from basal ganglia and cerebellum, respectively, while forming a feedback loop with cortex (Bosch-Bouju et al., 2013). This input from thalamus is required for motor cortex to generate reaches (Sauerbrei et al., 2020).

For motor areas to accurately direct movement, their computations must integrate information processed by the visual system. The visual scene is first captured by the

retina and transmitted to the lateral geniculate nucleus of the thalamus, which performs various initial information processing steps such as using contrast between adjacent receptive fields to identify features (Ghodrati et al., 2017; Usrey and Alitto, 2015). Processed information is then sent to primary visual cortex (Figure 1.4) (Usrey and Alitto, 2015), which extracts features such as the positions and orientations of edges and lines in the visual scene, before being transferred to higher order visual areas for more abstract processing (Huff et al., 2022; Resulaj, 2021; Wang et al., 2012).

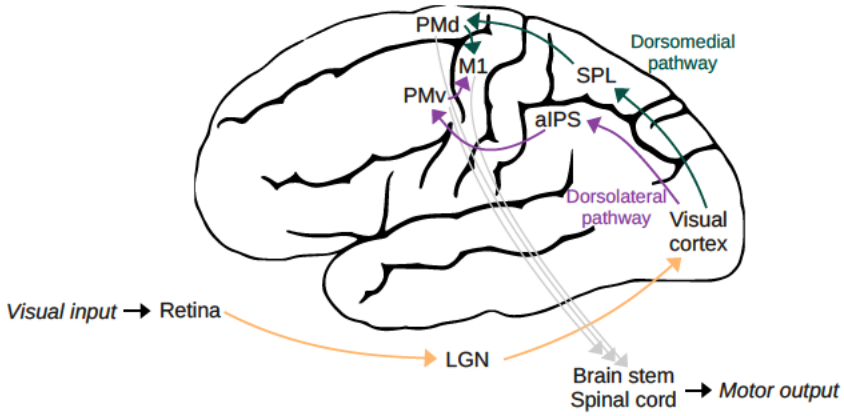

Figure 1.4: Flow of information in the primate brain during visually-directed reaching.
Illustration of regions in the macaque brain critical for processing visual information and using it to shape motor commands generated in premotor and motor cortex. Adapted from Karl and Whishaw (2013) and Fattori et al. (2017).
LGN, thalamic lateral geniculate nucleus; aIPS, anterior intraparietal sulcus; SPL, superior parietal lobule; PMd, dorsal premotor cortex; PMv, ventral premotor cortex; M1, primary motor cortex.

Visual cortical areas output to posterior parietal cortex (PPC) (Felleman and Van Essen, 1991; Gamberini et al., 2021; Resulaj, 2021), whose activity reflects advance selection of movement (Cui and Andersen, 2011; Fattori et al., 2010; Murata et al., 2000) and intrinsic features of objects targeted for grasping, such as shape, size and orientation (Murata et al., 2000; Schaffelhofer and Scherberger, 2016). These features are fed into the motor system to direct movement via projections from PPC to M1 and PM (Averbeck et al., 2009; Bakola et al., 2013; Caminiti et al., 1996; Marconi et al., 2001). Distinct parietofrontal networks between subregions within these areas have been described as the dorsomedial pathway, which connects the superior parietal lobule and PMd (Caminiti et al., 1996; Wise et al., 1997), and the dorsolateral pathway, which connects the anterior intraparietal sulcus to PMv (Figure 1.4) (Davare et al., 2011; Filimon, 2010).

Electrophysiological recordings have primarily linked the dorsomedial pathway to reaching (Cisek and Kalaska, 2005; McGuire and Sabes, 2011) and identified grasp-related activity in the dorsolateral pathway (Murata et al., 2000; Sakata et al., 1995; Umilta et al., 2007). Additionally, long-train electrical microstimulation of the dorsomedial or dorsolateral pathways elicits reach or grasp movements, respectively, (Gharbawie et al., 2011; Graziano et al., 2005; Kaas et al., 2013). These findings have led to the "dual visuomotor channel theory", according to which the dorsomedial pathway underlies extension of the hand to the reach target based on the target's extrinsic properties (such as its egocentric location), whereas the dorsolateral pathway ensures that the grasping hand is shaped appropriately based on the target's intrinsic properties (such as its shape and size) (Flindall and Gonzalez, 2019; Karl and Whishaw, 2013). These parietofrontal circuits between PPC and motor cortex continue to direct reaching throughout movement to ensure success even if limb or target positions undergo unexpected changes (Archambault et al., 2011; Buneo and Andersen, 2006; Desmurget et al., 1999; Lee and Donkelaar, 2006).

1.3 Neural control of reaching in rodents

Mirroring findings from primate experiments, rodent motor cortex has also been found to display movement-related activity preceding and during reaches (Estebanez et al., 2017; Galiñanes et al., 2018; Wang et al., 2017). Rodents have enabled research into motor cortical function to ask questions with cell-type and pathway specificity. For example, Estebanez et al. (2017) were able to specifically examine the activity profiles of layer 5 (L5) parvalbumin-expressing interneurons during reaching and compare them with other neurons. To do this, they used a genetically modified mouse line that expresses Cre recombinase in parvalbumin-expressing cells and delivered Cre-dependent Channelrhodopsin-2 into M1 using a virus vector (an example of using the Cre/*loxP* recombinase system for cell type-specific gene expression). They performed extracellular recordings in M1 and identified parvalbumin-expressing interneurons using 'opto-tagging', i.e. illuminating M1 and identifying neurons that exhibited short-latency spiking (Lima et al., 2009). They found that pre-reach M1 activity is led by this neuron subpopulation and propose that these interneurons may provide early inhibition for shifting the state of an M1 dynamical system or restricting the execution of inappropriate movements. Experiments probing the causal role of M1 in reaching have

also benefited from genetically modified mouse lines. By using mice expressing Channelrhodopsin-2 in interneurons, studies have been able to specifically photoactivate cortical interneurons to suppress M1 output with a high degree of temporal control, demonstrating that motor cortical output is required for reach initiation and ongoing limb control (Galiñanes et al., 2018; Guo et al., 2015; Sauerbrei et al., 2020).

Rodent M1 is complemented by secondary motor cortex (M2), a heterogeneous region that plays critical roles in the control of voluntary actions (Barthas and Kwan, 2017). While specific M2 subregions have been found to be required for reach and grasp behaviours (Galiñanes et al., 2018; Wang et al., 2017), the absence of a published visually-directed reaching task for mice has precluded research elucidating how motor cortex is influenced by visual areas to direct reaches. As primate and human research has placed the parietofrontal loop between PPC and PM as central to visual control of the forelimb (Archambault et al., 2015; Battaglia-Mayer et al., 2014), posterior M2 (pM2), which is the sole recipient of PPC inputs to motor cortex (Figure 1.5a) (Hovde et al., 2018; Itokazu et al., 2018; Zingg et al., 2014), appears uniquely placed to bridge visual and motor areas for guiding movement. Rodent studies have confirmed that PPC is required to perform visually-cued decision making behaviours (Goard et al., 2016; Harvey et al., 2012; Hwang et al., 2017; Licata et al., 2017) and have found that it becomes more active when mice push a lever in response to an auditory cue (Makino et al., 2017). The projections from PPC to pM2 are required for accurate control of forelimb movements (Hwang et al., 2017) and are reciprocated (Hovde et al., 2018; Itokazu et al., 2018), further supporting homology between pM2 and PM. To exert influence over motor commands, pM2 may modulate spinal cord activity via its projections to M1 L5b (Hooks et al., 2013), though some evidence suggests pM2 may have direct corticospinal projections (Figure 1.5a) (Liang et al., 2011; Wang et al., 2017).

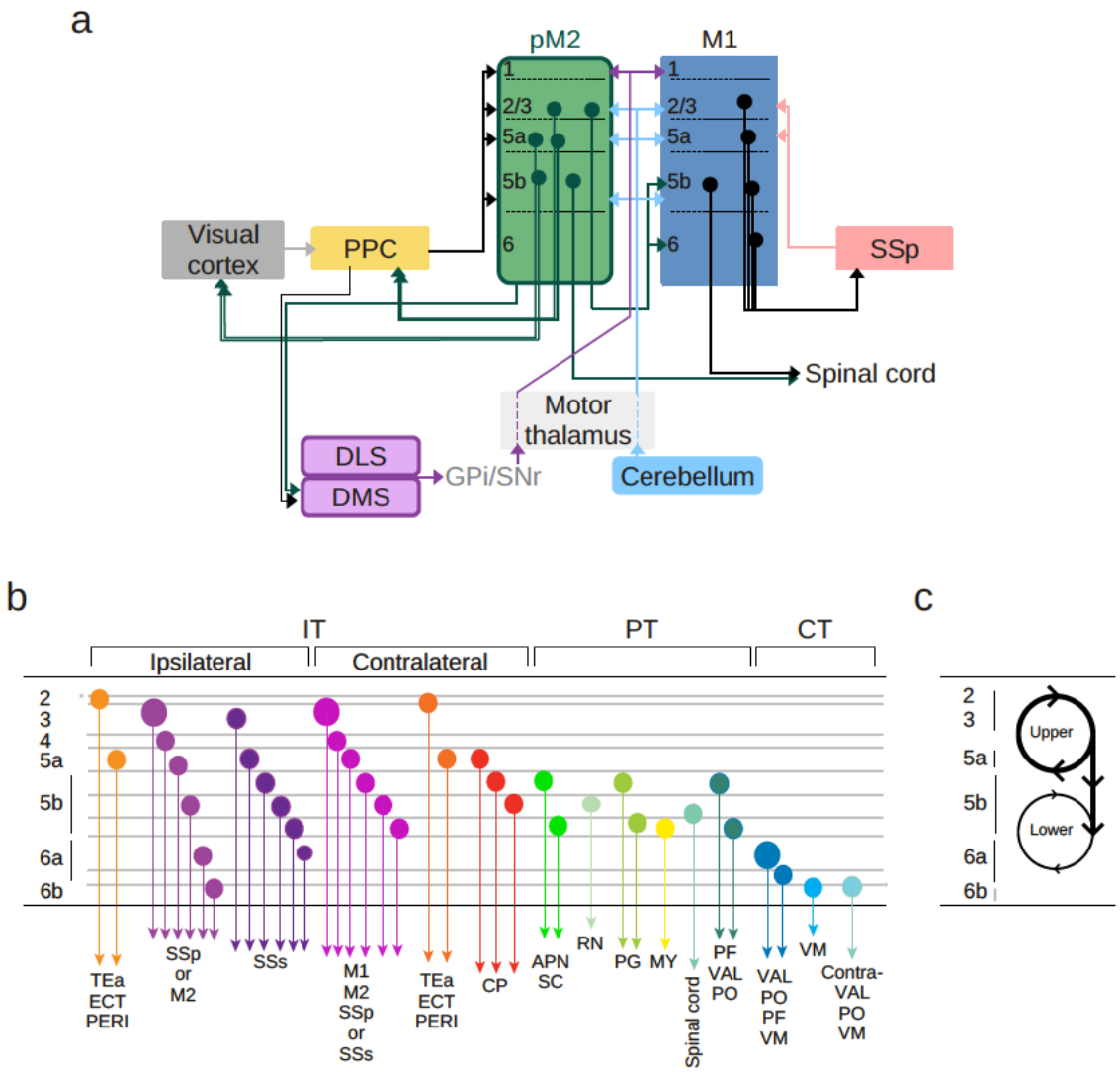

Figure 1.5: Motor cortical circuitry.

(a) Long-range inputs and outputs to pM2 and M1 with influence over the control of reaching.

(b) Laminar distributions and projection targets of excitatory neuron classes within motor cortex. IT, intratelencephalic; PT, pyramidal tract; CT, corticothalamic. Adapted from Muñoz-Castañeda et al. (2021).

(c) Top-down flow of excitation within motor cortex. Adapted from Weiler et al. (2008).

DLS, dorsolateral striatum; DMS, dorsomedial striatum; GPi, internal segment of the globus pallidus; SNr, substantia nigra pars reticulata; SSp, primary somatosensory cortex; IT, intratelencephalic; PT, pyramidal tract; CT, corticothalamic; TEa, temporal association area; ECT, ectorhinal area; PERI, perirhinal area; SSs, secondary somatosensory cortex; CP, caudate putamen; APN, anterior pretectal nucleus; SC, superior colliculus; RN, red nucleus; PG, pontine grey; MY, medulla; PF, parafascicular nucleus; VAL, ventral anterior-lateral thalamic complex; PO, posterior thalamic complex; VM, ventral medial thalamic nucleus.

Internal motor cortical circuits are composed of excitatory principal neurons and interneurons. Principal neurons comprise three broad and heterogeneous classes based on projection targets and laminar distributions (Figure 1.5b): intratelencephalic, corticothalamic, and pyramidal tract neurons. Intratelencephalic neurons have somata across L2-6 and primarily project bilaterally to motor and somatosensory cortex and striatum (Lin et al., 2018; Muñoz-Castañeda et al., 2021). From pM2, these neurons also output to PPC and visual cortex, conveying motor information thought to provide movement efference copies that support visually-directed movement (Itokazu et al., 2018; Leinweber et al., 2017). In deep layers, corticothalamic neurons primarily innervate thalamus and reside in L6, while pyramidal tract neurons, which demarcate L5b, form the principal output of motor cortex via projections to brain stem and spinal cord (Harris and Shepherd, 2015; Muñoz-Castañeda et al., 2021). These populations of excitatory neurons form complex relationships that are modulated by inhibition from interneurons (Yamawaki and Shepherd, 2015), which comprise an array of classes that display distinct electrophysiological, morphological, and gene expression properties (Blatow et al., 2005; Gupta et al., 2000; Harris and Shepherd, 2015; Jiang et al., 2015; Markram et al., 2004). While parvalbumin-expressing interneurons in M1 L5 have been found to display activity prior to movement when mice perform reaches (Estebanez et al., 2017), much remains to be investigated about how other interneuron classes might be involved in reaching. Compared with other cortical areas, motor cortex has a substantially reduced L4 (Yamawaki et al., 2014) and therefore deviates from the canonical cortical microcircuit, in which the dominant intracortical pathway of excitation flows from L4 to L2/3 then L5 (Harris and Mrsic-Flogel, 2013; Harris and Shepherd, 2015). Motor cortex instead exhibits a top-down organisation, where descending excitation from L2/3 shapes the activity of output neurons in deep layers (Figure 1.5c) (Weiler et al., 2008).

Long-range inputs to rodent motor cortex, which are largely reminiscent of those in primates, modulate motor commands generated by cortex. The cerebellum influences motor cortical activity via motor thalamus, which primarily innervates L2/3 and L5 (Figure 1.5a) (Hooks et al., 2013), forming a cerebellar-thalamocortical pathway that has been shown to be capable of triggering movement in a forelimb lever task (Dacre et al., 2021). This pathway arises from the anterior interpositus nucleus, which has a direct role in controlling the accuracy of reach trajectories (Becker and Person, 2019; Low et al., 2018), and thus may regulate visually-directed reaching via its inputs to pM2 (Hooks et

al., 2013; Hunnicutt et al., 2014). Basal ganglia, which have been linked to a diverse set of functions including action selection and initiation (Humphries and Gurney, 2002; Klaus et al., 2019; Mink, 2003, 1996), originate another significant thalamocortical pathway that terminates in L1 (Kaneko, 2013; Kuramoto et al., 2009). Signals from the striatum, which plays influential roles in regulating forelimb movement kinematics (Dhawale et al., 2021) and vigour (Dudman and Krakauer, 2016; Wang et al., 2013), are conveyed to motor cortex via this pathway (Kasahara et al., 2022). Motor cortex also receives corticocortical afferents in addition to those from PPC, including dense input to L2/3 and L5a pyramidal neurons from somatosensory cortex (Figure 1.5a) (Mao et al., 2011; Petrof et al., 2015), which is required for successful reach execution (Mirza Agha et al., 2021).

These motor cortical circuits generate motor commands that are output to the brain stem and spinal cord. In pM2, neurons also output to dorsomedial striatum (DMS) (Figure 1.5a) (Hintiryan et al., 2016; Pan et al., 2010), a subcortical area which uses learned action-outcome associations to guide action selection (Balleine and O'Doherty, 2010; Hwang et al., 2019). Like pM2, DMS receives substantial input from PPC, but these two projections originate from largely non-overlapping populations of neurons, giving rise to parallel pathways proposed to bias action selection and control movement, respectively (Hwang et al., 2019). Conflicting with this model, a region of M2 that overlaps with PPC inputs has also been linked to a role in adjusting action selection based on outcome (Gremel and Costa, 2013a). Moreover, DMS may contribute to motor control; movement-related spatial information is encoded by a small population of neurons in associative striatum in primates (i.e. homologous to rodent DMS) during visually-directed reaching (Ravel et al., 2006), though it is unclear whether this originates from PPC, PM, or elsewhere. To further understand the role of pM2, it would be valuable for future work to clarify the functional and anatomical relationships between pM2, DMS, and PPC.

1.4 Overview of thesis

Rodents have enabled researchers to ask questions with cell-type and pathway specificity, complementing primate research. However, as no published task trains rodents to perform visually-directed reaches, significant gaps remain in our knowledge of how the brain controls this behaviour. Critically, much remains to be understood

about how different populations of neurons in visual brain areas (such as visual cortex and PPC) influence activity in motor cortical populations. As described in the previous section, the parietofrontal loop between PPC and PM in primates, key for visually-directed reaching, may have a homologous circuit in rodents. If a suitable task were made available for rodents, characterising this homology would enable researchers to ask highly specific questions about the structure and function of these circuits. Similarly, it would be possible to investigate in greater detail the contributions of subcortical areas such as basal ganglia and cerebellum, which have been shown to be important for visually-directed reaching.

Our understanding of the neural systems that underlie visually-directed reaching remains limited by the absence of a visually-directed reaching task for mice. To address this, I designed and implemented a task for mice that neuroscientists can adopt to interrogate specific cellular and circuit mechanisms that underlie this behaviour.

The task is designed for freely moving mice and aims to be compatible with common neuroscience methods such as in vivo electrophysiological recordings. Chronically implanted devices using wire electrodes (Bhalla and Bower, 1997), tetrodes (Dhawale et al., 2017), or silicone probes (Bragin et al., 2000; Okun et al., 2016; Voroslakos et al., 2021) have been critical for performing neural recordings in unrestrained, behaving mice, and improvement of these tools continues to make freely moving recordings more powerful and accessible. For example, Neuropixels silicone probes, which can simultaneously record extracellular activity from hundreds of neurons, can be chronically implanted for use in freely moving animals (Juavinett et al., 2019; Jun et al., 2017; Steinmetz et al., 2021).

To validate the task and demonstrate its utility, I performed proof-of-concept recordings of the neural correlates of visually-directed reaching in pM2 and DMS. I performed extracellular recordings in mice engaging in the task via chronically implanted Neuropixels silicone probes. To simplify and expedite analysis of Neuropixels probe recordings collected during behavioural experiments, I developed a bespoke Neuropixels data processing and analysis pipeline, which was instrumental in understanding how motor cortical activity related to cued lever movements as part of two peer-reviewed studies (See appendices) (Currie et al., 2022; Dacre et al., 2021). Then, using the pipeline, I related firing rate changes in pM2 and DMS to visually-directed

reaching to gain novel insight into how these brain areas may be involved in the behaviour.

Chapter 2

A visually-directed reaching task for mice

2.1 Introduction

Reaching and grasping is a crucial behaviour that facilitates effective interaction with our environment. Humans and other primates use their forelimbs to perform basic, everyday tasks guided by visual perception of objects within their environment. Underlying purposive visually-directed movements is a complex interplay between brain areas required for visual processing and motor control. Research seeking to understand how the brain controls visually-directed movements often takes advantage of model animals that can be trained to perform these behaviours under controlled conditions.

While mice are understood to have inferior visual capabilities when compared to primates, they do require vision to guide their behaviour. A common experimental paradigm used to probe visual perception in mice involves training them to discriminate between gratings and other geometric shapes that are visually distinct. Using this approach, it has been shown that mice can discriminate between visual stimuli that differ in movement orientation and contrast (Andermann et al., 2010; Zatka-Haas et al., 2021), even when perception is degraded by the introduction of noise (Khastkhodaei et al., 2016; Stirman et al., 2016). Moreover, mice are capable of using visual information to navigate virtual reality environments (Harvey et al., 2009; Leinweber et al., 2017), and rely on vision for accurate approach and capture of prey (Hoy et al., 2016). Therefore, mice rely on vision to direct complex behaviours and are suitable for serving as an animal model for investigating the neural control of visually-directed movements.

Despite the mouse model's potential for high throughput experiments and improved genetic tractability compared with primates, the absence of a visually-directed reaching task for mice has so far precluded their use for studying this important behaviour. In this

chapter I will discuss the development of a novel visually-directed reaching task for freely moving mice, the methods I used, and will demonstrate its utility.

The task was designed to meet several important criteria:

- Reaches must be visually-directed. Visually-directed reaches are reaches *to* visual stimuli; the spatial location of a reach target is communicated to the animal by a visual cue originating from that location.
- Mice should perform high numbers of comparable reaches for statistical robustness.
- The learning regime should maximise the number of animals that are able to achieve an 'expert' level of task performance.
- The implementation must be compatible with common experimental techniques such as neurological recordings and optogenetic perturbations.

Next, I will describe the design and implementation of features that meet the above criteria.

2.2 Methods

2.2.1 Animals

All procedures were performed under license from the UK Home Office in accordance with the Animal (Scientific Procedures) Act 1986 and approved by the University of Edinburgh local ethical review committee. Female and male C57BL/6 mice (Charles River, UK) aged 6-12 weeks with baseline weights of 20-22 g were used. Baseline weights were calculated as the mean of 3 consecutive daily weights. Mice were housed in same-sex groups of 2-5, with male mice housed exclusively with littermates. Cages contained running wheels, tubes, tissue, and paper dens for enrichment, and mice were given *ad libitum* access to food. Mice were maintained on a reverse 12:12 hour light cycle and all procedures were carried out during the dark period.

Mice underwent a water restriction protocol to facilitate learning as described in Dacre et al. (2021). Briefly, mice were given 1 mL drinking water per day. Mice generally

consumed less than 1 mL of water while engaging with the task and therefore were supplemented up to 1 mL after training. Body weights were measured daily and animals that dropped below 85% of their baseline weight were supplemented with additional water. Providing mice with running wheels can cause a drop in body weight, so to ensure that weights had stabilised, baseline weights were calculated at least 3 days after mice were provided with running wheels. During the first 7 days of water restriction, mice underwent daily habituation to procedure rooms and handling areas. Behavioural training began after this habituation period.

2.2.2 Task hardware

The aim of the task was to train mice to perform visually-directed reaches, which are reaches targeted to the egocentric spatial position of visual stimuli. This required a task with more than one reach target, because otherwise mice would not need to pay attention to the position of the visual stimulus, where simply responding to the stimulus onset (i.e. via a change in ambient light originating from the stimulus) would be sufficient to signal mice to reach to the target. Therefore, to ensure that mice used the spatial location of stimuli to direct reaches, the task design used two independent targets.

The target hardware was designed so that mice associated reaching and grasping the visual stimuli with receiving water rewards. This was achieved by fixing a light-emitting diode (LED) and a touch sensor to the tip of a water spout. The LED provided a visual stimulus that when grasped immediately resulted in water being dispensed into the grasping hand.

Two targets were constructed and controlled by a Raspberry Pi 4 B (Figure 2.1a; RS Components 182-2096), a low-cost single-board computer commonly used for laboratory experiments in the biological sciences (Jolles, 2021). The Raspberry Pi executed custom-made Python-based software that asynchronously controlled outputs to and listened for events from a circuit controlling the task apparatus via general purpose input/output (GPIO) pins (Figure 2.1a).

LEDs: To generate visual stimuli from each of the reach targets, I used Cree XLamp XQ-A SMD LEDs (RS Components 103-4292). Small dimension LEDs (1.6 x 1.6 x 1.6 mm) were selected to facilitate embedding within the targets while not being too large for mice to

grasp. While white light was used in this project, they come in a range of colours, allowing for flexibility in experimental design if alternative colours are preferred. The LEDs were triggered by a 3.3 V signal from the Raspberry Pi and were grounded via a 680 Ω resistor.

Touch sensors: Each target was designed with a corresponding touch sensor in the form of a small piezoelectric sensor (RS Components 285-784) with dimensions 15 x 1.5 x 0.6 mm (Figure 2.1b). The piezoelectric sensors required an additional Arduino Uno microcontroller (RS Components 715-4081) to process the raw voltage signals (Figure 2.1a). Each sensor was powered by a 3.3 V output and was monitored via a GPIO socket on the Arduino. The Arduino relayed a binary signal to the Raspberry Pi representing whether the piezoelectric sensor was experiencing vibration-induced mechanical distortion above a threshold value (see Section 2.2.4), used to detect when mice made contact with the targets. Self-contained capacitive sensors can also be used in place of the combination of piezoelectric sensors and Arduino controller as they are able to output binary signals directly. However, during testing I found that the sensitivity of capacitive touch sensors often drifted over time making them unreliable. Furthermore, capacitive touch sensors can introduce electrical noise during electrophysiological recordings.

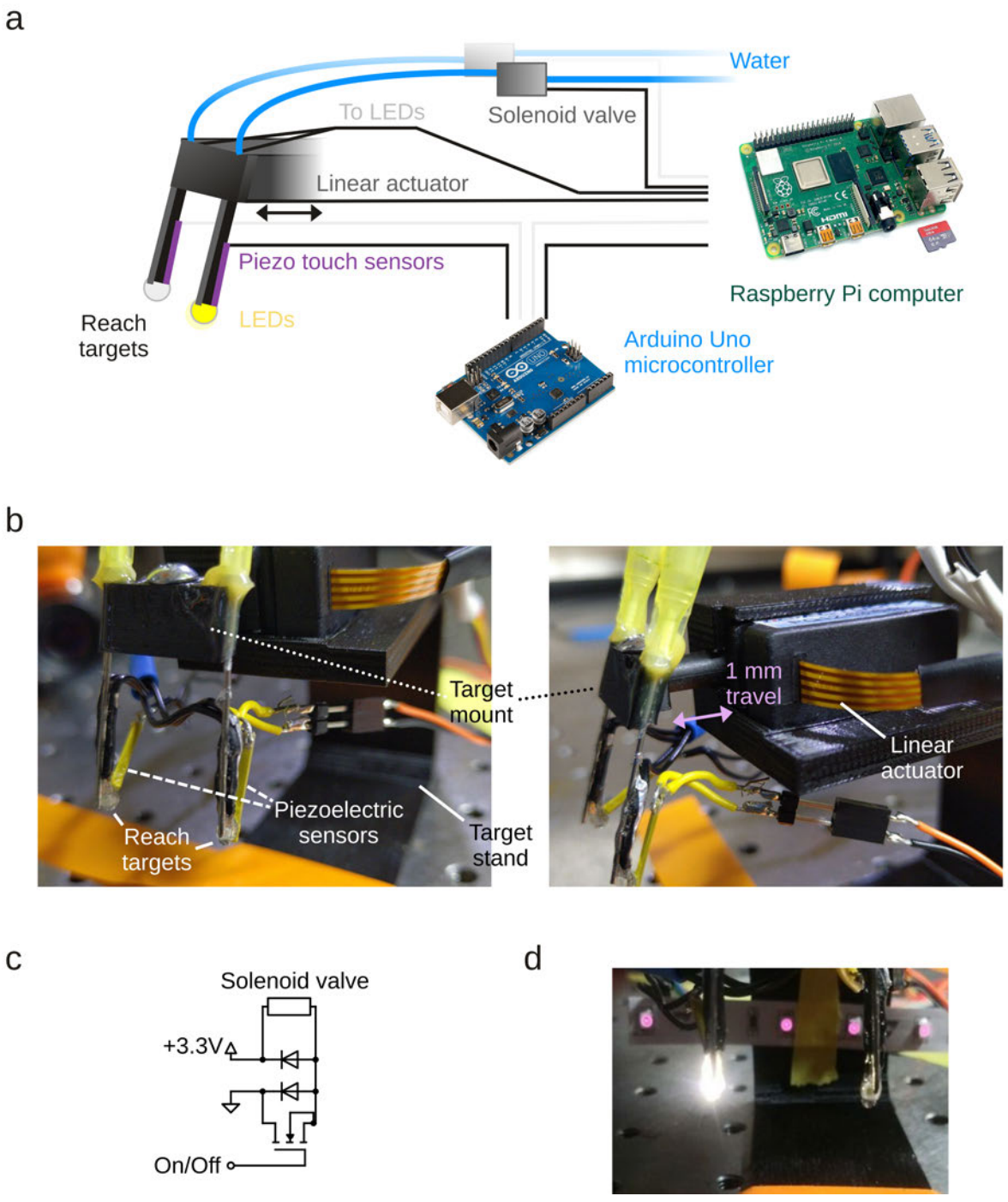

Figure 2.1: Behavioural task hardware.

(a) Overview of task hardware. All inputs (touch sensor events preprocessed by an Arduino Uno) and outputs (control of LEDs, solenoid valves and linear actuator) were controlled by a Raspberry Pi single-board computer. Raspberry Pi photo adapted from Jolles et al. 2021. Arduino Uno photo attributed to SparkFun Electronics Boulder USA licensed under Creative Commons 2.0.

(b) Reach targets were fixed to a 3D-printed target mount, which was attached to a linear actuator. The linear actuator was supported by a 3D-printed actuator stand. The direction of travel of the actuator is indicated by the pink arrow and has a 1 mm range of travel.

(c) Solenoid valve driver circuit. Each solenoid valve was controlled by a dedicated driver circuit connected to the Raspberry Pi ensuring consistent and reliable valve control.
(d) The reach targets from the mouse point-of-view with the left target illuminated. Note that from within the areana, the targets are visible through the slits.

Water spouts: The targets were each mounted on the end of a trimmed 19 gauge (19G) injection needle (BD Microlance). The top end of each needle was connected to a solenoid valve (Bibus Ltd) via 2 mm inside diameter silicone tubing (BRAND 143352), which in turn connected to a water reservoir (Figure 2.1a, top). The solenoid valves were powered and controlled from dedicated Raspberry Pi GPIO outputs via individual solenoid driver circuits (Figure 2.1c). The solenoid driver circuits aided in reliably opening and closing the values to provide reproducible water rewards.

Linear actuator: The spouts were mounted on a linear actuator (Actuonix PQ12-R 20 mm 63:1 6V) via a 3D printed target mount (Figure 2.1b). The actuator was then mounted on a 3D-printed stand (Figure 2.1b) allowing for controlled and precise forward/backward movement of the targets. To allow mice to make an association between the targets and water, mice were initially able to reach the targets with their nose and tongue through a slit in the task arena wall (see Section 2.2.3). Once mice started to engage with the task, the linear actuator enabled movement of the targets away, forcing mice to instead use their forelimb (further described below in Section 2.2.5). The 10 mm actuator travel was sufficient to move the targets beyond the reach of the tongue.

The above components were assembled in the configuration illustrated in Figure 2.1, following these steps:

1. The 19G needles were trimmed to remove the bevel and inserted into a custom 3D-printed target mount (Figure 2.1b), before being fixed in place using Araldite epoxy adhesive (RS Components 756-0102).
2. ~3 cm of silicone tubing was cemented into the top of each needle with Araldite.
3. The solenoid valves were connected via tubing to water reservoirs (Figure 2.1a, top).
4. The solenoid valves were plugged into solenoid driver circuits connected to the Raspberry Pi.

5. The LEDs were soldered to thin (< 1 mm) wires that ran along the back of the needles from the tip (Figure 2.1b, black wires). The LEDs and wires were fixed to the needles using UV-curing glue (Henkel Loctite 4305), which is ideal for this purpose due to its water-resistance and transparency. Layers of UV-curing glue were used to sculpt a round node at the end of each needle to form the reach targets. The LEDs and their solder joints were fully sealed within the glue, but the nearby needle openings remained unsealed to permit water flow onto the surface of each target.
6. The two LEDs were each connected to 3.3 V outputs on the Raspberry Pi and their ground wires were combined and connected via a 680 Ω resistor to a ground on the Raspberry Pi.
7. A piezoelectric touch sensor was cemented to the back of each target (Figure 2.1b) and connected to 3.3 V and a GPIO input on the Arduino Uno (Figure 2.1a, purple). A 1 MΩ resistor was connected in parallel to each sensor.
8. A GPIO output on the Arduino Uno was connected to a GPIO input on the Raspberry Pi for transmission of detected touch sensor events.
9. The linear actuator was mounted to a 3D printed stand, and the target mount was attached to the end of the actuator (Figure 2.1b).
10. The actuator's input pin was connected to a GPIO output on the Raspberry Pi.
11. The Arduino Uno, Raspberry Pi and linear actuator were each powered by dedicated power supplies to ensure that operation of each component was reliable.

The final design of the reach targets is shown in Figure 2.1d. The components list required to build a single set of task apparatus is documented in Table 2.1.

Table 2.1: Component list for a single task arena. Sources of generic components have been omitted.

Component	Quantity	Source
Raspberry Pi 4 B	1	RS Components 182-2096
Arduino Uno	1	RS Components 715-4081
Cree XLamp XQ-A SMD LEDs	2	RS Components 103-4292
Piezoelectric vibration sensor	2	RS Components 285-784
Araldite epoxy adhesive	1 tube	RS Components 756-0102
UV-curing glue	1 tube	Henkel Loctite 4305
19 G injection needles	2	BD Microlance
2-way 5V solenoid valve	2	Bibus Ltd
2 mm inside diameter silicone tubing	50 cm	BRAND 143352
Linear actuator 20 mm 63:1 6V	1	Actuonix PQ12-R
Target mount	1	3D printed
Actuator stand	1	3D printed
<= 1 mm wire	50 cm	-
1 MΩ resistor	2	-
680 Ω resistor	1	-
BS170 N-Channel MOSFET	2	-
1N4148 diode	4	-

2.2.3 Arena

To facilitate convenient and efficient training in the visually-directed reaching task, I designed and constructed a task arena for mice that permitted naturalistic freely moving behaviour and created an environment free of task-irrelevant stimuli. The arena design was similar to that used by Metz and Whishaw (2000) based on a simple rectangular box. The reach targets were positioned behind the front panel of the box, accessible through slits in the wall (Figure 2.2a). During early training, mice explored the arena, slits, and

reach targets, learning to associate visual stimuli with water rewards before continuing to learn visually-directed reaching.

The front panel was made from 3 mm thick transparent acrylic, allowing mice to see the reach targets from any location inside the arena. The remaining walls were made from 3 mm thick opaque black acrylic to prevent mice from getting distracted by external visual stimuli during training. An opaque black acrylic lid was used to prevent mice from escaping from the arena during early training.

The reach targets were placed outside the arena adjacent to the front panel, with the linear actuator oriented orthogonally (Figure 2.2b). Thus, extension and retraction of the actuator moved the reach targets towards and away from the front panel. The targets were initially placed 5 mm from the front panel parallel to the axis of the actuator movement (Figure 2.2b, target nearest to panel). During training the actuator retracted by up to an additional 10 mm (Figure 2.2b, faded target).

To permit naturalistic, ethologically relevant reaches, I sought to determine the optimal slit width that reduced the extent to which reach trajectories were obstructed by the slit edges. First, I trained a cohort of mice in the task (see Section 2.2.5) using a slit width of 7 mm based on published mouse pellet-reaching tasks (Esposito et al., 2014; Li and Hollis, 2021). Once mice had learned to perform reaches, I observed their posture and movement trajectory when reaching through slits with widths of 8, 9, 9.5 and 10 mm. Wider slits allowed for greater freedom of movement, but also resulted in greater variability in the distance that mice were able to place their snout through the slit, due to differences in face size and shape. This introduced undesirable variability in reaching posture and trajectory. To avoid this confound

a

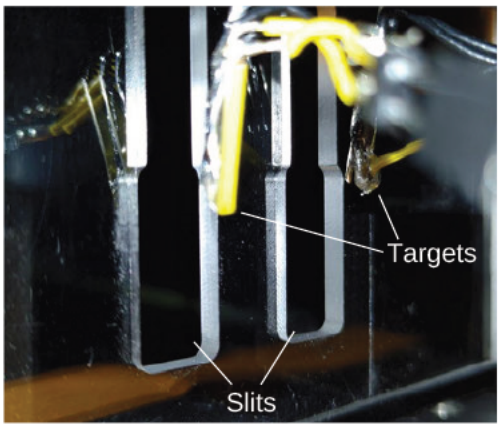
Targets
Slits

b

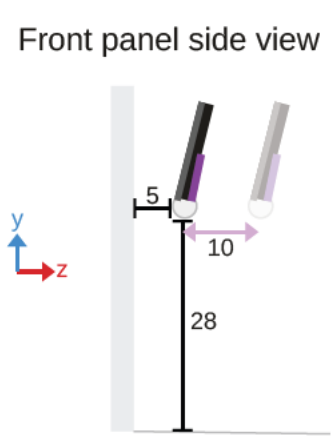
Front panel side view
y
z
5
10
28

c

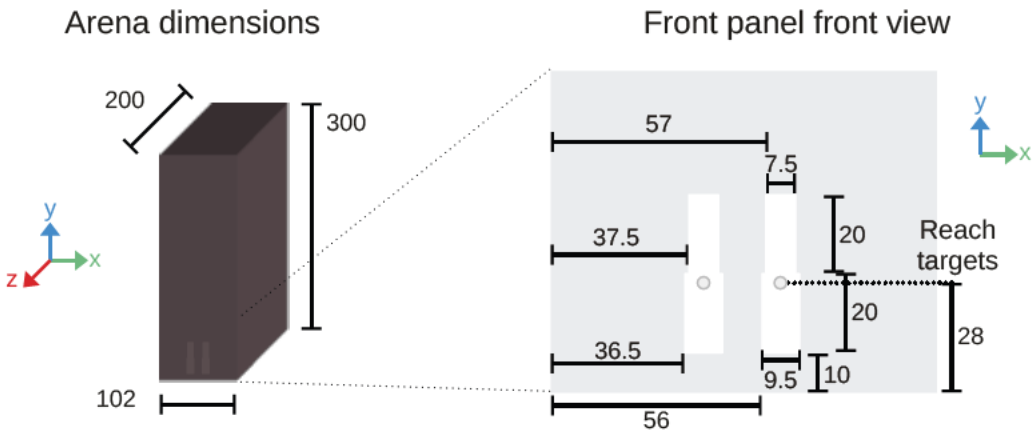
Arena dimensions
200
300
y
x
z
102
Front panel front view
57
7.5
y
x
37.5
20
Reach
targets
20
28
36.5
9.5
10
56

d

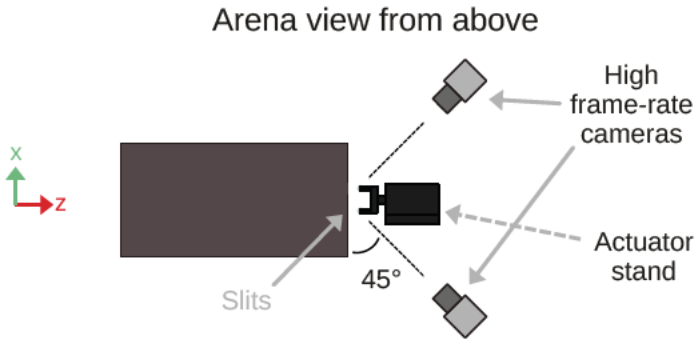
Arena view from above
High
frame-rate
cameras
x
z
Actuator
stand
Slits
45°

e

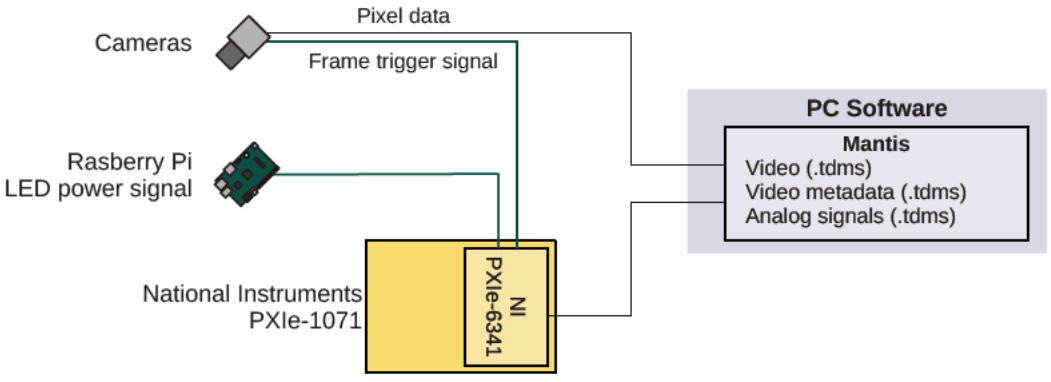
Cameras
Pixel data
Frame trigger signal
PC Software
Mantis
Video (.tdms)
Video metadata (.tdms)
Analog signals (.tdms)
Rasberry Pi
LED power signal
National Instruments
PXIe-1071
NI
PXIe-6341

Figure 2.2: Task arena design.
(a) Two slits in a 3 mm thick transparent panel provided the only access for mice to reach the two targets.
(b) Side view of the position of the targets relative to the front panel's outer surface in the y-z plane. With the actuator fully extended, the targets (left) were 5 mm from the outer edge of the front panel in z. When retracted, the targets (right, faded) were 15 mm from the front panel in z. The 10 mm actuator travel is represented by the pink arrow.
(c) Arena outer dimensions. The front panel was made from 3 mm thick transparent acrylic incorporating the 2 slits. Right, slit geometries for corresponding region of front panel, showing reach targets in the x-y plane. The targets were centred on the slits in x as indicated by grey circles.
(d) Top-down view of the arena and adjacent hardware. Two high frame-rate cameras were placed at 45° to the slits in the x-z plane as shown.
(e) Schematic diagram showing the organisation of the electronic hardware. The Raspberry Pi LED power signal and camera frame trigger signals were recorded by the National Instruments PXIe acquisition module. The acquisition module was controlled by a PC using Mantis64 software (https://www.mantis64.com), which directly acquires video pixel data from the cameras through a USB interface. All units are mm.

while limiting restriction of forelimb movement, I used a 9.5 mm width at forelimb height and a 7.5 mm width at head height (Figure 2.2c, right).

To enable motion tracking of reach trajectories with high temporal resolution, two high frame-rate infrared cameras (Mako U U-029, AlliedVision) were directed at the front panel, each rotated 45° to the axis of the slits as shown in Figure 2.2d. The arena was illuminated with infrared LEDs so that camera lighting did not affect the visual contrast of task stimuli. Frame timestamp signals were recorded via a National Instruments data acquisition module (NI PXIe-1071) with Mantis64 data acquisition software (https://www.mantis64.com) and saved in National Instruments TDMS format (Figure 2.2e). To enable synchronising of the video and behavioural data, a digital signal toggled simultaneously with the target LEDs was emitted from the Raspberry Pi and saved in parallel to the video frame timestamp signal.

2.2.4 Task control

The Raspberry Pi controlled the hardware by means of purpose-built software (Figure 2.3). The software, `reach`, available at https://github.com/DuguidLab/reach, is a small Python library for creating reaching tasks for rodents. `reach` provides a simple

object-oriented interface for designing, running and analysing training sessions. The hardware-interfacing code is encapsulated in a `Backend` class which can be extended for use in derivations of the task hardware described above (Section 2.2.2). Behavioural data can be analysed at the level of cohort, animal, or session by using corresponding Python representations:

- The `Session` class handles data for a single training session, and is responsible for managing the event sequence during training sessions.
- The `Mouse` class maintains an ordered list of `Session` objects that together represent the training history of a single animal. `Mouse` exposes methods that facilitate analysis of individual mouse training data.
- The `Cohort` class can be used to manage a set of `Mouse` objects and exposes methods that facilitate analysis of training data across multiple mice.

Training data is saved in JSON format per animal and can be conveniently loaded into Python analysis scripts using the above classes.

The Arduino Uno executed a simple Arduino Code filter that continuously read analog voltage signals from the two piezoelectric sensors, converted them into binary signals, and transmitted them to the Raspberry Pi. This analog-digital conversion involved thresholding the analog signal using a threshold that was calibrated individually per touch sensor. `reach` packages a utility script to assist with this calibration. This script logs touch events on the sensors while the threshold in the Arduino code is adjusted until the touch sensitivity is appropriate. The optimal threshold was a balance between being sufficiently sensitive to detect gentle touches, but insensitive to irrelevant vibrations while mice navigate around the arena.

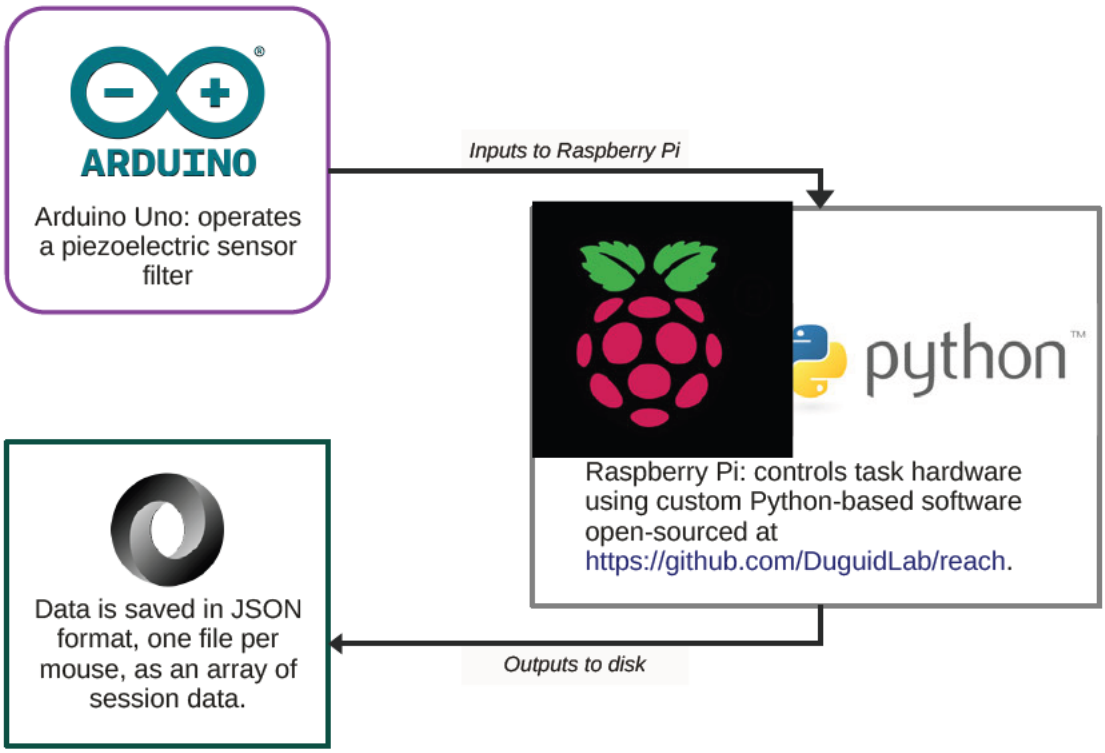

Figure 2.3: Overview of task software and data flow.
An Arduino Uno microcontroller and Raspberry Pi single-board computer were used to control hardware and monitor events during training sessions. The Arduino Uno executed a simple software filter on analog piezoelectric sensor inputs, converted these inputs to binary signals and transmitted them to the Raspberry Pi. The Raspberry Pi controlled the remaining hardware using custom software which saved task data and metadata in JSON format. Arduino logo, Public domain, via Wikimedia Commons. The Raspberry logo is a trademark of Raspberry Pi Ltd. The Python logo is a trademark of the Python Software Foundation. JSON logo attributed to Douglas Crockford, Public domain, via Wikimedia Commons.

2.2.4.1 Calibrating reward volume

A utility script packaged in the `reach` library was used for dispensing water on demand and ensuring that reward volumes had a consistent and known volume. Mice rapidly retract their limb after a successful grasp, so the duration used for opening the solenoid valves was limited to a maximum of 100 ms. Adjustment of the duration, position, and fullness of the water reservoirs allowed for precise control over reward delivery. I found a 6 µL reward volume to be suitable for motivating water-restricted mice during behavioural sessions and adjusted the water reservoirs aiming to dispense this volume in 70 ms.

2.2.5 Training regime

Next, I designed a training regime that enabled mice to learn to associate reaching to a visual cue with delivery of a water reward. The training regime had a structure typical of tasks used in the Duguid lab, such as the cued lever push task (Dacre et al., 2021) and cued lever push/pull task (Currie et al., 2022). Mice underwent a water-restriction protocol as described in Section 2.2.1 before undergoing daily 30 m training sessions. During a session, the Raspberry Pi continuously cycled an event sequence that scheduled sequential trials (Figure 2.4a).

When placed into the arena, mice were able to touch the targets freely. After an inter-trial interval (ITI) of 4-6 seconds, one of the two targets was illuminated (Figure 2.4a, cue). If a mouse touched the illuminated target, a 6 µL water reward was dispensed and the trial was deemed a *correct trial* (Figure 2.4b). If a mouse instead touched the non-illuminated target, this was deemed an *incorrect trial* and no water reward was dispensed (Figure 2.4c). If no touches occurred within a predetermined duration termed the *cue duration*, the cue switched off and the trial was deemed a *miss trial*. Any touches occurring during the ITI reset the trial. Thus, mice were trained to perform cued reaches towards visual stimuli.

Incorrect trials and spontaneous reaches made during the ITI were penalised with a timeout of 3 s to discourage reaches not directed by visual stimuli. The timeout duration was reduced to 1 s later in training to maximise the number of trials during sessions.

The target used in each trial was chosen pseudo-randomly. Unsuccessful trials (i.e. incorrect or miss trials) were followed by *correction trials* which presented the same target until the mouse performed a correct reach. Correction trials served to limit the number of rewards mice could obtain if they continuously reached for one of the two targets.

Mice first needed to learn to associate touching the visual stimuli with receiving rewards. To facilitate this, training began with a shaping period with a reduced task difficulty. The targets were initially positioned close to the slits so that mice were able to interact with them using their snout and/or tongue while exploring the arena (Figure 2.2b). When mice touched the illuminated target during exploration, a water

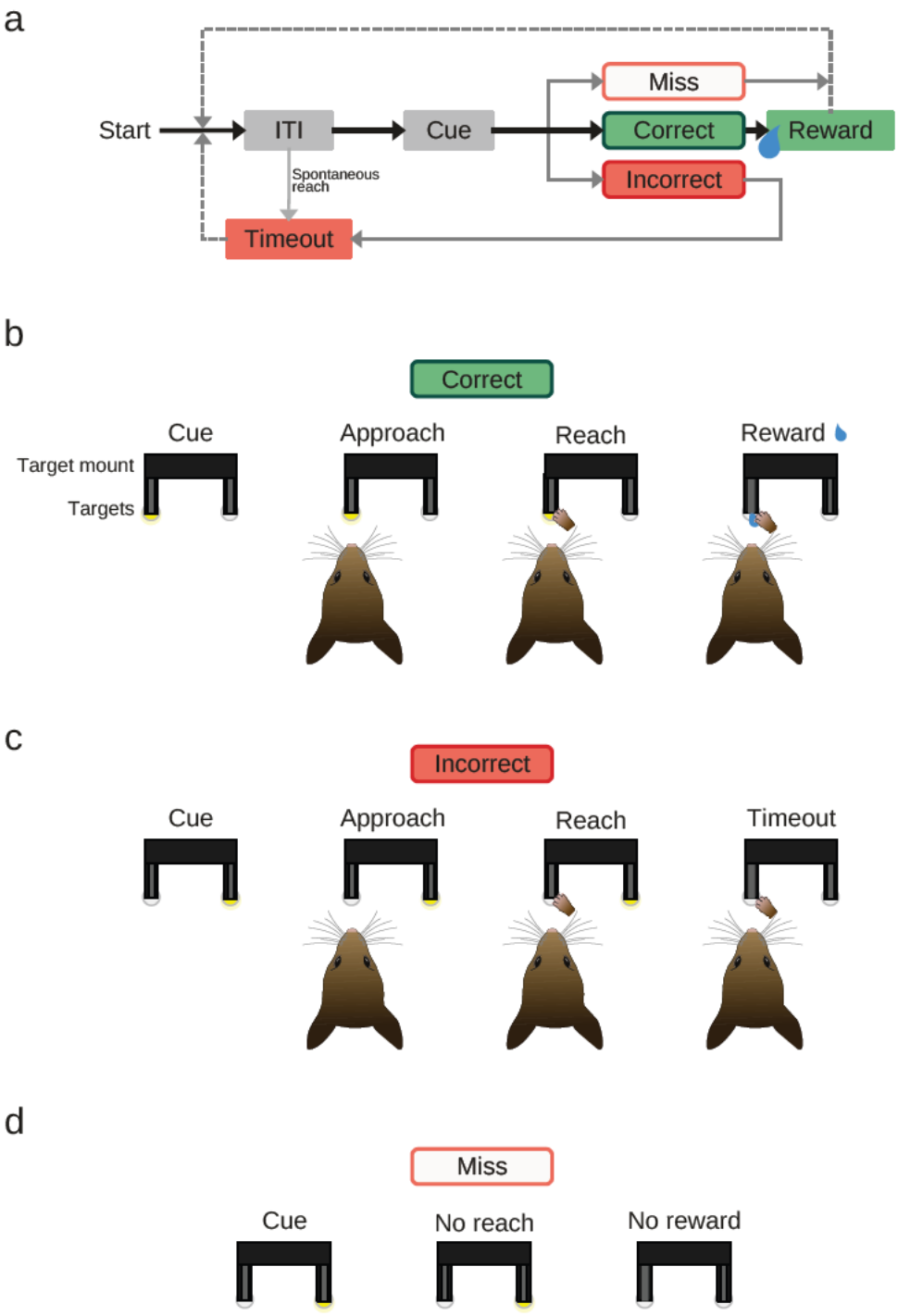

Figure 2.4: Behavioural task event sequence.

(a) The Raspberry Pi cycled an event sequence throughout training starting from a 4-6 second inter-trial interval (ITI). Following the ITI, a reach target was illuminated (the cue). Mice were rewarded with a 6 µL water droplet for performing correct trials, but miss trials were unrewarded. During incorrect trials, mice were penalised with a 3 s timeout, which was reduced to 1 s following an early shaping period. Spontaneous reaches during the ITI were also penalised with a timeout.

(b) Correct trials involved mice approaching and reaching to the illuminated target.

(c) Incorrect trials involved mice approaching and reaching to the non-illuminated target.
(d) Miss trials were trials during which neither target was touched.

reward was dispensed, resulting in rapidly increased engagement with the targets. The targets were retracted in 1 mm increments after every 5 trials if at least 13 of the last 15 trials involved target contacts (i.e. including both correct or incorrect trials). This progressive lengthening of slit-target distance resulted in an increase in task difficulty eventually resulting in mice having to reach to the target. At this point the shaping period ended and the targets remained stationary.

The cue duration was 10 s during the shaping period, and therefore one of the targets would be illuminated 2/3 of the time if no touches were made (i.e. as ITI durations average to 5 s). This meant that exploratory touches were likely to trigger rewards, facilitating fast learning of the stimulus-reward association. To reduce the likelihood that spontaneous reaches coincided with the presence of the visual stimuli, which would confound the results with correct trials that did not involve visually-directed reaches, the cue duration was slowly reduced after the shaping period. This also served to train mice to remain attentive to the stimuli and quickly respond by performing cued reaches. Cue durations were decreased following every correct trial by subtracting 0.3 % of the current duration to a minimum of 2 s.

2.2.6 Motion tracking

Reaching movements are complex actions composed of multiple epochs with distinct 3D kinematic signatures. To facilitate detailed investigation of the neural circuits underlying such movements, a high spatial and temporal resolution description of their limb trajectories is required. To track mouse position and reach trajectories, I used the DeepLabCut toolbox for markerless pose estimation (Mathis et al., 2018), which uses a deep learning-based approach to identify body parts of interest or other arbitrary features within video frames. I configured DeepLabCut to track 13 features to reliably track movement during the task: the tip of each finger, the centre of each palm, the tip of the nose, and the two reach targets. While the linear actuator position and thus target position was controlled and known, tracking the targets with DeepLabCut made it more convenient and reliable to estimate the relative distances between the targets and the mouse.

For each feature tracked by DeepLabCut, it generates an (x, y) coordinate time series representing that feature's location within each frame. DeepLabCut also reports a *p* value for each coordinate, which was used to identify coordinates that do not accurately represent a feature's location. Coordinates with *p* values above a threshold of 0.05 were replaced with a linear interpolation of coordinates from remaining frames. To further reduce the impact of poorly tracked features in a small number of frames, the median coordinate of the hand features (i.e. fingers and palm) was used to infer the position of the hands.

Motion tracking was performed on videos recorded from two cameras as illustrated in Figure 2.2d, enabling tracking of reach trajectories from two perspectives. However, when grasping a reach target, the view of the reaching hand by the contralateral camera becomes obscured by the target. Therefore, to further improve reliability, reach trajectories were determined using coordinates generated from the video recorded by the ipsilateral camera.

2.3 Results

2.3.1 Mice learned to perform visually-directed reaches

All mice (N = 11) interacted with the targets from the first training session. Following the initial shaping period, mice learned to obtain increasing numbers of rewards per 30-minute session (Figure 2.5a). This was mirrored by a steady increase in the percentage of trials that resulted in correct reaches (i.e. success rate) (Figure 2.5b).

The sensitivity index (d') is a statistic that originates from signal detection theory (Swets, 1988) and has since been applied to behavioural experiments to assess a subject's ability to detect a specific signal. Here, d' was used to assess an animal's ability to reach specifically to the spatial position of the visual stimuli. d' is defined as:

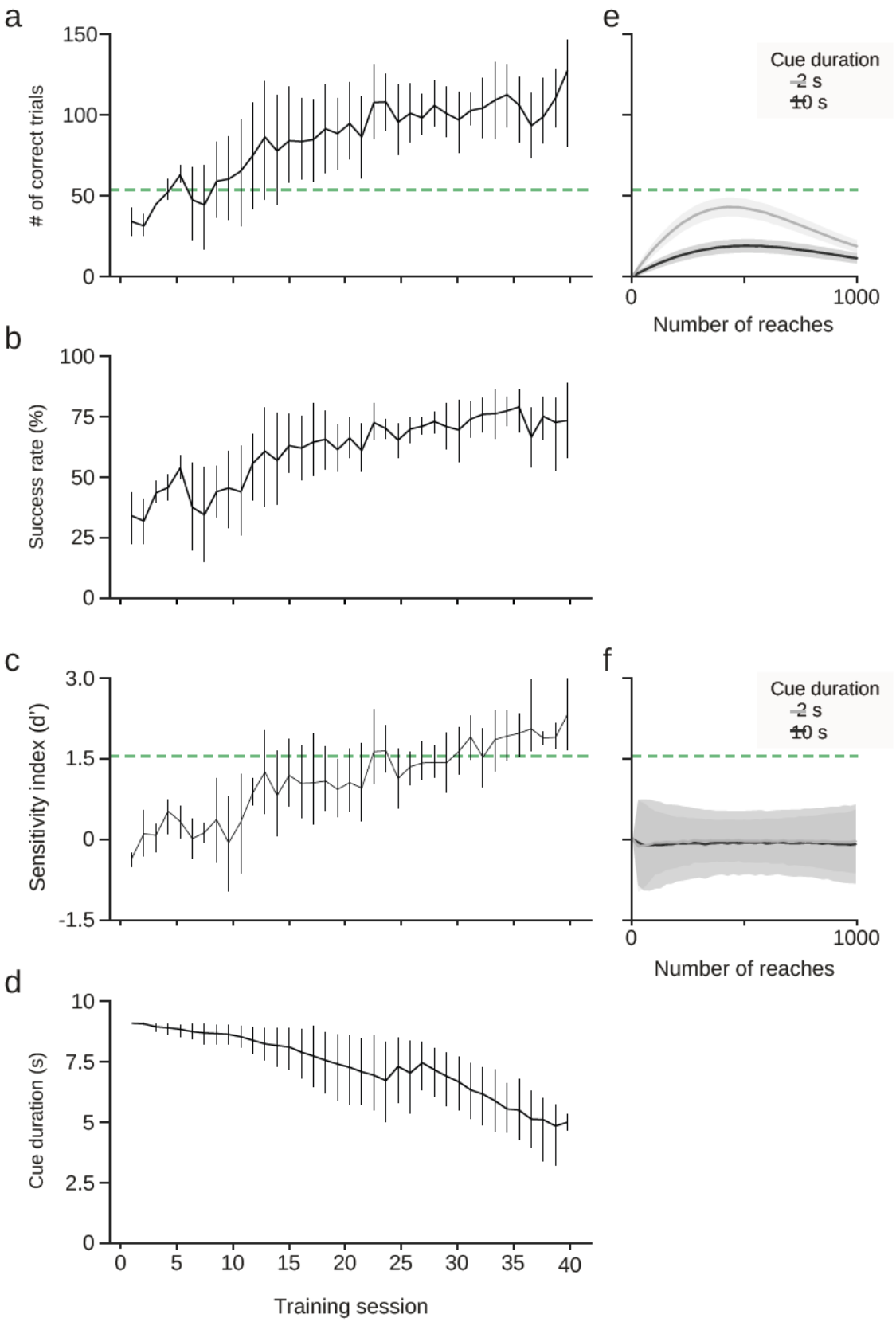

Figure 2.5: Mice learned to perform visually-directed reaches.

(a-d) Learning trajectories for expert mice (n = 8) showing number of correct trials obtained per session

(a), success rate (b), sensitivity index (d') (c), and the cue duration at the start of the session (d). Lines are mean ± 95% confidence interval.
(e-f) Chance levels of correct trials (e) and d' (f) estimated from simulated data (mean ± standard deviation) for simulated cue durations of 2 s and 10 s. The y axes correspond to those of (a) and (c) respectively. Green dashed lines show threshold values used to identify expert level task performance.

```
d' = norminv(hit rate) - norminv(false alarm rate)
```

where `norminv` is the inverse of the cumulative normal function (Andermann et al., 2010; Lee et al., 2012; Swets, 1988). To apply d' to this behavioural task, I calculated d' for each session using this derivation:

```
d' = norminv(left correct rate) - norminv(right incorrect rate)
```

where 'left' and 'right' correspond to left and right target trials. As discriminability improves, d' increases. Indeed, d' steadily increased across training (Figure 2.5c).

While mice maintained high performance, cue durations were slowly reduced as described in Section 2.2.5 to an average of 5.0 s in expert mice (Figure 2.5d).

To quantitatively determine whether mice had successfully learned the task, I estimated the performance that could be expected by chance. I performed a discrete-event simulation of 5000 repeated sessions for 0 to 1000 reaches randomly distributed throughout a 30 m period. This was repeated for cue durations of 2 and 10 s, corresponding to cue duration lower and upper bounds. The target of each reach was selected randomly. The simulation estimated that the maximum number of correct trials expected by chance is 27 and 54 for 2 and 10 s cue durations respectively (maximum of mean + 2 standard deviations; Figure 2.5e). For d', the maximum chance level (maximum of means for 2 and 10 s cue duration + 2 standard deviations) was estimated as 1.55 (Figure 2.5f). This is more conservative than values used in published studies (0.8, Andermann et al., 2010; 1.0, Lee et al., 2012). From these results, performance thresholds of 54 correct trials and 1.55 d' were used as criteria to identify training sessions in which mice had performed with above-chance success.

Mice that achieved above-chance performance for 4 consecutive sessions were deemed 'expert' (n = 8). This was achieved after 33.4 ± 6.7 training sessions (mean ± standard deviation). Mice with performance that did not show improvement were excluded from further analysis after 40 sessions (n = 3).

2.3.2 Characterisation of reaches

Reach trajectories were determined using a motion tracking approach as described in Section 2.2.6 and used to identify key timepoints during task engagement. During correct trials, expert mice performed a stereotyped sequence of actions upon cue presentation:

1. Locomote or perform a body re-orientation to face the slit directly in front of the illuminated target.
2. Adjust posture to prepare for the upcoming reach (i.e. placement of the hands on the floor of the arena in front of the slit).
3. Lift the dominant forelimb.
4. Extend the dominant forelimb through the slit and towards the target.
5. Grasp the target and collect the water reward.
6. Retract the forelimb back through the slit.
7. Consume the water reward.

This sequence of actions was used to decompose reaches into a series of distinct and well-defined epochs, termed: *approach*, *extension*, *retraction*, *consumption* (Figure 2.6a). The approach epoch encompasses the period from cue to reach onset, which was defined as when the reaching hand was lifted from the arena floor. Extension encompasses the period from reach onset to grasp. Retraction encompasses the period from grasp to reach offset, which was defined as the reaching hand returning through the slit. Lastly, on correct trials, reach offset is followed by the consumption epoch.

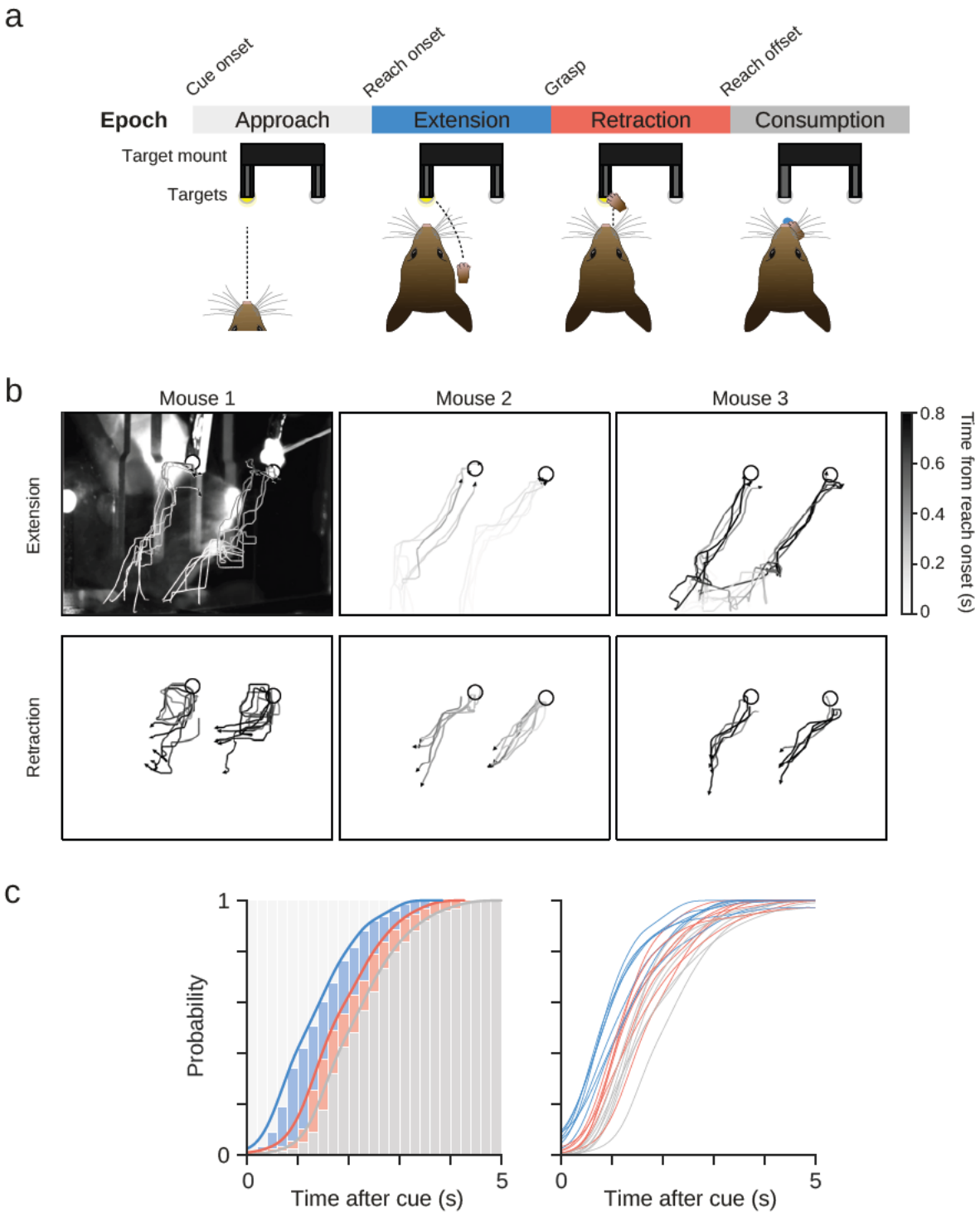

Figure 2.6: Definition of reach epochs.

(a) Behavioural timepoints during correct trials (top) were used to delimit four distinct epochs: approach, extension, retraction, and consumption.

(b) Representative reach trajectories made during 5 correct trials from 3 expert mice, split into extension and retraction epochs. The first panel is shown with a video frame to illustrate context. Trajectories start at reach onset and are coloured by time elapsed in seconds.

(c) Cumulative probability distribution of the start of each epoch during correct trials. Left: probability

histogram showing results from one session from an expert mouse. Kernel density estimates are overlaid representing the proportion of trials in which the start of each epoch had passed at a given time. Right: kernel density estimates for sessions with 7 expert mice.

Mice displayed variability in reach trajectories, possibly reflecting different strategies employed to complete the task (Figure 2.6b). For example, the trajectories in the first column in Figure 2.6b consistently curved downwards following grasp of the target, before moving towards the mouth. The second column displays trajectories which took a more direct route to and from the target. The third example shows similarly direct trajectories, but rather than positioning itself in front of the correct target prior to reach onset, the mouse positioned itself centred between both slits. Furthermore, all examples display different temporal profiles, representing variable reach duration.

To assess whether movement trajectories were similar when reaching to the left or right target, mean x and y coordinate trajectories were correlated between left and right target trials. Coordinates were taken from 150 ms before to 150 ms after grasp, encompassing the period during which the hand was beyond the slit in the arena wall. Pearson's *r* correlations found that x and y coordinate trajectories were significantly correlated between left and right target trials for all sessions (Bonferroni corrected *p* values). Thus, reach trajectories were similar regardless of reach target.

It is difficult to infer precisely what mice were doing during the approach epoch, as it is impossible to determine when mice first perceived the visual stimulus or chose to approach it. Interpretation of this epoch in future experiments may be improved by using an overhead camera to track locomotion throughout the arena, which would enable identification of when mice began to face or move towards the slits. This would provide an earlier approximation of reaction time than was possible with the current design, in which the earliest approximation was reach onset. As trials had a limited cue duration, mice were incentivised to quickly react to visual cues. Indeed, around 80% of reach onsets on correct trials happened within the first 2 seconds after cue onset (Figure 2.6c, blue). Moreover, the temporal distribution of events that marked the beginning of each epoch was similar across mice, suggesting that all mice had learned to quickly react to the visual cues (Figure 2.6c, right).

Reach durations (i.e. time from reach onset to offset) varied between mice and averaged 0.61 s (Figure 2.7a). Reaches displayed stereotyped velocity profiles with two distinct

peaks (Figure 2.7b), which correspond to the maximal velocities of the extension epoch at ~50 ms before grasp (mean 25 cm/s) and the retraction epoch at ~50 ms after grasp (mean 24 cm/s).

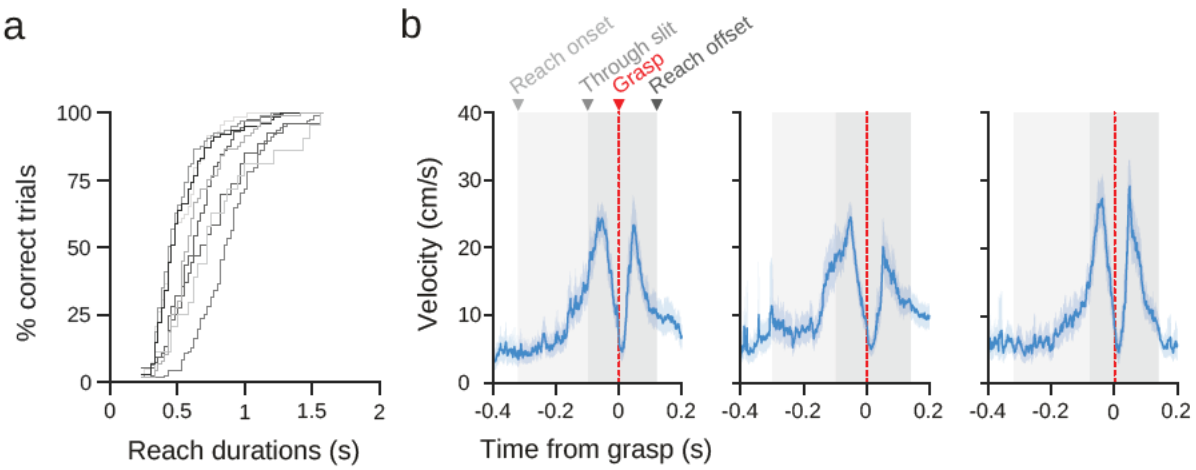

Figure 2.7: Time profile of reaches during correct trials.

(a) Cumulative histogram showing the distribution of reach durations for a cohort of expert mice (N = 8), showing variability across individuals but relative consistency within individuals. The average reach duration was 0.61 s.

(b) Velocity profiles of reaches made for 3 representative expert mice (mean ± 95% confidence interval) show velocity maxima in the centre of the extension and retraction epochs.

After reward consumption, mice typically performed repetitive reaches to collect any residual water left on the target. This behaviour was variable across mice and trials (Figure 2.8). Most mice performed a single reach on fewer than 10% of trials, and during the remaining trials performed up to 10 repetitive reaches within 5 seconds following the cued reach (Figure 2.8a). In contrast to the cued reach, repetitive reaches did not involve repositioning of the hands on the arena floor; mice had already prepared for reaching and initiated repetitive reaches from a standing position. Consequently, the earliest well-defined timepoint that marked the beginning of each repetitive reach was when the reaching hand moved through the slit after consumption. The time intervals between cued and first repetitive reaches, and each consecutive pair of repetitive reaches, were similar, indicating that mice performed repetitive reaches at regular intervals without a longer period after the cued reach, and without burst-like series of reaches (Figure 2.8b). The majority of the water was collected on the initial, cued reach with repetitive reaches collecting decreasing volumes. Therefore, as movement vigour is

modulated by expected reward outcome (Wang et al., 2013), a reduction in velocity between the cued and repetitive reaches is to be expected (Figure 2.8c). To test whether peak velocity varied between cued and repetitive reaches, a one-way repeated measures ANOVA within mouse subjects was used ($F(4, 28) = 19$, $p < 0.001$) and found significant differences between cued reaches and all 4 sets of repetitive reaches (post-hoc pairwise t-tests $p < 0.003$, $t(7) = 6.54, 5.06, 4.47, 4.58$ for repetitive reaches respectively). Thus, cued reaches had greater peak velocities than repetitive, self-initiated reaches, consistent with a decline in movement vigour in response to reduced reward expectation.

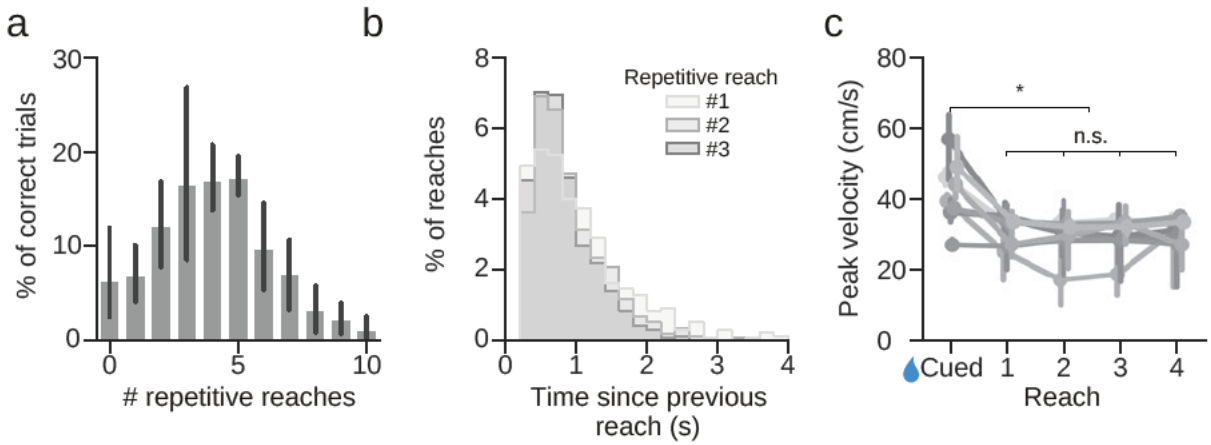

Figure 2.8: Mice performed multiple reaches during correct trials.

(a) Distribution of the number of repetitive reaches performed by a cohort of expert mice (N = 8) (mean ± 95% confidence interval).

(b) Distribution of intervals between the first three repetitive reaches and their preceding reaches show that the intervals between these reaches were similar.

(c) Peak velocities for the cued and first 4 repetitive reaches (median ± 95% confidence intervals) show that the repetitive reaches displayed reduced peak velocities compared with cued reaches. Significant differences are indicated by *.

To determine whether movement trajectories were similar during cued and repetitive reaches, mean x and y coordinate trajectories were compared as described above. Pearson's *r* correlations found that coordinate trajectories were significantly correlated for all sessions (Bonferroni corrected *p* values), thus reach trajectories were similar regardless whether movements were cued or self-initiated.

2.4 Discussion

In this chapter I have described the design, implementation and use of a novel visually-directed reaching task. Once trained in the task, mice reliably performed high numbers of naturalistic visually-directed reaches, providing a robust model system with which to investigate the neural control of this fundamental behaviour.

The design and construction of the task hardware is simple and does not require specialised equipment or knowledge to build, and the ease of adoption is facilitated by the use of inexpensive and readily available materials. While the present design trained mice to perform reaches to two visual targets, the straightforward arena, target, and circuit design are easily modified to alternative configurations. For example, the arena or slits could be built with different dimensions, or could contain a different number of targets. Similarly, the software that controls the task hardware can be customised, for example to change the brightness or colour of the visual stimuli. The modular design of the hardware and software means that the present design can be used as a foundation for researchers aiming to employ adaptations of the task.

During the task, mice were required to reach to the location of the independent visual stimuli, ensuring the task was visually-directed. This represents a critical feature of the task: rather than an arbitrary stimulus-response association, which would likely be sufficient to achieve high performance if the task involved a single target (i.e. a visually-triggered task), mice were required to use spatial information to drive their behavioural response. The task design offers a turnkey solution for researchers seeking to investigate visually-directed reaching, while leveraging the power of the mouse model, and thus bridges the technical gap between mouse and primate research focussing on this important behaviour.

Published studies employing rodent reaching tasks have provided valuable insight into how the brain controls reaching (Klein et al., 2012; Nicola et al., 2022). However, the visual element of the behaviour, which is a critical part of natural reaching behaviour in primates, has so far remained unexplored in mice. My task design can be combined with detailed analytical approaches, such as delineating the accelerative and decelerative phases of reaches (Becker and Person, 2019) or tracking individual digits and joints

(Azim et al., 2014; Esposito et al., 2014), thus taking full advantage of the kinematic richness of the behaviour.

Overall, the task offers a cost-effective and accessible tool for leveraging the mouse model to answer neuroscience questions about visually-directed reaching. The task is designed to be compatible with common experimental methodologies used with freely moving animals, such as electrophysiological recordings and optogenetics, allowing researchers to correlate or causally link neural activity with movement. While the task does have some limitations, it is highly adaptable and can be extended to be useful for answering additional questions. For example, the task could be extended to vary LED brightness or use both LEDs during each trial, enabling reward contingencies experiments. In this case, an experiment could adjust illumination of the targets proportional to available reward volume or to illuminate both targets simultaneously with different illumination levels to assess stimulus discrimination. Secondly, integrating real-time motion tracking or motion sensors could provide closed-loop feedback for triggering optogenetic manipulations at specific points during movement, allowing researchers to investigate the requirement of intact neural activity of different brain areas from different timepoints during the reach. Another limitation of the task is that the targets are static, and so the task does not allow for the investigation of dynamic aspects of the behaviour, such as target tracking or interception. However, while extending the task to include moving targets may be challenging, researchers could then study the continuous stimulus-response dynamics that underlie movements that update in real-time.

Importantly, the task design is compatible with common experimental methodologies used with freely moving animals, such as extracellular recordings via chronically implanted silicone probes. In Chapter 4, I take advantage of this to investigate how the activity of neurons in posterior secondary motor cortex and dorsomedial striatum relates to visually-directed reaching.

Chapter 3

A Neuropixels data processing and analysis pipeline for trial-based behavioural experiments

3.1 Introduction

In recent years, the Neuropixels 1.0 silicone probe (Jun et al., 2017) become a popular tool for performing extracellular recordings during neuroscience experiments. Each probe can simultaneously record from 384 out of 960 electrodes spanning a 10 mm long shank, yielding well-isolated spiking activity from hundreds of neurons during each recording. While their use has become popular for assaying neural activity in behaving animals, researchers have so far been required to independently develop *ad-hoc* data processing scripts based on often out-dated and inflexible code snippets shared online. To make it easier to perform Neuropixels data analyses and reduce the time spent writing custom scripts, I aimed to develop an easy-to-use data processing and analysis pipeline that can be applied to any kind of behavioural experiment with minimal customisation.

The objective of the pipeline is to enable researchers who have collected simultaneous Neuropixels and behavioural data to easily perform common electrophysiological data processing steps, automatically manage data storage on the file system, and extract behaviourally-aligned segments of neural data. Existing, mature software will be harnessed to perform specialised tasks such as spike sorting and motion tracking of behaviour videos. Thus, the pipeline will act as a core, general-purpose interface for all steps required to get from raw Neuropixels and behavioural data to neural activity in various forms, such as spike times or firing rates, aligned to behavioural events. This output will be provided in a standard format for subsequent visualisation or statistical analysis.

By providing a simple and intuitive interface for performing common data processing and manipulation tasks, researchers can spend less time writing highly customised scripts to fit the format of their behavioural data (which often varies between research groups and experimental apparatus) and individual scripts for the various processing steps (such as spike sorting or behaviour alignment). As neuroscientists are often unfamiliar with software development and its best practices, having an accessible tool available for performing these tasks not only reduces duplicate work being performed across the community but also accelerates the analysis stages of experiments, helping researchers focus on extracting meaningful insight from their valuable data.

While the pipeline will provide access to common functionalities such as spike sorting, generation of firing rates, and behavioural alignment, it does not aim to be a monolithic tool that can do many highly specialised functions. For example, deep learning-based methods such as DeepInsight (Frey et al., 2021), a toolbox for the interpretation of raw wide-band neural activity, are not implemented or integrated directly. Instead, the pipeline should have an extensible design to facilitate integration of other third-party tools by the user with relative ease.

In this chapter, I first discuss the requirements of the pipeline, followed by a description of its final design, structure, and usage.

3.1.1 Functional requirements

The pipeline should fulfil several requirements regarding its function, which have been selected based on the needs of researchers who perform behavioural experiments utilising Neuropixels probes.

Generalisability: A critical requirement is that the pipeline has a generalised design that makes it straight forward to apply to different trial-based behavioural experiments. Implementing support for new behavioural tasks should be simple and when possible streamlined by adapting implementations for similar tasks that are already supported. Helper methods should be provided to assist with testing and confirmation that behavioural data is correctly aligning to neural data.

Data management: When managing files, data integrity and storage efficiency should be maintained. To facilitate this, the pipeline should manage data in three distinct stages,

each with a corresponding set of directories on the storage file system: `raw`, `interim`, and `processed`. The `raw` folder should contain the raw data as collected, preserving the data for long-term storage and reproducible analysis; the `interim` folder should contain intermediate files that can be deleted and later regenerated from the raw data as needed; and the `processed` folder should contain the final output of data processing steps, which should be compact and information-dense to reduce the financial cost of its storage. To help reduce storage requirements, raw data should be compressed and transparently decompressed when accessed. When raw data is needed, it should be copied into the `interim` folder (decompressed if necessary) before use, ensuring that any third-party software being used via `pixels` cannot directly access the raw data. This would guarantee that the integrity of raw data is maintained and not at risk of modification or corruption.

Efficiency: Some data processing tasks can be costly in terms of data reading/writing or computation and thus take long periods of time. This would add friction to the workflow of users, so steps should be taken to reduce this friction and improve usability. For example, if tasks have already run and performing them again would be redundant, then they should be skipped. Similarly, caching should be used where possible to improve the user experience. Optimised and battle-tested open source libraries should be exploited to maximise the performance of computationally intensive tasks.

3.1.2 Interface requirements

The pipeline should also fulfil several interface requirements that describe how it should interface with users and other software. These requirements are critical for ensuring that the pipeline is usable and accessible for neuroscientists who may have limited programming experience.

User interface: The user interface must be accessible for users unfamiliar with programming. A script-based workflow is generally friendly for such users, suggesting that the pipeline should take the form of a simple library. To facilitate onboarding, the source repository should provide a basic, well-documented template script to serve as a tutorial for the main tasks supported by the pipeline. It should be implemented in Python, which has become the most popular programming language used for scientific work due to the wide availability of powerful and well-documented libraries for data manipulation and statistical analysis, such as numpy (Harris et al., 2020) and scipy

(Virtanen et al., 2020). Interfacing with third-party libraries, such as Kilosort for spike-sorting (Steinmetz et al., 2021), should be transparent and hidden from the user, but configurable where appropriate.

Application programming interface (API): The API should be idiomatic and intuitive such that simple workflows become trivial to perform, but a flexible and open design should allow for custom logic to be straightforward to implement using standard Python approaches such as class inheritance. Applying the "deep module" software design philosophy, wherein the library provides a wide range of useful functionalities that are exposed through a relatively small and simple interface, could reduce the cognitive overhead for performing the most common, basic tasks, which would be available 'out of the box' with minimal customisation.

3.2 Design

The software is implemented as a Python package named `pixels`, which contains the core pipelining logic and is used as a library to process experimental data. `pixels` aims to perform all processing steps required for analysis of data collected in these experiments. Here I describe the design of `pixels`, which is open-sourced on GitHub at https://github.com/DuguidLab/pixels.

3.2.1 Data model

`pixels` has a simple object-oriented design centred around two classes: `Experiment` and `Behaviour`. The `Experiment` class represents a set of one or more recording sessions that are managed together (i.e. their data files are organised together in the same folder) and provides methods for batch processing the set of sessions. An instance of `Behaviour` represents a single one of those sessions. `Behaviour` is an abstract base class that requires behavioural task-specific subclasses to 'fill in the blanks' by providing an implementation for a single method, namely that which pertains to parsing the raw behavioural data and converting it into a standard format. For new users to apply the pipeline to their custom task, implementing that method is the main setup step.

3.2.2 Pipeline

`Behaviour`'s methods implement pipeline tasks that can be used to process different streams of raw data, including behavioural data, behavioural video data (i.e. for motion tracking of animals), Neuropixels action potential (AP) data and Neuropixels local field potential (LFP) data (Figure 3.1, left to right). These tasks convert each data stream into a more useful format (e.g. raw action potential data into spike times) before aligning streams to a common timeline and sample rate, enabling easy and efficient manipulation of processed data.

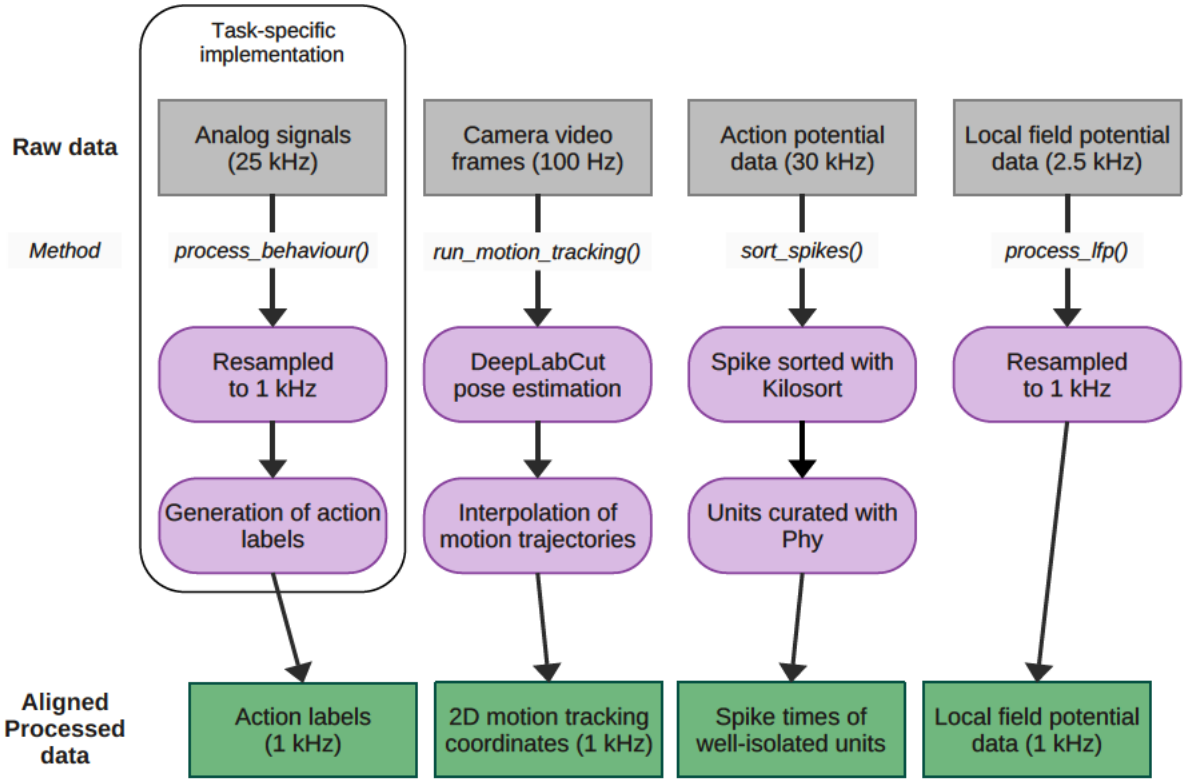

Figure 3.1: Data processing pipeline.
Overview of processing steps in the `pixels` pipeline for different data streams acquired during behavioural experiments with Neuropixels recordings. Methods belonging to the `Behaviour` class that are used to execute each task are shown.

The first step in the pipeline involves parsing the behavioural data and using it to generate a 1 kHz vector (referred to as 'action labels') where each value encodes the set of task-specific events that occurred at that timepoint (Figure 3.1, left). This requires custom logic per behavioural task. Action labels are represented as a `2 x N` array for

duration `N`. The two rows encode the 'actions' and 'events', respectively, where actions are defined as high-level sets of events (e.g. in the reaching task, a cued reach to the left target is one specific action), and events are defined as low-level, instantaneous events (e.g. the timepoint when the cue became illuminated is one event within the action). Each element in the array is an unsigned integer created by summing bitflags that represent unique actions/events (Figure 3.2). For example, if two actions that are represented by the integers `2` and `4` occurred at the same timepoint, then the action label for that timepoint would be `6` (Figure 3.2, right). This encoding has two key advantages. First, computations that scan the action labels are performant due to vectorised bitwise operations, and consequently aligning electrophysiological or other data to a specific action takes little time. Second, the encoding is generic and capable of representing a wide range of trial-based tasks with predefined sets of actions and events. While the example in Figure 3.2 uses an array of 8-bit integers and is therefore capable of representing up to 8 unique actions and 8 unique events, 16-, 32- or 64-bit arrays can also be used.

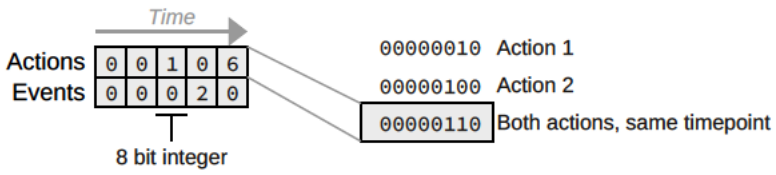

Figure 3.2: Action labels encode task events as bitflags.
Task events that occurred during a session are extracted from raw behavioural data and encoded into 'action labels'. Action labels are represented by a two-row array where each column is a single timepoint containing an 8-bit unsigned integer (left). Each integer encodes the set of actions that occurred at that timepoint, each of which is represented by a unique bit flag. In the example (right) two actions occurred at that timepoint.

The first step also aligns the action labels with other data streams. This requires that each data stream is recorded alongside a common 'sync channel' with an unambiguous correspondence between sync channels recorded as part of each data stream (Figure 3.3), easily accomplished by generating a random frequency-modulated square wave and recording it alongside all data streams. Finding the correspondence between sync channels enables conversion of all processed data into a common timeline

(Figure 3.3). Processing of the remaining types of data (i.e. video, AP, and LFP data) is optional and available for experiments that require them.

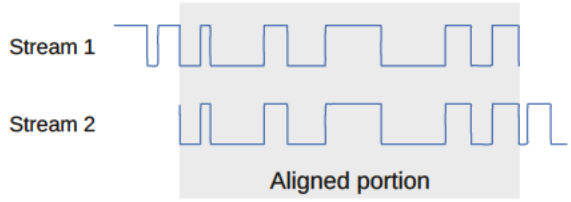

Figure 3.3: Sync channels support alignment of data streams.
Sync channels from different data streams are used to identify the period of time common to each stream, facilitating temporal alignment between different types of data.

The DeepLabCut toolbox for markerless pose estimation (Mathis et al., 2018) is closely integrated into the `pixels` pipeline, providing an interface for performing motion tracking on videos saved during Neuropixels experiments (Figure 3.1, centre-left). DeepLabCut outputs an x-y coordinate for each tracked feature per frame, and a *p* value for each coordinate that reports the confidence of feature detection in that frame. The `pixels` pipeline first aligns video frames to the action labels (i.e. by using a camera trigger signal) to calculate timestamps for each frame (and thus coordinate), then performs a 1 kHz linear interpolation of x-y coordinates with corresponding *p* values below a threshold of 0.05. This generates a 2D coordinate vector for each feature tracked by DeepLabCut with the same timeline and sample rate as the action labels.

Processing of AP data first involves spike-sorting to identify clusters of spikes corresponding to individual units (Figure 3.1, centre-right). `pixels` uses Spikeinterface (Buccino et al., 2020) to configure and execute Kilosort 3 (Steinmetz et al., 2021) for spike sorting. Prior to sorting, common (median) average referencing, a technique that reduces the impact of global noise and movement artefacts (Jun et al., 2017), and 300 kHz high-pass filtering is applied to the data. Following spike sorting by Kilosort 3, spike clusters are manually curated using phy (https://github.com/cortex-lab/phy). With phy, clusters of spikes are compared to spikes from similar clusters to determine whether they should be merged based on waveform similarity, cross-correlogram features, and drift patterns. The curated spike cluster dataset then contains the spike times of well-isolated units representing putative neurons.

The pipeline provides a few methods for processing LFP data, such as resampling and temporal alignment to the action labels (Figure 3.1, right), however functionality operating on this data stream is limited.

3.2.3 Usage

3.2.3.1 Installation

To begin using the `pixels` software, a conda environment ('Anaconda software distribution', 2020) can be used to manage third-party dependencies:

```
conda create -n pixels -c conda-forge numpy pandas \
    nptdms scipy matplotlib opencv
conda activate pixels
pip install ffmpeg-python spikeinterface probeinterface
```

Then, using `pip`, install the `pixels` package into the conda environment:

```
pip install git+https://github.com/DuguidLab/pixels.git
```

This setup does not include DeepLabCut and its dependencies, which are optional. For their installation steps, see the DeepLabCut documentation.

3.2.3.2 Supporting a new task

The first thing required when setting up the pipeline for use with a new behavioural task is to implement a `Behaviour` subclass that contains the logic for interpreting the task's raw behavioural data. This logic defines the body of the `_extract_action_labels` method, which receives the raw data as a numpy array, and the method must return the newly created action labels.

For example, we can define a new class `ReachTask` in the file `reach_task.py` for processing sessions using the reaching task described in the previous chapter:

```
# reach_task.py
import numpy as np
from pixels.behaviours import Behaviour

class ReachTask(Behaviour):
    def _extract_action_labels(self, behavioural_data: np.array):
        # Task-specific implementation added here to generate the
        # action labels from raw behavioural data.
        return action_labels
```

We must also define the tasks set of actions and events, for example:

```
# reach_task.py

class ActionLabels:
    miss_left = 1
    miss_right = 2
    correct_left = 4
    correct_right = 8
    incorrect_left = 16
    incorrect_right = 32

class Events:
    led_on = 1
    led_off = 2
    reach_onset = 4
    grasp = 8
```

These classes serve as enumerations of the values contained in the action labels, and can be used in `_extract_action_labels` to create the action labels and then later for selecting which action(s) to align data to during downstream analyses.

3.2.3.3 Processing raw data

With the above steps completed, the new task-specific classes can be used in simple scripts to run pipeline tasks or extract aligned data. We first create an instance of `Experiment` to manage our set of recording sessions, passing our list of animal IDs (used to identifying relevant files on disk), the new `ReachTask`, and the path to the folder containing all data:

```
# my_experiment.py
from pixels import Experiment
from reach_task import ReachTask, ActionLabels, Events

my_exp = Experiment(
    ["Mouse1", "Mouse2", "Mouse3"],
    ReachTask,
    '~/path/to/data/folder/',
)
```

When instantiated, the `Experiment` object creates a `ReachTask` object for each recording session and stores these in a list at `Experiment.sessions`. The `Behaviour` methods listed in Figure 3.1 can be accessed on the `ReachTask` objects to perform processing steps on individual sessions. For example, to generate action labels for all sessions:

```
# my_experiment.py

for session in myexp.sessions:
    session.process_behaviour()
```

The `Experiment` class exposes methods for batch processing tasks across all sessions; this is equivalent:

```
# my_experiment.py

myexp.process_behaviour()
```

Most processing steps will be transparently skipped if their output already exists and they are idempotent, reducing processing time.

3.2.3.4 Analysing processed data

Subsequent analysis of extracellular data is facilitated by methods that conveniently select events of interest in the action labels (e.g. cue onset during correct trials) and align other data to these events (e.g. spike times, instantaneous firing rates, motion tracking trajectories). Alignment of data is performed using the `align_trials` method of `Behaviour` (or `Experiment` when batching across sessions). For example, we can extract the instantaneous firing rate for all units during correct, left target trials (the action), aligned to LED onset (the event), for 1 s total duration (0.5 s either side of the event), as follows:

```
# firing_rates.py
from my_experiment import myexp, ActionLabels, Events

firing_rates = myexp.align_trials(
    ActionLabels.correct_left,
    Events.led_on,
    "spike_rate",
    duration=1.0,
)
```

`align_trials` handles the generation of processed data formats transparently, such as the creation of instantaneous firing rates by convolving spike times with a Gaussian kernel. The output of `align_trials` is a `DataFrame`, which is a human-readable, table-like data structure from the popular pandas library (The pandas development team, 2020). This is a standard format commonly used for data manipulation and statistical analysis and has a shallow learning curve for those unfamiliar with it. In

essence, the output is a multi-dimensional table in which each column contains the aligned data type (e.g. firing rates) for a single session, Neuropixels probe (in the case of sessions that involved simultaneous recordings from multiple probes), unit, and trial. This design makes it intuitive to access the firing rates. For example, using the `matplotlib` library (Hunter, 2007), we can plot the firing rates for a single unit across all trials as follows:

```
# firing_rates.py
import matplotlib.pyplot as plt

# Select the 1st session, 1st probe, and 10th unit
session = 0
probe = 0
unit = 9

plt.plot(
    firing_rates[session][probe][unit]
)
```

`align_trials` accepts a number of options alternative to `"spike_rate"` when selecting which data to extract, including `"spike_times"`, `"lfp"`, and `"motion_tracking"`. This method represents the primary output of the pipeline: an interface for extracting conveniently structured, task-aligned processed data for use in question-specific analysis scripts.

3.2.3.5 Selecting subsets of units

A common requirement when extracting aligned spike data is the ability to select a subset of units of interest. To enable this, the `Behaviour` class has a `Behaviour.select_units()` method that can be used to define a named set of units. Units can be selected using a depth range (i.e. within a minimum and maximum distance along the probe) or spike width range. For example, we can select units with an implanted depth of 500 to 1200 µm and minimum spike width of 0.4 ms as follows:

```
# firing_rates.py

units = myexp.select_units(
    min_depth=500,
    max_depth=1200,
    min_spike_width=0.4,
)
```

This can then be passed directly to `align_trials` to extract data only for that subset of units:

```
# firing_rates.py

firing_rates = myexp.align_trials(
    ActionLabels.correct_left,
    Events.led_on,
    "spike_rate",
    units=units,
)
```

This is useful for investigating the activity of specific brain areas or cell types.

3.3 Discussion

After collecting raw data during a recording session, a researcher must traverse two steps before they can gain insight from their experiment. First, raw data must be processed and converted into formats that are more directly useful, such as extracting unit spike times from raw extracellular voltage data. Second, the researcher must visualise and statistically test the processed data as appropriate for answering their scientific question. The `pixels` pipeline streamlines and reduces the work required to perform the first of these steps so that researchers can be more focussed on interrogating their data. The pipeline was written to be generalised for trial-based behavioural tasks and straightforward to extend to new tasks.

To date, the pipeline has been used as part of two peer-reviewed studies, in which it was critical for examining how activity in primary motor cortex related to cued lever movements (See appendices) (Currie et al., 2022; Dacre et al., 2021). The pipeline was also used to analyse the recordings in the next chapter, and has been adopted for use by researchers in at least one other group.

The extensible design is not limited to new tasks, but also alternative types of time series data for task-alignment. For example, a 'motion index' metric used to measure broad pixel intensity changes in behavioural videos (Dacre et al., 2021) has been used and aligned to events using the same `align_trials` method described above. It would be possible to similarly extend the set of align-able data types to other common recording techniques such as calcium imaging or patch-clamp recordings, providing similar workflow improvements to researchers using these techniques.

As `pixels` is open source and available on GitHub at https://github.com/DuguidLab/pixels, others are free to fork and modify the codebase to suit their needs. However, it may be beneficial for users to collaborate on one master copy of the repository so that researchers can benefit from each other's improvements and reduce duplicate work.

Chapter 4

Neural correlates of visually-directed reaching in secondary motor cortex and dorsomedial striatum

4.1 Introduction

The reaching behaviours that we depend on for survival are directed by visual input. In primates, premotor cortex (PM) is thought to be a key node bridging visual and motor areas. Recent evidence has implicated a subdomain of secondary motor cortex (M2) as playing a similar role in mice. However, how activity in this area of M2 relates to visually-directed reaching remains unknown.

Neural recordings in primates trained to perform reaches to visual targets have shown that neurons in PM exhibit target-specific activity beginning prior to movement execution (Boussaoud and Wise, 1993; Cisek and Kalaska, 2005; Lara et al., 2018). This activity reflects both motor and visual features relating to reaching movements and their targets (Gregoriou et al., 2005; Murata et al., 2000; Schaffelhofer and Scherberger, 2016), with motor-related activity encoding variables such as hand position, speed, and movement direction (Archambault et al., 2011; Schaffelhofer and Scherberger, 2016). The visual features encode intrinsic properties of objects targeted for grasping, such as shape, size and orientation (Murata et al., 2000; Schaffelhofer and Scherberger, 2016), and are believed to be received from posterior parietal cortex (PPC), an area involved in visual processing that forms the parietofrontal loop together with PM (Archambault et al., 2011; Caminiti et al., 2017; Marconi et al., 2001; Schaffelhofer and Scherberger, 2016). Based on these findings, and manipulation experiments demonstrating a causal role for PM in performing reaches (Fogassi et al., 2001; Stepniewska et al., 2014), current models place PM as a critical integrator for incorporating visual information into motor computations during behaviour (Battaglia-Mayer et al., 2014).

In mice, recent findings have suggested that posterior M2 (pM2) plays a comparable role during visually-directed reaching. In an experiment where head-fixed mice were trained to perform reaches to olfactory stimuli at different locations, Galiñanes et al. (2018) found that optogenetic inactivation of pM2 during reach extension disrupted kinematic trajectories. Another study found that blocking input to pM2 from PPC immediately before a visually-cued lever press perturbed forelimb kinematics (Hwang et al., 2019). Mirroring the primate parietofrontal loop, rodent pM2 and PPC form reciprocal connections (Hovde et al., 2018; Itokazu et al., 2018; Zingg et al., 2014) conveying predominantly motor and visual signals, respectively (Itokazu et al., 2018). These observations, taken with the finding that pM2 projects to other regions of motor cortex (Luo et al., 2019), suggest that pM2 is a region that is integral for visually-directed reaching.

Another brain area likely to play a role in the behaviour is dorsomedial striatum (DMS). DMS is a subcortical area involved in action selection during visually-directed behaviours (Hwang et al., 2019) and has been shown to regulate movement vigour according to reward value (Wang et al., 2013). As repetitive reaches performed during the task are self-initiated and yield little to no reward, examining differences in DMS activity between cued and repetitive reaching may reveal differences in how these two behaviours are motivated.

In this chapter, I aim to characterise the activity of neurons in pM2 and DMS during visually-directed reaching. This will be achieved by recording the spiking activity of populations of neurons in mice trained in the visually-directed reaching task described in Chapter 2 and examining how their activity relates to different aspects of the behaviour. I take advantage of recent advances in silicone probe technology to yield high unit count population recordings with high temporal resolution, which is critical for understanding population dynamics during the rich time-modulated behaviour. The long linear probes enable recording in multiple brain areas, so I will optimise the probe implantation angle to record simultaneously from pM2 and DMS. After describing experimental and analytical methods, I explore how activity patterns of units in pM2 and DMS correlate with the behaviour, then finally discuss the implications of the findings for understanding the neural mechanisms underlying visually-directed reaching.

4.2 Methods

Mice expert in the visually-directed reaching task were chronically implanted with Neuropixels silicone probes (imec; Jun et al. (2017)) to enable recording of population-level neural activity while engaging in the freely moving task. Neuropixels 1.0 probes (Figure 4.1a; Jun et al. (2017)) enable simultaneous extracellular recording of hundreds of neurons with high temporal resolution. Each probe has 960 electrodes spanning a 1 cm long shank from which 384 recording channels can be used at any one time. For my experiments, the 384 electrodes closest to the tip were used, permitting simultaneous recording of pM2 and DMS.

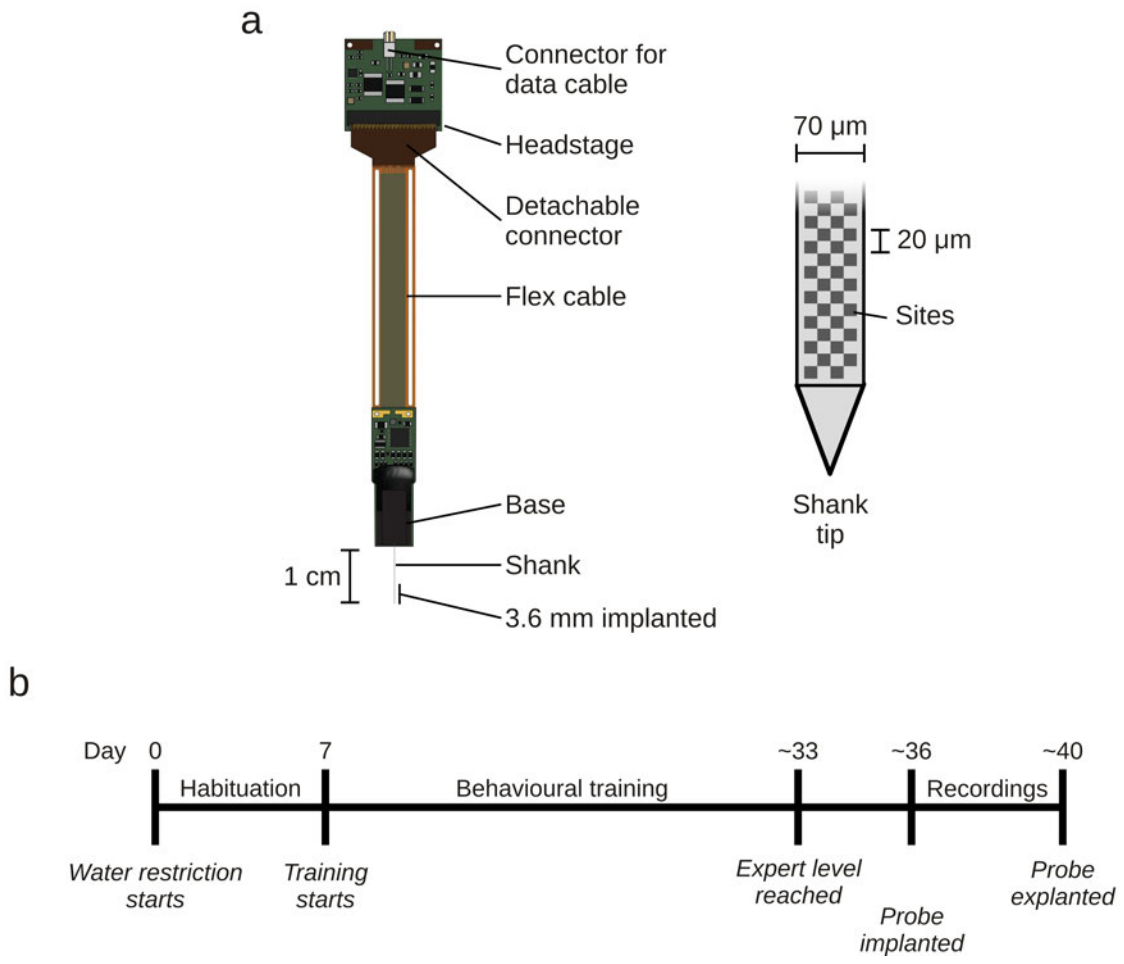

Figure 4.1: Experimental design overview.

(a) Neuropixels 1.0 silicone probe (imec) used for recordings. Adapted from Steinmetz et al. 2021.

(b) Experimental timeline including water restriction, habitation, behavioural training, and recording phases. Expert level was reached after an average of 33 days. Mice then needed to maintain performance for 4 days, after which they underwent probe implementation and recording was started.

4.2.1 Animals

Female and male C57BL/6 mice (Charles River) aged 6-12 weeks and weight matched to 20-22 g baseline weights were maintained as described in Section 2.2.1. Mice underwent a water restriction protocol to facilitate task learning, with 6 µl water rewards dispensed after successful trial completion (see Section 2.2.1). Following 7 days of water restriction and habituation to handling and procedure rooms, mice began training in the visually-directed task described in Chapter 2 (Figure 4.1b). Mice that reached and maintained expert level performance for 4 days were deemed to have successfully learned the task and underwent chronic implantation of a Neuropixels probe (Figure 4.1b).

4.2.2 Handedness testing

The implantation procedure described below is limited to implantation of a single probe, so recordings of pM2 and DMS required selection of a target hemisphere. As neural control of movement displays a high degree of lateralisation (Dacre et al., 2021; Galiñanes et al., 2018; Soma et al., 2017; Tennant et al., 2011), it was necessary to ascertain handedness before probe implantation. Neuropixels recordings were then performed in the hemisphere contralateral to the dominant hand.

Once mice had reached expert level, defined as an above-chance number of correct trials and a sensitivity index (d') of above 1.5 (see Section 2.3.1), they were required to maintain performance for 4 days to ensure consistency. Mice were monitored during one behavioural session in this 4-day period and the reaching hand was recorded for at least 30 correct trials. If the same hand was used for 95% or more reaches, it was deemed to be the dominant hand. If the mouse did not have a dominant hand, the mouse was excluded from the remainder of the experiment to avoid invasive surgery and the risk of implant-related probe damage. During optimisation of the task (see Chapter 2), only one mouse used both forelimbs to engage in the task, likely reflecting an idiosyncratic alternative learned strategy for reaching.

4.2.3 Chronic implantation of Neuropixels probes

To reduce animal use and the risk of probe damage, probe implantations were only performed once mice had successfully learned to perform visually-directed reaches with a high level of success (Figure 4.1b). To record from pM2 and DMS, Neuropixels probes

were implanted 0.5 mm lateral and 0.3 mm anterior to bregma at an angle of 16° in the coronal plane (Figure 4.2).

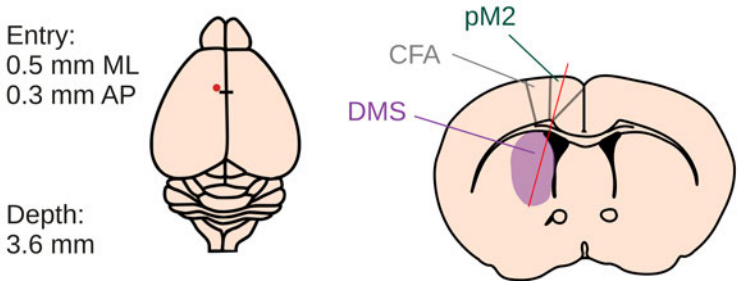

Figure 4.2: Implant target position.

View of implant entry point (left) and path (right). At right, the red line corresponds to the recordable length of probe shaft.

pM2, posterior secondary motor cortex; DMS, dorsomedial striatum; CFA, caudal forelimb area.

The implant scaffolding and procedure was adapted from a protocol published by Juavinett et al. (2019). In this protocol, an implant scaffolding composed of two lightweight 3D printed plastic parts, an internal mount and an external casing, together fix a Neuropixels probe and headstage in position on the skull. The probe base was glued to the internal mount with cyanoacrylate adhesive (RS Pro Super Glue, RS Components). During surgery, the internal mount was screwed into a stereotactic adapter (Figure 4.3a) and the external casing was placed around the internal mount and fixed in place with tape (Figure 4.3b). The headstage was connected to the probe (Figure 4.3c) and the adapter was then mounted to the stereotax, before the shank was lowered into the brain to the target position (Figure 4.3d). Lastly, the external casing was disconnected from the internal mount, positioned to maximise contact with the skull, and cemented to the internal mount (Figure 4.3d). This approach resulted in a stable head-mounted implant that exposes the data transfer connector of the headstage and permits recording of the same brain volume across multiple days.

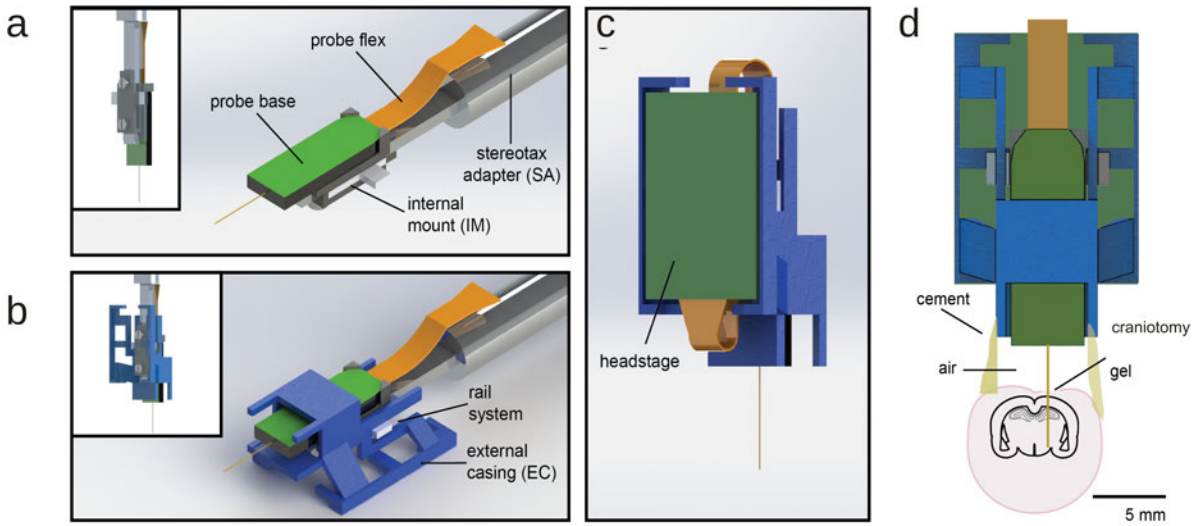

Figure 1. Schematic of Neuropixels AMIE. a. Probe base mounted onto 3D printed internal casing and attached to machined metal stereotax

Figure 4.3: Neuropixels probe chronic implant.

(a) The probe base was fixed to the internal mount and connected to a stereotactic adapter.

(b) The external casing was positioned around the probe using a rail system.

(c) The headstage was connected to the probe base and taped into the back of the external casing.

(d) The casing was cemented to the skull.

Figure adapted from Juavinett et al. 2019.

To perform this procedure, mice were anaesthetised with 4% isofluorane (IsoFlo, Zoetic Inc) in an induction chamber. After shaving the head with an electric shaver, mice were mounted in a stereotactic frame (Kopf instruments). Isofluorane was then reduced and maintained at 1.2 - 2% throughout the procedure. Mice were subcutaneously injected with carprofen analgesic (Rimadyl, Zoetis Inc) and 0.5 ml Ringer's solution (Steriflex). Protective eye cream (Bepanthen) was applied to the eyes to prevent drying. An isothermal heat pad and aluminium foil drapes were used to maintain body temperature at 37 ºC and mice were covered in sterile film to ensure an aseptic surgical environment (Glad Press n'Seal). Anaesthetic depth was confirmed by checking for the absence of the pedal pinch reflex.

To provide access to the brain, a craniotomy was performed above pM2. First, the scalp was cleaned with iodine solution before being removed with surgical scissors. A sterile scalpel was used to remove the exposed periosteum and the skull was scratched with a small injection needle to increase the surface area to which glue could bond. The edges of the skin were sealed to the skull with tissue adhesive (Vetbond, 3M), and

cyanoacrylate adhesive was applied to the sealed edges and skull for strengthening. To ensure the skull was level, a pulled glass micropipette (Drummond Scientific Company) was mounted to the stereotax and used to confirm that the height difference of the skull surface 1.5 mm either side of bregma was less than 0.2 mm, and similarly between bregma and lambda. If the height difference was found to be greater than 0.2 mm, the head was repositioned until the skull was deemed level. More ridges were then scratched into the dried adhesive to increase the surface area to which dental cement could bond. Next, a dental drill (NSK Volver Max, 0.3 mm diameter burr) was used to create a small burr hole 0.5 mm lateral and 0.3 mm anterior to bregma above the hemisphere contralateral to the dominant hand (see Section 4.2.2). A small hole was made in the dura using #5 forceps (Dumont). The probe with internal mount and external casing, mounted to the stereotactic adapter (Figure 4.3c), was attached to the stereotax and rotated 16° in the coronal plane (Figure 4.2). DiI (Vybrant DiI, Thermo Fisher Scientific), a stable, lipophilic stain used to obtain histological confirmation of implant positions following recordings, was applied to the first 3-4 mm of the shank using a 1 µL pipette tip. The tip of the shank was then positioned above the hole in the dura and slowly lowered. If the shank fouled the edge of the dura (i.e. missed the entry point as evidenced by a bending of the shank), the probe was retracted and the hole was slightly enlarged using fine forceps. The shank was lowered into the brain at a speed of 25 µm/s until it reached a depth of 3.7 mm (i.e. parallel to the shank). The shank was then retracted back 100 µm to the final position with an implanted length of 3.6 mm. Next, the tape securing the external casing to the stereotactic adapter was removed so that the casing could move. The casing was then lowered and repositioned to maximise contact with the skull, and cemented using dental cement (Jet Denture Repair Acrylic, Lang Dental Manufacturing Co.). The casing was cemented to the internal mount at the interface provided by the rail system (Figure 4.3b), and the internal mount was unscrewed from the stereotactic adapter, which was subsequently retracted, leaving the mount and casing in place. To protect the exposed portion of the shank, masking tape (3M Scotch 101E) was used to cover any gaps around the scaffolding and it was then fixed in place with dental cement, fully sealing the implant except for the data cable connector on the headstage. Lastly, mice were left to recover from the anaesthesia and transferred to a heated recovery chamber. Once recovered, mice were housed individually to prevent damage to the implants caused by cage mates. Carprofen analgesic was provided at 24, 48 and 72 hours post-surgery.

4.2.4 Explantation of probes and tissue fixation

Neuropixels probes have a significant financial cost and so re-use is essential. To enable re-use of implanted probes following an experiment, mice underwent an explantation procedure. This procedure was immediately followed by transcardial perfusion fixation to harvest the brain for histological confirmation of implant location.

Mice were anaesthetised and mounted to a stereotactic frame as described above. Large forceps and scissors were used to remove the tape around the implant scaffolding and expose the probe, external casing and internal mount (Figure 4.3). Next, an adapter was mounted to the stereotax and rotated 16° in the coronal plane to be parallel with the implant. The adapter was lowered into and screwed to the internal mount. The cement fixing the external casing and internal mount together at the rail system (Figure 4.3b) was removed using a dental drill (NSK Volver Max), disconnecting the internal mount and probe from the casing and skull. The adapter was then retracted, lifting the mount and probe away from the skull. Thus, the probe shank was explanted from the brain along the implant path. As the internal mount was permanently fixed to the probe base, it was also re-used, and therefore care was taken to ensure the internal mount does not get damaged due to drilling. The probe shank was then placed in Tergazyme solution (Alconox), a detergent with protease, for overnight cleaning.

The explantation procedure was immediately followed by perfusion fixation. Anaesthetised mice were given an overdose of pentobarbital (Euthatal, Merial) via intra-peritoneal injection and transcardially perfused with 30 ml Ringer's solution (Steriflex) followed by 30 ml 4% paraformaldehyde (Sigma-Aldrich). Brains were extracted and stored overnight in 4% paraformaldehyde at 4 °C, before being transferred to phosphate-buffered saline until used to confirm implant path (see Section 4.2.8).

4.2.5 Neuropixels recording apparatus

A task arena (see Section 2.2.3) was placed inside a Faraday cage table for recordings. Techspray anti-static spray (RS Components) was applied to the arena as test recordings determined that this reduced noise artefacts related to mice reaching to the target. To prevent twisting of the data cable and to improve mouse comfort during recordings, a commutator (Adafruit Industries, slip ring 1196) was installed above the arena (Figure 4.4a).

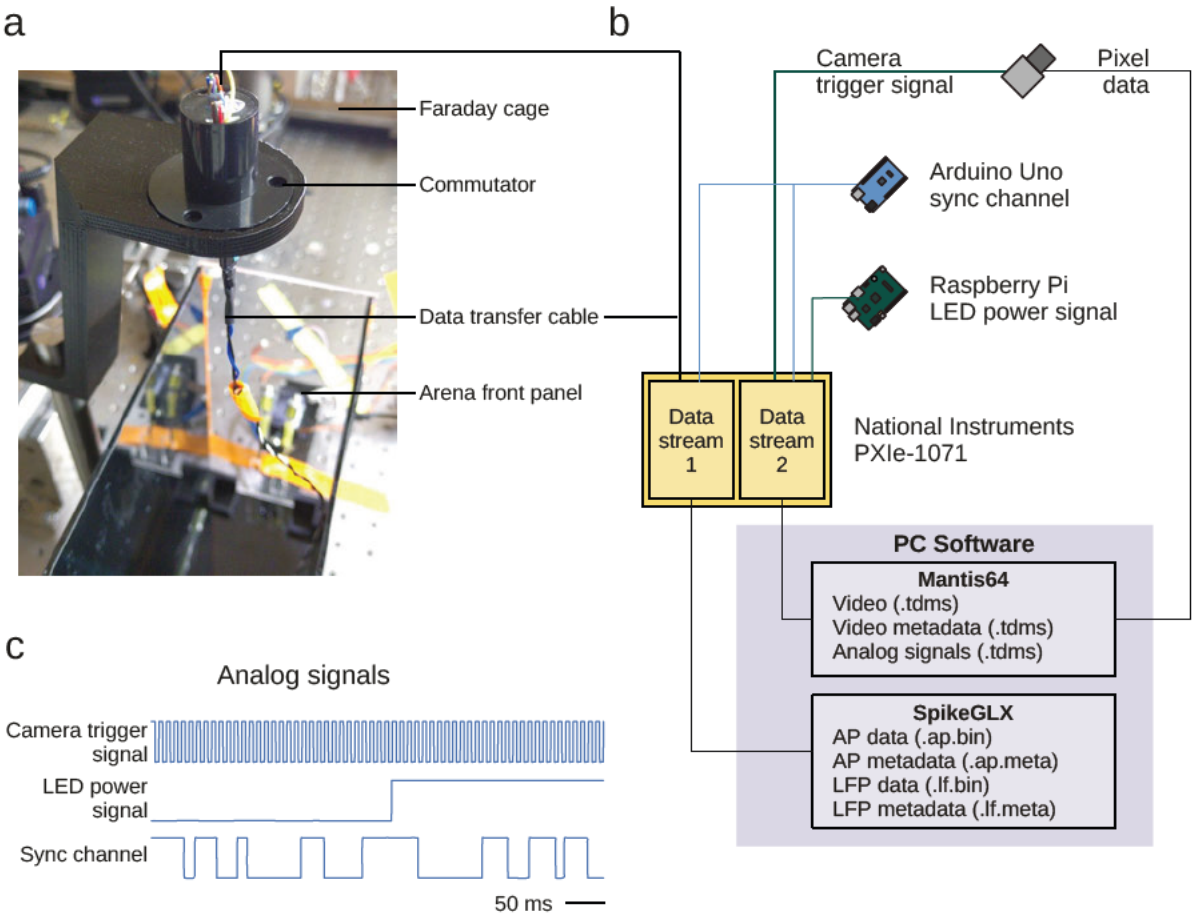

Figure 4.4: Neuropixels recording system.

(a) Task arena with commutator used for recordings.

(b) Data acquisition (DAQ) system used to concurrently acquire two data streams, with the full set of data files that are output.

(c) Analog signals recorded as part of data stream 2.

Task hardware was controlled by a Raspberry Pi computer as described in Section 2.2.4. A desktop PC was used to control the Raspberry Pi and manage data acquisition. The data acquisition (DAQ) system used for recordings was composed of two data streams (Figure 4.4b). Both data streams were transmitted to the PC via a single National Instruments PXIe-1071 DAQ chassis, each with a dedicated PXIe card.

Data stream 1, acquired via a Neuropixels PXIe acquisition card (imec), recorded data from 2 sources:

1. Dual-band raw analog signals from 384 channels, originating from the Neuropixels probe.

2. A ‘sync channel’ analog signal (described below) generated by a dedicated Arduino Uno (Figure 4.4c, bottom).

This data stream was configured and recorded using SpikeGLX software (Jun et al., 2017). SpikeGLX was used to configure the probe hardware to select which electrodes on the shank were enabled and in all experiments I used the 384 electrodes nearest to the shank tip (“bank 0”). SpikeGLX was also used to configure the electrode on the shank tip as an internal voltage reference. The dual-band data was saved per band, generating ‘action potential’ (AP) and ‘local field potential’ (LFP) binary data files, each storing their voltage data alongside a copy of the sync channel at 30 and 2.5 kHz, respectively (Figure 4.4b, bottom).

Data stream 2, acquired via a National Instruments PXIe-6341 DAQ card, recorded data from 3 sources:

1. Outputs from the 2 high-speed cameras used for motion tracking, including a frame trigger signal (Figure 4.4c, top) and pixel data. Pixel data bypassed the DAQ chassis and was transmitted to the PC via USB interface (Figure 4.4b, right).
2. An analog signal originating from the Raspberry Pi that represented the power sent to the reach target LEDs (Figure 4.4c, middle). From this signal, behavioural data saved by the Raspberry Pi (as described in Section 2.2.4) could be aligned to this data stream.
3. The same ‘sync channel’ analog signal saved in data stream 1 (Figure 4.4c, bottom).

This data stream was acquired using Mantis64 DAQ software (https://www.mantis64.com) and saved in National Instruments TDMS format (Figure 4.4b, bottom). Analog signals were recorded at 2.5 kHz; camera pixel data were recorded at 100 Hz. Additionally, Mantis64 was used to generate an analog signal transmitted to the cameras to trigger frame capture at 100 Hz; this trigger signal was fed back into the data stream to be recorded as an analog signal (Figure 4.4c, top).

Thus, the complete dataset for a single recording comprised: metadata and binary data for AP and LFP voltage data recorded from the Neuropixels probe, two videos (see Section 2.2.3 for camera positions), camera trigger signals (used to calculate frame timestamps), task LED signals, and a sync channel. The sync channel was a random

frequency-modulated square wave continuously generated by a dedicated Arduino Uno and was saved to both data streams (Figure 4.4c, bottom). Following the experiment, this was used to temporally align data from the two data streams as described in Section 3.2.2.

4.2.6 Recording in awake, behaving mice

Neuropixels recordings were performed in expert mice at least 24 hours after the probe implantation surgery. If mice appeared to still be recovering from the surgical procedure, the recording was postponed until the following day.

After preparation of the recording hardware and software (see Section 4.2.5), a short data transfer cable was used to connect the commutator to the headstage connector on the implant. Successful communication between the software and probe was confirmed using SpikeGLX. Next, the mouse was placed into the task arena, the Faraday cage was closed, and all lights were turned off. Recording of the two data streams (Figure 4.4b) was then enabled in SpikeGLX and Mantis64, followed by the behavioural task sequence controlled by the Raspberry Pi (see Section 2.2.4).

The software and the mouse were monitored throughout the session to ensure that recordings proceeded without issue. If mice were not engaging with the task (for example, if all trials within the first 3-4 minutes were miss trials), the session was aborted. This happened on few occasions when recordings were attempted on day one following surgery.

4.2.7 Data processing and analysis using the `pixels` pipeline

The `pixels` pipeline described in Chapter 3 was used to process and align the electrophysiological and behavioural data (i.e. data streams 1 and 2, respectively; see Section 4.2.5). In brief, the action potential data was first spike-sorted using Kilosort 3 (Steinmetz et al., 2021) and spike clusters curated with phy (https://github.com/cortex-lab/phy) to yield well-isolated units representing putative neurons. The sync channels were used to convert each data stream into a common timeline, facilitating alignment of neural data to behavioural timepoints.

As described in Section 2.2.6, the DeepLabCut toolbox for markerless pose estimation (Mathis et al., 2018) was used for extracting reach trajectories from camera data. The camera trigger signals (Figure 4.4c, top) were then used to calculate timestamps for each frame, which enabled aligning inferred motion trajectories to the behavioural and neural data.

4.2.8 Probe tract reconstruction

Implant placements were confirmed using a histological approach. This served to ensure that recordings were performed in pM2 and DMS and to accurately align neural activity with anatomical features and areas found along the implanted shank. Following the explantation and tissue fixation procedure described above, brains were cut into 100 µm coronal sections using a vibratome (Leica VT1000S) and mounted with Vectashield Antifade Mounting Medium with DAPI (H-1200, Vector Laboratories). Slices were imaged with an automated slide scanner (Axioscan 7, Zeiss) configured to detect DAPI and DiI. Anatomical location of tissue was determined by referencing features to the Paxinos and Franklin mouse brain atlas (Paxinos, 2001). The paths of implanted shanks within the brain were reconstructed and used to identify spiking activity in pM2 and DMS. pM2 layer boundaries were estimated by referencing pM2 tissue to the Allen Reference Atlas (Mouse Brain) and measuring the lengths of implanted shank that penetrated each layer.

Probe tracts were further confirmed by examining the raw extracellular voltage data and identifying the boundary between low and high noise recorded inside and outside of the brain, respectively. For each recording, the standard deviation of extracellular voltage recorded from each electrode provided a measure of that electrode's overall noise level. The distribution of noise levels across electrodes was then clustered using the *k*-means clustering algorithm. The number of clusters within the distribution of noise levels was identified using the elbow method: clustering was performed using 1 to 5 clusters (*k*), then the variance explained was plotted as a function of *k* and the position of the 'elbow' of the curve was selected as the optimal number of clusters. This method reproducibly reveals two clusters of noise levels that correspond to two non-overlapping series of electrodes along the probe shank. The boundary between these two sets of electrodes was deemed as the surface of the brain. The results of this method were used to corroborate histologically-determined probe tracts, which were re-examined if their

estimated implant length (i.e. depth parallel to the shank) differed from the noise-based estimation by over 50 µm. This method provided an objective and quantitative measure of the length of probe tracts, serving as a 'quality assurance' step to improve the accuracy of estimations compared to relying solely on inspection of histological images.

4.2.9 Identification of principal neurons and interneurons

To distinguish between spike clusters corresponding to principal cells and interneurons, I applied a clustering method to the spike widths of individual units, which have previously been shown to be a reliable method for separating pyramidal neurons and interneurons in cortex (Currie et al., 2022; Dacre et al., 2021; Guo et al., 2014b; Ison et al., 2011; Mitchell et al., 2007) and striatum (Gage et al., 2010; Planert et al., 2013; Wang et al., 2013). First, the median spike width for each unit was calculated. The extracellular waveforms for all spikes were loaded from file using `phylib` (https://github.com/cortex-lab/phylib) and spike widths were calculated as the duration from trough to following maxima (Jia et al., 2019). Unit spike widths were computed as the median width across individual spikes. For each of pM2 and DMS, *k*-means clustering was applied to the distribution of spike widths across all recordings. The optimal number of clusters was then estimated using the elbow method, and boundaries between adjacent clusters were calculated as the centre point between their closest values.

4.2.10 Detection of movement-related firing rate changes

To identify units that exhibited reproducible reach-related activity, I analysed their firing rates during correct trials. Firing rates, computed by convolving spike times with a Gaussian kernel (σ = 50 ms), were calculated for three task-aligned epochs and compared to a baseline period defined as the 1 s preceding visual stimulus onset. The first epoch was defined as -300 to 0 ms before reach onset, which was detected using a motion tracking approach (see Section 2.3.2), representing the period encompassing preparation and initiation of movement (Dacre et al., 2021). The second and third epochs corresponded to reach extension and retraction, respectively. In brief, the extension epoch began at reach onset (i.e. when the hand lifted from the arena floor) and ended at the point of grasp of the reach target. The retraction epoch began when the grasp was released and ended at reach offset (i.e. when the hand returned through the slit in the arena wall). For each trial, the mean firing rate was calculated for the

baseline period and each epoch. Next, a bootstrapped distribution of changes from baseline to epoch was generated across trials (10,000 samples of 20 randomly sampled trials) and deemed significant if the 95% confidence interval (CI) did not overlap 0. A unit's activity during each epoch was considered to be increased if the CI for that epoch was greater than 0, or decreased if the CI was below 0.

Neurons involved in sensory or decision-making processes may display reproducible changes in activity between stimulus onset and the beginning of the first epoch. If this change in activity continues into the first epoch, this approach would identify the neuron as having "movement-related" activity when in fact this may not be the case. To avoid this potential confound, I identified units where firing rate changes occurred during -600 to -300 ms before reach onset. If a unit exhibited increased or decreased activity during this period that was sustained into the subsequent epoch, those sustained firing rate changes were deemed non-movement related and excluded from further analysis.

To test whether units displayed significant activity changes during repetitive reaches, firing rates during the first self-initiated reach following the initial, cued reach were analysed as above. Repetitive reaches were included if they occurred within 3 s of the cued reach, which was the case during most trials (see Section 2.3.2). This is a more conservative time window than used in Figure 2.8b, which shows repetitive reach counts within 5 s of the cued reach. In contrast to the cued reaches, repetitive reaches were initiated from a standing posture and consequently their earliest well-defined and reliably motion-tracked event was when the hand passed through the slit. The baseline period used was -400 to -200 ms before the hand passed through the slit, chosen to exclude limb movement while maximising the number of trials to include for comparison; repetitive reaches that passed the slit within 450 ms of the cued reach were excluded on the basis that the baseline period partially included movement from the cued reach. Firing rates were calculated during a response period from when the hand passed through the slit to reach offset, and the distribution of changes from baseline for each unit was tested for reproducible increases or decreases as above.

4.2.11 Clustering of units based on firing rate profiles

For each recording, pair-wise correlations were made between trial-averaged firing rate profiles of units within pM2 and DMS. The mean firing rate profile of each unit was calculated across correct trials for the period starting from the earliest 2.5th percentile

of cue onsets to the latest 2.5th percentile of reach offsets. Use of this period aimed to minimise the time within the inter-trial interval that was included in correlations. The Spearman's rank correlation coefficient was calculated between the average firing rates of pairs of units. Hierarchical clustering was then performed on the resultant correlation coefficient matrix using average linkage clustering (i.e. the UPGMA algorithm; Müllner (2011)) to construct a similarity hierarchy. The hierarchy was subsequently divided to produce flat clusters; the number of clusters was chosen to best describe the similarities and differences between units, and was the same for all recordings.

To make generalisable statements about pM2 and DMS functional organisation, correspondence between clusters from different recordings was determined. First, the average firing rate profile of each cluster was calculated as the grand mean across normalised mean firing rates of units within the cluster for a 4 second window centre-aligned on reach onset. Next, clusters were grouped such that each group contained 1 cluster per recording, and the Spearman's rank correlation coefficient was calculated for all pairs of clusters within each group. The sum of correlation coefficients across all pairs and groups was used to assess the quality of the groupings. This was repeated for all possible groupings, and the grouping with the greatest sum of correlation coefficients was deemed as the best correspondence of clusters between recordings.

4.3 Results

Probe tracts were confirmed histologically using DiI for all mice (Figure 4.5a). A systematic error in implantation path resulted in the initial cohort of mice having recordings from only pM2. Histological assessment of implantation path identified this error as an erroneous rotation of probe trajectory towards the posterior of the brain. The surgical procedure was revised to correct for this error, resulting in successful penetrations of pM2 and DMS in later cohorts. Histologically-estimated probe tracts were corroborated by identification of the boundary between relative low and high noise electrodes (Figure 4.5b), which corresponds to the surface of the brain. In total, recordings were made from pM2 in 10 mice and DMS in 5 mice.

High noise levels within an electrophysiological recording can result in masking or filtering of spiking events. Therefore, to identify particularly noisy recordings, a global

measure of noise was calculated for each recording, defined as the median of the standard deviations of raw voltage recorded on each electrode. Comparing global noise levels across recordings was useful during the implementation and refinement of the implantation procedure and optimisation of the recording setup. For example, the amount of cement used to secure implant casings to the skull impacted noise levels significantly; increasing the thickness of the cement (and thus stability of the implant and casing) significantly reduced noise levels. Similarly, the application of Techspray anti-static spray to the task arena was also found to reduce noise levels.

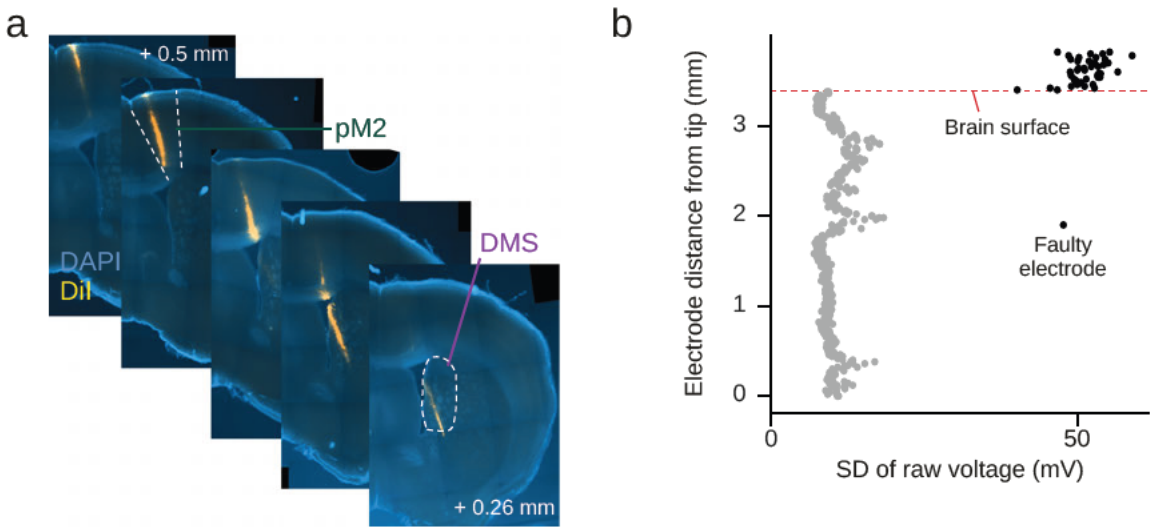

Figure 4.5: Identification of probe tracts.

(a) Coronal sections from a representative mouse showing a single probe tract. The path is revealed by DiI, which was applied to the probe shank prior to implantation (yellow), with DAPI counterstain. Annotated positions are in mm relative to bregma.

(b) Identification of the position of the brain surface on the probe by clustering of electrode noise levels, defined as the standard deviation of voltages.

For analysis of how neural activity related to the behaviour, one recording session was selected for each mouse. First, sessions were excluded if behavioural performance did not reach the expert level criteria described in Section 2.3.1. Probe implantations were performed in mice that had maintained expert performance across 4 training sessions and were performed on the same day as the fourth of these sessions. Recordings were attempted from the following day, and thus low task performance, which only occurred in some recordings attempted the day after implantation, were likely to be due to ongoing recovery from surgery. Next, global noise levels were compared and recordings

were excluded if their noise level exceeded those observed in other recordings from the same mouse by 10% or more. Lastly, following spike sorting with Kilosort 3 (Steinmetz et al., 2021) and manual curation of spike clusters with phy, the recording with the greatest number of single-unit clusters for each mouse was selected.

Following the assessment of implantation tract and recording quality, I selected a list of recordings for further analysis, as shown in Table 4.1. Mice with recordings from both pM2 and DMS had an average of 129 well-isolated units, consistent with published freely moving Neuropixels recordings (Jia et al., 2019; Juavinett et al., 2019).

Table 4.1: Summary of recordings used for analysis. pM2, posterior secondary motor cortex. DMS, dorsomedial striatum.

Cohort	Mouse	pM2 Units	DMS Units	Sex	Handedness
1	1	46	-	male	left
	2	61	-	male	left
	3	18	-	male	right
	4	11	-	male	left
2	5	93	86	female	right
	6	66	51	male	left
	7	28	38	male	left
	8	90	114	male	right
	9	15	64	female	right
	10	34	-	female	right
Count:	10	462	353	5:5	5:5

4.3.1 Unit identification

As neural circuits are composed of principal cells and interneurons, which have different functional roles (Harris and Shepherd, 2015), interpretation of the firing rate properties of recorded units would be improved by the identification of which of these two cell

populations units belonged to. Therefore, to distinguish between them, I applied a clustering method using spike widths as described in Section 4.2.9 (Figure 4.6).

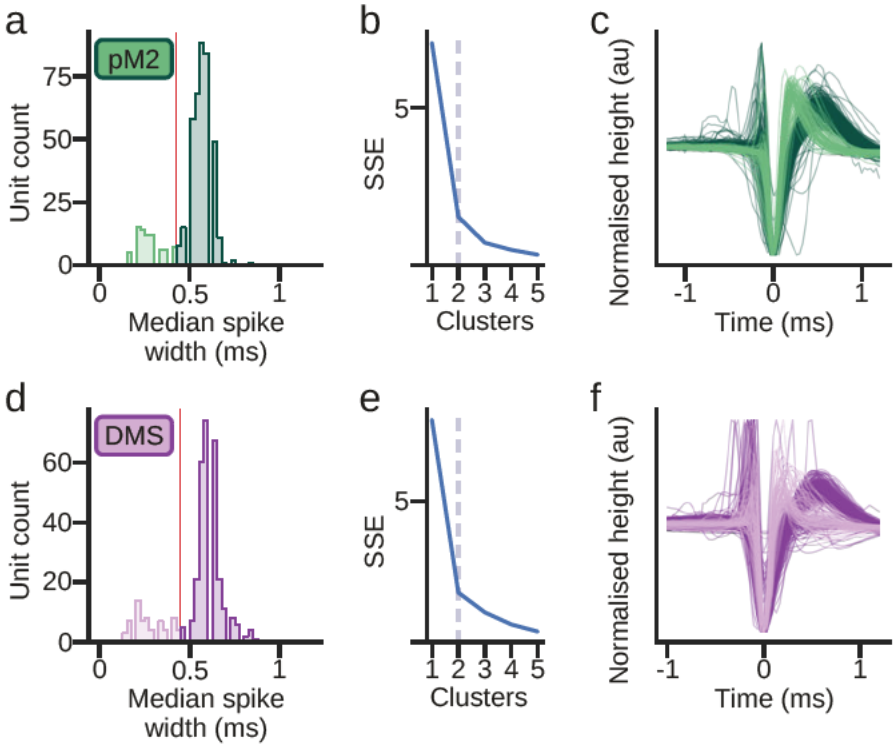

Figure 4.6: Identification of putative principal cells and interneurons.

(a) Distribution of median spike widths of posterior secondary motor cortex (pM2) units, shaded by cluster as determined by *k*-means clustering. The red line indicates the boundary between clusters; units with spike widths greater than 0.42 ms were identified as putative pyramidal neurons. Data from 10 mice.

(b) Sum of squared errors (SSE) produced when clustering pM2 spike widths for *k* of 1-5. The elbow method, a heuristic that identifies the optimal number of clusters in a distribution by examining the 'elbow' in SSE as a function of *k* (grey dashed line), determined that separating spike widths into 2 clusters best described the distribution.

(c) Normalised mean spike waveforms of pM2 units, coloured by cluster.

(d-f) Same as (a-c) but for dorsomedial striatum (DMS) units. Spike widths similarly separated into 2 clusters with a boundary at 0.45 ms. Data from 5 mice with DMS recordings.

Inspection of the distribution of unit spike widths in pM2 revealed a bimodal distribution (Figure 4.6a), consistent with previous observations in cortex (Guo et al., 2014b; Ison et al., 2011; Jia et al., 2019; Mitchell et al., 2007). *k*-means clustering and the elbow method indicated that the optimal number of clusters was 2 (Figure 4.6b). The boundary between the clusters was 0.42 ms (Figure 4.6c), in line with published findings (Currie et

al., 2022; Dacre et al., 2021; Jia et al., 2019), and was used to identify putative pyramidal cells (>0.42 ms) and interneurons (<0.42 ms). Moreover, spike waveforms of the two clusters were indicative of pyramidal cells and interneurons and their differences in spike widths as previously reported (Figure 4.6c) (Guo et al., 2014b; Mitchell et al., 2007). Pyramidal neurons and interneurons constituted 80.1% and 19.9% (± 5.9% [SD]) of pM2 units, respectively, in accordance with previous observations in secondary motor cortex (Guo et al., 2014b).

I then subdivided DMS units into putative striatal principal cells (i.e. medium spiny neurons (MSNs)) and interneurons using the same clustering method (Figure 4.6d-f). *k*-means clustering of unit spike widths in DMS identified 2 clusters (Figure 4.6e) with a boundary of 0.45 ms, slightly higher than in pM2. This is consistent with published observations in rodent striatum (Gage et al., 2010; Planert et al., 2013). Furthermore, spike waveforms of the two clusters are indicative of MSNs and interneurons (Figure 4.6f) (Berke et al., 2004; Keller et al., 2016). Overall, MSNs and striatal interneurons constituted 71.5% and 28.5% (± 13.7% [SD]) of DMS units, respectively, in line with previous findings (Wang et al., 2013).

Next, I determined the anatomical locations of units across pM2 and DMS. The electrode that recorded the mean spike waveform with the largest amplitude for a unit was used to determine its position along the probe track. Figure 4.7 summarises the anatomical distributions of putative pM2 and DMS neurons. While spikes were detected in L2/3 of pM2, Kilosort was less able to separate spikes from different units, and consequently fewer well-isolated single unit spike clusters were detected in L2/3 compared to deeper layers (Figure 4.7b). The underlying cause for this is unclear. A possible explanation is that Kilosort determined that waveforms in these spike clusters were sufficiently variable to label the cluster as 'multi-unit', but with overlapping distributions of features such that Kilosort could not separate spikes into distinct units with sufficient confidence. Recordings in primary motor cortex that led to the results published in Dacre et al. (2021) and Currie et al. (2022) similarly found a greater proportion of spike clusters in L2/3 containing multi-unit activity rather than single-unit activity, suggesting that the ability of Kilosort to separate spikes from L2/3 units is limited compared with units in deeper layers of motor cortex. Consequently, the following results for pM2 will focus on units in deeper layers.

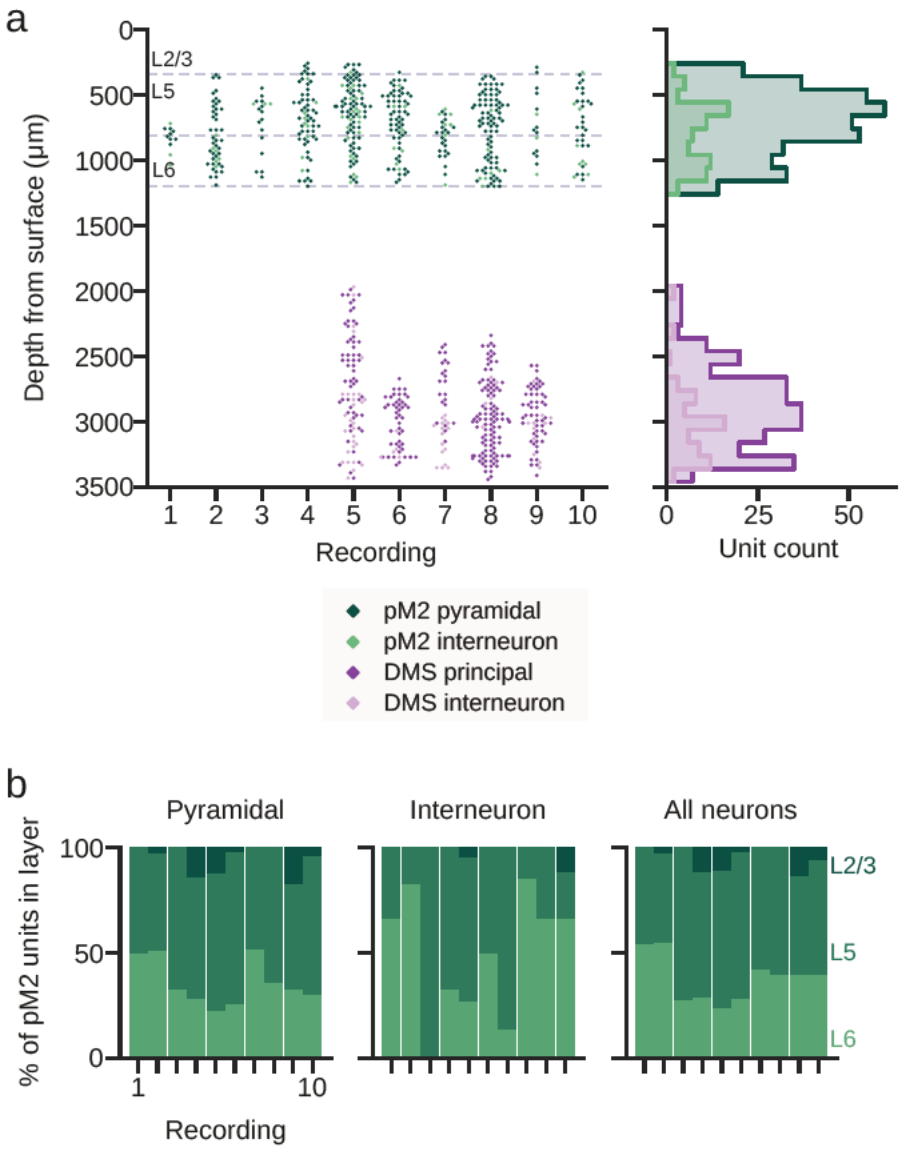

Figure 4.7: Anatomical distribution of pM2 and DMS units.

(a) Depth profile of units, colour coded by unit subgroup. Cortical layer boundaries were estimated by referencing tissue to the Allen Reference Atlas (Mouse Brain). Each recording is a separate mouse. Right, histogram showing the total number of units recorded at each depth (100 µm bins) for each unit subgroup.

(b) The percentage of pM2 units that were recorded in each cortical layer.

4.3.2 Firing rate changes in pM2 and DMS during visually-directed reaches

While recent findings have linked pM2 to a role in visually-directed movement (Hwang et al., 2019; Itokazu et al., 2018) and the execution of voluntary forelimb movements

(Galiñanes et al., 2018; Hwang et al., 2019), its activity patterns during visually-directed reaching have yet to be investigated. To gain insight into activity patterns within pM2 and DMS and how they may contribute to movement, I examined the timing and direction of firing rate changes displayed by pM2 and DMS units during correct trials.

Initiation of forelimb lever pushes has been found to be driven by a thalamocortical motor timing signal that appears in primary motor cortex 300 ms prior to movement onset (Dacre et al., 2021). Motor thalamus also projects to pM2 (Hooks et al., 2013; Hunnicutt et al., 2014), so it is likely that this signal is also received by pM2. Therefore, as described in Section 4.2.10, spiking activity was compared between a baseline period and three epochs: a 300 ms pre-reach period ending at reach onset, extension (i.e. reach onset to grasp; see Section 2.3.2), and retraction (i.e. grasp to reach offset). Firing rate changes during the pre-reach epoch may be indicative of thalamus-driven activity related to movement initiation, whereas activity during the extension and retraction epochs may be more suggestive of contributions to the control of ongoing movements. Units displaying reproducible firing rate changes in one or more epoch will be referred to as *active units*.

Units in pM2 and DMS displayed a variety of movement-related firing rate changes. For example, Figure 4.8a shows an example pyramidal cell in pM2 that increased spiking from 2 Hz to a peak of 16 Hz approximately 60 ms before reach onset. The pre-reach change in firing rate, which was also exhibited by the example DMS principal cell in Figure 4.8e, suggests a possible contribution to the initiation or preparation of reaching. In contrast, the example pM2 pyramidal cells shown in Figure 4.8b-c and DMS principal cells shown in Figure 4.8f-g displayed activity changes only after reach onset, which is more indicative of a role in movement execution. Movement-related activity was also exhibited by interneurons in both brain areas (Figure 4.8d,h).

Across the population of pM2 units, 57% of pyramidal cells and 75% of interneurons were deemed movement related (Figure 4.9, top). In both subgroups, the dominant activity profile was a decrease in firing rate (pyramidal cells, 37% decreased vs 17% increased; interneurons, 60% decreased vs 4% increased). Principal cells in DMS were less

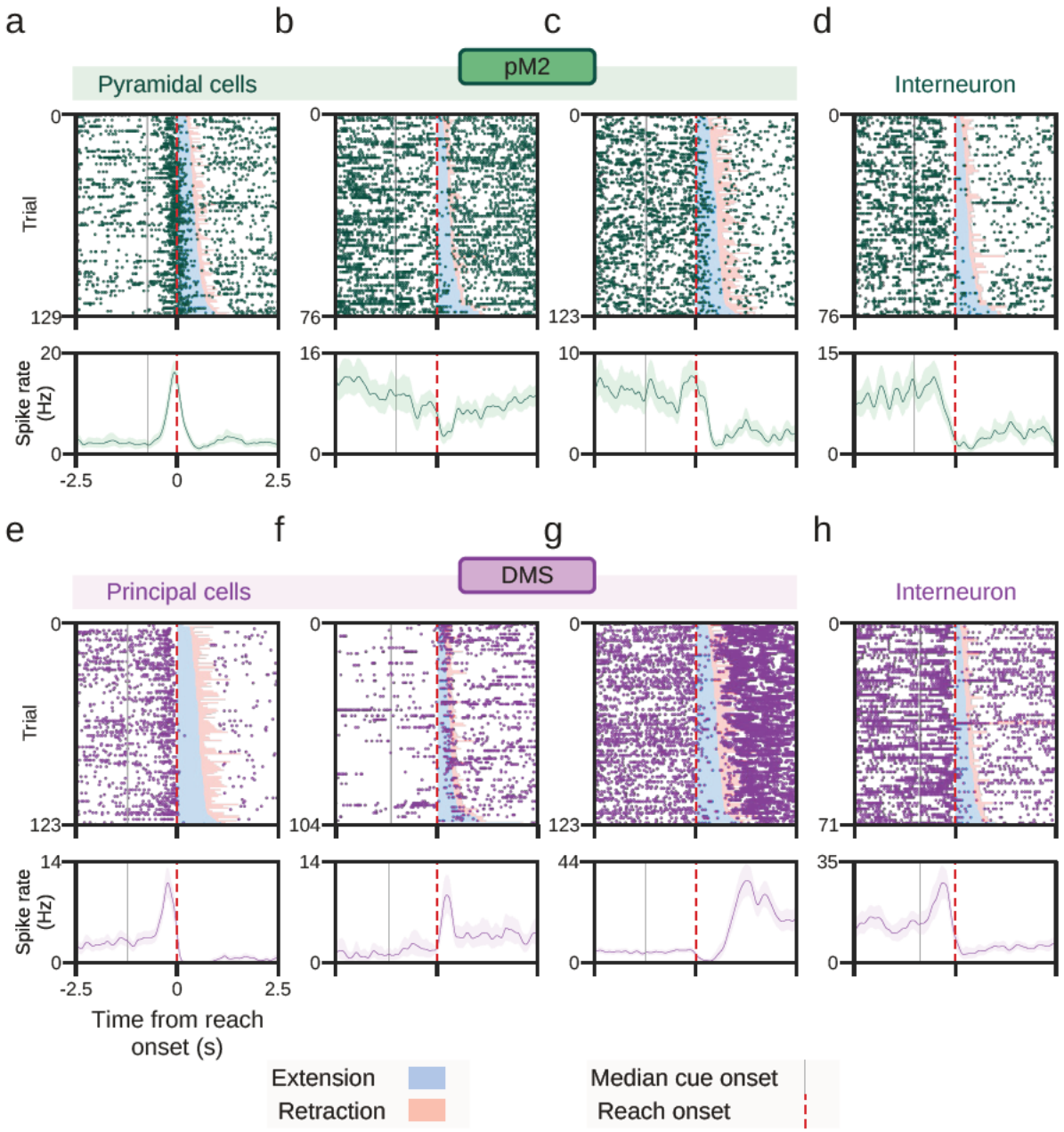

Figure 4.8: Example active unit spike rasters during visually-directed reaching.

(a) Spike raster (top) and average firing rate (mean ± 95% bootstrapped confidence intervals; bottom) aligned to correct trial reach onset for an example pM2 pyramidal cell that displayed reproducible movement-related activity during the pre-reach epoch. In the raster, trials are ordered by duration of the extension epoch (blue), i.e. the interval between reach onset and grasp. Grey vertical lines indicate median cue onset.

(b) Same as (a) for a pM2 pyramidal cell which responded during the extension epoch.

(c) Same as (a) for a pM2 pyramidal cell which responded during the retraction epoch.

(d) Same as (a) for an example pM2 interneuron.

(e-g) Same as (a-c) for 3 example DMS principal cells.

(h) Same as (d) for an example DMS interneuron.

likely to be active units (36%), but the percentages of units with increased or decreased activity were similar (18% increased vs 16% decreased) (Figure 4.9, bottom). However, DMS interneurons, 61% of which were active units, were also dominated by decreased activity.

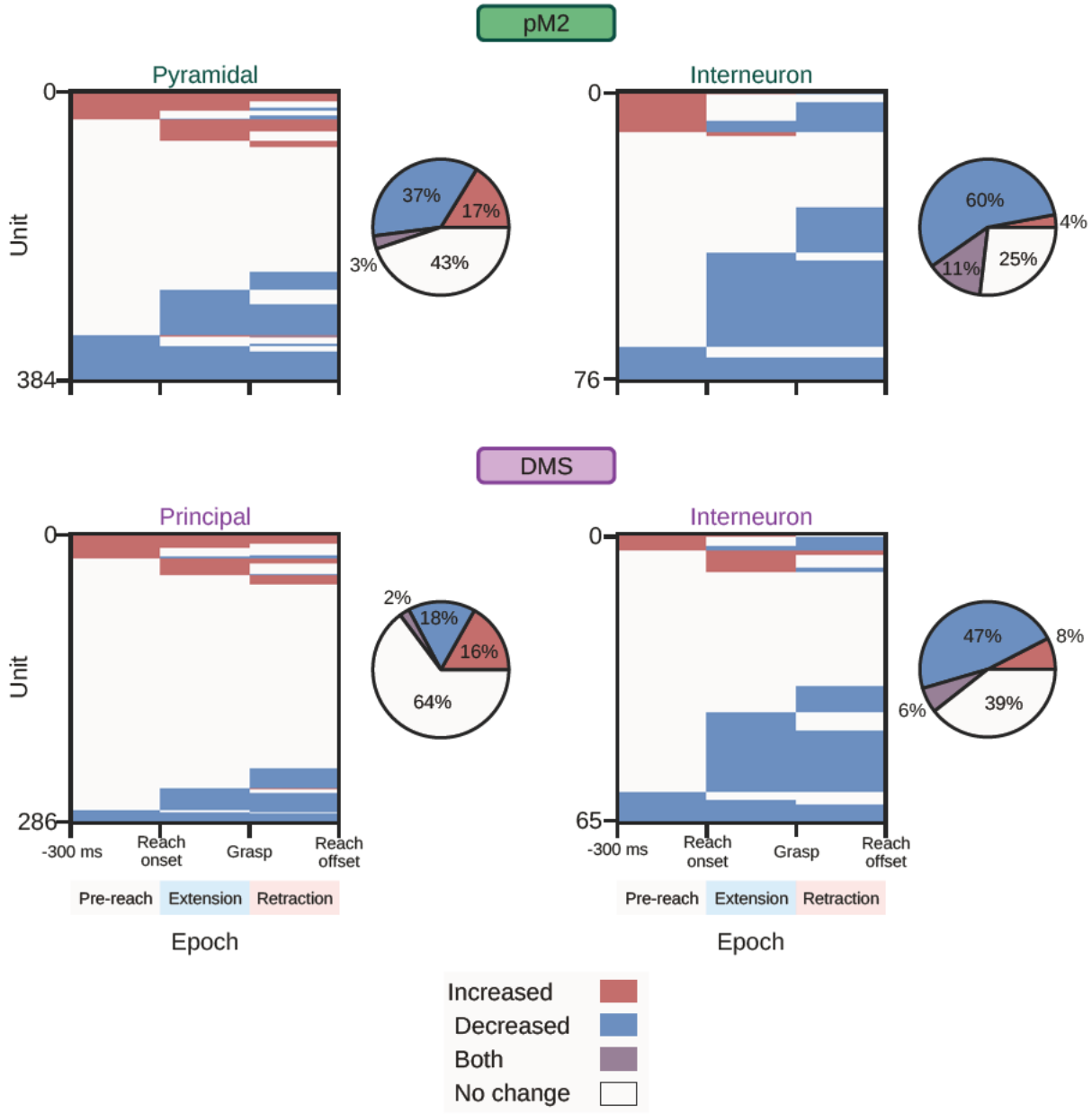

Figure 4.9: Reach-related firing rate changes in pM2 and DMS neurons.
Categorical heatmaps showing the distribution of significant firing rate changes across epochs for each unit, per area and subgroup. Each row represents a single unit, where activity can be unchanged (white), an increased firing rate (red), or a decreased firing rate (blue) for each of the pre-reach, extension and retraction epochs. Pie charts summarise the percentage of units within each subgroup that displayed reproducible movement-related activity in any epoch.

The percentage of neurons with increased or decreased activity was compared between epochs, confirming that reduced activity became progressively more widespread throughout each neuron population (Figure 4.10, blue; one-way repeated measures ANOVAs with post-hoc pairwise *t*-tests; pM2 pyramidal cells, $F(2, 18) = 8$, $p = 0.004$; pM2 interneurons, $F(2, 18) = 24$, $p < 0.001$; DMS principal cells, $F(2, 8) = 27$, $p < 0.001$; DMS interneurons, $F(2, 8) = 12$, $p = 0.004$; repeated measures ANOVA *p*-values are Greenhouse-Geisser corrected to adjust for any lack of sphericity). In contrast, units displaying increased activity were less common in both pM2 and DMS. Pyramidal cells in pM2 displayed a peak in the percentage with increased activity of only 15% during extension, while pM2 interneurons showed increased activity in 15% of units mostly before reach onset (Figure 4.10a-b, red). In DMS, around 10% of principal cells had increased activity throughout movement, roughly similar to the percentage with decreased activity. Overall, the dominant activity profile in pM2, and interneurons in DMS, was a reduction of activity that became more widespread across the population throughout the movement.

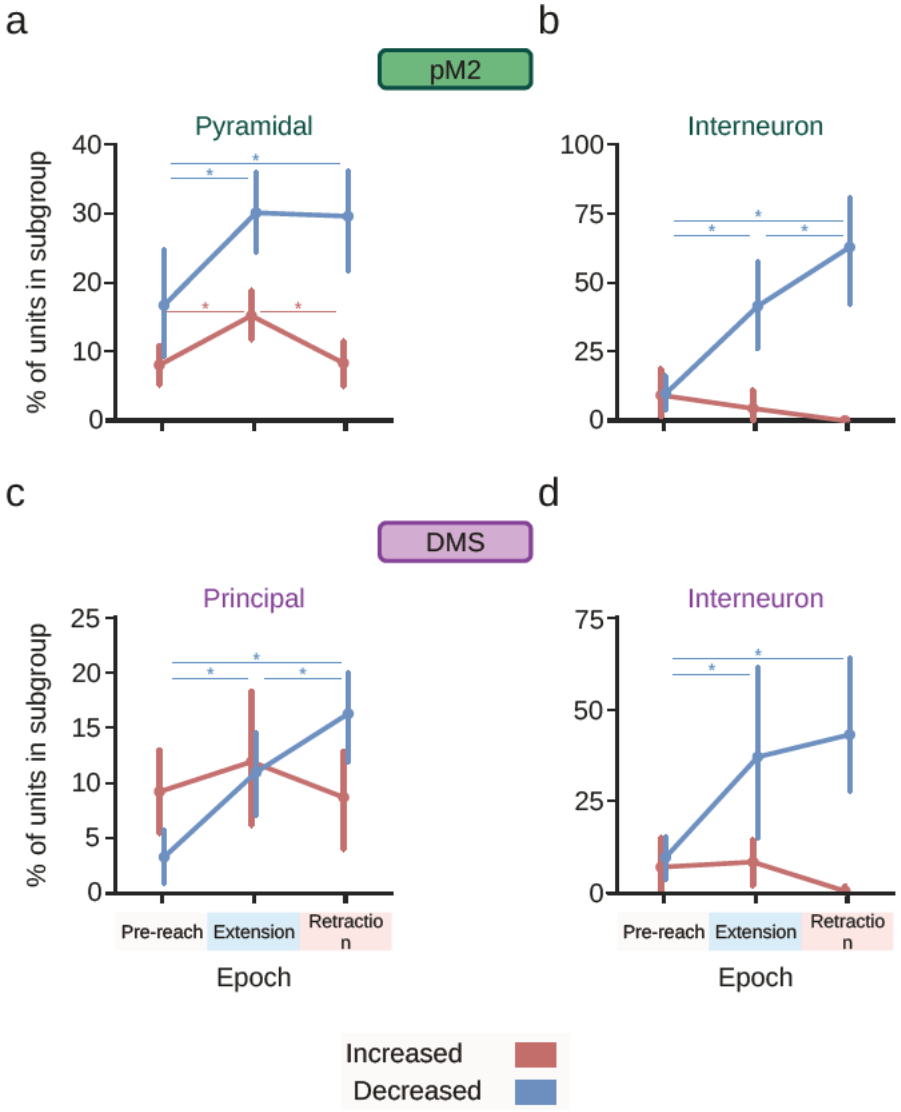

Figure 4.10: Population activity profiles were increasingly dominated by decreased activity during reaches.

(a) Mean and 95% bootstrapped confidence intervals of the percentage of pM2 pyramidal cells that displayed increased or decreased activity across epochs. Significant differences between epochs are indicated by *.

(b) Same as (a) for pM2 interneurons.

(c) Same as (a) for DMS principal cells.

(d) Same as (a) for DMS interneurons.

4.3.3 Depth-dependent changes in movement-related activity in pM2

While pM2 displayed time-modulated reach-related activity, understanding local circuit function in pM2 requires knowledge of the functional differences between cortical

layers. To assess depth-dependent activity patterns, I examined how the distribution of active units related to cortical layers, which were estimated by referencing tissue to the Allen Reference Atlas (Mouse Brain) (see Section 4.2.8).

To examine depth-related effects among active unit populations, their depth distributions were compared between epochs. Among pyramidal cells, the only depth-related effect was that the depths of pyramidal cells with increased activity had shifted towards deeper layers between the pre-reach and retraction epochs, which was due to L5 units disengaging and L6 units engaging during the retraction epoch (Figure 4.11a; Welch's ANOVAs with post-hoc Games-Howell tests; increased, $F(2, 82.1) = 3.21$, $p = 0.045$; decreased, $F(2, 156.1) = 1.37$, $p = 0.257$). Two depth-dependent patterns were observed amongst interneurons. Firstly, increased and decreased pre-reach active units were mostly non-overlapping and restricted to L5 and L6, respectively (Figure 4.11b). Secondly, a greater proportion of interneurons displayed reduced activity after reach onset and grasp, primarily as a result of firing rate decreases in L5 interneurons (Figure 4.11b, blue; Welch's ANOVA as above for interneurons; increased, $F(1, 2.7) = 0.97$, $p = 0.404$; decreased, $F(2, 27) = 6.34$, $p = 0.006$).

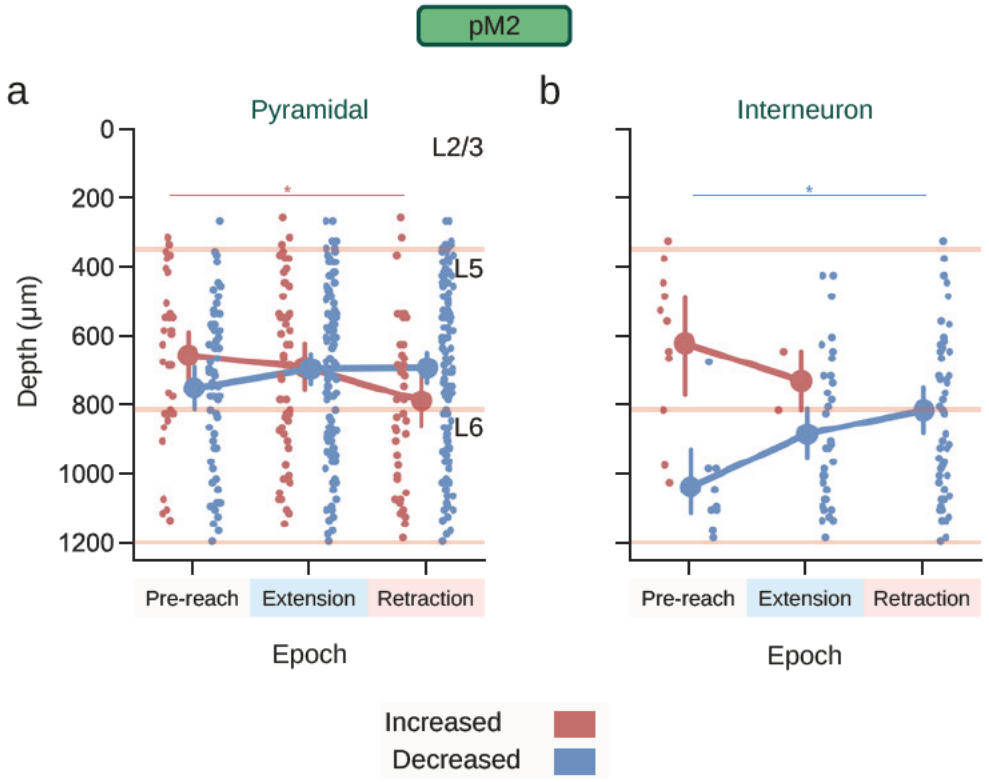

Figure 4.11: Cortical depths of active pM2 neurons.

Distribution of depths (mean ± 95% confidence interval) of active pyramidal cells (a) and interneurons (b) for the pre-reach, extension, and retraction epochs. Significant changes in the distribution of depths are indicated by *. Red lines indicate cortical layer boundaries as estimated using the Allen Reference Atlas (see Section 4.2.8).

Similar patterns of population activity were observed when aggregating per layer (Figure 4.12). While the percentage of pyramidal cells with increased activity was similar between layers and remained relatively stable across epochs, the percentage with decreased activity rose by the extension and retraction epochs for all layers. Additionally, Figure 4.12 shows that interneurons in all layers that displayed pre-reach increased activity reduced their firing during movement. As mentioned in Section 4.3.1, the yield of units in L2/3 was low and thus it is difficult to make conclusions regarding L2/3 activity.

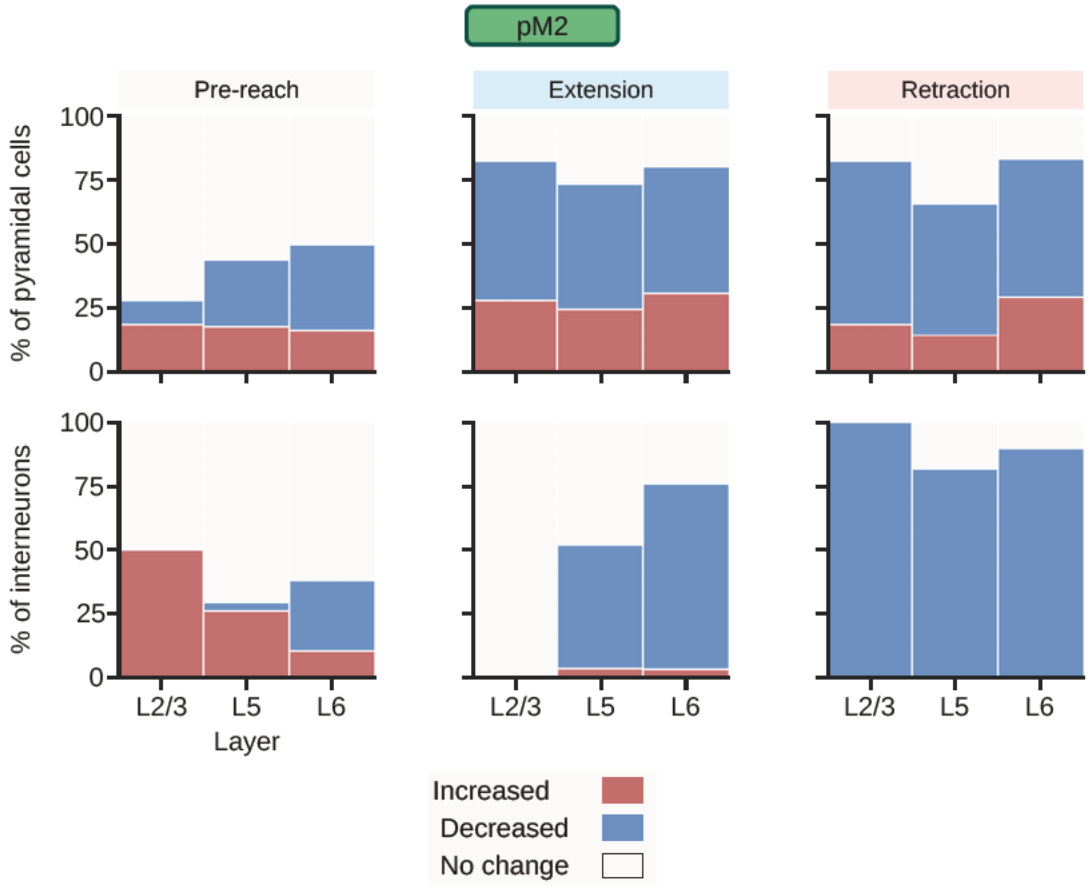

Figure 4.12: Reach-related changes in pM2 active unit population by cortical layer.

The percentage of pyramidal cells (top) and interneurons (bottom) within each layer that displayed

increased, decreased, or no change in activity per epoch. A minority of pyramidal cells displayed increased activity at all times, while an increasing proportion of pyramidal cells and interneurons displayed reduced activity.

4.3.4 Functional clustering of pM2 and DMS units

To further understand the functional organisation of local circuits within pM2 and DMS, I clustered units within each area based on similarities and differences in their firing rate profiles as described in Section 4.2.11.

While selecting the number of clusters is arbitrary and depends on the desired granularity of the description (Hennig, 2015), flattening the similarity hierarchies (e.g. the dendrogram in Figure 4.13a) into 3 clusters revealed patterns consistent across recordings. Generally, increasing the number of clusters resulted in clusters with qualitatively similar average firing rate profiles, appearing, for example, as slightly offset versions of the same profile.

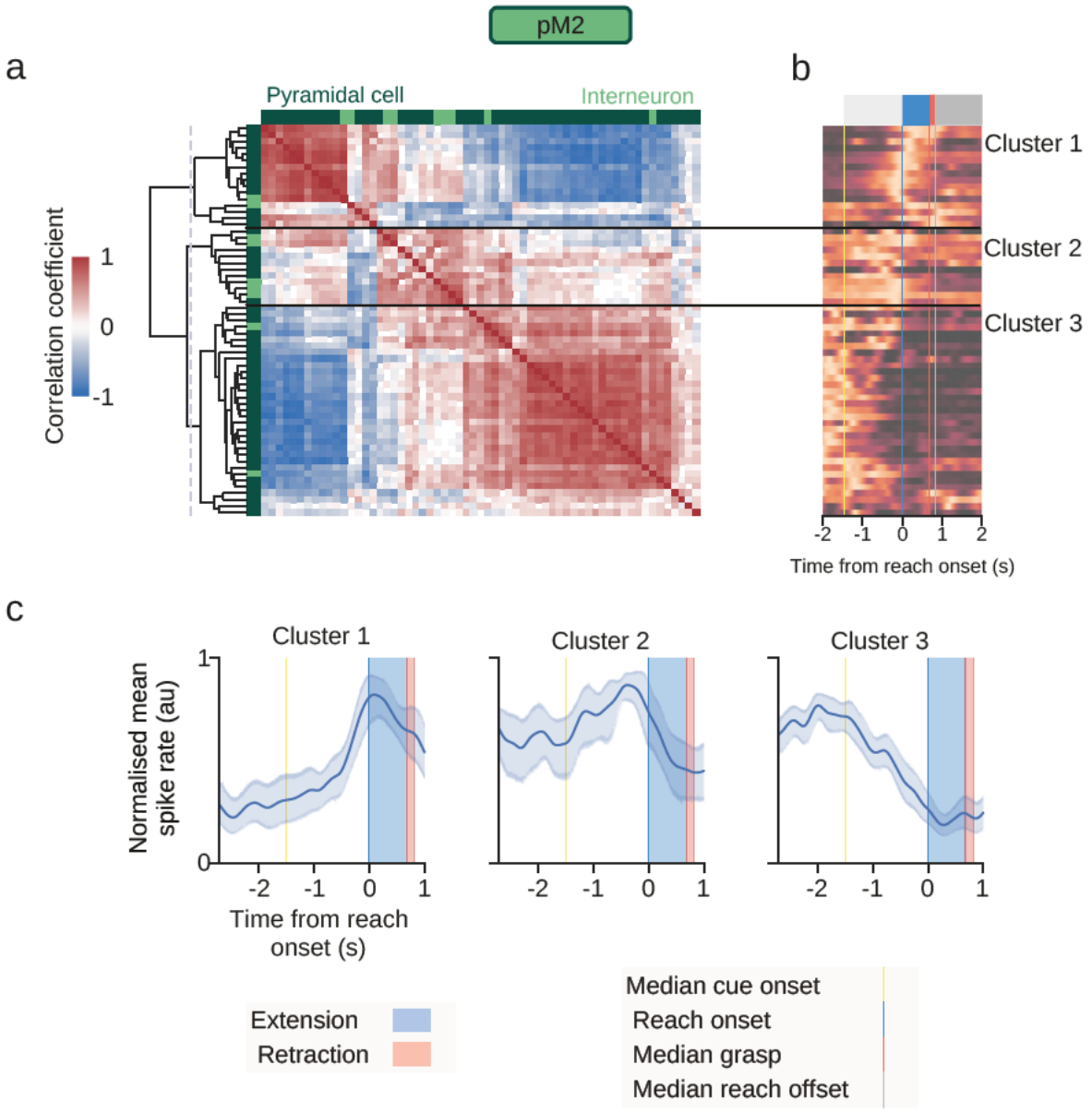

Figure 4.13: Firing rate clustering of pM2 units from an example recording.

(a) Correlation coefficient matrix and hierarchical clustering dendrogram showing cross-correlations of firing rates within 3 clusters. Non-significant correlations ($p > 0.01$) are represented as white. The dashed line indicates where the dendrogram was divided into 3 clusters.

(b) Normalised mean firing rates of units corresponding to rows in (a) during correct trials, showing different temporal profiles for units in each cluster.

(c) Mean (± 95% confidence interval) of normalised mean firing rates of units within each cluster as shown in (b). The time period shown corresponds to the period used for firing rate correlations (see Section 4.2.11).

As exemplified by the single recording in Figure 4.13, pM2 units formed 3 clusters with distinct activity profiles during correct trials. In addition to strong correlations within each cluster, significant anti-correlations were found between clusters 1 and 3 (Figure 4.13a, blue). The firing rate profiles of clusters 2 and 1 show task-related increased activity peaking approximately 300 ms before and 100 ms after reach onset, respectively (Figure 4.13c). In contrast, the activity of cluster 3 is more indicative of task-related decreased activity between cue onset and reach onset (Figure 4.13c).

Clusters with similar firing rate profiles were observed across recordings, revealing a reproducible pattern of pM2 population activity across animals (Figure 4.14). While two clusters displayed increased activity preceding movement, peaking at approximately 300 ms after and 100 ms before reach onset (Figure 4.14a-b), a third cluster displayed decreased activity from -500 to 500 ms after reach onset with maximal suppression by the point of retraction (Figure 4.14c). These clusters indicate

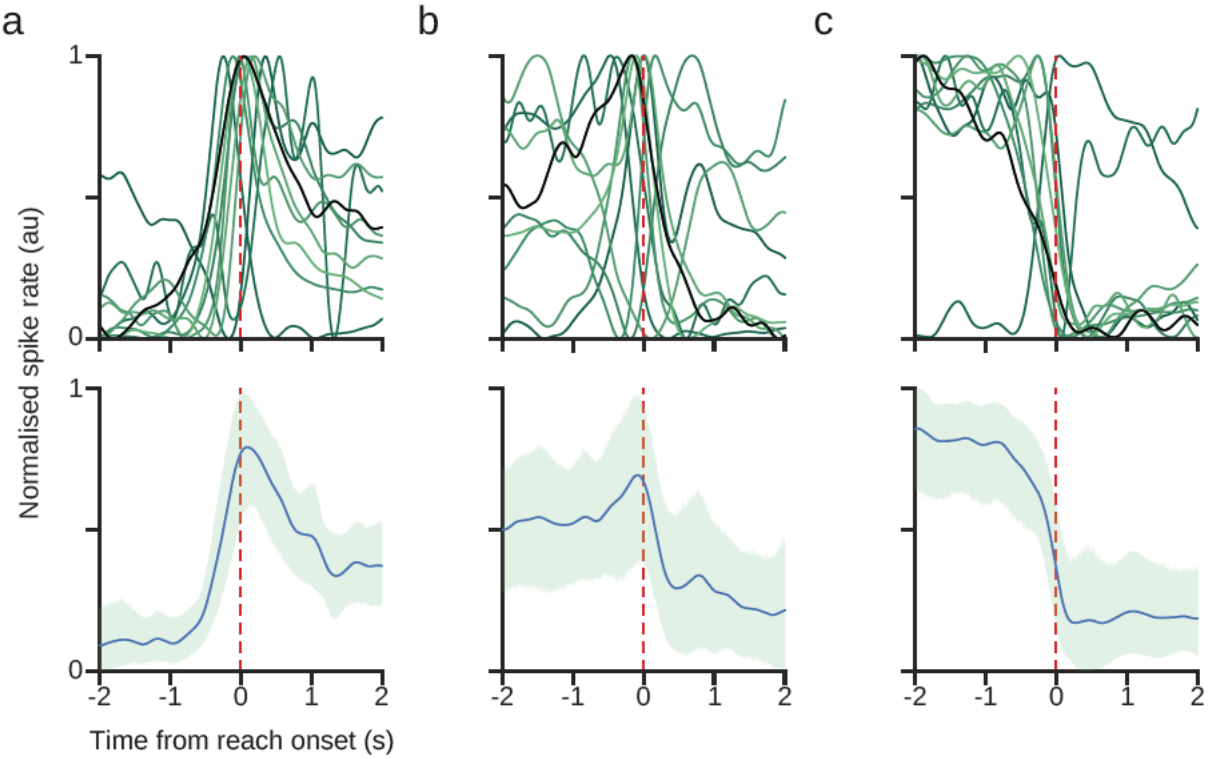

Figure 4.14: Conserved pM2 clusters across recordings.

(a) Normalised mean firing rate profiles across units in cluster 1 for each recording (*N* = 10) during correct trials (top), with the profile of cluster 1 in Figure 4.13 indicated in black. Below, the grand mean firing rate profile across recordings (± 95% confidence interval).

(b) Same as (a) for cluster 2.

(c) Same as (a) for cluster 3.

functionally distinct subpopulations of neurons in pM2 that vary in timing and direction of firing rate changes during visually-directed reaching.

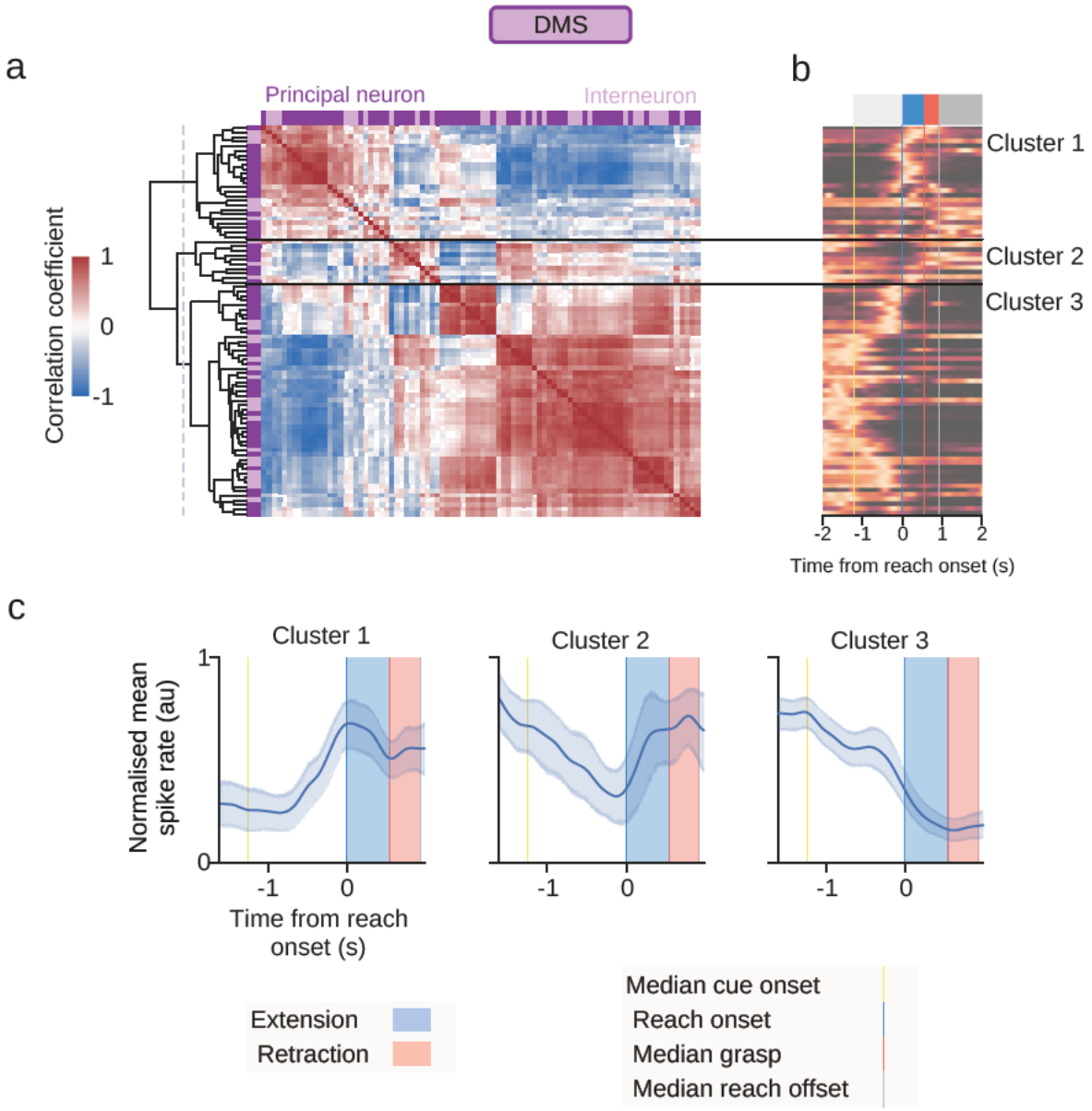

Figure 4.15: Firing rate clustering of DMS units from an example recording.

(a) Correlation coefficient matrix and hierarchical clustering dendrogram showing cross-correlations of firing rates within 3 clusters. Non-significant correlations (p > 0.01) are represented as white. The dashed line indicates where the dendrogram was divided into 3 clusters.

(b) Normalised mean firing rates of units corresponding to rows in (a) during correct trials, showing

different temporal profiles for units in each cluster.

(c) Mean (± 95% confidence interval) of normalised mean firing rates of units within each cluster as shown in (b). The time period shown corresponds to the period used for firing rate correlations (see Section 4.2.11).

As with pM2, large subsets of DMS units showed firing rate correlations and anti-correlations, as shown in the example recording in (Figure 4.15). While the timing of DMS unit activity appeared more variable than pM2 (Figure 4.15b), the within-cluster average firing rate profiles of clusters 1 and 3 were reminiscent of those for pM2 clusters 1 and 3 (Figure 4.15c). Firing rate profiles of cluster 1 were reproducible across animals end exhibited a peak in the average firing rate profile at approximately 50 ms after reach onset (Figure 4.16a). Cluster 3, which displayed a reduction in average firing rate between -500 to 500 ms after reach onset, also appeared to be similar across animals to a lesser extent (Figure 4.16c).

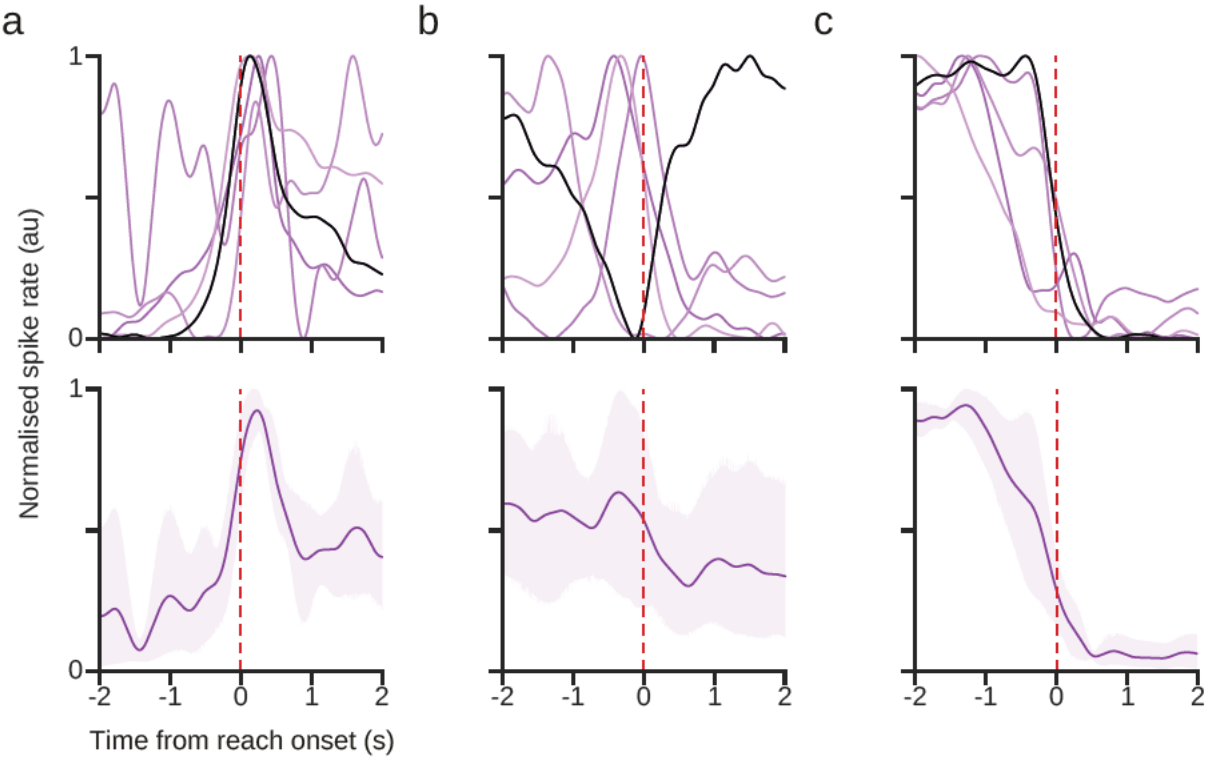

Figure 4.16: Conserved DMS clusters across recordings.

(a) Normalised mean firing rate profiles across units in cluster 1 for each recording (*N* = 5) during correct trials (top), with the profile of cluster 1 in Figure 4.15 indicated in black. Below, the grand mean firing rate profile across recordings (± 95% confidence interval).

(b) Same as (a) for cluster 2.
(c) Same as (a) for cluster 3.

4.3.5 Cued vs repetitive reaches

As described in Section 2.3.2, the initial, cued reaches made during correct trials were typically followed by a series of repetitive reaches. Firing rates were compared between the cued reach and the first repetitive reach of correct trials to explore whether units responded selectively to the cued reach or generally to movement.

Unlike during cued reaches, movement during repetitive reaches did not start at the arena floor (see Section 2.3.2). Instead, reaches started from near the animal's mouth (i.e. due to reward consumption) and limb extension travelled from there, through the slit, then towards the target. The earliest event during repetitive reach extension epochs that was reliably tracked was when the hand passed through the slit. Therefore, to enable comparison of neural activity between cued and repetitive reaches, they were temporally aligned to when the hand passed through the slit. Consequently, activity presented here is late-shifted compared with the reach onset-aligned activity in Figure 4.8.

Task-related activity was either exclusive to cued reaches or occurred during both cued and repetitive reaches (Figure 4.17). Repetitive reach-related activity was observed in pM2 units that displayed increased or decreased activity during the initial, cued reach, and this was observed in both pyramidal cells and interneurons (Figure 4.17a-c). This was also the case for the two DMS subgroups (Figure 4.17e-g). However, both areas also contained units that responded exclusively during cued reaches (Figure 4.17d,h). Note that repetitive reach firing rates shown in Figure 4.17 reflect a temporally shifted and 'smeared' version of the initial reach-aligned firing rates. For example, the smaller peak in Figure 4.17a (light green) at ~-400 ms corresponds to the large cued reach-aligned peak at ~400 ms.

Active units were tested for significant repetitive reach-related activity as described in Section 4.2.10. Among active pM2 units, 58% (± 27% [SD]) of pyramidal cells and 50% (± 36% [SD]) of interneurons were also active during repetitive reaches (Figure 4.18a; no difference between subgroup as determined by t-test, $t(18) = 0.69$, $p = 0.50$).

Interestingly, these proportions were similar between cortical layers and independent of the direction of activity change (two-way ANOVA between layer and direction of change, $p > 0.05$). Similarly, no difference in proportions was detected

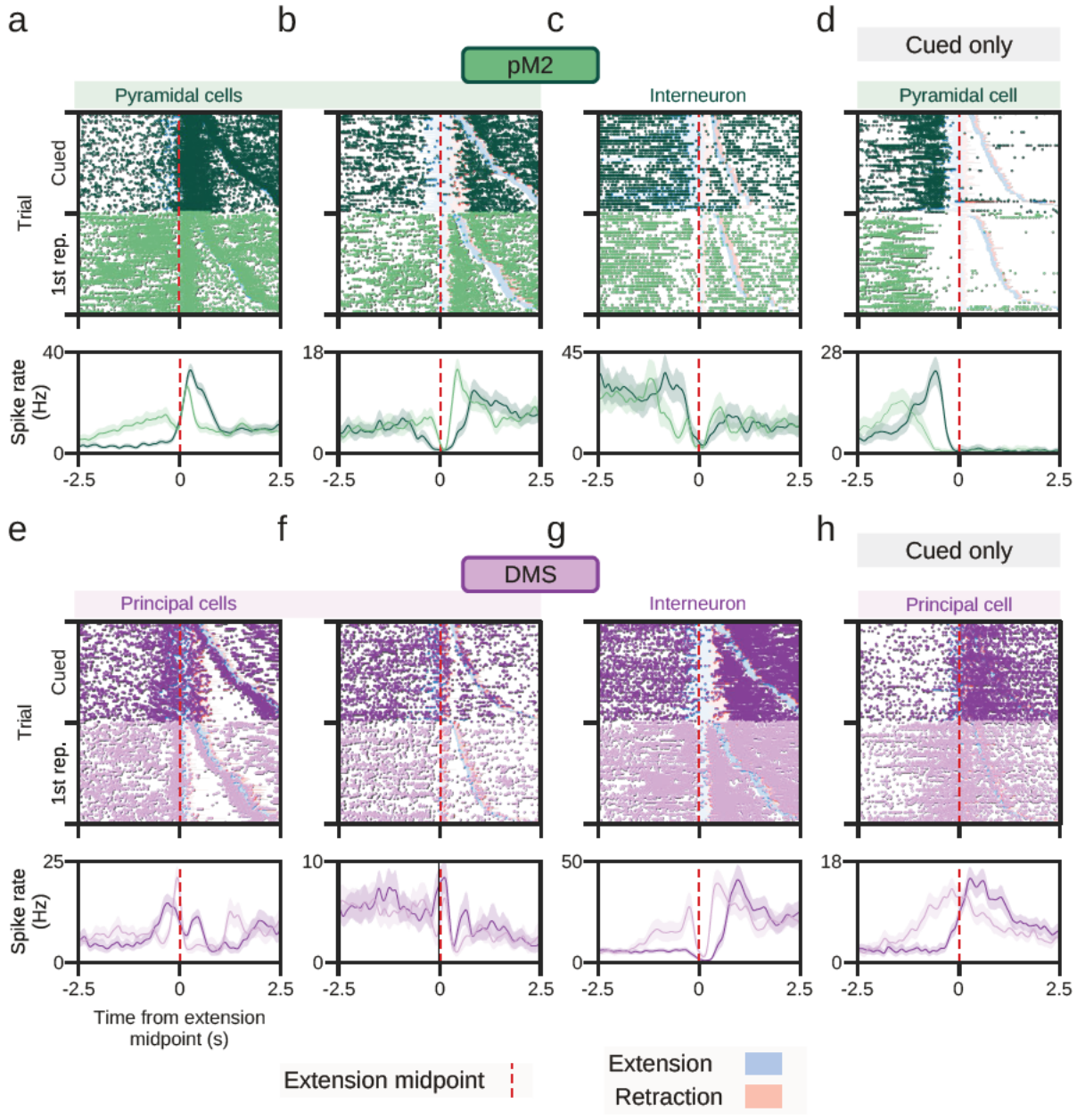

Figure 4.17: Example unit activity during cued and repetitive reaching.

(a) Spike raster for an example pM2 pyramidal cell aligned to the cued reach (top half) and first repetitive reach (bottom half) of correct trials. Reaches are centre-aligned to when the hand passed through the slit. Extension and retraction epochs are indicated for the aligned and following reaches. Rows in each half are ordered by the interval between the aligned reach and the following reach. Below, corresponding firing rate profiles (mean ± 95% bootstrapped confidence intervals). This example unit displayed increased activity during the extension and retraction epochs of both cued and repetitive

reaches.

(b) An example pM2 pyramidal cell that displayed decreased activity during both cued and repetitive reaches.

(c) An example pM2 interneuron that displayed decreased activity during both cued and repetitive reaches.

(d) An example pM2 pyramidal cell that only showed reproducible firing rate changes during the pre-reach epoch of cued reaches.

(e-f) Example DMS principal cells that displayed firing rate changes during both cued and repetitive reaches.

(g) Same as (c) for an example DMS interneuron.

(h) Same as (d) for an example DMS principal cell.

between the 3 functional clusters described in the previous section (ANOVA, $p > 0.05$). In DMS, significant repetitive reach-related firing rate changes were found in only 24% (± 28% [SD]) of principal cells, but were more common in interneurons (55% ± 40% [SD]; Figure 4.18b; t-test, $t(8) = -2.325$, $p < 0.05$). The proportion of DMS units that were also active during repetitive reaches was not different between clusters (ANOVA, $p > 0.05$). Thus, approximately half of pM2 pyramidal cells, pM2 interneurons, and DMS interneurons, as well as 76% of DMS principal cells, exhibited firing rate changes during the cued reach only and not during repetitive reaches.

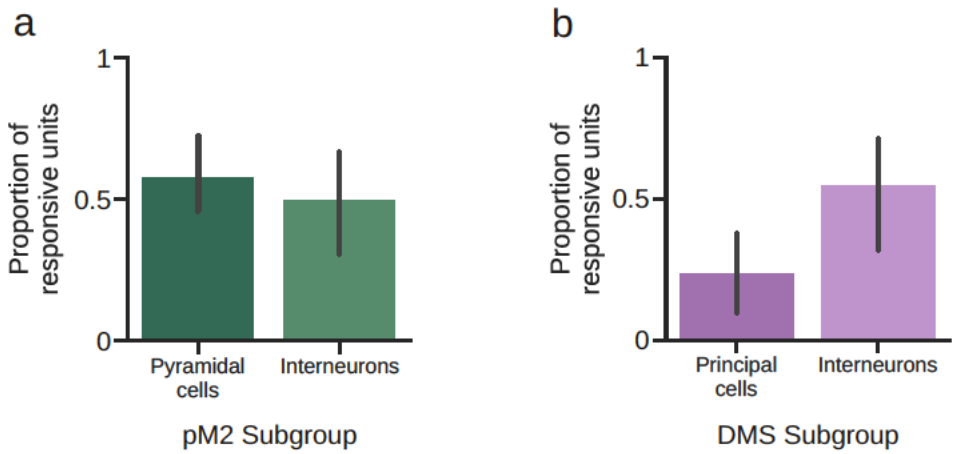

Figure 4.18: Proportions of active units also active during repetitive reaches.

(a) The proportion of cued reach-active pM2 pyramidal cells and interneurons that also displayed significant changes in firing rate during repetitive reaches.

(b) Same as (a) but for DMS principal cells and interneurons.

Error bars are mean ± 95% confidence interval.

4.4 Discussion

4.4.1 A proof-of-concept for the novel visually-directed reaching task

The experiments performed in this chapter serve as a proof-of-concept demonstrating the use and utility of the novel visually-directed reaching task described in Chapter 2. By combining extracellular electrophysiological recordings with the behavioural task, neural activity profiles could be correlated with reaching movements with a high level of temporal resolution. While comparable experimental designs involving non-human primates have yielded useful insights into how the brain processes sensory information to generate visually-directed reaches (Archambault et al., 2011; Dickey et al., 2013; Lara et al., 2018; Sani et al., 2021), until now this has not been possible in experiments using mice.

4.4.2 Analytical considerations

When analysing and describing the activity of populations of neurons, choosing an appropriate method to categorise neurons is crucial. In this chapter, I chose to categorise neurons based on whether they displayed significant firing rate increases or decreases during different epochs of visually-directed reaching. This approach allowed for the identification of subpopulations of neurons with similar activity profiles, and a comparison of their sizes between epochs using an ANOVA clarified global behaviourally-relevant activity changes. The strength of this method is that it provides a clear and interpretable way to describe the recorded brain areas.

However, this approach has limitations. For example, it does not account for the magnitude of firing rate changes, which may be important for understanding the functional role of different subpopulations of neurons. A further loss of information is applied by binning firing rates during the epochs, which impacts the validity of making inferences about population activity based on comparing these bins. A more detailed analysis could involve fitting firing rate changes to a model that allows for continuous changes in firing rate over time, such as a GLM. This may account for the hierarchical nature of the data (i.e. neurons and animals) and potential pseudoreplication, and may provide a more nuanced understanding of the relationship between neural activity and behaviour, at the cost of simplicity and interpretability.

More advanced approaches for describing population dynamics may avoid categorising neurons and instead focus on the distribution of activity across all neurons and timepoints. For example, latent variable modelling or state space analysis could be used to examine the collective activity of all neurons and relate this to behavioural variables, such as the motion tracking data (e.g. Pandarinath et al., 2017). This would provide a more data-driven approach to understanding the population activity that may account for all available variability, revealing structure in the data that may not be apparent with the current analysis.

4.4.3 Reduced firing rates dominate pM2 population activity during visually-directed reaching

In this chapter I aimed to assess how the activity of neurons in pM2 relates to visually-directed reaching. To this end, I recorded spiking activity from pM2 in behaving mice using chronically implanted silicone probes and found that 60% of pM2 neurons exhibited reproducible firing rate changes as mice initiated and executed visually-directed reaches. During the 300 ms pre-reach window, ~24% of neurons displayed increased or decreased activity relative to baseline, indicative of a role in movement preparation or initiation. During reach execution, pM2 units were progressively recruited with reduced activity dominating firing rate changes.

At approximately 300 ms before movement onset, thalamocortical signals drive motor cortical activity to trigger movement (Dacre et al., 2021). While this would coincide with the observed pre-reach firing rate changes, pyramidal cell (PC) firing rate changes were twice as likely to decrease than increase (17% vs 9%) and therefore less likely to be the result of direct thalamocortical input, which is excitatory. However, a small population of deep layer INs (8%) displayed increased pre-reach activity, possibly as a result of direct thalamic input to layer 5 (Hooks et al., 2013), and thus may have driven the reduced activity by inhibiting PCs and other INs. Input from thalamus also targets parvalbumin-expressing INs (Ji et al., 2016; Nashef et al., 2022), generating a feedforward inhibitory connection from which layer 2/3 INs may suppress deep layer neurons. Other inputs to pM2, for example from ipsi- and contralateral motor cortex, posterior parietal cortex (PPC), or higher visual cortical areas (Hwang et al., 2019; Itokazu et al., 2018; Luo et al., 2019; Zingg et al., 2014), likely also shape deep layer pM2 activity directly or via superficial layers. Currently little is known about the specific cell type or laminar

distributions of inputs to pM2, besides inferences made based on reports aggregating all of motor cortex or secondary motor cortex. Input patterns to pM2 specifically must be characterised to understand in detail how pM2 is controlled by other areas. As the current experiment was unable to characterise the activity of superficial pM2, how its activity relates to the behaviour or activity in deeper layers remains an open question.

What function may be served by the widespread reduction of pM2 activity during reach execution? One possibility is that motor control signals may be conveyed via the relatively small excitatory component of pM2's activity (i.e. the 9-15% of PCs with increased activity), in which case widespread inhibition may act to enhance the signal-to-noise ratio of the excitatory signals in recipient areas. In this model, excited and inhibited ensembles of neurons may act in competition (e.g. via mutual inhibition) to shape pM2 output and suppress inappropriate motor output (Zagha et al., 2015), thereby ensuring that reaches are on-target. This gating of motor output would be consistent with an action selection function that has previously been attributed to secondary motor cortex (Barthas and Kwan, 2017; Erlich et al., 2011; Sul et al., 2011). Alternatively, decreased firing rates may directly convey movement-related information to downstream areas. Decreased activity has previously been linked to a role in controlling movement in M1 corticospinal neurons (Peters et al., 2017; Quallo et al., 2012). For example, Peters et al. (2017) found that a majority of corticospinal neurons in M1 exhibited reduced activity when mice pressed a lever, and this effect became more widespread throughout learning as movements became increasingly stereotyped. Even after learning, a minority of neurons displayed increased activity during movement, mirroring the current findings. This mechanism in M1 is further supported by studies that found blocking M1 output resulted in an increase of non-productive movement rather than a reduction of movement (Gao et al., 2003; Stoltz et al., 1999; Zagha et al., 2015). While these observations specifically relate to M1 corticospinal neurons, a similar mechanism may apply to pM2 neurons. Indeed, there is evidence of corticospinal projections originating from pM2 (Liang et al., 2011; Wang et al., 2017).

The causal role of pM2 in visually-directed reaching remains unclear. Short-term, reversible pM2 inactivation using optogenetic techniques have shown that it plays a role in the execution of forelimb movement (Galiñanes et al., 2018; Hwang et al., 2019). Additional evidence in support of a causal role for pM2 in directly controlling movement is the finding that optogenetic stimulation of PPC in rats engaging in a lever-press task

can trigger lever presses (Soma et al., 2019), likely driving motor cortex via pM2 (Itokazu et al., 2018). Soma et al. (2019) found that photoactivation-evoked movements (and movement-related activity in PPC) displayed an ipsilateral bias, although movement-related M2 activity displayed a contralateral bias, albeit more weakly than M1 (Soma et al., 2017). Future experiments should clarify whether the PPC to pM2 pathway is indeed capable of driving movement by selectively activating PPC axons in pM2. Another possible function that pM2 may support is in communicating upcoming movement plans for the purpose of comparing expected and real visual feedback resulting from the movement (i.e. an efference copy as part of a forward model). pM2 densely projects to primary visual cortex (V1) and sends a motor-based prediction of visual flow that V1 uses for detecting sensory mismatches during visually-directed locomotion (Leinweber et al., 2017). Thus, pM2 works with V1 to detect unexpected deviations from planned movements, supporting feedback mechanisms that guide ongoing movement. pM2 contributions to feedback mechanisms performing online movement correction may be assessed by manipulating projections to visual areas (i.e. PPC and V1) during behaviours that demand updates to movement trajectory. In humans and non-human primates, the parietofrontal loop between premotor cortex and PPC is believed to support updating of ongoing reaches (Archambault et al., 2015; Lee and Donkelaar, 2006). As pM2 is the main motor cortical recipient of PPC projections (Hwang et al., 2019; Itokazu et al., 2018; Zingg et al., 2014), this parietofrontal loop may likewise underlie reach updating in mice.

4.4.4 pM2 activity changes are more prevalent during cued reaches than repetitive reaches

Of pM2 units that were active during cued reaches, approximately half were selective for the cued reach, while the remainder also displayed reach-related activity correlated with successive self-initiated reaches. As movement trajectories were similar between cued and repetitive reaches (Section 2.3.2), what explains the differences in activity? One possibility is that cued reaches trigger a motor pattern that rhythmically generates a sequence of repetitive reaches, and that pM2 is differentially involved in voluntary and rhythmic behaviours. A role in voluntary behaviour has been identified for anterior M2, which when lesioned causes self-initiated lever-pressing to become insensitive to outcome devaluation and biases mice towards 'habitual' action strategies (Gremel and Costa, 2013a). pM2 may function similarly, whereby it first facilitates voluntary responses to visual stimuli before disengaging and permitting automatic behaviours to

be driven elsewhere, such as in subcortical motor circuits (Kawai et al., 2015). An alternative (not necessarily mutually exclusive) explanation is that the two types of reaches may be similar behaviourally (i.e. neither are rhythmic) and the difference in pM2 activity may reflect a difference in valence, i.e. mice expect outcome value to diminish rapidly following the initial reach. This would be consistent with previous experiments that have found action valuation signals in rat M2 (Gremel and Costa, 2013a; Sul et al., 2011).

Which of these two possibilities is more accurate may be assessed by covarying the brightness of the visual stimuli and available reward value while recording pM2 activity. Relating pM2 activity to expected changes in reward value during cued reaches would reveal whether pM2 is indeed sensitive to outcome valuation. Examining pM2 activity during repetitive reaches would then clarify whether repetitive reaches are represented in a fundamentally different way in pM2 than cued reaches, or whether their relatively low reward valuation and more sparse firing rate changes match the relationship between reward value and activity determined from cued reaches.

4.4.5 Task-related activity in dorsomedial striatum

Dorsomedial striatum (DMS) principal cells (i.e. medium spiny neurons (MSNs)) formed two similarly sized subpopulations of neurons that displayed increased or decreased firing rates during visually-directed reaching. This is consistent with previous findings of MSNs displaying a range of increases or decreases in activity following learning of a lever-press task (Vandaele et al., 2019). In contrast, INs were dominated by reduced activity, mirroring findings from a subpopulation of DMS INs that displayed decreased activity between movement initiation and achievement of reward in an odor-cued decision making task (Stalnaker et al., 2012). Kim et al. (2021) also found that task-relevant motor-related DMS neurons predominantly displayed reduced activity around movement, a pattern they determined to be mediated by projections from anterior cingulate cortex (ACC). Photoactivation of visual cortical inputs to ACC suppressed movement-related ACC neurons, activated movement-related DMS neurons, and triggered movement, leading them to propose that this pathway is important for inhibitory control during goal-directed behaviour (Kim et al., 2021). Corticostriatal projections target INs to mediate feedforward inhibition of MSNs (Mallet et al., 2005), a mechanism that has been suggested to support action selection by filtering MSN activity

reflecting inappropriate actions (Parthasarathy and Graybiel, 1997), disruption of which leads to uncontrolled initiation of inappropriate movement (Gernert et al., 2000). While DMS receives projections from across the brain, most inputs arise from cortex or thalamus (Wall et al., 2013), including from pM2 (Hintiryan et al., 2016), PPC (Hwang et al., 2019), and visual cortical areas (Hintiryan et al., 2016; Zingg et al., 2014). Recent work has started to clarify the functional relationships between DMS and various cortical areas, such as ACC (Kim et al., 2021), PPC (Hwang et al., 2019), and prefrontal cortex (Terra et al., 2020), but much remains to be understood about how these diverse inputs interact to support DMS and modulate its activity during visually-directed reaching.

Interestingly, both over-activation and suppression of parvalbumin-expressing INs attenuates MSN activity, so the MSNs with reduced activity observed here may have been suppressed by local INs, though this effect is reduced across learning (Lee et al., 2018). Nevertheless, reductions of MSN activity seem to become more prominent across task acquisition (Thorn et al., 2010). It is unlikely that mice in the present experiment were over-trained, as the criteria used to determine expert level in the task did not require that learning metrics had plateaued (Figure 2.5). Presumably, therefore, DMS continued to support acquisition of the task's action-outcome association. Functions relating to learning and reinforcement, previously linked to DMS (Hart et al., 2014; Kravitz et al., 2012), may explain the observed differences in DMS activity between cued and repetitive reaches. Only approximately a quarter of cued reach-related MSNs and a half of cued reach-related INs also displayed firing rate changes during repetitive reaches, consistent with a role in reinforcing the association between the visual stimuli and reward. Previous experiments have shown that DMS neurons encode the net value of actions and that lesions of DMS diminish the effects of net value on motivation and movement vigour (Wang et al., 2013; Yin et al., 2005). As the initial reach of a sequence of repetitive reaches provided the water reward, and repetitive reaches had significantly reduced peak movement velocities (Section 2.3.2), differences in reward expectation (and consequently movement vigour) between cued and repetitive reaches likely explain the respective differences in DMS activity. This is consistent with existing results that have shown that DMS is more active during voluntary than rhythmic behaviours (Gremel and Costa, 2013b) and is more concerned with 'higher-level' decision making than with 'lower-level' motor control (Bolkan et al., 2022; Dhawale et al., 2021).

Chapter 5

General Discussion

The ability to visually direct reaching and grasping enables humans and animals to interact with their environment, manipulate objects, and obtain food and other necessary resources. As one of our most critical behavioural outputs, researchers have spent decades studying how the movement is performed and how it is supported by the human and primate brain. Human studies have yielded insight about which brain areas are involved in visually-directed reaching by comparing behaviours between healthy and lesioned patients (Bonnefoi-Kyriacou et al., 1998; Gréa et al., 2002; Pisella et al., 2000), reversibly inactivating specific brain areas with transcranial magnetic stimulation (Della-Maggiore et al., 2004; Desmurget et al., 1999), and recording neural activity with functional magnetic resonance imaging (Himmelbach et al., 2013). Studies using non-human primate models have benefitted from more invasive techniques, such as neuronal recordings (Archambault et al., 2011; Battaglia-Mayer et al., 2013; Dickey et al., 2013; Mountcastle et al., 1975; Schwartz et al., 1988), focal inactivation mediated by the injection of muscimol (Battaglia-Mayer et al., 2013; Hwang et al., 2012), intra-cortical microstimulation (ICMS) (Gharbawie et al., 2010), and anatomical tracing (Bakola et al., 2013; Gerbella et al., 2011; Gharbawie et al., 2010). The mouse model system can provide further advantages, such as enabling cell type- and pathway-specific interrogations of circuit function (Luo et al., 2008; Navabpour et al., 2020), which can be combined with manipulation methods such as optogenetics to probe brain function with high specificity (Chen et al., 2018; Zhang et al., 2007). However, until now, studying visually-directed reaching in mice has not been possible.

The goal of this thesis was to address this issue and enable researchers studying the behaviour to take full advantage of the mouse as a tractable model system. To this end, I designed and implemented a visually-directed reaching task for freely moving mice. Previously published non-visual reaching tasks have been used by researchers to study the motor component of the behaviour in relative isolation (Baird et al., 2001; Galiñanes

et al., 2018; Levy et al., 2020; Li and Hollis, 2021; Manita et al., 2022), but do not permit investigation into how visual and motor areas interact to direct movement. My task design bridges this gap.

The task is performed by mice that are freely moving, which provides a number of benefits versus a design that uses head restraint. Firstly, head restraint induces stress, which can cause behavioural and neurophysiological changes (Chiba et al., 2012; Juczewski et al., 2020; Ota et al., 2015; Sadler and Bailey, 2016), potentially confounding experimental outcomes. Juczewski et al. (2020) examined blood corticosterone concentration (an indicator of stress) across 25-day behavioural protocols in head restrained and freely moving mice and found that although mice did appear to habituate to the head restraint, they continued to have elevated blood corticosterone concentrations when compared to freely moving mice. Based on their results, they recommended that behavioural experiments using head restraint are preceded by a 10-day habituation protocol to allow blood corticosterone concentration and body weight to stabilise. Secondly, head restraint disrupts neural responses to head and eye movement. For example, Parker et al. (2022) noted that visual research had overlooked how movement influences visual processing due to the use of head restraint procedures, and by performing neural recordings in freely moving mice, found that many neurons in primary visual cortex are modulated by changes in head position. Similar self-motion signals have been observed throughout the brain, even in sensory areas, but the role of these signals can be difficult to interpret when head restraint disrupts naturalistic sensory exploration (Parker et al., 2020). Thirdly, head restraint stops mice from being able to control or adjust their posture and limits their freedom of movement, causing them to perform reaches with a modified trajectory (Whishaw et al., 2017). This can also cause mice to develop an alternative strategy to succeed in a reaching task; Whishaw et al. (2017) found that freely moving mice located food pellet reach targets by sniffing, whereas head restrained mice instead relied on remembered target positions and haptic (i.e. tactile and kinaesthetic) feedback from touching targets to successfully locate pellets. By designing the task for unrestrained mice, animals can engage in more naturalistic behaviours for both sensory exploration and reaching movements, more closely mimicking the natural situation.

It is worth noting that head restriction has provided practical advantages, such as greater control over task parameters and metrics, and easier compatibility with neural

recording and manipulation techniques (Schwarz et al., 2010). Tracking movement in restrained mice is likely made easier by the limited range of viewing angles and positions in videos directed at the animal. However, as demonstrated in the present experiments and previously published studies (Becker and Person, 2019), reach trajectories can be accurately tracked in freely moving animals thanks to sophisticated markerless motion tracking software (Mathis et al., 2018). The gap between head restrained and freely moving experiments in available neural recording and manipulation techniques is also narrowing. As discussed earlier (Section 1.4), extracellular recordings can be performed in freely moving mice via wire electrodes (Bhalla and Bower, 1997), tetrodes (Dhawale et al., 2017), and silicone probes (Bragin et al., 2000; Okun et al., 2016; Voroslakos et al., 2021), including cutting edge Neuropixels silicone probes (Juavinett et al., 2019; Jun et al., 2017; Steinmetz et al., 2021). Glass electrode single cell recordings are also possible (Valero and English, 2019), and more recently miniaturised, head-mounted microscopes have enabled two-photon (Zong et al., 2022) and three-photon (Klioutchnikov et al., 2023) calcium imaging in unrestrained mice. Similarly, optogenetic approaches for stimulating or silencing neural activity are possible by chronically implanting optic fibres into the brain with fixtures for later connecting/disconnecting cables for light delivery (Berg et al., 2020; Moulin, 2021). Underlining the flexibility of possible experimental designs, some studies have combined optical fibres with tetrodes (Osanai et al., 2019; Zhang et al., 2019) or silicone probes (Levi et al., 2022) to simultaneously manipulate and record from neurons in freely moving mice.

To validate the task, I performed extracellular recordings in posterior secondary motor cortex (pM2) and dorsomedial striatum (DMS) in behaving mice and related pM2 and DMS spiking patterns to cued and self-initiated reaches. I found that a majority of pM2 neurons reproducibly modulated their firing rate as mice initiated and executed visually-directed reaches, with the proportion of neurons displaying reduced activity growing throughout the movement. The dominant reduction of activity and small excitatory component may reflect a mutual inhibition process that gates excitatory outputs, which would be consistent with a role for M2 in action selection (Barthas and Kwan, 2017; Erlich et al., 2011; Sul et al., 2011). pM2 is distinguished from other areas of M2 by its dense reciprocal connectivity with posterior parietal cortex (PPC) (Hovde et al., 2018; Hwang et al., 2017; Itokazu et al., 2018; Zingg et al., 2014), which is also involved in action selection (Cui and Andersen, 2011; Fattori et al., 2010; Murata et al., 2000). This circuit forms the parietofrontal loop, which in primates is critical for performing visually-

directed reaching and grasping (Archambault et al., 2015; Battaglia-Mayer et al., 2014). According to the dominant "dual visuomotor channel theory" of prehension, reaching and grasping are controlled by largely independent parallel processes (Goodale, 2011; Jeannerod, 1984). These processes have been linked to parallel pathways between dedicated subdivisions of PPC and premotor/motor cortex (Binkofski et al., 1998; Flindall and Gonzalez, 2019; Gharbawie et al., 2011; Goodale, 2011; Graziano et al., 2005; Kaas et al., 2013; Karl and Whishaw, 2013), which are organised somatotopically and can trigger complex, multi-joint behaviours when electrically stimulated (Kaas and Stepniewska, 2016; Stepniewska et al., 2014, 2009). Intuitively, at least for humans, reaching and grasping seem to be necessarily linked movements, so what explains the evolution of parallel pathways to control them? Reaching uses extrinsic features of an object (such as its egocentric spatial location) to coordinate upper arm muscles and bring the hand towards the object. In contrast, grasping uses intrinsic features (such as size and shape) to coordinate wrist and hand muscles to shape the hand into a suitable configuration to pick up the object. Karl and Whishaw (2013) propose that reaching may have evolved from stepping movements that became increasingly independently controllable, likely to traverse obstacles or uneven terrain, and that reach-related cortical pathways may have their origins in locomotion-related pathways. They suggest that grasping likely evolved later to enable manipulation of food items, a behaviour that is particularly reliant on online haptic feedback. To facilitate accurate visually-guided reaching and fine motor skills for grasping and object manipulation, the cortical pathways underlying these types of movements developed unique relationships with visual and somatosensory areas.

The extent to which homologous parallel pathways for reaching and grasping exist in rodents remains unclear. Whishaw et al. (2017) used high-speed cameras to track reach and grasp movements in mice with the aim to determine whether the two movement components can be controlled independently. They found that while reaching could be performed offline towards remembered egocentric spatial locations, mice never pre-shaped their hand prior to contact with a food pellet, consistent with the observation that rats do not scale their grasping hand shape when reaching to different sizes of food pellets (Metz and Whishaw, 2000). However, upon contact, mice used touch-related cues to shape their hands online. These behavioural observations suggest that reaching and grasping can be controlled as independent processes in mice. Neurological experiments have started to delineate brain areas that contribute differentially to these movement components. Characteristic roles for reaching and grasping have been linked to the

caudal forelimb area (CFA) and rostral forelimb area (RFA) of motor cortex, respectively. In rats, long-duration ICMS of these areas has been found to elicit primarily either reaching or grasping (Ramanathan et al., 2006), although elicited movements appear to be complex, multi-joint movements that may involve both the limb and hand (Bonazzi et al., 2013). Calcium imaging recordings in corticospinal neurons, the main outputs of motor cortex, in mice reaching to food pellets found that CFA was dominated by reach-related activity and RFA was dominated by grasp-related activity (Wang et al., 2017), but reach- and grasp-related activity was not completely mutually exclusive. Inactivating CFA and RFA disrupts reaching and grasping, respectively, but both areas are required for the transitional step between them (Brown and Teskey, 2014; Wang et al., 2017). Similarly, a series of studies focussing on CFA have found that its activity is required for initiating as well as maintaining ongoing reaches (Galiñanes et al., 2018; Guo et al., 2015; Manita et al., 2022). The imperfect split between these areas and reaching and grasping is indicative that describing them as parallel pathways may be too simplistic. Indeed, at odds with this model, Tennant et al. (2011) performed ICMS in mice and found that while stimulation of both CFA and RFA caused elbow or wrist movements, CFA stimulation was much more likely to elicit digit movements. Future work should seek to add clarity to the roles of these areas, perhaps modelling them on their ICMS-elicited complex, ethologically relevant behaviours rather than simple reach or grasp movements. In particular, given their differences in sensory requirements and thus the types of sensory-driven behaviours they support, understanding how visual brain areas interact with motor cortex during reaching may provide novel clues on whether motor cortex is receiving relevant information such as extrinsic features about reach targets. If so, the pathway providing this information may be capable of supporting visually-directed reaching, but not visually-directed grasping, which may not be possible for mice. In contrast, grasp-related areas may have a closer functional relationship with somatosensory areas to facilitate online touch-based object manipulations.

Appendices

Included here are two peer-reviewed publications to which I made significant methodological and experimental contributions.

Appendix A: A cerebellar-thalamocortical pathway drives behavioural context-dependent movement initiation

Dacre, J., Colligan, M., Clarke, T., Ammer, J.J., Schiemann, J., Chamosa-Pino, V., Claudi, F., Harston, J.A., Eleftheriou, C., Pakan, J.M.P., Huang, C.-C., Hantman, A.W., Rochefort, N.L., Duguid, I., 2021. Neuron 109, 2326-2338.e8. https://doi.org/10.1016/j.neuron.2021.05.016

Actions made in response to sensory cues require to be appropriately timed by the motor system. The cerebellum is thought to shape cortical output and control the timing of movements, possibly through a pathway arising from the dentate/interpositus cerebellar nuclei (DN/IPN), which project to motor thalamus and directly drive neurons that output to motor cortex (Hooks et al., 2013; Schäfer et al., 2021). Neural activity in DN/IPN and the DN/IPN-recipient region of motor thalamus ($MTh_{DN/IPN}$) has previously been linked to movement initiation (Anderson and Turner, 1991; Butler et al., 1996; Butler et al., 1992; Fortier et al., 1989; Mushiake and Strick, 1993), and perturbing this activity can disrupt movement timing (Donkelaar et al., 2000; Nashef et al., 2019; Spidalieri et al., 1983). However, whether the cerebellar-thalamocortical pathway emanating from DN/IPN plays a role in movement initiation was uncertain. To address this issue, we recorded activity in $MTh_{DN/IPN}$ and the caudal forelimb area of motor cortex (CFA) in mice performing a cued lever-push task and used gain- and loss-of-function manipulations to identify causal roles for the pathway in movement initiation (see attached paper).

First, to elucidate how neuronal activity in the pathway is transformed during movement, I performed two-photon population calcium imaging in $MTh_{DN/IPN}$ while mice

engaged in the task (Figures 1i-m, 2). To record from $MTh_{DN/IPN}$, I used chronically implanted gradient-index (GRIN) lenses, which enabled imaging of deep brain structures. I found that most $MTh_{DN/IPN}$ neurons displayed significant movement-related activity with 42% becoming more active and 13% becoming less active prior to movement onset, reminiscent of bidirectional movement-related activity patterns observed in layer 5 of primary motor cortex (Zagha et al., 2015) and in posterior secondary motor cortex (Chapter 4). The pre-movement changes in fluorescence recorded from these thalamic neurons occurred consistently ~300 ms before movement, regardless of the time interval between cue onset and movement onset, suggesting that $MTh_{DN/IPN}$ conveys a motor timing signal to motor cortex. In contrast, movement-related activity was absent during miss trials (i.e. trials in which mice did not push the lever).

Next, to better understand the anatomical connectivity via which activity in $MTh_{DN/IPN}$ may influence CFA, we sought to quantify the density of CFA-projecting neurons $MTh_{DN/IPN}$. I injected a retrograde tracer (cholera toxin B subunit) into CFA in 3 mice and, after 7 days of incubation, perfused the mice and counted the frequency of tracer labelling against a counterstain in $MTh_{DN/IPN}$ sections (Figures 1h, S2a-b). I determined that ~76% of $MTh_{DN/IPN}$ neurons send projections to CFA. In a separate experiment, Dr Joshua Dacre assessed the proportion of CFA-projecting $MTh_{DN/IPN}$ neurons that received glutamatergic input from DN/IPN and found that this was 100% of neurons. Taken together, these two observations reveal that $MTh_{DN/IPN}$ is a key node bridging the cerebellum and CFA.

To identify causal contributions of the pathway to motor control, we sought to determine whether DN/IPN output is necessary to perform the behaviour. To assess this, Dr Joshua Dacre inactivated DN/IPN by injecting muscimol (a GABA-A receptor agonist) into DN/IPN while mice were engaged in the task. Following injection, mice performed significantly fewer successful trials, consistent with a role for DN/IPN in movement initiation. Since DN/IPN projections target other motor-related areas in addition to motor thalamus (Asanuma et al., 1983; Teune et al., 2000), we next examined whether DN/IPN output to motor thalamus specifically could trigger movement. Dr Joshua Dacre performed injections of an adeno-associated virus vector to target Channelrhodopsin-2 expression to DN/IPN, then stimulated DN/IPN axon terminals in $MTh_{DN/IPN}$ in behaving mice via optic fibres implanted directly above $MTh_{DN/IPN}$. Photoactivation in the absence of the cue triggered complete lever pushes in ~30% of

Neuron

Article

A cerebellar-thalamocortical pathway drives behavioral context-dependent movement initiation

Graphical abstract

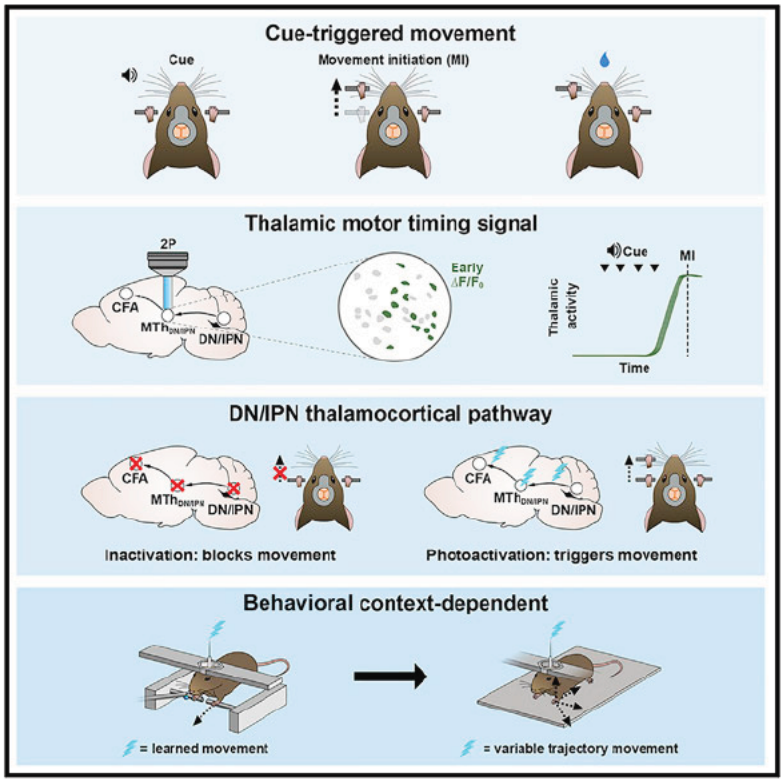

Authors

Joshua Dacre, Matt Colligan, Thomas Clarke, ..., Adam W. Hantman, Nathalie L. Rochefort, Ian Duguid

Correspondence

In brief

Dacre et al. show the contribution of a cerebellar-thalamocortical pathway to movement initiation. Using gain- and loss-of-function manipulations they demonstrate that output from dentate/interpositus nuclei, via the thalamus, shapes cortical activity dynamics necessary for learned behavioral context-dependent movement initiation.

Highlights

- DN/IPN thalamocortical activity conveys a reliable feedforward motor timing signal
- Silencing DN/IPN or recipient regions of thalamus blocks movement initiation
- Photostimulation of the DN/IPN thalamocortical pathway triggers movement
- Thalamocortical activation drives behavioral context-dependent movement initiation

Dacre et al., 2021, Neuron *109*, 2326–2338
July 21, 2021
https://doi.org/10.1016/j.neuron.2021.05.016

CellPress

CellPress
OPEN ACCESS

Neuron

Article

A cerebellar-thalamocortical pathway drives behavioral context-dependent movement initiation

Joshua Dacre,[1] Matt Colligan,[1,4] Thomas Clarke,[1,4] Julian J. Ammer,[1,4] Julia Schiemann,[1,5] Victor Chamosa-Pino,[1] Federico Claudi,[1,6] J. Alex Harston,[1,7] Constantinos Eleftheriou,[1,2] Janelle M.P. Pakan,[1,8] Cheng-Chiu Huang,[3,9] Adam W. Hantman,[3] Nathalie L. Rochefort,[1,2] and Ian Duguid[1,2,10,*]

[1]Centre for Discovery Brain Sciences, Edinburgh Medical School: Biomedical Sciences, University of Edinburgh, Edinburgh, UK
[2]Simons Initiative for the Developing Brain, Centre for Discovery Brain Sciences, University of Edinburgh, Edinburgh, UK
[3]Janelia Research Campus, HHMI, Ashburn, VA, USA
[4]These authors contributed equally
[5]Present address: Center for Integrative Physiology and Molecular Medicine, Saarland University, Homburg, Germany
[6]Present address: UCL Sainsbury Wellcome Centre for Neural Circuits and Behaviour, London, UK
[7]Present address: Brain and Behaviour Lab, Department of Bioengineering, Royal School of Mines, Imperial College London, UK
[8]Present address: Center for Behavioral Brain Sciences, Institute for Cognitive Neurology and Dementia Research, Otto von Guericke University, Magdeburg, Germany
[9]Present address: Eli Lilly and Company, Lilly Cambridge Innovation Center, Cambridge, MA, USA
[10]Lead contact
*Correspondence:
https://doi.org/10.1016/j.neuron.2021.05.016

SUMMARY

Executing learned motor behaviors often requires the transformation of sensory cues into patterns of motor commands that generate appropriately timed actions. The cerebellum and thalamus are two key areas involved in shaping cortical output and movement, but the contribution of a cerebellar-thalamocortical pathway to voluntary movement initiation remains poorly understood. Here, we investigated how an auditory "go cue" transforms thalamocortical activity patterns and how these changes relate to movement initiation. Population responses in dentate/interpositus-recipient regions of motor thalamus reflect a time-locked increase in activity immediately prior to movement initiation that is temporally uncoupled from the go cue, indicative of a fixed-latency feedforward motor timing signal. Blocking cerebellar or motor thalamic output suppresses movement initiation, while stimulation triggers movements in a behavioral context-dependent manner. Our findings show how cerebellar output, via the thalamus, shapes cortical activity patterns necessary for learned context-dependent movement initiation.

INTRODUCTION

The ability to generate appropriately timed motor actions in response to sensory cues is a hallmark of mammalian motor control. Movement timing is controlled in part by the cerebellum, as dysfunction leads to the execution of poorly timed actions (Bastian and Thach, 1995; Holmes, 1939; Milak et al., 1997; Thach, 1975). However, the pathway and circuit dynamics involved in initiating movements remain unclear. Two distinct pathways could contribute to movement initiation, the cerebellar-rubrospinal tract (Asanuma et al., 1983; Gibson et al., 1985; Teune et al., 2000) or the cerebellar-thalamocortical pathway (Bostan et al., 2013; Gornati et al., 2018; Horne and Butler, 1995; Kuramoto et al., 2009; Nashef et al., 2019). The latter is supported by neuronal activity in dentate/interpositus nuclei (DN/IPN) and recipient motor thalamic regions preceding cortical activity (Nashef et al., 2018; Strick, 1976; Thach, 1975, 2014) and movement initiation (Anderson and Turner, 1991; Butler et al., 1992, 1996; Fortier et al., 1989; Harvey et al., 1979; Horne and Porter, 1980; Kurata, 2005; Macpherson et al., 1980; Mushiake and Strick, 1993; Schmied et al., 1979; Strick, 1976; van Donkelaar et al., 1999), while disrupting activity in either region alters the timing of sensory-triggered actions (Meyer-Lohmann et al., 1977; Nashef et al., 2019; Spidalieri et al., 1983; Thach, 1975; van Donkelaar et al., 2000). Beyond a proposed role in movement initiation, DN/IPN and recipient regions of motor thalamus coordinate the timing and accuracy of ongoing movements given that focal inactivation alters endpoint accuracy (dysmetria/hypermetria), reach path curvature and grasping (Becker and Person, 2019; Bracha et al., 1999; Butler et al., 1992; Cooper et al., 2000; Horne and Butler, 1995; Ishikawa et al., 2014; Martin et al., 2000; Mason et al., 1998; Thanawalla et al., 2020), and loss of anticipatory limb adjustments to unexpected obstacles during complex locomotion (Martin et al., 2000; Milak et al., 1997). In contrast, disrupting output from fastigial nucleus results in deficits in posture, locomotion, and motor planning, with minimal effects on reaching (Li et al., 2015; Martin et al., 2000; Thach and Bastian, 2004). Thus, individual cerebellar nuclei provide

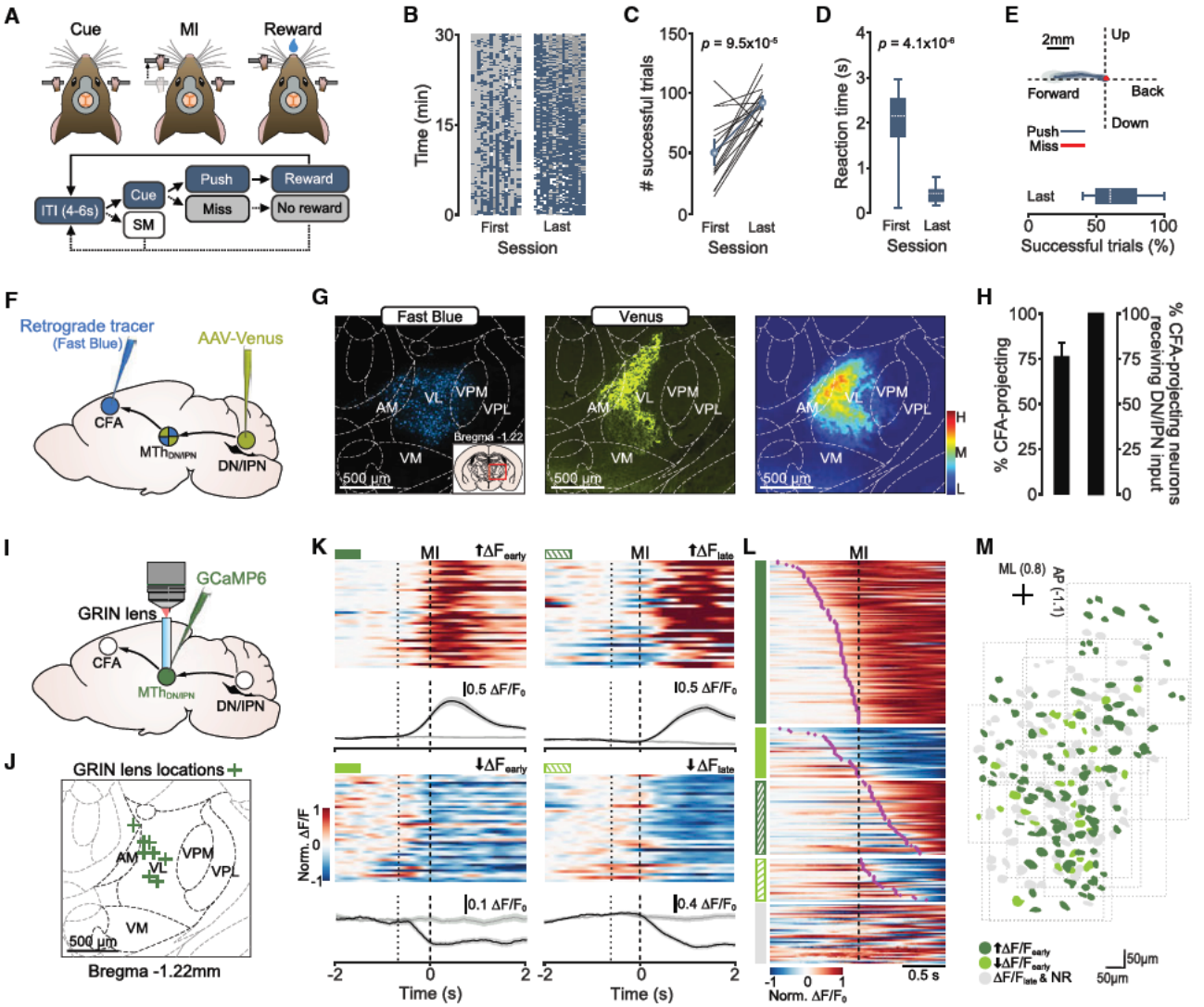

Figure 1. Increased activity dominates trial-to-trial $MTh_{DN/IPN}$ population responses prior to movement initiation

(A) Top: cued forelimb push task. MI, movement initiation. Bottom: behavioral task structure. ITI, inter-trial interval; SM, spontaneous movement.

(B) Trial outcome rasters with each column representing individual mice (N = 16 mice). Blue, push trials; gray, miss trials; white, spontaneous movements.

(C) Number of successful trials per 30-min behavioral session (N = 16 mice, two-sample t test). Mean ± 96% CIs.

(D) Box-and-whisker plots showing mouse reaction times across learning (N = 16 mice, two-sample t test).

(E) Top: forepaw trajectories for push (blue) and miss (red) trials from the mouse in Video S1. Thick line, average paw trajectory overlaid with 95% CI of paw position variance. Bottom: box-and-whisker plot of the percentage of successful trials in "expert" mice.

(F) Mapping the dentate/interpositus thalamocortical pathway. CFA, caudal forelimb area; $MTh_{DN/IPN}$, dentate/interpositus nuclei-recipient region of motor thalamus; DN, dentate nucleus; IPN, interpositus nucleus.

(G) Left: retrograde labeling of CFA-projecting motor thalamic neurons. Middle: anterograde labeling of DN/IPN axons in motor thalamus. Right: density plot of regions of overlap of DN/IPN axons and CFA-projecting neurons across thalamic nuclei (N = 6 hemispheres from four mice). Inset: location of motor thalamic nuclei. AM, anteromedial; VL, ventrolateral; VPM, ventral posteromedial; VPL, ventral posterolateral; VM, ventromedial nuclei.

(H) Left: percentage of CFA-projecting $MTh_{DN/IPN}$ neurons. Right: percentage of CFA-projecting $MTh_{DN/IPN}$ neurons receiving glutamatergic synaptic input from DN/IPN. Mean ± 95% CIs.

(I) Two-photon population calcium imaging in $MTh_{DN/IPN}$.

(J) Locations of GRIN lenses in $MTh_{DN/IPN}$ (N = 8 mice).

(K) Activity of four example $MTh_{DN/IPN}$ neurons. Clockwise from top left: early-onset increase (dark green), late-onset increase (dark green hatching), late-onset decrease (light green hatching), and early-onset decrease (light green). Top: normalized $\Delta F/F_0$ across successive trials. Bottom: $\Delta F/F_0$ mean ± SEM. Black lines, push trials; gray lines, miss trials; dotted lines, median cue onset; dashed lines, movement initiation (MI).

(legend continued on next page)

differing contributions to movement control, where DN/IPN likely convey motor timing signals via thalamus to cortex in order to initiate and modify ongoing movements (Kurata, 2005; Nashef et al., 2018; Thach, 2014).

In rodents, cerebellar nuclei project to different regions of ventral thalamus. The fastigial nucleus primarily targets ventromedial (VM), while DN/IPN target the anteromedial (AM), and ventral anterolateral (VAL) subdivisions (Angaut et al., 1985; Gornati et al., 2018; Haroian et al., 1981; Kuramoto et al., 2009; Teune et al., 2000). DN/IPN axon terminal fields overlap substantially displaying morphological and functional characteristics consistent with strong feedforward driver inputs, such as large synaptic boutons (Aumann and Horne, 1996a, b; Aumann et al., 1994; Gornati et al., 2018) and large unitary responses (Gornati et al., 2018; Sawyer et al., 1994; Schäfer et al., 2021). Cerebellar input drives short-latency spiking in thalamic neurons that project to superficial and deep layers of motor cortex (Hooks et al., 2013; Kuramoto et al., 2009; Schäfer et al., 2021), transforming output via top-down excitation through layer 2/3 (Weiler et al., 2008) or direct excitation of layer 5 (Hooks et al., 2013; Sauerbrei et al., 2020). Key remaining questions are whether ventral motor thalamus plays a role in movement initiation and whether this is dependent on cerebellar input.

To address these questions, we developed a cued lever push task for mice requiring execution of a basic stimulus-response behavior for reward. This habitual behavior depends on antecedent stimuli rather than goal value, likely recruiting feedback reinforcement circuits, including VAL thalamus (Balleine, 2019; Graybiel, 2008). Using imaging, electrophysiology, and gain- and loss-of-function experiments, we investigated how an auditory go cue transforms thalamic and motor cortical activity patterns during movement initiation. Population responses in DN/IPN-recipient regions of motor thalamus were dominated by a time-locked increase in activity immediately prior to movement initiation, providing a fixed-latency feedforward timing signal to motor cortex. Consistent with this view, membrane potential dynamics of layer 5B projection neurons matched premovement timing of thalamic activation, while suppressing cerebellar or thalamic output blocked movement initiation. Conversely, photostimulation of DN/IPN or recipient thalamic regions triggered movement initiation, but in a context-dependent manner. Our results demonstrate an important and causal contribution of a cerebellar-thalamocortical pathway to voluntary movement initiation.

RESULTS

Motor thalamic population activity increases prior to movement initiation

To investigate voluntary movement initiation, we developed a cued forelimb push task for mice. The design of the task required mice to execute horizontal push movements (4 mm) after a randomized inter-trial interval (4–6 s) and in response to a 6-kHz auditory go cue. Miss trials, partial pushes, or spontaneous lever movements resulted in no reward and a lever reset (Figure 1A; Video S1). Mice rapidly learned the task (mean = 7.5 days [6.3, 8.6] 95% confidence interval [CI], N = 16 mice; all data unless otherwise stated are presented as mean [bootstrapped 95% CI]; percentage of successful trials [last session], mean = 63.7% [56.0, 71.7]), displaying moderate reaction times (RTs; last session median = 0.32 s [0.30, 0.34]) and reproducible push trajectories (Figures 1B–1E; Video S1). Even in expert mice, we observed miss trials, likely reflecting changing levels of attention or satiation within sessions (Figure 1E; Video S1).

Since both DN and IPN are implicated in motor timing and send glutamatergic projections to ventral motor thalamus (Aumann and Horne, 1996b; Bosch-Bouju et al., 2013; Gornati et al., 2018; Kuramoto et al., 2009), we sought to define the region of thalamus that receives input from DN/IPN and projects to the caudal forelimb area (CFA) of motor cortex using a dual labeling strategy (Figure 1F). A region of dense overlap centered on VAL and AM nuclei, with sparse colocalization in the ventral posteromedial nucleus (VPM). We found no overlap in the ventromedial nucleus (VM), which primarily receives input from the fastigial nucleus (Gao et al., 2018; Gornati et al., 2018) (Figures 1G and S1A–S1E). Although injections were targeted to DN/IPN, low-level expression was detected in some adjacent vestibular nuclei, which do not send direct projections to VAL (Figures S1A and S1C). Within the dense region of overlap, ~76% of neurons project to CFA, and all CFA-projecting neurons received glutamatergic input (vesicular glutamate transporter 2 [VGluT2] positive) from DN/IPN (Bosch-Bouju et al., 2013; Kuramoto et al., 2009; Rovó et al., 2012; Schäfer et al., 2020) (Figures 1H and S2A–S2D). This degree of connectivity is consistent with DN/IPN-recipient regions of motor thalamus ($MTh_{DN/IPN}$) being an important functional node connecting the cerebellum and CFA.

To explore whether $MTh_{DN/IPN}$ population responses were consistent with a role in movement initiation, we employed gradient-index (GRIN) lens-mediated two-photon population calcium imaging (Figures 1I and 1J). Lens implantation above $MTh_{DN/IPN}$ did not affect overall behavior when compared to control (control versus GRIN lens-implanted mice: two-sample Kolmogorov-Smirnov test, RT $p = 0.56$, push duration $p = 0.22$, number of successful pushes $p = 0.35$, N = 23 control versus 9 GRIN lens-implanted mice, data not shown). Most $MTh_{DN/IPN}$ neurons displayed push-related activity (210/248 neurons) either prior to movement initiation (early-onset increase in $\Delta F/F_0$, 104/210 neurons; early-onset decrease in $\Delta F/F_0$, 32/210 neurons) or during the execution/reward period (late-onset increase in $\Delta F/F_0$, 47/210 neurons; late-onset decrease in $\Delta F/F_0$, 27/210 neurons), while during miss trials, $MTh_{DN/IPN}$ population responses were absent (11 fields of view [FOVs], N = 8 mice) (Figures 1K–1L). Increased activity appeared as the dominant population response prior to movement (early-onset neurons: increased

(L) Average $\Delta F/F_0$ across trials for individual neurons. Groupings: early-onset increase (dark green, n = 104/248 neurons); early-onset decrease (light green, n = 32/248 neurons); late-onset increase (dark green hatching, n = 47/248 neurons); late-onset decrease (light green hatching, n = 27/248 neurons), and nonresponsive (gray, n = 38/248 neurons), ordered by $\Delta F/F_0$ onset, purple circles (n = 11 fields of view, N = 8 mice).
(M) Spatial distribution of early-onset increase (dark green), early-onset decrease (light green) and late-onset/nonresponsive neurons (gray) in $MTh_{DN/IPN}$. Dotted boxes, individual fields of view. ML, medial-lateral; AP anterior-posterior.

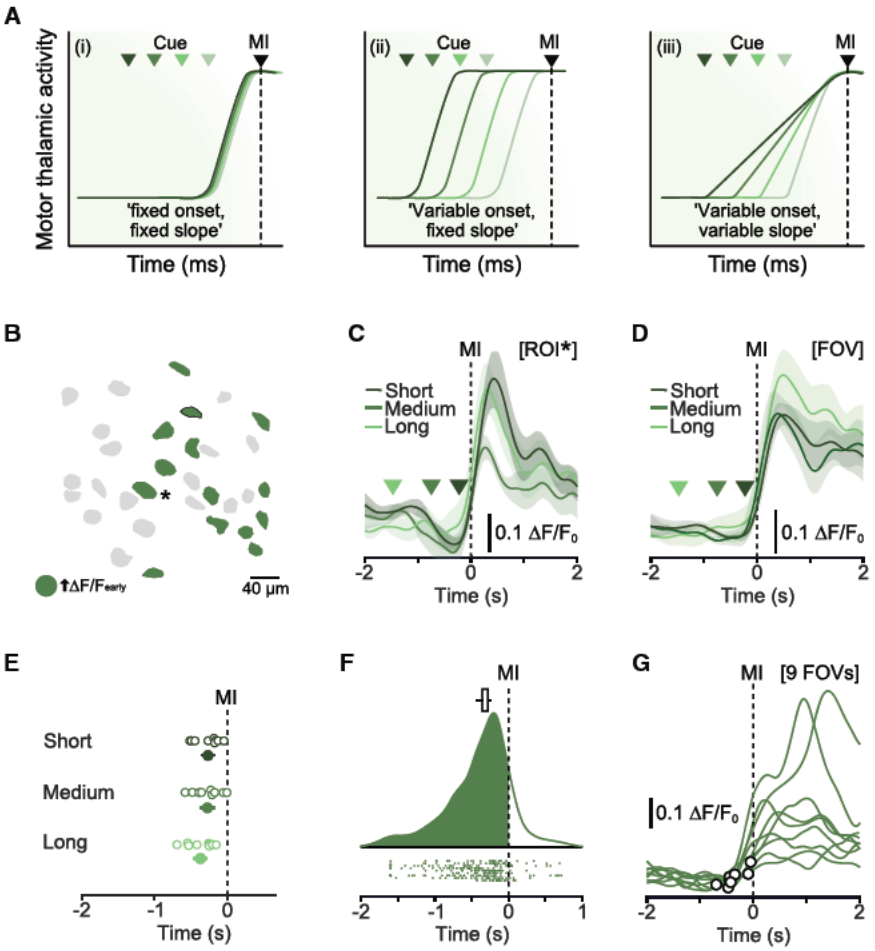

Figure 2. $MTh_{DN/IPN}$ neurons provide a reliable time-locked signal prior to movement initiation

(A) Trial-to-trial $MTh_{DN/IPN}$ population response models. Green triangles, cue onset; MI, movement initiation.

(B) Example field of view (FOV). Green, early-onset increase in activity.

(C) Average $\Delta F/F_0$ from an early-onset increase neuron (asterisk in B), aligned to movement initiation (MI) and split by short, medium, and long reaction times. Colored triangles, median cue presentation; [ROI], region of interest. Error bars represent 95% CIs.

(D) Average $\Delta F/F_0$ from all early-onset increase activity neurons in (B) FOV, aligned to movement initiation (MI) and split by reaction time. Triangles, median cue presentation. Error bars represent 95% CIs.

(E) Mean onset times of trials split by reaction time. Open circles, individual FOVs; filled circles, means ± 95% CI (n = 9 fields of view, N = 6 mice).

(F) Distribution of bootstrapped trial-to-trial response onsets for all early-onset increased activity neurons across nine FOVs. Top: median onset bootstrapped estimate. Middle: kernel density estimation of trial-to-trial motor thalamic response onsets. Bottom: raster of trial-to-trial population onsets (n = 297 trials from nine fields of view, N = 6 mice).

(G) Single-trial $\Delta F/F_0$ population responses from nine different FOVs (one response per FOV). Black circles, population response onsets.

activity, 76.4%; decreased activity, 23.5%) (Figure 1L) and was found across the extent of $MTh_{DN/IPN}$ (Figure 1M).

$MTh_{DN/IPN}$ output provides a reliable fixed-latency motor timing signal

If $MTh_{DN/IPN}$ conveys a motor timing signal, then population responses could be described by three hypothetical models. First, thalamic activity is uncoupled from the go cue rising immediately before movement onset. In this regard, rapidly increasing thalamic activity dictates the time of movement initiation (model i). Second, thalamic activity rises at the go cue and is maintained until additional inputs trigger movement. Thus, thalamic activity contributes to, but does not dictate, the time of initiation (model ii). Third, thalamic activity reflects a continuous sensorimotor transformation from cue to movement. The slope dictates the time of movement initiation (model iii) (Figure 2A). To distinguish between these models, we grouped trials by short, medium, and long RTs and aligned trial-averaged $\Delta F/F_0$ responses to movement initiation, focusing on early increased activity as this was the dominant population response (Figure 2B). Changes in $\Delta F/F_0$ occurred immediately prior to movement initiation, irrespective of RT (median onsets: short RT, −267 ms [−361, −178] 95% CI; medium RT, −276 ms [−374, −177] 95% CI; long RT, −367 ms [−464, −271] 95% CI, n = 104 neurons/9 FOVs, N = 6 mice, p = 0.46, one-way ANOVA). During medium and long RTs, baseline $\Delta F/F_0$ was maintained upon cue presentation, rising immediately before movement (Figures 2C and 2D). Response profiles were consistent trial to trial and across mice, indicative of a reliable motor timing signal that is temporally uncoupled from the auditory go cue (i.e., model i) (Figures 2E–2G).

Early-onset activity in CFA correlates with $MTh_{DN/IPN}$ response timing

In rodents, projections from VAL thalamus target deep layers of motor cortex (Hooks et al., 2013; Kuramoto et al., 2009). This feedforward glutamatergic input provides monosynaptic excitation and disynaptic inhibition to CFA principal neurons (Apicella et al., 2012; Hooks et al., 2013), shaping cortical output and behavior (Hooks et al., 2013; Kuramoto et al., 2009; Sauerbrei et al., 2020; Schiemann et al., 2015; Tanaka et al., 2018) (Figure 3A). We reasoned that if the $MTh_{DN/IPN}$ thalamocortical pathway conveys a pre-movement motor timing signal, then this should be reflected in the subthreshold membrane potential (V_m) dynamics of CFA layer 5 pyramidal neurons. We confirmed that layer 5 neurons receive direct input from $MTh_{DN/IPN}$ using monosynaptic retrograde rabies tracing in Rbp4-Cre transgenic mice (Gerfen et al., 2013; Kuramoto et al., 2009) (Figure S3A)

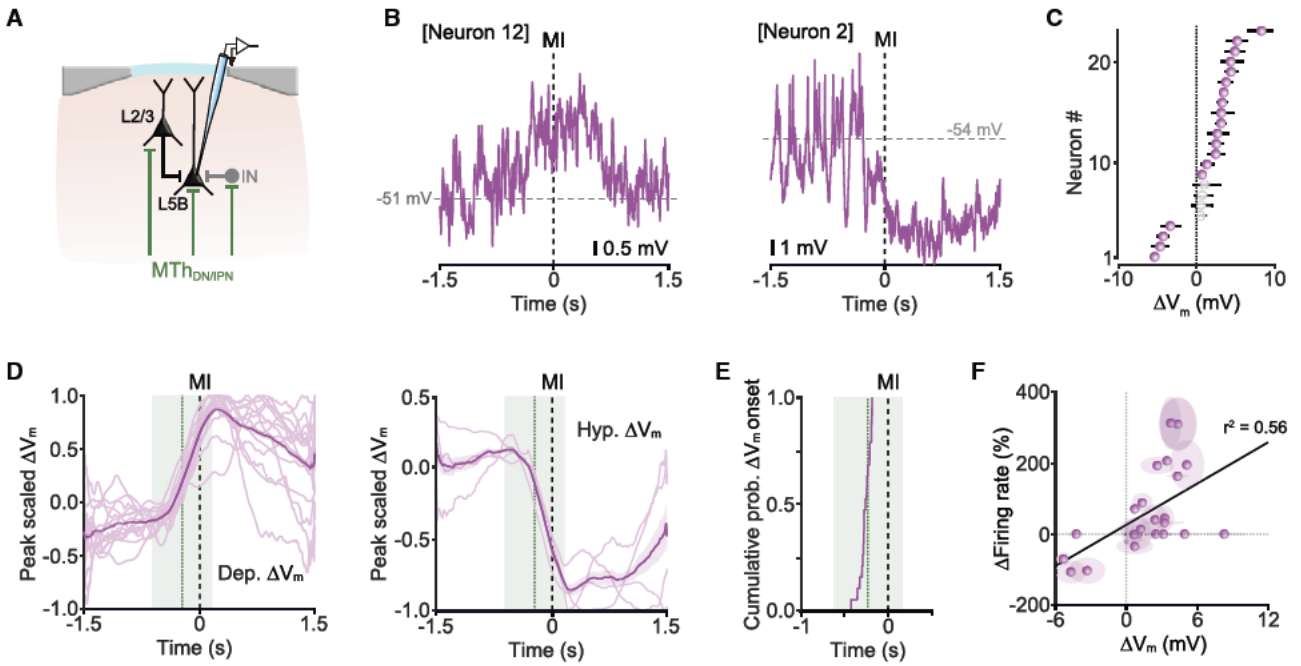

Figure 3. Early-onset changes in CFA layer 5B membrane potential dynamics

(A) Patch-clamp recording in layer5B CFA. IN, interneuron; MTh$_{DN/IPN}$, dentate/interpositus nucleus-recipient region of motor thalamus.

(B) Single-trial subthreshold membrane potential (V_m) trajectories from two layer 5B projection neurons (spikes clipped). MI, movement initiation.

(C) Peri-movement ΔV_m ± 95% CI. Purple and white indicate significant and non-significant changes in ΔV_m, respectively (n = 23 neurons from N = 23 mice).

(D) Overlaid peak scaled subthreshold V_m split by direction of change (left: depolarizing, n = 15/23 neurons; right: hyperpolarizing, n = 4/23 neurons). Thick line, population mean ± 95% CI; green dotted line, mean MTh$_{DN/IPN}$ activity onset ± 95% CI (green shading) shown in Figure 2E; black dashed line, movement initiation (MI).

(E) Cumulative probability of ΔV_m onsets (n = 19/23 neurons).

(F) Movement-related subthreshold ΔV_m and firing rate change correlation. Symbols, mean ± 95% CI from individual neurons; black line, linear fit to the data (Pearson's *r*).

before performing patch-clamp recordings (Figures 3A and S3B). When aligned to push onset, neurons displayed a rapid change in subthreshold activity, either depolarizing or hyperpolarizing, prior to movement initiation (depolarizing n = 15/23 neurons; hyperpolarizing, n = 4/23 neurons; nonresponsive, n = 4/23 neurons, N = 23 mice), with the direction of change being consistent trial to trial (Figures 3B and 3C). The timing of membrane potential changes (ΔV_m) in layer 5B neurons closely matched MTh$_{DN/IPN}$ population onsets (Figures 3D and 3E), consistent with direct feedforward modulation. Subthreshold V_m changes linearly correlated with firing rate in both intratelencephalic (IT-type) and pyramidal tract (PT-type) neurons that send projections to subcortical, brainstem, and spinal cord areas necessary for movement execution (Esposito et al., 2014; Kita and Kita, 2012; Park et al., 2021; Shepherd, 2013) (Figures 3F and S3C–S3J). During miss trials, ΔV_m was reduced, but not abolished, likely reflecting a lack of input from MTh$_{DN/IPN}$ (see Figure 1K), but maintained behavior-related inputs from other brain areas (Hooks et al., 2013) (Figure S3K).

Inactivating DN/IPN or MTh$_{DN/IPN}$ blocks movement initiation

To test whether the DN/IPN thalamocortical pathway is necessary for movement initiation, we performed loss-of-function experiments by focally injecting a small bolus of the GABA$_A$ receptor antagonist muscimol centered on DN/IPN, MTh$_{DN/IPN}$, or CFA (Figures 4A and S4A–S4C). Injecting muscimol during task execution allowed the immediate effects to be recorded 10 min after injection, restricting diffusion beyond targeted regions. Mapping the spread of fluorescent muscimol (see STAR Methods) indicated limited spread (~600 μm radius from the point of injection after 10 min) and localized inactivation of targeted nuclei (Figures 4B, 4C, and S4A–S4C). Our cortical injection strategy targeted all layers of CFA (spread diameter: anterior-posterior [AP], 1,240 ± 28.3 [SD] μm; mediolateral [ML], 1,133.2 ± 35.7 [SD] μm, N = 3 mice), without spreading to other cortical and subcortical areas (Figure S4A); similar results were found with DN/IPN injections (spread diameter: AP, 820 ± 89.4 [SD] μm; ML, 1,221.2 ± 265.4 [SD] μm, N = 4 mice) (Figure S4B). In ventral thalamus, spread was confined to MTh$_{DN/IPN}$, with minimal overlap in VM (spread diameter: AP, 960 ± 73.5 [SD] μm; ML, 957.5 ± 34.9 [SD] μm, N = 4 mice) (Figure S4C). Mapping muscimol diffusion using silicon probe recordings *in vivo* further confirmed limited spread beyond 600 μm 10 min after injection (Figure S4D), consistent with previously published estimates (Allen et al., 2008; Krupa et al., 1999; Martin, 1991). Inactivation of each node along the DN/IPN thalamocortical pathway significantly reduced the number of successful push trials (normalized number successful trials

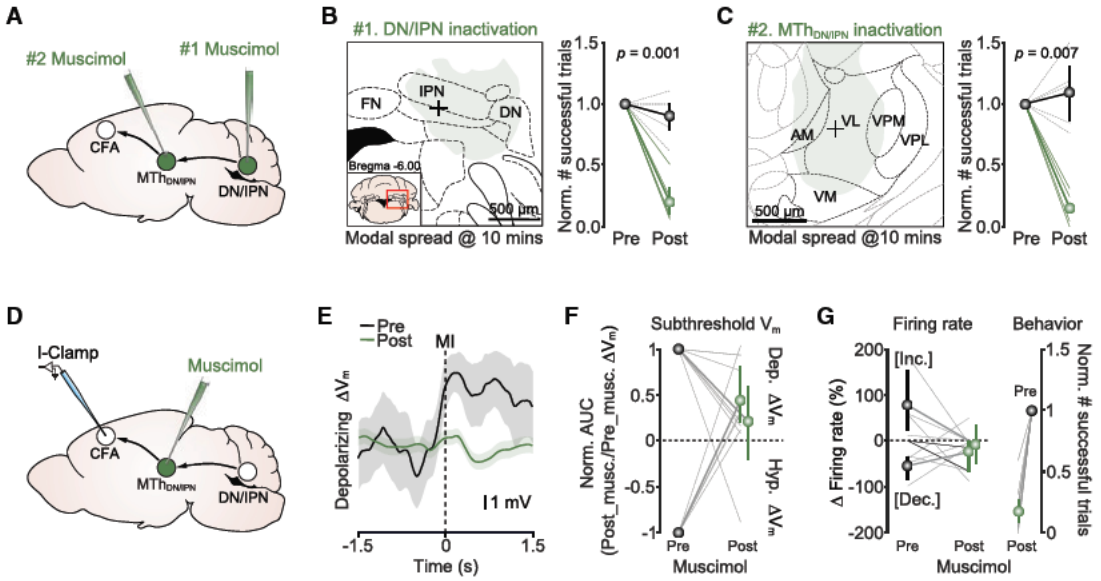

Figure 4. Activity in DN/IPN and MTh$_{DN/IPN}$ is required for cue-triggered movement initiation

(A) Muscimol inactivation of MTh$_{DN/IPN}$ or DN/IPN.

(B) Left: modal spread of fluorescent muscimol 10 min after injection into DN/IPN (inset, location of DN/IPN). Black cross, median point of IPN injection (N = 4 mice). Right: number of successful push trials 10 min after injection of saline (black, N = 6 mice) or muscimol (green, N = 6 mice), two-sample t test. Symbols, population means ± 95% CI. FN, fastigial nucleus; IPN, interpositus nucleus; DN, dentate nucleus.

(C) Left: modal spread of fluorescent muscimol 10 min after injection into MTh$_{DN/IPN}$ (inset, location of thalamic nuclei). Black cross, median point of injection (N = 4 mice). Right: number of successful push trials 10 min after injection of saline (black, N = 5 mice) or muscimol (green, N = 5 mice), two-sample t test. Symbols, population means ± 95% CI. AM, anteromedial; VL, ventrolateral; VPM, ventral posteromedial; VPL, ventral posterolateral; VM, ventromedial nuclei.

(D) Patch-clamp recording in layer 5B CFA during muscimol inactivation of MTh$_{DN/IPN}$. I-Clamp, current clamp.

(E) Subthreshold ΔV$_m$ ± 95% CI from a layer 5B projection neuron before (Pre; black) and after muscimol injection (Post; green) targeted to MTh$_{DN/IPN}$.

(F) Ratio of normalized area under the curve for V$_m$ trajectories before (Pre) and after (Post) muscimol injection into MTh$_{DN/IPN}$. Data grouped by V$_m$ change prior to muscimol injection. Green symbols, population means ± 95% CI (n = 10 cells from N = 10 mice).

(G) Left: change in firing rate before (Pre) and after (Post) muscimol injection into MTh$_{DN/IPN}$. Colored symbols, population means ± 95% CI; dotted lines, individual neurons (n = 8 cells from N = 8 mice); black lines, neurons with no change in firing rate prior to muscimol injection (n = 2 cells from N = 2 mice). Right: number of successful push trials 10 mins after injection of muscimol (green, N = 10 mice).

post muscimol: DN/IPN, 0.20 [0.10, 0.34], p = 0.0013; MTh$_{DN/IPN}$, 0.15 [0.05, 0.25], p = 0.007; CFA, 0.19 [0.08, 0.30] 95% CI, p = 0.025, N = 6, 5, and 5, respectively, two-sample t test; comparison of effect size across manipulations: p = 0.85, one-way ANOVA with Tukey-Kramer post hoc test) due to an increase in miss trials rather than incomplete lever pushes (Figures 4B, 4C, and S4E–S4G; Video S2). Miss trials did not result from task disengagement, as the go cue reproducibly evoked short-latency whisking and increased arousal (see Video S2). Silencing DN/IPN and CFA reduced paw position accuracy in some trials (i.e., the forepaw was not placed on the lever), indicative of a role in controlling posture and movement initiation, while inactivating MTh$_{DN/IPN}$ selectively blocked movement initiation with no effect on paw placement accuracy (Figures S4E–S4G; Video S2).

To better understand how MTh$_{DN/IPN}$ output shapes cortical activity and behavior, we performed patch-clamp recordings of CFA layer 5B projection neurons while inactivating MTh$_{DN/IPN}$ (Figure 4D). Comparing the integral of subthreshold ΔV$_m$ before and after silencing highlighted a reduction in ΔV$_m$ magnitude irrespective of whether responses were depolarizing or hyperpolarizing. On average, neurons displaying depolarizing ΔV$_m$ were reduced by ~80% (normalized area under the curve [AUC] after muscimol, 0.22 [−0.27, 0.64] 95% CI, p = 0.03, two-sample t test, N = 6 mice), while hyperpolarizing responses switched polarity to become moderately depolarizing (normalized AUC after muscimol, 0.44 [0.17, 0.85] 95% CI, p = 0.006, two-sample t test, N = 4 mice) (Figures 4E and 4F). Residual ΔV$_m$ changes likely reflect convergence of other long-range inputs conveying task-related information (Guo et al., 2018; Hooks et al., 2013) (see Figures 1K and S3K), which combine with MTh$_{DN/IPN}$ input to trigger movement. As expected, blocking MTh$_{DN/IPN}$ activity reduced layer 5B firing rate changes and the number of successful push trials (Figure 4G).

Photoactivation of DN/IPN or MTh$_{DN/IPN}$ mimics go cue-evoked movement initiation

Although our loss-of-function experiments suggest the DN/IPN thalamocortical pathway is necessary for movement initiation, cerebellar and thalamic nuclei send projections to multiple brain regions involved in motor control (Asanuma et al., 1983; Hunnicutt et al., 2014; Kuramoto et al., 2009; Teune et al., 2000); therefore, we next tested whether stimulating MTh$_{DN/IPN}$ input to CFA or cerebellar input to MTh$_{DN/IPN}$ triggered movement. We reasoned that if the DN/IPN thalamocortical pathway conveys a movement timing signal, then photoactivation should mimic the effects of the go cue. To stimulate MTh$_{DN/IPN}$, we injected AAV-ChR2 unilaterally, centered on MTh$_{DN/IPN}$,

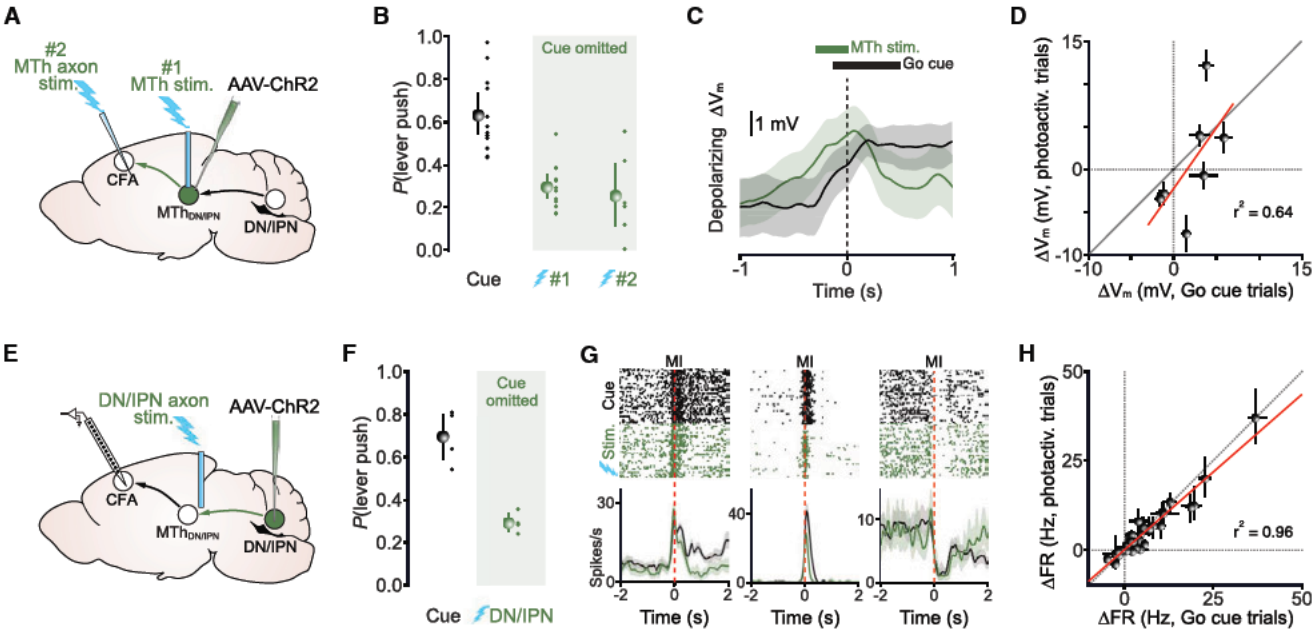

Figure 5. Stimulation of DN/IPN or MTh$_{DN/IPN}$ axon terminals triggers movement initiation

(A) Dual MTh photoactivation strategy; ChR2 expression targeted to MTh$_{DN/IPN}$, stimulation via optic fiber directly above MTh$_{DN/IPN}$ (#1) or tapered fiber in CFA (#2).

(B) Full lever push probability during an auditory go cue (black) or photoactivation of MTh$_{DN/IPN}$ (#1) or MTh$_{DN/IPN}$ axons in CFA (#2) in the absence of a go cue (green). Colored dots, individual mice; colored circles, mean ± 95% CI (cue, 1 and 2; N = 12, 12, and 6 mice, respectively).

(C) Change in subthreshold V$_m$ ± 95% CI in a layer 5B projection neuron during the go cue (black) or photoactivation of MTh$_{DN/IPN}$ (green) in the absence of a cue. Dashed line, movement initiation.

(D) Peri-movement cue-evoked and photoactivated subthreshold ΔV$_m$ correlation during push trials (n = 7 neurons, N = 6 mice). Filled symbols, mean ± 95% CI; red line, linear fit to the data (Pearson's *r*).

(E) Recording and photoactivation strategy: silicone probe recordings of deep-layer putative pyramidal cells in CFA during photoactivation of ChR2-expressing DN/IPN axon terminals in MTh$_{DN/IPN}$.

(F) Full lever push probability during an auditory go cue or photoactivation of DN/IPN axon terminals in MTh$_{DN/IPN}$ in the absence of a go cue. Colored dots, individual mice; colored circles, mean ± 95% CI (N = 4 and 4 mice).

(G) Spike rasters and peri-stimulus time histograms (PSTHs) from deep-layer CFA neurons aligned to movement initiation (dashed line). Black, cue trials; green, photoactivation trials.

(H) Peri-movement cue-evoked and photoactivated Δfiring rate correlation during push trials (n = 30/47 neurons, N = 4 mice). Symbols, mean ± 95% CI; red line, linear fit to the data (Pearson's *r*).

chronically implanted an optic fiber directly above thalamus, and acutely inserted a tapered optic fiber directly into CFA (Figures 5A and S5A). ChR2 expression was restricted to the center of MTh$_{DN/IPN}$ (i.e., VAL thalamic nuclei) with minimal off-target expression (Figures S5B and S5C). Direct stimulation of MTh$_{DN/IPN}$ or axon terminals in CFA in the absence of an auditory cue-triggered full lever push movements in ~30% of trials (go cue, lever push probability: *P*(lever push) 0.63 [0.53, 0.73] 95% CI; direct MTh$_{DN/IPN}$ stimulation, *P*(lever push) 0.29 [0.24, 0.35] 95% CI; axon terminal stimulation, *P*(lever push) 0.25 [0.11, 0.40] 95% CI) and a small proportion of partial lever pushes (N = 12 mice) (Figures 5B, S5D, and S5E; Video S3). RTs and duration of photoactivated push movements were comparable to cue-evoked trials (Figures S5F and S5G), while stimulating in the absence of ChR2 expression did not evoke any detectable forelimb movements (go cue, *P*(lever push) 0.95 [0.89, 1.00] 95% CI; direct MTh$_{DN/IPN}$ stimulation, *P*(lever push) 0.03 [0.00, 0.07] 95% CI, N = 2 mice) (data not shown). To compare cortical activity during go cue and photoactivation trials, we performed patch-clamp recordings from CFA layer 5B projection neurons. Go cue- and photoactivation-evoked ΔV$_m$ were remarkably similar, both in the timing and direction of change, suggesting recruitment of the same inputs to CFA (Figures 5C, 5D, and S5H). Since stimulation of the ventral thalamus, including VM and VAL, has been shown to trigger short-latency licking (Catanese and Jaeger, 2021; Inagaki et al., 2020), we investigated whether MTh$_{DN/IPN}$ acts as a convergence hub coordinating motor timing signals necessary for triggering both tongue and forelimb movements. However, photoactivation of MTh$_{DN/IPN}$ rarely evoked short-latency licking or orofacial movements similar to those observed during a tactile delayed-response licking task (cue, *P*(lick): 0.77 [0.67, 0.87] 95% CI; photoactivation *P*(lick): 0.04 [0.00, 0.10] 95% CI, N = 12 mice, p = 4.1 × 10^{-11}, two-sample t test) (Figure S5I) (Catanese and Jaeger, 2021; Guo et al., 2014; Inagaki et al., 2020). The selective triggering of forelimb push movements in our behavior suggests parallel but distinct thalamocortical pathways for tongue and limb movements.

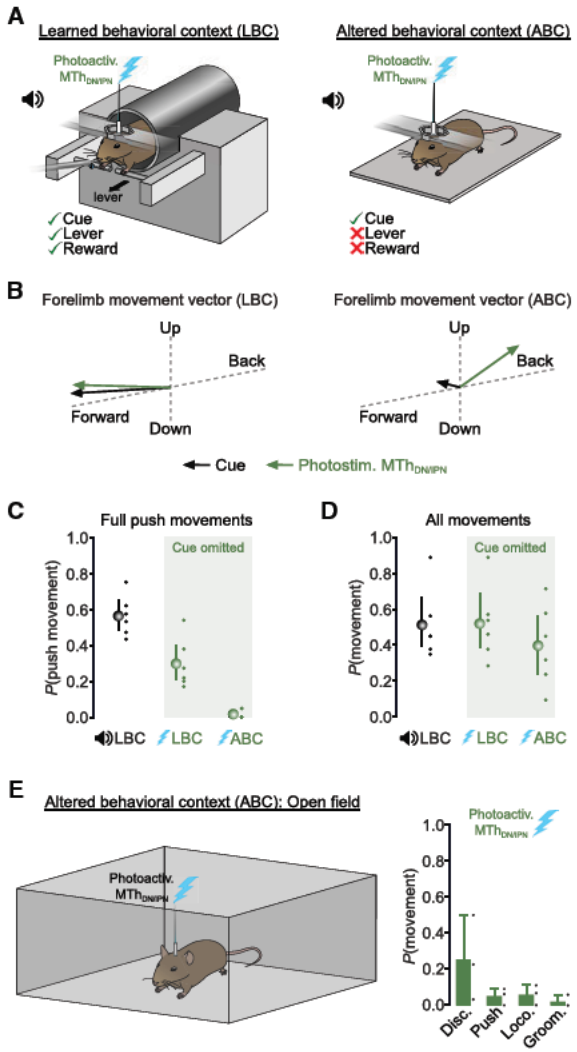

Figure 6. Photoactivation of $MTh_{DN/IPN}$ evokes behavioral context-dependent movement initiation

(A) $MTh_{DN/IPN}$ photoactivation in a learned behavioral context (LBC; left) or altered behavioral context (ABC; right).

(B) Average forelimb movement vectors from an example mouse during an auditory go cue (black arrows) or photoactivation of $MTh_{DN/IPN}$ in the absence of a cue (green arrows). Arrow length, scaled by total number of across trial movements.

(C) Push or push-like movement probability during an auditory go cue (black) or photoactivation of $MTh_{DN/IPN}$ in the absence of a go cue (green). Dots, individual mice; symbols, mean ± 95% CI (N = 6 mice).

(D) Forelimb movement probability during an auditory go cue (black) or photoactivation of $MTh_{DN/IPN}$ in the absence of a go cue (green). Mean ± 95% CI (N = 6 mice).

(E) Forelimb movement probability evoked by photoactivation of $MTh_{DN/IPN}$ in an open-field environment (N = 3 mice). Disc., discrete movements; Push, push-like movements; Loco., locomotion; Groom, grooming behavior. Bars, mean ± 95% CI; dots, individual mice.

We next investigated whether cerebellar input to $MTh_{DN/IPN}$ can initiate movement by targeting ChR2 expression to DN/IPN and stimulating axons terminals in $MTh_{DN/IPN}$ (Figures 5E and S5J–S5O). ChR2 expression was restricted to DN/IPN with minimal or no expression in surrounding nuclei (Figures S5J, S5K, and S5O). Photoactivation in the absence of the auditory go cue-triggered full lever push movements in ~30% of trials (go cue, *P*(lever push) 0.70 [0.59, 0.80] 95% CI; DN/IPN axon terminal stimulation, *P*(lever push) 0.29 [0.25, 0.33] 95% CI, N = 4 mice), similar to direct $MTh_{DN/IPN}$ stimulation (Figure 5F; Video S4). To investigate whether overlapping populations of CFA neurons were recruited during go cue and photoactivation trials, we used silicon probe recordings, focusing on a subset of deep-layer putative pyramidal neurons that were movement responsive (n = 47/216 neurons; N = 4 mice) (Figures S5P–S5U). Responses in individual neurons were highly consistent trial to trial, with movement-related activity patterns varying widely across the population (Figures 5G and S5U), consistent with our ground truth intracellular data (see Figures 3A–3C). A large proportion of cue-responsive neurons also displayed significant responses during photoactivation trials (30/47 neurons, 63.8%, from N = 4 mice), irrespective of the direction of firing rate change (Figures 5G, 5H, and S5U), suggesting photoactivation of the DN/IPN thalamocortical pathway mimics cue-evoked activity patterns in CFA.

$MTh_{DN/IPN}$ stimulation triggers behavioral context-dependent movement initiation

Presentation of a go cue or photoactivation of $MTh_{DN/IPN}$ triggers lever pushes in a learned behavioral context (LBC). But whether push movements would be generated in an altered behavioral context (ABC) is unclear. If thalamocortical stimulation alone is sufficient to trigger the learned behavior, then photoactivation in an ABC should still generate "push-like" movements. However, if $MTh_{DN/IPN}$ simply conveys a motor timing signal that combines with behavioral context-dependent inputs from other brain areas, then photoactivation of $MTh_{DN/IPN}$ in an ABC will likely trigger movement, but not learned push movements. To address this, we designed an ABC, which consisted of a flat baseplate in the absence of any support/movable levers, reward spout, or water reward and compared cue- and $MTh_{DN/IPN}$-photoactivation-evoked movements across contexts (LBC versus ABC) (Figure 6A). Mice were first trained in the LBC before being habituated to the ABC within and across training sessions to ensure cued lever push movements were not extinguished in the LBC. As expected, trained mice generated cue-evoked lever pushes in 56% of trials in the LBC but very few push movements in the ABC (LBC, *P*(push movement) = 0.56 [0.49, 0.65] 95% CI; ABC, *P*(push movement) = 0.01 [0.00, 0.03] 95% CI, $p = 3.9 \times 10^{-7}$, two-sample t test, N = 6 mice), confirming that mice acknowledged the difference between the two behavioral contexts (Figures 6B–6D and S6; Video S5). Direct photoactivation of $MTh_{DN/IPN}$ in the LBC, and in the absence of a cue, evoked forelimb movements in 52% of trials, where 30% of trials were successful lever pushes (LBC, *P*(movement) = 0.52 [0.39, 0.69] 95% CI; LBC, *P*(push movement) = 0.30 [0.21, 0.41] 95% CI, N = 6 mice). While in the ABC, direct $MTh_{DN/IPN}$ stimulation reliably evoked forelimb movements in 40% of trials but only 2% contained "push-like" movements (ABC, *P*(movement) = 0.40 [0.24, 0.56] 95% CI; ABC, *P*(push movement) = 0.02 [0.00, 0.03] 95% CI, $p = 1.9 \times 10^{-3}$, two-sample t test, N = 6 mice) (Figures 6B–6D and S6; Video S5). The absence of push-like movements could result from differences in posture; however,

photostimulated movements in mice mounted on a flat baseplate (ABC) or in a behavioral context that recapitulated the LBC mouse posture (ABC2) were not different (Figure S6). In addition, photostimulation of $MTh_{DN/IPN}$ in an open-field environment triggered discrete forelimb movements in ~25% of trials, consistent with a role in movement initiation, but very few push-like movements (N = 3 mice) (Figure 6E). Together, these data suggest that the DN/IPN thalamocortical pathway conveys motor timing signals that trigger behavioral context-dependent movement initiation.

DISCUSSION

The cerebellum and motor thalamus are brain areas thought to control movement timing, since activity in both regions precedes movement initiation (Anderson and Turner, 1991; Butler et al., 1992, 1996; Fortier et al., 1989; Harvey et al., 1979; Horne and Porter, 1980; Kurata, 2005; Macpherson et al., 1980; Mushiake and Strick, 1993; Schmied et al., 1979; Strick, 1976; van Donkelaar et al., 1999) and local inactivation disrupts motor timing (Meyer-Lohmann et al., 1977; Nashef et al., 2019; Spidalieri et al., 1983; Thach, 1975; van Donkelaar et al., 2000). Our anatomical mapping identified a high degree of connectivity between DN/IPN and CFA-projecting neurons in VAL, AM, and VPM. In rodents, VAL neurons receive strong driver-like inputs (Gornati et al., 2018) that facilitate rapid depolarization of thalamic projection neurons (Aumann and Horne, 1996a, 1996b; Aumann et al., 1994; Gao et al., 2018; Gornati et al., 2018; Sawyer et al., 1994; Schäfer et al., 2021). This driving input, when integrated with GABAergic input from the basal ganglia and thalamic reticular nucleus, shapes the magnitude and timing of thalamic excitability (Bosch-Bouju et al., 2013; Catanese and Jaeger, 2021; Kim et al., 2017; Kuramoto et al., 2011; Lam and Sherman, 2015; Sakai et al., 1998; Tanaka et al., 2018). Early-onset $MTh_{DN/IPN}$ activity was temporally uncoupled from the go cue but tightly locked to movement initiation, suggestive of a pure motor timing signal that indicates the intention to move rather than a sensorimotor transformation from cue to movement (see Figure 2). Consistent with this view, cue presentation during miss trials did not evoke a change in activity, likely reflecting a lack of intention to move and absence of direct auditory input in VAL thalamus, while suppressing $MTh_{DN/IPN}$ generated a selective block of forelimb movement initiation.

Although we focused on the DN/IPN thalamocortical pathway, projections from DN/IPN also target the ventral tegmental area, substantia nigra reticulata, brainstem reticular nucleus, and magnocellular red nucleus (Carta et al., 2019; Gornati et al., 2018; Houck and Person, 2015; Low et al., 2018; Sakayori et al., 2019; Sathyamurthy et al., 2020; Thanawalla et al., 2020). Direct projections to the brainstem provide an alternate pathway to initiate movement. We found that recruitment of the DN/IPN thalamocortical pathway is necessary for learned forelimb movement initiation given that photoactivation of DN/IPN axon terminals in $MTh_{DN/IPN}$ mimics cue-triggered CFA population dynamics and behavior, while silencing each node along the pathway blocked initiation. These observations differ from photomodulation of cerebellar output in locomoting mice, where stimulation initiates or modifies sequences of limb movements via descending projections to the brainstem (Hoogland et al., 2015; Jelitai et al., 2016; Witter et al., 2013). Direct photoactivation of $MTh_{DN/IPN}$ in an open-field environment triggered discrete, but not rhythmic, forelimb movements, suggesting selective recruitment of descending or thalamocortical pathways depending on movement type and behavioral context. In addition to a proposed role in movement initiation, DN/IPN contribute to the coordination of ongoing movements. IPN inactivation results in disrupted endpoint accuracy, hypermetria, and instability of the forelimb (Becker and Person, 2019; Bracha et al., 1999; Low et al., 2018; Martin et al., 2000; Mason et al., 1998), while DN inactivation increases path curvature and generates hypermetria and a general impairment in coordination (Ishikawa et al., 2014; Martin et al., 2000). The fact that DN/IPN inactivation reduced both paw position accuracy (i.e., the ability to maintain postural control) and movement initiation is consistent with a role in both motor timing and coordination.

Changes in $MTh_{DN/IPN}$ and CFA layer 5B neuron activity occurred prior to movement and peaked around movement completion, indicative of rapid preparatory activity that transforms into output dynamics necessary for execution (Lara et al., 2018). In rodents, rapid go cue-evoked changes in activity have been observed in a delayed directional licking task for mice (Catanese and Jaeger, 2021; Gao et al., 2018; Guo et al., 2014; Li et al., 2015), where input from the pedunculopontine nucleus, midbrain reticular nucleus, and substantia nigra reticulata, via ventral motor thalamus, triggers rapid reorganization of preparatory dynamics to initiate directional licking (Catanese and Jaeger, 2021; Inagaki et al., 2020). Thus, ventral thalamus appears ideally positioned to act as a central convergence hub, integrating input from the cerebellum, brainstem, and basal ganglia in order to initiate precisely timed movements. However, direct photoactivation of $MTh_{DN/IPN}$ did not reproducibly evoke short-latency tongue or orofacial movements, suggesting parallel, non-overlapping thalamocortical pathways for movement initiation. Directional licking requires channeling of information through VM, VAL, mediodorsal, and intralaminar nuclei for both movement planning and execution (Catanese and Jaeger, 2021; Inagaki et al., 2020), while forelimb movements require activity in VAL, AM, and VPM nuclei. Together, this suggests that parallel processing of motor timing signals through different ventral motor thalamic nuclei could provide an anatomical substrate for initiating complex, multifaceted motor behaviors.

Using monosynaptic rabies tracing, we confirmed a direct pathway from $MTh_{DN/IPN}$ to layer 5B projection neurons in CFA, consistent with the idea that VAL projects to both superficial and deep layers of motor cortex, while neurons in VM project primarily to L1 (Hooks et al., 2013; Kuramoto et al., 2009, 2015). Strong thalamic input generates monosynaptic excitation and disynaptic feedforward inhibition in principal neurons (Apicella et al., 2012; Hooks et al., 2013), shaping cortical output via top-down control or direct activation of output layers (Hooks et al., 2013; Sauerbrei et al., 2020; Weiler et al., 2008). Since photoactivation of the $MTh_{DN/IPN}$ thalamocortical pathway reproduced go-cue-evoked layer 5B neuronal dynamics, thalamic input may directly influence cortical output by bypassing top-down processing from layer 2/3 to inform PT-type and IT-type neurons of the intention to move (Hooks et al., 2013; Weiler

et al., 2008). This direct timing signal would be integrated with other long-range task-relevant inputs to generate specific output patterns necessary for forelimb motor control (Esposito et al., 2014; Kita and Kita, 2012; Park et al., 2021; Sauerbrei et al., 2020). Although we focused solely on the contribution of CFA, VAL also sends projections to the rostral forelimb area (RFA) (Hooks et al., 2013; Oh et al., 2014), which plays an integral role in movement coordination (Brown and Teskey, 2014; Morandell and Huber, 2017). Given its strong reciprocal connectivity with CFA (Hira et al., 2013; Mohammed and Jain, 2016; Rouiller et al., 1993), assessing the contribution of the VAL-RFA pathway to movement initiation will be an important next step.

Our behavioral context experiments further support $MTh_{DN/IPN}$ conveying a generic motor timing signal that converges, at the level of motor cortex, with other task-relevant inputs. In the absence of thalamic input to $MTh_{DN/IPN}$ (i.e., miss trials or MTh inactivation), layer 5B V_m and firing rate changes were significantly reduced, with residual V_m changes being insufficient to trigger movement, suggesting input convergence is a prerequisite for learned movement initiation. The origin of the additional input(s) remains unknown, but likely candidates are cortico-cortical interactions between frontal motor areas and CFA (Hooks et al., 2013; Reep et al., 1990), thought to accumulate task-relevant information required for motor planning and execution (Gao et al., 2018; Li et al., 2015), or basal ganglia thalamocortical interactions involved in selecting, timing, and invigorating different actions (Dudman and Krakauer, 2016; Inase et al., 1996; Klaus et al., 2019; Thura and Cisek, 2017; Williams and Herberg, 1987). Directly activating the $MTh_{DN/IPN}$ thalamocortical pathway in the LBC mimicked the go cue by triggering push movements, while in the ABC, photoactivation evoked highly variable forelimb trajectories. Why does photoactivation result in learned movement initiation in the absence of an external sensory cue? We suggest that the DN/IPN thalamocortical pathway provides one of the main driving inputs to CFA, which combines with other task-relevant inputs (e.g., behavioral context, stimulus-reward associations, and reward expectancy) to generate "learned" cortical output patterns and behavior. In the ABC, task-relevant inputs are likely absent, thus mimicking the thalamic "timing signal" is in itself sufficient to generate cortical output patterns necessary for movement (Tanaka et al., 2018), but not the learned movement.

In summary, our findings extend our understanding of how specific subdivisions of the motor thalamus contribute to motor timing, suggesting that the DN/IPN thalamocortical pathway plays a critical role in generating cortical dynamics necessary for context-dependent movement initiation.

STAR★METHODS

Detailed methods are provided in the online version of this paper and include the following:

- KEY RESOURCES TABLE
- RESOURCE AVAILABILITY
  - Lead contact
  - Materials availability
  - Data and code availability
- EXPERIMENTAL MODEL AND SUBJECT DETAILS
- METHOD DETAILS
  - General surgery
  - Behavioral training
  - *In vivo* pharmacology
  - GRIN lens imaging
  - Whole-cell patch-clamp electrophysiology
  - Immunohistochemistry
  - Motor thalamic activation
  - Cerebellar-motor thalamic pathway tracing and activation
  - Monosynaptic retrograde rabies tracing
  - Extracellular recording and spike sorting
  - Quantifying muscimol diffusion
  - Forelimb kinematic tracking
- QUANTIFICATION AND STATISTICAL ANALYSIS

SUPPLEMENTAL INFORMATION

Supplemental information can be found online at https://doi.org/10.1016/j.neuron.2021.05.016.

ACKNOWLEDGMENTS

We are grateful to T. Branco, B. Grewe, J. Gründemann, M. Nolan, G. Sürmeli, B. Mensh, and members of the Nolan, Sürmeli, and Duguid labs for experimental discussions and comments on the manuscript. We thank M. Zechner for graphic design. Rabies virus was a gift from E. Callaway (Salk Institute) to A.W.H. GCaMP6s was a gift from Douglas Kim and the GENIE Project (Addgene 100844-AAV1). ChR2-Venus-AAV was a gift from Karel Svoboda (Addgene plasmid #20071). This study was supported by the BBSRC (UK) (BB/R018537/1), DFG (Germany) (SCHI1267/2-1 to J.S. and AM 443/1-1 to J.J.A.), the Shirley Foundation (UK), HHMI (USA) (A.W.H. and C.-C.H.), and a Wellcome SRF (UK) (110131/Z/15/Z) to I.D.

AUTHOR CONTRIBUTIONS

Conceptualization, J.D., M.C., J.J.A., J.S., A.W.H., and I.D.; methodology & investigation, J.D., M.C., T.C., J.J.A., J.S., V.C.-P., F.C., J.A.H., and C.-C.H.; resources, J.P., and N.L.R.; writing – review & editing, all authors (see Table S1, contributions matrix).

DECLARATION OF INTERESTS

The authors declare no competing interests.

Received: September 23, 2019
Revised: April 7, 2021
Accepted: May 11, 2021
Published: June 18, 2021

REFERENCES

Allen, T.A., Narayanan, N.S., Kholodar-Smith, D.B., Zhao, Y., Laubach, M., and Brown, T.H. (2008). Imaging the spread of reversible brain inactivations using fluorescent muscimol. J. Neurosci. Methods *171*, 30–38.

Anderson, M.E., and Turner, R.S. (1991). Activity of neurons in cerebellar-receiving and pallidal-receiving areas of the thalamus of the behaving monkey. J. Neurophysiol. *66*, 879–893.

Angaut, P., Cicirata, F., and Serapide, F. (1985). Topographic organization of the cerebellothalamic projections in the rat. An autoradiographic study. Neuroscience *15*, 389–401.

Apicella, A.J., Wickersham, I.R., Seung, H.S., and Shepherd, G.M. (2012). Laminarly orthogonal excitation of fast-spiking and low-threshold-spiking interneurons in mouse motor cortex. J. Neurosci. *32*, 7021–7033.

Asanuma, C., Thach, W.T., and Jones, E.G. (1983). Brainstem and spinal projections of the deep cerebellar nuclei in the monkey, with observations on the brainstem projections of the dorsal column nuclei. Brain Res. *286*, 299–322.

Aumann, T.D., and Horne, M.K. (1996a). A comparison of the ultrastructure of synapses in the cerebello-rubral and cerebello-thalamic pathways in the rat. Neurosci. Lett. *211*, 175–178.

Aumann, T.D., and Horne, M.K. (1996b). Ramification and termination of single axons in the cerebellothalamic pathway of the rat. J. Comp. Neurol. *376*, 420–430.

Aumann, T.D., Rawson, J.A., Finkelstein, D.I., and Horne, M.K. (1994). Projections from the lateral and interposed cerebellar nuclei to the thalamus of the rat: a light and electron microscopic study using single and double anterograde labelling. J. Comp. Neurol. *349*, 165–181.

Balleine, B.W. (2019). The meaning of behavior: discriminating reflex and volition in the brain. Neuron *104*, 47–62.

Bastian, A.J., and Thach, W.T. (1995). Cerebellar outflow lesions: a comparison of movement deficits resulting from lesions at the levels of the cerebellum and thalamus. Ann. Neurol. *38*, 881–892.

Becker, M.I., and Person, A.L. (2019). Cerebellar Control of Reach Kinematics for Endpoint Precision. Neuron *103*, 335–348.e5.

Bosch-Bouju, C., Hyland, B.I., and Parr-Brownlie, L.C. (2013). Motor thalamus integration of cortical, cerebellar and basal ganglia information: implications for normal and parkinsonian conditions. Front. Comput. Neurosci. *7*, 163.

Bostan, A.C., Dum, R.P., and Strick, P.L. (2013). Cerebellar networks with the cerebral cortex and basal ganglia. Trends Cogn. Sci. *17*, 241–254.

Bracha, V., Kolb, F.P., Irwin, K.B., and Bloedel, J.R. (1999). Inactivation of interposed nuclei in the cat: classically conditioned withdrawal reflexes, voluntary limb movements and the action primitive hypothesis. Exp. Brain Res. *126*, 77–92.

Brown, A.R., and Teskey, G.C. (2014). Motor cortex is functionally organized as a set of spatially distinct representations for complex movements. J. Neurosci. *34*, 13574–13585.

Butler, E.G., Horne, M.K., and Hawkins, N.J. (1992). The activity of monkey thalamic and motor cortical neurones in a skilled, ballistic movement. J. Physiol. *445*, 25–48.

Butler, E.G., Finkelstein, D.I., Harvey, M.C., Churchward, P.R., Forlano, L.M., and Horne, M.K. (1996). The relationship between monkey ventrolateral thalamic nucleus activity and kinematic parameters of wrist movement. Brain Res. *736*, 146–159.

Carta, I., Chen, C.H., Schott, A.L., Dorizan, S., and Khodakhah, K. (2019). Cerebellar modulation of the reward circuitry and social behavior. Science *363*, eaav0581.

Catanese, J., and Jaeger, D. (2021). Premotor ramping of thalamic neuronal activity is modulated by nigral inputs and contributes to control the timing of action release. J. Neurosci. *41*, 1878–1891.

Chen, T.-W., Wardill, T.J., Sun, Y., Pulver, S.R., Renninger, S.L., Baohan, A., Schreiter, E.R., Kerr, R.A., Orger, M.B., Jayaraman, V., et al. (2013). Ultrasensitive fluorescent proteins for imaging neuronal activity. Nature *499*, 295–300.

Cooper, S.E., Martin, J.H., and Ghez, C. (2000). Effects of inactivation of the anterior interpositus nucleus on the kinematic and dynamic control of multijoint movement. J. Neurophysiol. *84*, 1988–2000.

Dudman, J.T., and Krakauer, J.W. (2016). The basal ganglia: from motor commands to the control of vigor. Curr. Opin. Neurobiol. *37*, 158–166.

Esposito, M.S., Capelli, P., and Arber, S. (2014). Brainstem nucleus MdV mediates skilled forelimb motor tasks. Nature *508*, 351–356.

Fortier, P.A., Kalaska, J.F., and Smith, A.M. (1989). Cerebellar neuronal activity related to whole-arm reaching movements in the monkey. J. Neurophysiol. *62*, 198–211.

Gao, Z., Davis, C., Thomas, A.M., Economo, M.N., Abrego, A.M., Svoboda, K., De Zeeuw, C.I., and Li, N. (2018). A cortico-cerebellar loop for motor planning. Nature *563*, 113–116.

Gerfen, C.R., Paletzki, R., and Heintz, N. (2013). GENSAT BAC cre-recombinase driver lines to study the functional organization of cerebral cortical and basal ganglia circuits. Neuron *80*, 1368–1383.

Gibson, A.R., Houk, J.C., and Kohlerman, N.J. (1985). Magnocellular red nucleus activity during different types of limb movement in the macaque monkey. J. Physiol. *358*, 527–549.

Gornati, S.V., Schäfer, C.B., Eelkman Rooda, O.H.J., Nigg, A.L., De Zeeuw, C.I., and Hoebeek, F.E. (2018). Differentiating cerebellar impact on thalamic nuclei. Cell Rep. *23*, 2690–2704.

Graybiel, A.M. (2008). Habits, rituals, and the evaluative brain. Annu. Rev. Neurosci. *31*, 359–387.

Guo, Z.V., Li, N., Huber, D., Ophir, E., Gutnisky, D., Ting, J.T., Feng, G., and Svoboda, K. (2014). Flow of cortical activity underlying a tactile decision in mice. Neuron *81*, 179–194.

Guo, K., Yamawaki, N., Svoboda, K., and Shepherd, G.M.G. (2018). Anterolateral motor cortex connects with a medial subdivision of ventromedial thalamus through cell type-specific circuits, forming an excitatory thalamo-cortico-thalamic loop via layer 1 apical tuft dendrites of layer 5B pyramidal tract type neurons. J. Neurosci. *38*, 8787–8797.

Haroian, A.J., Massopust, L.C., and Young, P.A. (1981). Cerebellothalamic projections in the rat: an autoradiographic and degeneration study. J. Comp. Neurol. *197*, 217–236.

Harvey, R.J., Porter, R., and Rawson, J.A. (1979). Discharges of intracerebellar nuclear cells in monkeys. J. Physiol. *297*, 559–580.

Hira, R., Ohkubo, F., Tanaka, Y.R., Masamizu, Y., Augustine, G.J., Kasai, H., and Matsuzaki, M. (2013). In vivo optogenetic tracing of functional corticocortical connections between motor forelimb areas. Front. Neural Circuits *7*, 55.

Holmes, G. (1939). The cerebellum of man. Brain *62*, 1–30.

Hoogland, T.M., De Gruijl, J.R., Witter, L., Canto, C.B., and De Zeeuw, C.I. (2015). Role of synchronous activation of cerebellar purkinje cell ensembles in multi-joint movement control. Curr. Biol. *25*, 1157–1165.

Hooks, B.M., Mao, T., Gutnisky, D.A., Yamawaki, N., Svoboda, K., and Shepherd, G.M. (2013). Organization of cortical and thalamic input to pyramidal neurons in mouse motor cortex. J. Neurosci. *33*, 748–760.

Horne, M.K., and Butler, E.G. (1995). The role of the cerebello-thalamo-cortical pathway in skilled movement. Prog. Neurobiol. *46*, 199–213.

Horne, M.K., and Porter, R. (1980). The discharges during movement of cells in the ventrolateral thalamus of the conscious monkey. J. Physiol. *304*, 349–372.

Houck, B.D., and Person, A.L. (2015). Cerebellar premotor output neurons collateralize to innervate the cerebellar cortex. J. Comp. Neurol. *523*, 2254–2271.

Huang, C.-C., Sugino, K., Shima, Y., Guo, C., Bai, S., Mensh, B.D., Nelson, S.B., and Hantman, A.W. (2013). Convergence of pontine and proprioceptive streams onto multimodal cerebellar granule cells. Elife *2*, e00400. https://doi.org/10.7554/eLife.00400.

Hunnicutt, B.J., Long, B.R., Kusefoglu, D., Gertz, K.J., Zhong, H., and Mao, T. (2014). A comprehensive thalamocortical projection map at the mesoscopic level. Nat. Neurosci. *17*, 1276–1285.

Inagaki, H.K., Chen, S., Ridder, M.C., Sah, P., Li, N., Yang, Z., Hasanbegovic, H., Gao, Z., Gerfen, C.R., and Svoboda, K. (2020). A midbrain-thalamus-cortex circuit reorganizes cortical dynamics to initiate planned movement. bioRxiv. https://doi.org/10.1101/2020.12.16.423127.

Inase, M., Buford, J.A., and Anderson, M.E. (1996). Changes in the control of arm position, movement, and thalamic discharge during local inactivation in the globus pallidus of the monkey. J. Neurophysiol. *75*, 1087–1104.

Ishikawa, T., Tomatsu, S., Tsunoda, Y., Lee, J., Hoffman, D.S., and Kakei, S. (2014). Releasing dentate nucleus cells from Purkinje cell inhibition generates output from the cerebrocerebellum. PLoS ONE *9*, e108774.

Jelitai, M., Puggioni, P., Ishikawa, T., Rinaldi, A., and Duguid, I. (2016). Dendritic excitation-inhibition balance shapes cerebellar output during motor behaviour. Nat. Commun. *7*, 13722.

Jun, J.J., Steinmetz, N.A., Siegle, J.H., Denman, D.J., Bauza, M., Barbarits, B., Lee, A.K., Anastassiou, C.A., Andrei, A., Aydın, Ç., et al. (2017). Fully integrated silicon probes for high-density recording of neural activity. Nature *551*, 232–236.

Keemink, S.W., Lowe, S.C., Pakan, J.M.P., Dylda, E., van Rossum, M.C.W., and Rochefort, N.L. (2018). FISSA: A neuropil decontamination toolbox for calcium imaging signals. Sci. Rep. *8*, 3493.

Kim, J., Kim, Y., Nakajima, R., Shin, A., Jeong, M., Park, A.H., Jeong, Y., Jo, S., Yang, S., Park, H., et al. (2017). Inhibitory basal ganglia inputs induce excitatory motor signals in the thalamus. Neuron *95*, 1181–1196.e8.

Kita, T., and Kita, H. (2012). The subthalamic nucleus is one of multiple innervation sites for long-range corticofugal axons: a single-axon tracing study in the rat. J. Neurosci. *32*, 5990–5999.

Klaus, A., Alves da Silva, J., and Costa, R.M. (2019). What, if, and when to move: basal ganglia circuits and self-paced action initiation. Annu. Rev. Neurosci. *42*, 459–483.

Krupa, D.J., Ghazanfar, A.A., and Nicolelis, M.A. (1999). Immediate thalamic sensory plasticity depends on corticothalamic feedback. Proc. Natl. Acad. Sci. USA *96*, 8200–8205.

Kuramoto, E., Furuta, T., Nakamura, K.C., Unzai, T., Hioki, H., and Kaneko, T. (2009). Two types of thalamocortical projections from the motor thalamic nuclei of the rat: a single neuron-tracing study using viral vectors. Cereb. Cortex *19*, 2065–2077.

Kuramoto, E., Fujiyama, F., Nakamura, K.C., Tanaka, Y., Hioki, H., and Kaneko, T. (2011). Complementary distribution of glutamatergic cerebellar and GABAergic basal ganglia afferents to the rat motor thalamic nuclei. Eur. J. Neurosci. *33*, 95–109.

Kuramoto, E., Ohno, S., Furuta, T., Unzai, T., Tanaka, Y.R., Hioki, H., and Kaneko, T. (2015). Ventral medial nucleus neurons send thalamocortical afferents more widely and more preferentially to layer 1 than neurons of the ventral anterior-ventral lateral nuclear complex in the rat. Cereb. Cortex *25*, 221–235.

Kurata, K. (2005). Activity properties and location of neurons in the motor thalamus that project to the cortical motor areas in monkeys. J. Neurophysiol. *94*, 550–566.

Lam, Y.W., and Sherman, S.M. (2015). Functional topographic organization of the motor reticulothalamic pathway. J. Neurophysiol. *113*, 3090–3097.

Lara, A.H., Elsayed, G.F., Zimnik, A.J., Cunningham, J.P., and Churchland, M.M. (2018). Conservation of preparatory neural events in monkey motor cortex regardless of how movement is initiated. eLife *7*, e31826.

Li, N., Chen, T.W., Guo, Z.V., Gerfen, C.R., and Svoboda, K. (2015). A motor cortex circuit for motor planning and movement. Nature *519*, 51–56.

Low, A.Y.T., Thanawalla, A.R., Yip, A.K.K., Kim, J., Wong, K.L.L., Tantra, M., Augustine, G.J., and Chen, A.I. (2018). Precision of Discrete and Rhythmic Forelimb Movements Requires a Distinct Neuronal Subpopulation in the Interposed Anterior Nucleus. Cell Rep. *22*, 2322–2333.

Macpherson, J.M., Rasmusson, D.D., and Murphy, J.T. (1980). Activities of neurons in "motor" thalamus during control of limb movement in the primate. J. Neurophysiol. *44*, 11–28.

Martin, J.H. (1991). Autoradiographic estimation of the extent of reversible inactivation produced by microinjection of lidocaine and muscimol in the rat. Neurosci. Lett. *127*, 160–164.

Martin, J.H., Cooper, S.E., Hacking, A., and Ghez, C. (2000). Differential effects of deep cerebellar nuclei inactivation on reaching and adaptive control. J. Neurophysiol. *83*, 1886–1899.

Mason, C.R., Miller, L.E., Baker, J.F., and Houk, J.C. (1998). Organization of reaching and grasping movements in the primate cerebellar nuclei as revealed by focal muscimol inactivations. J. Neurophysiol. *79*, 537–554.

Mathis, A., Mamidanna, P., Cury, K.M., Abe, T., Murthy, V.N., Mathis, M.W., and Bethge, M. (2018). DeepLabCut: markerless pose estimation of user-defined body parts with deep learning. Nat. Neurosci. *21*, 1281–1289.

Meyer-Lohmann, J., Hore, J., and Brooks, V.B. (1977). Cerebellar participation in generation of prompt arm movements. J. Neurophysiol. *40*, 1038–1050.

Milak, M.S., Shimansky, Y., Bracha, V., and Bloedel, J.R. (1997). Effects of inactivating individual cerebellar nuclei on the performance and retention of an operantly conditioned forelimb movement. J. Neurophysiol. *78*, 939–959.

Mohammed, H., and Jain, N. (2016). Ipsilateral cortical inputs to the rostral and caudal motor areas in rats. J. Comp. Neurol. *524*, 3104–3123.

Morandell, K., and Huber, D. (2017). The role of forelimb motor cortex areas in goal directed action in mice. Sci. Rep. *7*, 15759.

Mushiake, H., and Strick, P.L. (1993). Preferential activity of dentate neurons during limb movements guided by vision. J. Neurophysiol. *70*, 2660–2664.

Nashef, A., Cohen, O., Israel, Z., Harel, R., and Prut, Y. (2018). Cerebellar Shaping of Motor Cortical Firing Is Correlated with Timing of Motor Actions. Cell Rep. *23*, 1275–1285.

Nashef, A., Cohen, O., Harel, R., Israel, Z., and Prut, Y. (2019). Reversible Block of Cerebellar Outflow Reveals Cortical Circuitry for Motor Coordination. Cell Rep. *27*, 2608–2619.e4.

Nenadic, Z., and Burdick, J.W. (2005). Spike detection using the continuous wavelet transform. IEEE Trans. Biomed. Eng. *52*, 74–87.

Oh, S.W., Harris, J.A., Ng, L., Winslow, B., Cain, N., Mihalas, S., Wang, Q., Lau, C., Kuan, L., Henry, A.M., et al. (2014). A mesoscale connectome of the mouse brain. Nature *508*, 207–214.

Pachitariu, M., Steinmetz, N., Kadir, S., and Carandini, M. (2016). Kilosort: real-time spike-sorting for extracellular electrophysiology with hundreds of channels. bioRxiv. https://doi.org/10.1101/061481.

Park, J., Phillips, J., Martin, K., Hantman, A., and Dudman, J. (2021). Descending neocortical output critical for skilled forelimb movements is distributed across projection cell classes. bioRxiv. https://doi.org/10.1101/772517.

Paxinos, G., and Franklin, K. (2008). The Mouse Brain in Stereotaxic Coordinates, Compact: The Coronal Plates and Diagrams, 3rd edition (Elsevier Science Publishing/Academic Press).

Petreanu, L., Mao, T., Sternson, S.M., and Svoboda, K. (2009). The subcellular organization of neocortical excitatory connections. Nature *457*, 1142–1145.

Pnevmatikakis, E.A., and Giovannucci, A. (2017). NoRMCorre: An online algorithm for piecewise rigid motion correction of calcium imaging data. J. Neurosci. Methods *291*, 83–94.

Reep, R.L., Goodwin, G.S., and Corwin, J.V. (1990). Topographic organization in the corticocortical connections of medial agranular cortex in rats. J. Comp. Neurol. *294*, 262–280.

Rouiller, E.M., Moret, V., and Liang, F. (1993). Comparison of the connectional properties of the two forelimb areas of the rat sensorimotor cortex: support for the presence of a premotor or supplementary motor cortical area. Somatosens. Mot. Res. *10*, 269–289.

Rovó, Z., Ulbert, I., and Acsády, L. (2012). Drivers of the primate thalamus. J. Neurosci. *32*, 17894–17908.

Sakai, S.T., Grofova, I., and Bruce, K. (1998). Nigrothalamic projections and nigrothalamocortical pathway to the medial agranular cortex in the rat: single- and double-labeling light and electron microscopic studies. J. Comp. Neurol. *391*, 506–525.

Sakayori, N., Kato, S., Sugawara, M., Setogawa, S., Fukushima, H., Ishikawa, R., Kida, S., and Kobayashi, K. (2019). Motor skills mediated through cerebellothalamic tracts projecting to the central lateral nucleus. Mol. Brain *12*, 13.

Sathyamurthy, A., Barik, A., Dobrott, C.I., Matson, K.J.E., Stoica, S., Pursley, R., Chesler, A.T., and Levine, A.J. (2020). Cerebellospinal Neurons Regulate Motor Performance and Motor Learning. Cell Rep. *31*, 107595.

Sauerbrei, B.A., Guo, J.Z., Cohen, J.D., Mischiati, M., Guo, W., Kabra, M., Verma, N., Mensh, B., Branson, K., and Hantman, A.W. (2020). Cortical pattern generation during dexterous movement is input-driven. Nature *577*, 386–391.

Sawyer, S.F., Young, S.J., Groves, P.M., and Tepper, J.M. (1994). Cerebellar-responsive neurons in the thalamic ventroanterior-ventrolateral complex of rats: in vivo electrophysiology. Neuroscience *63*, 711–724.

Schäfer, C.B., Gao, Z., De Zeeuw, C.I., and Hoebeek, F.E. (2020). Cerebello-Thalamic Spike Transfer via Temporal Coding and Cortical Adaptation. bioRxiv. https://doi.org/10.1101/2020.01.19.911610.

Schäfer, C.B., Gao, Z., De Zeeuw, C.I., and Hoebeek, F.E. (2021). Temporal dynamics of the cerebello-cortical convergence in ventro-lateral motor thalamus. J. Physiol. *599*, 2055–2073.

Schiemann, J., Puggioni, P., Dacre, J., Pelko, M., Domanski, A., van Rossum, M.C., and Duguid, I. (2015). Cellular mechanisms underlying behavioral state-dependent bidirectional modulation of motor cortex output. Cell Rep. *11*, 1319–1330.

Schindelin, J., Arganda-Carreras, I., Frise, E., Kaynig, V., Longair, M., Pietzsch, T., Preibisch, S., Rueden, C., Saalfeld, S., Schmid, B., et al. (2012). Fiji: an open-source platform for biological-image analysis. Nat. Methods *9*, 676–682.

Schmied, A., Benita, M., Conde, H., and Dormont, J.F. (1979). Activity of ventrolateral thalamic neurons in relation to a simple reaction time task in the cat. Exp. Brain Res. *36*, 285–300.

Shepherd, G.M. (2013). Corticostriatal connectivity and its role in disease. Nat. Rev. Neurosci. *14*, 278–291.

Spidalieri, G., Busby, L., and Lamarre, Y. (1983). Fast ballistic arm movements triggered by visual, auditory, and somesthetic stimuli in the monkey. II. Effects of unilateral dentate lesion on discharge of precentral cortical neurons and reaction time. J. Neurophysiol. *50*, 1359–1379.

Strick, P.L. (1976). Activity of ventrolateral thalamic neurons during arm movement. J. Neurophysiol. *39*, 1032–1044.

Tanaka, Y.H., Tanaka, Y.R., Kondo, M., Terada, S.I., Kawaguchi, Y., and Matsuzaki, M. (2018). Thalamocortical Axonal Activity in Motor Cortex Exhibits Layer-Specific Dynamics during Motor Learning. Neuron *100*, 244–258.e12.

Teune, T.M., van der Burg, J., van der Moer, J., Voogd, J., and Ruigrok, T.J. (2000). Topography of cerebellar nuclear projections to the brain stem in the rat. Prog. Brain Res. *124*, 141–172.

Thach, W.T. (1975). Timing of activity in cerebellar dentate nucleus and cerebral motor cortex during prompt volitional movement. Brain Res. *88*, 233–241.

Thach, W.T. (2014). Does the cerebellum initiate movement? Cerebellum *13*, 139–150.

Thach, W.T., and Bastian, A.J. (2004). Role of the cerebellum in the control and adaptation of gait in health and disease. Prog. Brain Res. *143*, 353–366.

Thanawalla, A.R., Chen, A.I., and Azim, E. (2020). The Cerebellar Nuclei and Dexterous Limb Movements. Neuroscience *450*, 168–183.

Thura, D., and Cisek, P. (2017). The Basal Ganglia Do Not Select Reach Targets but Control the Urgency of Commitment. Neuron *95*, 1160–1170.e5.

van Donkelaar, P., Stein, J.F., Passingham, R.E., and Miall, R.C. (1999). Neuronal activity in the primate motor thalamus during visually triggered and internally generated limb movements. J. Neurophysiol. *82*, 934–945.

van Donkelaar, P., Stein, J.F., Passingham, R.E., and Miall, R.C. (2000). Temporary inactivation in the primate motor thalamus during visually triggered and internally generated limb movements. J. Neurophysiol. *83*, 2780–2790.

Weiler, N., Wood, L., Yu, J., Solla, S.A., and Shepherd, G.M. (2008). Top-down laminar organization of the excitatory network in motor cortex. Nat. Neurosci. *11*, 360–366.

Wickersham, I.R., Finke, S., Conzelmann, K.K., and Callaway, E.M. (2007). Retrograde neuronal tracing with a deletion-mutant rabies virus. Nat. Methods *4*, 47–49.

Wickersham, I.R., Sullivan, H.A., and Seung, H.S. (2010). Production of glycoprotein-deleted rabies viruses for monosynaptic tracing and high-level gene expression in neurons. Nat. Protoc. *5*, 595–606.

Williams, S.F., and Herberg, L.J. (1987). Motivational vs. motor effects of striatal and pallidal gabergic projections to subthalamic and entopeduncular nuclei, ventromedial thalamus, and ventral globus pallidus. Pharmacol. Biochem. Behav. *26*, 49–55.

Witter, L., Canto, C.B., Hoogland, T.M., de Gruijl, J.R., and De Zeeuw, C.I. (2013). Strength and timing of motor responses mediated by rebound firing in the cerebellar nuclei after Purkinje cell activation. Front. Neural Circuits *7*, 133.

Xu, C., Krabbe, S., Gründemann, J., Botta, P., Fadok, J.P., Osakada, F., Saur, D., Grewe, B.F., Schnitzer, M.J., Callaway, E.M., and Lüthi, A. (2016). Distinct Hippocampal Pathways Mediate Dissociable Roles of Context in Memory Retrieval. Cell *167*, 961–972.e16.

Zong, W., Heldt, T., Moody, G.B., and Mark, R.G. (2003). An Open-Source Algorithm to Detect Onset of Arterial Blood Pressure Pulses. Comput. Cardiol. *30*, 4.

STAR★METHODS

KEY RESOURCES TABLE

REAGENT or RESOURCE	SOURCE	IDENTIFIER
Antibodies		
Mouse monoclonal anti-Satb2	Thermo Fisher Scientific	Abcam Cat# ab51502; RRID:AB_882455
Rat monoclonal anti-Ctip2	Thermo Fisher Scientific	Abcam Cat# ab18465; RRID: AB_2064130
Anti-VGluT2 Antibody	Sigma-Aldrich	Cat# AB2251-I; RRID:AB_2665454
Cy5 AffiniPure donkey anti-guinea pig	Jackson ImmunoResearch Europe Ltd.	Cat# AB2251-I; RRID:AB_2340462
AlexaFluor-568 goat anti-mouse	Molecular Probes	Cat#: A- 21124; RRID: AB_2535766
AlexaFluor-647 goat anti-rat	Molecular Probes	Cat#: A-21247; RRID: AB_141778
Bacterial and virus strains		
AAV2/1-CAG-FLEX-mTagBFP2-2A-TVA	Kimberly Ritola at Janelia Farm-Molecular Biology Shared Resource; Huang et al., 2013	N/A
Pseudotyped SADΔG-mCherry(EnvA) rabies	Salk Institute Vector Core; Wickersham et al., 2007	N/A
AAV2/1-CAG-EGFP	Penn Vector Core	Addgene 28014
AAV1-Syn-GCaMP6s	Penn Vector Core; Chen et al., 2013	Addgene 100844
AAV1-CAG-ChR2-Venus	UNC Vector Core; Addgene; Petreanu et al., 2009	Addgene 20071
AAV2-CAG-mCherry	Homemade: McClure at Edinburgh	Addgene 108685
Chemicals, peptides, and recombinant proteins		
Muscimol hydrobromide	Sigma-Aldrich, Missouri, USA	Cat#: G019-5MG
Muscimol, BODIPY TMR-X Conjugate	Thermo Fisher Scientific	Cat#: M23400
Fast Blue	Polysciences	Cat#: 17740
Red Retrobeads™	Lumaflor	N/A
Green Retrobeads™	Lumaflor	N/A
Vybrant DiI Cell-Labeling Solution	Thermo Fisher Scientific	Cat#: V22885
NeuroTrace Blue Fluorescent Nissl Stain	Thermo Fisher Scientific	Cat#: N21479
Cholera Toxin Subunit B (Recombinant), Alexa Fluor 647	Thermo Fisher Scientific	Cat#: C34778
Deposited data		
Raw and analyzed data	This paper	N/A
Experimental models: organisms/strains		
Mouse: C57BL/6J	The Jackson Laboratory	RRID: IMSR_JAX:000664
Mouse: Rbp4-Cre: Tg(Rbp4-cre) KL100Gsat	The Jackson Laboratory	RRID:MMRRC_031125-UCD
Software and algorithms		
MATLAB	MathWorks (https://www.mathworks.com/)	RRID: SCR_001622
Python 3	Python (https://www.python.org/)	RRID: SCR_008394
AxonpCLAMP 10	Molecular Devices (https://www.moleculardevices.com/)	RRID:SCR_011323
Streampix 7.0	Norpix (https://www.norpix.com/products/streampix/streampix.php)	RRID:SCR_015773
NIS-Elements	Nikon (https://www.microscope.healthcare.nikon.com/products/software)	RRID:SCR_014329
Arduino IDE 1.6.5	Arduino (https://www.arduino.cc/en/software)	N/A

(*Continued on next page*)

Continued

REAGENT or RESOURCE	SOURCE	IDENTIFIER
SpikeGLX	Jun et al., 2017 (http://billkarsh.github.io/SpikeGLX/)	N/A
Mantis64	https://www.mantis64.com/	N/A
Kilosort3	https://github.com/MouseLand/Kilosort	N/A
Phy	Jun et al., 2017 (https://github.com/cortex-lab/phy)	N/A
FIJI	Schindelin et al., 2012 (https://github.com/fiji)	N/A
Deeplabcut	Adaptive Motor Control Lab (https://github.com/DeepLabCut/DeepLabCut)	N/A
NoRMCorre	Pnevmatikakis and Giovannucci, 2017 (https://github.com/flatironinstitute/NoRMCorre)	N/A
nmf_sklearn	Keemink et al., 2018 (https://github.com/rochefort-lab/fissa)	N/A
Onset detection algorithm	Zong et al., 2003	N/A
Data acquisition		
Data acquisition system	Molecular Devices	Digidata 1440A
Amplifier	Molecular Devices	Multiclamp 700B
Neuropixel probes	Janelia/IMEC	Phase 3B
Gradient-index (GRIN) lens	Grintech	Cat#: NEM-060-15-15-520-S-1.0p
Laser, Ti:Sapphire pulsed	Coherent	Chameleon Vision-S
Other		
Fiber optic cannula	ThorLabs	Cat#: CFMLC12L05
Optogenix tapered optic fiber cannula	Plexon	LambdaB (0,39, 200, 1.5, 225, 1.25)
Optic fiber patch cable		N/A
Laser, 473 nm	Civillaser	473nm 100 mW Blue DPSS Laser with Power Supply
Shutter	Uniblitz	Cat#: LS3S2T1
Arduino UNO	Arduino (https://www.arduino.cc/en/Guide/ArduinoUno/)	RRID:SCR_017284

RESOURCE AVAILABILITY

Lead contact

Further information and requests for resources and reagents should be directed to and will be fulfilled by the lead contact, Ian Duguid).

Materials availability

This study did not generate new unique reagents.

Data and code availability

Data analyzed and code generated in this study are available upon written request to corresponding author.

EXPERIMENTAL MODEL AND SUBJECT DETAILS

All experiments and procedures were approved by the University of Edinburgh local ethical review committee and performed under license from the UK Home Office in accordance with the Animal (Scientific Procedures) Act 1986. Male adult C57BL/6J wild-type (RRID: IMSR_JAX:000664) and Rbp4-Cre (RRID:MMRRC_031125-UCD) mice (5-14 weeks old, 20-30 g, one to six animals per cage) were maintained on a reversed 12:12 hour light:dark cycle (lights off at 7:00 am) and provided *ad libitum* access to food and water except during behavioral training and experimentation (see below).

METHOD DETAILS

General surgery

Mice undergoing surgery were induced under 4% and maintained under ~1.5% isoflurane anesthesia, with each animal receiving fluid replacement therapy (0.5 ml sterile Ringer's solution; to maintain fluid balance) and buprenorphine (0.5 mg/kg; for pain relief) at the beginning of each surgery. Additionally, buprenorphine (0.5 mg/kg) was administered in the form of an edible jelly cube ~24 hours after recovery from surgery. For surgeries involving removal of the periosteum, each animal received an injection of carprofen (5 mg/kg). A small lightweight headplate (0.75 g) was implanted on the surface of the skull using cyanoacrylate super glue and dental cement (Lang Dental, USA) and mice were left for 24-48 hours to recover. Craniotomies were performed in a stereotactic frame (Kopf, USA) using a hand-held dentist drill with 0.5 mm burr (craniotomy diameter: whole-cell patch-clamp recording ~⌀300 μm; viral / tracer / pharmacological compound injection ⌀500-1000 μm). Viral vectors and tracing compounds were delivered via pulled glass pipettes (5 μl, Drummond) using an automated injection system (Model Picospritzer iii, Intracell). At the end of each experiment, mice were anesthetized with euthatal (0.10–0.15 ml) and transcardially perfused with 30 mL of ice-cold 0.1 M phosphate-buffered saline (PBS) followed by 30 mL of 4% paraformaldehyde (PFA) in 0.1 M PBS solution. Brains were post-fixed in PFA overnight at 4°C then transferred to 10% sucrose solution for longer-term storage.

Behavioral training

Mice were handled extensively before being head restrained and habituated to the behavioral setup. To increase task engagement, mice were placed on a water control paradigm (1 ml/day) and weighed daily to ensure body weight remained above 85% of baseline. Mice were trained for one 30-minute session per day, during which they had to hold a moveable lever still during a random inter-trial-interval (ITI) of 4-6 s, before pushing the lever 4 mm during presentation of a 6 KHz auditory 'go cue' to receive a 5 μl water reward. The duration of the auditory cue (and thus response period) was reduced across training sessions in three stages: stage 1) 10 s, stage 2) 5 s, stage 3) 2 s, with mice advancing to the next stage after achieving > 80 rewards during a single session or > 50 rewards during two consecutive sessions. Mice were deemed "expert" after achieving > 80 rewards on two consecutive days of stage 3 training. Lever movements during the ITI would result in a lever reset and commencement of a subsequent ITI. After each 30-minute session, mice were removed from head restraint and given the remainder of their daily water allowance before being returned to their home cage.

In vivo pharmacology

To assess the behavioral effects of CFA, $MTh_{DN/IPN}$ or DN/IPN inactivation, a craniotomy was performed above the target area under general anesthesia. After 5/10 minutes of baseline task execution, the lever was locked and a small volume of the $GABA_A$ receptor agonist muscimol (dissolved in external solution containing 150 mM NaCl, 2.5 mM KCl, 10 mM HEPES, 1.5 mM $CaCl_2$ and 1 mM $MgCl_2$) or saline was injected into the target area (CFA: 200 nl of 2 mM muscimol at each of 5 sites centered on AP: 0.6, ML: 1.6, DV: −0.7 mm; $MTh_{DN/IPN}$: 200 nl of 1 mM muscimol, AP: −1.1, ML: 1.0, DV: −3.4 mm; ipsilateral DN: 100 nl of 1 mM muscimol, AP: −6.0, ML: −2.25, DV: −2.4 mm; ipsilateral IPN: 50nl of 1 mM muscimol, AP: −6.0, ML: −1.75, DV: −2.4 mm) at a rate of 5-20 nl/s. To confirm the anatomical location of drug injection, 1% w/v of retrobeads (Lumaflor Inc.) was included in the muscimol/saline solution. Mice were randomly assigned to drug or control groups, and experiments performed blinded. After each experiment, mice were transcardially perfused and coronal sections (60 μm) of CFA, $MTh_{DN/IPN}$ or DN/IPN were cut with a vibratome (Leica VT1000S), mounted with Vectashield mounting medium (H-1000, Vector Laboratories), imaged using a fluorescence microscope (Leica DMR, 5x objective) and manually referenced to the Paxinos and Franklin Mouse Brain Atlas (Paxinos and Franklin, 2008). Behavioral metrics were analyzed in 5-minute epochs using custom-written MATLAB (MathWorks) scripts, a two-sample t test was used to compare experimental cohorts during the first post injection epoch, and a one-way ANOVA was used to compare data between manipulation experiments. Behavioral video data for all pharmacology experiments was captured using a high speed camera (Genie HM640, Dalsa), and paw position accuracy was calculated as the proportion of trials in which mice were holding the moveable lever with their contralateral forepaw at the onset of the auditory cue.

GRIN lens imaging

To perform population calcium imaging in motor thalamus, 200 nl of AAV1-Syn-GCaMP6s was injected into contralateral $MTh_{DN/IPN}$ (AP: − 1.1, ML: 1.0, DV: − 3.4 mm) and mice were implanted with a lightweight headplate. 7-10 days after virus injection, a gradient-index (GRIN) lens (Grintech NEM-060-15-15-520-S-1.0p; 600 μm diameter, 4.83 mm length, 0.5 numerical aperture) was implanted as described previously (Xu et al., 2016). In brief, a sterile needle (1.1 mm OD) surrounding the GRIN lens was lowered to a depth of 3.2 mm and subsequently retracted leaving the lens at the desired depth. The lens was then secured in place with UV curing glue (Norland Products, USA) and dental cement. Fields of view were checked for clarity and GCaMP6s expression after implantation. After 4-8 weeks mice began water restriction and behavioral training. Two-photon calcium imaging was performed in expert mice during lever task execution with a 318 × 318 μm field of view (600 × 600 pixels) at 40 Hz frame rate, using a Ti:Sapphire pulsed laser (Chameleon Vision-S, Coherent, CA, USA; < 70 fs pulse width, 80 MHz repetition rate) tuned to 920 nm wavelength with a 40x objec-

tive lens. For confirmation of GRIN lens location and viral expression, mice were perfused, sagittal sections (100 μm) of $MTh_{DN/IPN}$ were cut with a vibratome, counterstained with Nissl blue, and imaged using a slide scanner (Axioscan, Zeiss). GRIN lens location was referenced to the Paxinos and Franklin Mouse Brain atlas.

Raw imaging videos were motion corrected using NoRMCorre (Pnevmatikakis and Giovannucci, 2017). In brief, NoRMCorre performs non-rigid motion correction by splitting each FOV into overlapping patches, estimating the xy translation for each patch, and upsampling the patches to create a smooth motion field, correcting for non-uniform motion artifacts caused by raster scanning or brain movement. Regions of interest (ROIs, polygonal areas) were drawn manually using Fiji (Schindelin et al., 2012). Signals were extracted and neuropil decontaminated using nmf_sklearn (Keemink et al., 2018). Normalized signal was calculated as $\Delta F/F_0$, where F_0 was calculated as the bottom 5th percentile of the 1Hz low pass filtered raw signal, and $\Delta F = (F-F_0)$. Normalized signals were then aligned to the behavioral data and analyzed using custom-written MATLAB scripts.

To detect activity changes of cells, a Friedman test was used to compare 250 ms time binned Ca^{2+} signals from 500 ms before movement to 1500 ms after movement with a significance threshold of $p < 0.01$. A Tukey-Kramer post hoc test was used to identify significantly different bins, and the direction of each response was defined based on the difference between baseline and the mean value of the Ca^{2+} signal in the earliest two significantly different bins. The median onset time of each cell was calculated by employing a previously published onset detection algorithm using a slope sum function (SSF; Zong et al., 2003) with the decision rule and window of the SSF adapted to the calcium imaging data (threshold 10% of peak, SSF window 375 ms, smoothed with a Savitzky Golay filter across 27 frames with order 2) and reported as the median of 10,000 bootstrapped samples to reduce the influence of noisy individual trials. Neurons whose bootstrapped samples had inter-quartile ranges exceeding 3 standard deviations of the median inter-quartile range were considered to have undetectable onset times and categorized as non-responsive. Prior to extracting $\Delta F/F_0$ onsets, we verified this algorithm with simulated data thereby accounting for any bias in the onset detection potentially introduced by filtering and/or the decision rule. To simulate the rising phase of the movement related calcium events in our data we used linear ramps with defined onset times and a rise time of 0.5 s mimicking GCaMP6s kinetics. We then calibrated the onset detection algorithm on the simulated data (100 simulated cells with 30 simulated trials per cell and artificially added noise in each trial matching the noise level in the imaging data) and updated it by a small FOV-specific correction factor.

Onset times were used to classify $MTh_{DN/IPN}$ neurons as preceding movement initiation (early) from those occurring after movement initiation (late). To investigate the relationship between $\Delta F/F_0$ trajectories and reaction time, reaction times were split into thirds (short [0 – 350 ms], medium [350 - 900 ms] and long [> 900 ms]) and only FOVs with a sufficient number of trials per reaction time category were included in further analysis. To compare the onset times across short, medium and long reaction time trials, the onset time of each neuron was calculated using only these subsets of trials. Movement-aligned time binned Ca^{2+} signals were presented smoothed with the loess method using a 40-frame sliding window and baseline corrected to the mean of the 500 ms pre-cue period. A kernel density estimate was calculated for each onset across all trials to calculate a mean. The area under the mean population kernel density estimate was calculated using numerical trapezoidal integration.

To investigate whether GRIN lens implantation surgery affected lever task execution, a two-sample Kolmogorov-Smirnov goodness-of-fit test was used to compare reaction time, push duration and task success (the ratio of the number of rewarded trials to total number of cued trials) of the GRIN lens-implanted cohort and a control group.

Whole-cell patch-clamp electrophysiology

Whole-cell patch-clamp recordings targeted to layer 5B, 550–1000 μm from the pial surface, were obtained from awake head restrained mice after performing a craniotomy and durotomy centered above CFA. Signals were acquired at 20 kHz using a Multiclamp 700B amplifier (Molecular Devices) and filtered at 10 kHz using PClamp 10 software in conjunction with a DigiData 1440 DAC interface (Molecular Devices). No bias current was injected during recordings and the membrane potential was not corrected for junction potential. Resting membrane potentials were recorded immediately after attaining the whole-cell configuration (break-in). Series resistances (Rs) ranged from 23.6 to 45.5 MΩ. Patch pipettes (5.5–7.5 MΩ) were filled with internal solution (285–295 mOsm) containing: 135 mM K-gluconate, 4 mM KCl, 10 mM HEPES, 10 mM sodium phosphocreatine, 2 mM MgATP, 2 mM Na_2ATP, 0.5 mM Na_2GTP, and 2 mg/ml biocytin (pH adjusted to 7.2 with KOH). External bath solution contained: 150 mM NaCl, 2.5 mM KCl, 10 mM HEPES, 1 mM $CaCl_2$, and 1 mM $MgCl_2$ (adjusted to pH 7.3 with NaOH). All electrophysiology recordings were analyzed using custom-written scripts in MATLAB. Individual action potentials (APs) were detected with a wavelet-based algorithm (Nenadic and Burdick, 2005) and AP threshold was defined as the membrane potential (V_m) at maximal d^2V/dt^2 up to 3 ms before AP peak and manually verified. For subthreshold V_m analysis APs were clipped by removing data points between −1 and +9 ms peri-AP threshold. Average AP firing frequencies were calculated by convolving spike times with a 50 ms Gaussian kernel. Significant changes in subthreshold V_m and AP firing frequency were defined by comparing bootstrapped 95% confidence intervals of mean movement-aligned V_m and AP frequency trajectories to zero (baseline epoch = 200 ms pre-cue; movement epoch = −100 to +100 ms peri-movement). Mean ΔV_m trajectories were calculated by subtracting the mean V_m during baseline (1 s epoch prior to cue) from the mean V_m during the peri-movement epoch (−250 to +250 ms when aligned to movement onset). All mean ΔV_m trajectories were decimated and median filtered with a 50 ms sliding window. Population mean ΔV_m trajectories were normalized to the largest absolute mean ΔV_m value in a 1.5 s peri-movement window. Peri-movement ΔV_m onsets were detected as the 10% rise-time of V_m trajectories when aligned to movement.

To inactivate motor thalamus during patch clamp recordings we performed a second craniotomy above $MTh_{DN/IPN}$ and a pipette containing 1 mM muscimol (dissolved in external solution) and 1% w/v red retrobeads was targeted to $MTh_{DN/IPN}$ (AP: −1.1, ML: 1.0, DV: −3.4 mm). Once the whole-cell recording configuration had been obtained, 5-10 minutes of baseline behavior and electrophysiological data were acquired before 200 nL of muscimol was injected at a rate of 5-10 nl/s. Mice were perfused, and data analyzed from animals in which retrobeads were found within $MTh_{DN/IPN}$. To compare subthreshold V_m dynamics during pre- and post- injection epochs, cue-aligned periods of V_m were baseline subtracted and the area under the $|\Delta V_m|$ trajectory from cue onset to median reward delivery was calculated via trapezoidal numerical integration with a 50 ms sample rate. To compare firing rate dynamics, the proportional difference between peri-median reaction time versus baseline Gaussian kernel smoothed firing rate was calculated in both epochs using bin sizes described previously.

Immunohistochemistry

To morphologically identify neurons after whole-cell patch-clamp recording, mice were transcardially perfused and coronal sections (60 μm) of CFA were cut with a vibratome. To recover neurons, sections were incubated in streptavidin AlexaFluor-488 (1:1000, Molecular Probes) in 0.1 M PBS containing 0.5%Triton X-100, mounted, imaged using a confocal microscope (Zeiss LSM800, 20x objective) and referenced to the Paxinos and Franklin Mouse Brain Atlas. To identify projection targets of individually recorded neurons (Schiemann et al., 2015), sections were further processed by heat-mediated antigen retrieval in 10 mM sodium citrate buffer (pH 6.0) for 3 hours at 80°C. Sections were incubated in blocking solution (0.01 M PBS, 10% normal goat serum (NGS), 0.5% Triton X-100) at 22°C for 2 hours and incubated overnight at 22°C in a primary antibody mixture containing mouse monoclonal anti-Satb2 (1:200, Cat. No. ab51502, Abcam) and rat monoclonal anti-Ctip2 (1:1000, Cat. No. ab18465, Abcam) dissolved in carrier solution (0.01 M PBS, 1% NGS, 0.5% Triton X-100). Slices were then incubated overnight at 22°C in a secondary antibody mixture containing AlexaFluor-568 goat anti-mouse (1:750, Molecular Probes) and AlexaFluor-647 goat anti-rat (1:750, Molecular Probes) dissolved in carrier solution (0.01 M PBS, 1% NGS, 0.5% Triton X-100), mounted and imaged using a confocal microscope (Zeiss LSM800, 20x objective).

To assess the proportion of CFA-projecting $MTh_{DN/IPN}$ neurons that receive glutamatergic synaptic input from dentate/interpositus nuclei, selected motor thalamic coronal sections (60 μm) were rinsed thee times with 0.1 M PBS for 10 minutes, incubated for 2 hours at room temperature in blocking solution (containing 10% normal horse serum (NHS) and 0.5% triton diluted in 0.1 M PBS), rinsed briefly in 0.1 M PBS and incubated overnight with a primary antibody for vesicular glutamate transporter type 2 (VGluT2) (anti-guinea pig, Millipore Bioscience; diluted 1:2000 in 0.1 M PBS containing 1% NHS and 0.5% Triton-X). Slices were then rinsed four times in 0.1 M PBS for 10 minutes before being incubated for at least 2 hours with secondary antibody anti-Guinea Pig Cy5 (diluted 1:200 in in 0.1 M PBS containing 1% NHS and 0.5% Triton-X). Sections were rinsed four times in 0.1 M PBS for 10 minutes, mounted with Vectashield mounting medium and imaged using a confocal microscope (Leica LS8; 63x objective). Fast Blue labeled cells with overlapping Venus-labeled + VGluT2 +ve axons (with 1 μm) were manually counted.

Motor thalamic activation

For optogenetic activation of $MTh_{DN/IPN}$ neurons or their axon terminals in CFA, 250 nl of AAV1-CAG-ChR2-Venus ($2.3x10^{12}$ GC/ml, Addgene 20071; control virus: AAV2-CAG-mCherry ($5.2x10^{11}$ GC/ml)) was injected into contralateral $MTh_{DN/IPN}$ (AP: −1.1, ML: 1.0, DV: −3.4 mm). For direct $MTh_{DN/IPN}$ stimulation, an optic fiber (200 μm diameter, 0.39 NA; Thorlabs) was implanted ~300 μm dorsal to the viral injection site (sealed with RelyX Unicem2 Automix cement, 3M) and trains of pulsed 473 nm light (5-8 mW, 16.6 Hz pulse frequency, 33.3% duty cycle) were delivered using a solid-state laser (DPSS, Civillaser, China) and shutter (LS3S2T1, Uniblitz) controlled by an Arduino control system, coupled to the implanted optic fiber by means of an optic patch cable (Thorlabs, FT200UMT). For direct simulation of $MTh_{DN/IPN}$ axon terminals, a tapered optic fiber (Optogenix, Italy) was implanted to a depth of 1 mm at the center of CFA (AP: 0.6, ML: 1.6, DV: −1.0 mm) and 12 mW, 473 nm light was delivered as above. Prior to optogenetic stimulation experiments, mice were trained to expert level performance and habituated to light emanating from an uncoupled optic patch cable and the sound of shutter activation. During habituation and experimental sessions, mice were exposed to 3 different trial types: (1) cue and shutter; (2) laser and shutter; and (3) shutter only. Trials were presented with the following pattern: 1, 1, 3, 1, 1, 2,... repeating for 30 minutes. $MTh_{DN/IPN}$ axon terminal stimulation in CFA was performed on the following day, while whole-cell patch-clamp recordings from CFA were performed in combination with direct $MTh_{DN/IPN}$ stimulation in a separate cohort of mice. To investigate the effects of behavioral context, mice which had previously undergone $MTh_{DN/IPN}$ stimulation were head restrained above a 3D printed baseplate (Wanhao i3 Duplicator) without support/movable levers or reward spout (ABC), or within the same lever pressing apparatus with the reward and moveable levers replaced by a 3D printed platform (ABC2), and habituated for 2 sessions, interleaved with normal training to ensure that the cued motor behavior was not extinguished. To compare effects of $MTh_{DN/IPN}$ stimulation in the learned and altered behavioral contexts, mice first underwent a 15-minute optogenetic stimulation protocol in the learned context, before being exposed to an identical 15-minute optogenetic stimulation protocol in one of the two altered behavioral contexts (ABC or ABC2). To investigate the effects of $MTh_{DN/IPN}$ stimulation during freely moving behavior, mice were placed in an open field arena (dimensions 30 × 20 cm) with a camera phone (Samsung Galaxy S5) recording the full arena from beneath. A patch cable was coupled to the $MTh_{DN/IPN}$ optic fiber, and mice underwent a 15-minute optogenetic stimulation protocol. Peri-trial movements

were classified from the videos as push-like (a single movement of the left forepaw in a defined forward direction), discrete (a single movement of the left forepaw in any other direction), locomotion (> 2 consecutive steps/strides made by the left forelimb) and grooming, by two researchers and cross validated.

For histological confirmation of the injection site and optic fiber placement, mice were transcardially perfused, decapitated and the whole head (including headplate and optic fiber) was post-fixed in 4% PFA for 2 days to improve preservation of the optic fiber tract. Coronal sections (60 μm) of CFA and $MTh_{DN/IPN}$ were cut with a vibratome, mounted with Vectashield, and imaged using a slidescanner (Axioscan, Zeiss). The center of the optic fiber (COF) was defined as the most ventral extent of the optic fiber tract across all slices from each brain as measured from the pial surface. Where tracts of equal depth were present, the coronal section containing the largest diameter tract tip was identified as the COF. The expression of ChR2-Venus in $MTh_{DN/IPN}$ was coarsely defined by first referencing three coronal slices (120 μm spacing) centered on the COF to the Paxinos and Franklin Mouse Brain Atlas before manually evaluating the proportion of each of the principle motor thalamic nuclei (AM, anteromedial; VL, ventrolateral; VPM, ventral posteromedial nucleus; VPL, ventral posterolateral; VM, ventromedial) containing fluorescence, and categorizing three levels based on expression covering 0%–5%, 5%–50% and 50%–100% of each nucleus. Data were not included from mice in which the COF was misaligned to virus expression. To investigate whether photostimulation of $MTh_{DN/IPN}$ evokes tongue movements, a ROI was drawn in front of the mouth and tongue movements were detected using a motion index threshold (see below).

The proportion of full and partial push-like movements in cue- and laser- trials were calculated by correcting for the behavioral "error" rate, i.e., subtracting the proportion of pushes observed in shutter only trials (trial type 3) to obtain a lower bound. ΔV_m trajectories for both cue-evoked and photoactivation-evoked movement trials were calculated as described previously, and trial-by-trial ΔV_m changes were based on comparing the 200ms pre-cue or pre-photoactivation epoch with the 200 ms peri-movement epoch within each trial.

Cerebellar-motor thalamic pathway tracing and activation

For tracing and activation of the dentate/interpositus-motor thalamus pathway, AAV1-CAG-ChR2-Venus ($2.3x10^{12}$ GC/ml, Addgene 20071) was injected unilaterally into ipsilateral dentate (AP: −6.0, ML: −2.25, DV: −2.6 & −2.2 mm) and interpositus (AP: −6.0, ML: −1.75, DV: −2.4 mm) cerebellar nuclei, with 75 nl injected at each depth within each nucleus. For activation of dentate/interpositus axons in motor thalamus, an optic fiber (200 μm diameter, 0.39 NA; Thorlabs) was implanted into contralateral $MTh_{DN/IPN}$ (AP: −1.1, ML: 1.0, DV: −3.2 mm) and trains of pulsed 473 nm light (8 mW, 16.6 Hz pulse frequency, 33.3% duty cycle) were delivered as previously described. Mice were trained to expert level performance, habituated to light emanating from an uncoupled optic fiber and the sound of shutter activation and exposed to the same alternating trial structure as for $MTh_{DN/IPN}$ activation experiments described previously. For histological confirmation of the injection site, mice were transcardially perfused and coronal sections (60 μm) of $MTh_{DN/IPN}$ and DN/IPN were cut with a vibratome, mounted, and imaged using a slidescanner (Axioscan, Zeiss). Optic fiber location within $MTh_{DN/IPN}$ was ascertained as described previously. The expression of ChR2-Venus in DN/IPN was coarsely defined by first referencing the three coronal slices centered on the DN and IPN to the Paxinos and Franklin Mouse Brain Atlas before manually evaluating the proportion of each of the cerebellar (DN, dentate; IPN, interpositus; FN, fastigial) and vestibular nuclei containing fluorescence, and categorizing three levels based on expression covering 0%–5%, 5%–50% and 50%–100% of each nucleus. Data were not included from mice that had insufficient ChR2-Venus expression in DN and IPN, or in which the COF was not aligned to $MTh_{DN/IPN}$.

To map DN/IPN projections to CFA-projecting neurons in $MTh_{DN/IPN}$, some mice underwent surgery to perform an additional craniotomy above contralateral CFA (AP: 0.6, ML: 1.6 mm), where Fast Blue retrograde tracer (Polysciences; 0.2% Fast Blue in 1 M PB with 0.2% DMSO) was injected at four points equidistant from the center of the CFA craniotomy, with 100 nl injected at two depths, −800 μm and −400 μm below the pial surface. After recovery, mice were returned to the home cage for a further 5 days, before being transcardially perfused. Coronal sections (60 μm) of CFA, $MTh_{DN/IPN}$ and DN/IPN were cut with a vibratome, mounted using Vectashield, and imaged using a confocal microscope (Leica SP8; 20x objective). Raw data images of coronal sections of the motor thalamus were manually referenced to the Paxinos and Franklin Mouse Brain Atlas, aligned and cropped to the same exact motor thalamic subregion. These cropped images were combined into a stack using Fiji and an average intensity projection of each channel (Venus & Fast Blue) was calculated. The resultant average image for each channel were considered as a matrix of gray-scale pixel values in MATLAB, and to calculate a matrix of proportional overlap of the two channels, the two matrices were square-rooted and then multiplied together. A 2-D Gaussian smoothing kernel with SD = 5 pixels was then used to smooth the resultant image which was then remapped with the Jet colormap. For the density plots of individual channels, the average projection matrices were similarly smoothed and remapped.

To assess the density of CFA-projecting neurons in ventrolateral motor thalamus, 200 nl of CTB-Alexa647 (ThermoFisher) was injected into contralateral CFA (AP: 0.6, ML: 1.6, DV: −0.7 mm). After recovery, mice were returned to the home cage for ~7 days before being perfused. Coronal sections (100 μm) of $MTh_{DN/IPN}$ were collected, counterstained with NeuroTrace Nissl blue (ThermoFisher), mounted using Vectashield mounting medium and imaged with a confocal microscope (Leica LSM800). Cells were counted in a representative 300 × 300 μm region and counts were independently verified.

To quantify vestibular nuclei projections to motor thalamus, we performed a craniotomy above contralateral $MTh_{DN/IPN}$ (AP: −1.1, ML: 1.0 mm) and injected 100 nl of Fast Blue at a depth of 3.4 mm below the pial surface. After recovery, mice were returned to the home cage for 5 days, before being perfused, and brains processed and imaged as described above.

Monosynaptic retrograde rabies tracing

For monosynaptic retrograde rabies tracing, conditional expression of TVA receptor was achieved by injecting 60 nl of AAV2/1-CAG-FLEX-mTagBFP2-2A-TVA ($9.0x10^{12}$ GC/ml) into contralateral $M1_{FL}$ (AP: 0.6, ML: 1.6, DV: −0.7 mm) of three Rbp4-Cre mice. Pseudotyped SADΔG-mCherry(EnvA) rabies virus (produced as previously described (Wickersham et al., 2007, 2010) was injected into CFA three weeks after the initial injections. Mice were perfused seven days post-rabies virus injection. Coronal sections (60 μm) were cut, mounted and imaged using a Nanozoomer Slide Scanner (Hamamatsu, 20x objective). Raw data images were manually referenced to the Paxinos and Franklin Mouse Brain Atlas and the distribution of fluorescence was manually outlined and independently verified.

Extracellular recording and spike sorting

To compare neural activity during cue-evoked and photoactivated movements, extracellular unit recordings in CFA were performed using acutely implanted silicone probes (Neuropixels Phase 3B probes, IMEC). Data were acquired from the 384 channels closest to the probe tip. Data were acquired with SpikeGLX software at 30 KHz with an amplifier gain of 500 for each channel and high-pass filtered with a cutoff frequency of 300 Hz. Spike sorting was performed using Kilosort3 to automatically cluster units from raw data (Pachitariu et al., 2016). The resulting spike clusters were manually curated using Phy (https://github.com/cortex-lab/phy), and any unit with sufficient refractory period violations, inconsistent waveform amplitude across the duration of the recording, or clipped amplitude distribution was excluded from analyses. Probe location was confirmed via DiI (Thermofisher) reconstruction of the recording track, and units from 500-1200 μm below the pial surface were included in our analyses. To detect changes in activity, firing rates were calculated by convolving spike times with a 200 ms Gaussian kernel and mean changes in firing rate were calculated by subtracting the firing rate during a baseline period (200 ms period before cue or laser presentation) from a response period (−100 to +100 ms peri-movement onset). Significant changes were identified by comparing bootstrapped 95% confidence intervals of these mean changes in firing rates to 0. Firing rate trajectories are presented as spike times convolved with a 50 ms Gaussian kernel. Spike time rasters are presented showing a random sample of cue trials matching the number of photostimulation trials. Spike widths were calculated as the duration from trough to peak of the spike waveform.

Quantifying muscimol diffusion

To measure muscimol diffusion, a small volume of muscimol-BODIPY TMR-X Conjugate (ThermoFisher Scientific; dissolved in 0.1 PBS w/1% dimethyl sulfoxide) was injected into $MTh_{DN/IPN}$ (200 nl of 1 mM), CFA (100 nl of 2 mM at −700 μm and −400 μm below the pial surface at 5 sites centered on CFA) or DN/IPN (100 nl and 50 nl of 1mM, respectively). To mark the center of injection, pipettes were backfilled with a small volume (~20 nl) of green (505 nm) retrobeads (Lumafluor Inc.) prior to filling with muscimol-BODIPY. Following injection, animals were transcardially perfused and brains snap-frozen on dry ice within 10 minutes of completion of muscimol injection. Brains were stored on dry ice, coronal sections (60 μm) collected with a cryostat (Leica) at −20°C and imaged with a light microscope (Leica DMR, 5x objective). We assumed maximum fluorescence ≈ maximum injected concentration and that grayscale pixel intensity was proportional to muscimol-BODIPY concentration. Therefore, pixel values were thresholded at the equivalent pixel value of an EC_{20} concentration of muscmiol and fluorescence outlines were drawn to generate a 'spread profile'. Green retrobeads were used to mark the center of each injection, and images were aligned to the injection center of gravity. From the aligned profiles, a modal spread profile (i.e., pixels with positive grayscale values across all mice) was generated and aligned to the Paxinos and Franklin Mouse Brain Atlas.

To assess the functional time course of muscimol inactivation, a silicone probe was vertically implanted into CFA (AP: 0.6, ML: 1.2-1.6, DV: −2.0 mm) of naive head restrained mice at rest. 15 minutes of baseline activity was recorded, after which 200 nl of 1 mM muscimol (containg 1% w/v red retrobeads) was injected at a point 500-700 μm horizontal from the shank of the probe (AP: 0.6, ML: 1.8-2.4, DV: −1.0 mm). The recording was continued for a further 30 minutes before perfusing and collecting tissue as described previously. Probe location was confirmed by DiI labeling, neural activity was spike sorted and analyzed as previously described, individual units were localized and the change in spike rate over time was correlated with the distance of each individual unit from the center of muscimol injection.

Forelimb kinematic tracking

Behavior was recorded using a high-speed camera (Pharmacological experiments: Genie HM640, Dalsa; optogenetic experiments: Mako U U-029, Allied Vision) and acquired with Streampix 7 (Norpix), synced using a TTL output from the DigiData 1440 DAC interface. Forepaw and wrist positions during pharmacological inactivation experiments were calculated by tracking forepaw markers using a custom written tracking script in Blender (2.79b, Blender Foundation). Directional tracking of forelimb movement in the learned/altered behavioral contexts was performed using Deep Lab Cut, a markerless video tracking toolbox (Mathis et al., 2018). Initial paw vector trajectories were plotted for the 50 ms post movement onset epoch in the learned behavioral context (LBC), and for the altered behavioral contexts (ABC & ABC2) we plotted trajectories in the epoch 50 ms after the LBC median reaction time. Push-like movements were defined as trials with an initial paw trajectory vector between 170° and 210°, and manually verified. To measure gross forelimb movement, we defined a region-of-interest (ROI) covering the contralateral (left) forelimb and calculated a motion index (MI) for each successive frame f as $MI_f = \sum_i^N {}_1(c_{f+1,i} - c_{f,i})^2$, where $c_{f,i}$ is the grayscale level of the pixel of the ROI, pixels per ROI (Schiemann et al., 2015). Movement trials were defined by calculating the MI > θ within 500 ms of cue/photostimulation

onset, with the threshold θ defined as three standard deviations above the mean MI for detecting forelimb movements, and 10 standard deviations above the mean MI for detecting licking.

QUANTIFICATION AND STATISTICAL ANALYSIS

Data analysis was performed using custom-written scripts in MATLAB or Python3 and code will be made available on request. All statistical details of experiments can be found in the figure legends, including description of the specific test used and sample sizes. Data are reported as mean ± 95% bootstrapped confidence interval, 10,000 bootstrap samples, unless otherwise indicated. Where multiple measurements were made from a single animal, suitable weights (proportional to the contribution from each animal) were used to evaluate summary population statistics and to obtain unbiased bootstrap samples. Statistical comparisons using the significance tests stated in the main text were made in MATLAB, and statistical significance was considered when $p < 0.05$ unless otherwise stated. Data were tested for normality with the Shapiro–Wilk test, and parametric/non-parametric tests were used as appropriate and as detailed in the text. Data inclusion/exclusion criteria have been listed throughout the method details section where relevant.

Neuron, Volume *109*

Supplemental information

A cerebellar-thalamocortical pathway drives behavioral context-dependent movement initiation

Joshua Dacre, Matt Colligan, Thomas Clarke, Julian J. Ammer, Julia Schiemann, Victor Chamosa-Pino, Federico Claudi, J. Alex Harston, Constantinos Eleftheriou, Janelle M.P. Pakan, Cheng-Chiu Huang, Adam W. Hantman, Nathalie L. Rochefort, and Ian Duguid

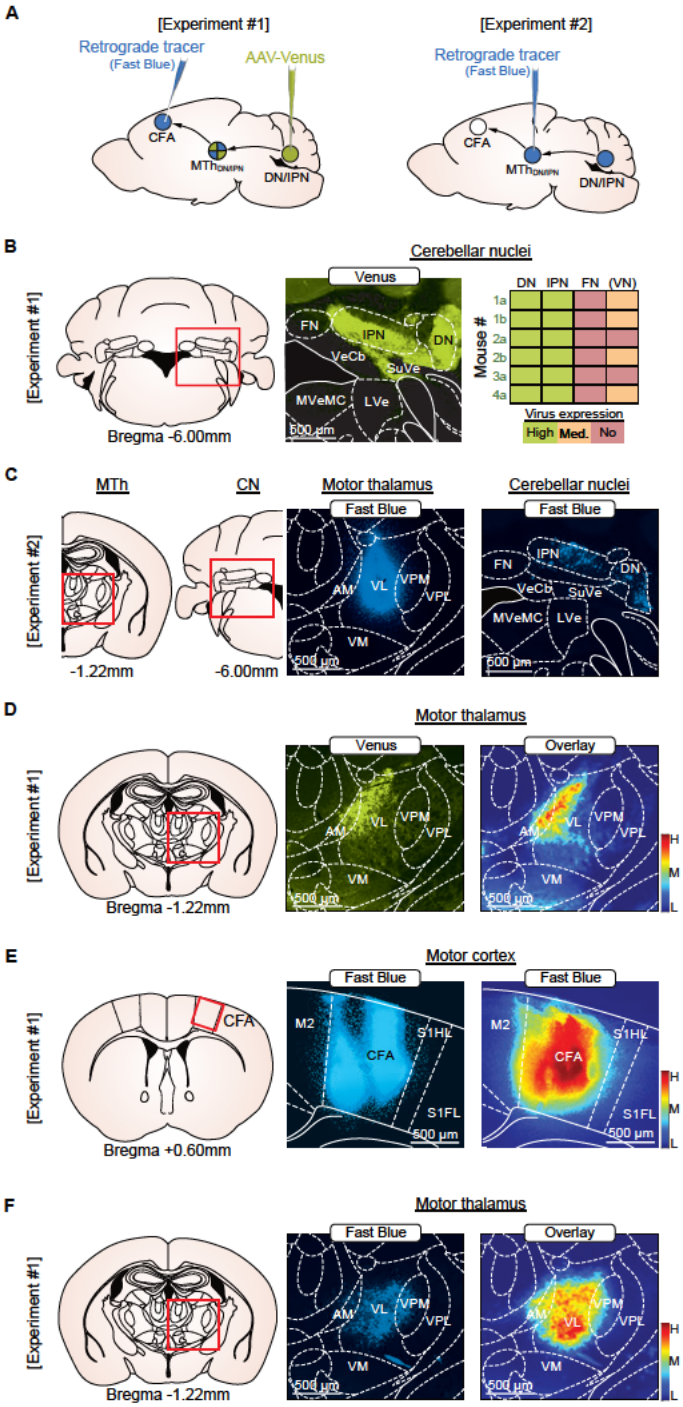

Figure S1. Mapping the DN/IPN thalamocortical pathway, related to Figure 1.
(A) *Experiment #1*, retrograde tracing of CFA-projecting neurons (Fast Blue) and anterograde tracing of DN/IPN axons (AAV-Venus) in motor thalamus. *Experiment #2*, retrograde tracing of VAL-projecting neurons in cerebellar nuclei (Fast Blue). (B) *Left & middle*, Virus labelling of cerebellar nuclei. *Right*, quantification of Venus expression in cerebellar and vestibular nuclei (red/no = <5 %, orange/medium = 5-50 % & green/high = 50-100 % expression within each nuclei) (bilateral injection, n = 6 slices from N = 4 mice). DN, dentate nucleus; IPN, interpositus nucleus; FN, fastigial nucleus, VN, vestibular nuclei including: VeCb, vestibulocerebellar nuclei; SuVe, superior vestibular nucleus; MVeMC, medial vestibular nucleus magnocellar part; LVe, lateral vestibular nucleus. (C) *Left & middle*, Fast Blue injection site in motor thalamus centered on VL. *Right*, retrograde labelling of cerebellar and vestibular nuclei neurons. AM, anteromedial; VL, ventrolateral; VPM, ventral posteromedial; VPL, ventral posterolateral; VM, ventromedial thalamic nuclei. (D) *Left & Middle*, Anterograde labelling of DN/IPN axons in motor thalamus. *Right*, average density of DN/IPN axons across motor thalamic nuclei (N = 6 slices from 4 mice). Scale bar, H - high, M - medium, L - low-level expression. (E) *Left & centre*, Fast Blue injection site in CFA. Right, average density of Fast Blue in CFA (N = 6 slices from 4 mice). Scale bar, H - high, M - medium, L - low-level fluorescence. (F) *Left & Middle*, Retrograde labelling of CFA-projecting thalamic neurons. *Right*, average density of CFA-projecting neurons across thalamic nuclei (N = 6 slices from 4 mice). Scale bar, H - high, M - medium, L - low-level expression.

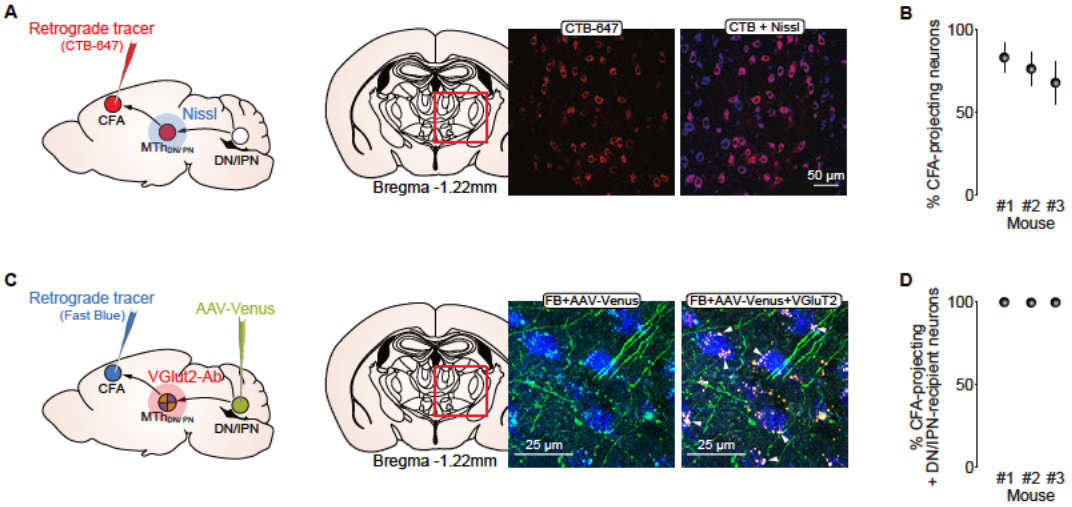

Figure S2. Quantification of CFA-projecting & DN/IPN-recipient neurons in ventral motor thalamus, related to Figure 1.
(A) *Left*, Nissl stain and retrograde labelling of CFA-projecting neurons in ventrolateral thalamus (CTB-647). *Right*, retrograde labelling of CFA-projecting neurons in ventrolateral thalamus (CTB-647) with all neurons labelled with Nissl. (B) Proportion of CFA-projecting motor thalamic neurons in VL thalamus (N = 3 mice, 4-6 slices per mouse, mean ± bootstrapped 95% CI). Filled circles represent population means ± 95% CI. (C) *Left & right*, retrograde tracing of CFA-projecting neurons (Fast Blue) and anterograde tracing of DN/IPN axon terminals (AAV-Venus + VGluT2) in ventrolateral motor thalamus. (D) Proportion of CFA-projecting motor thalamic neurons in VL thalamus that receive glutamatergic synaptic input from dentate/interpositus nuclei (N = 3 mice, 2-4 slices per mouse, mean ± bootstrapped 95% CI). Filled circles represent population means ± 95% CI.

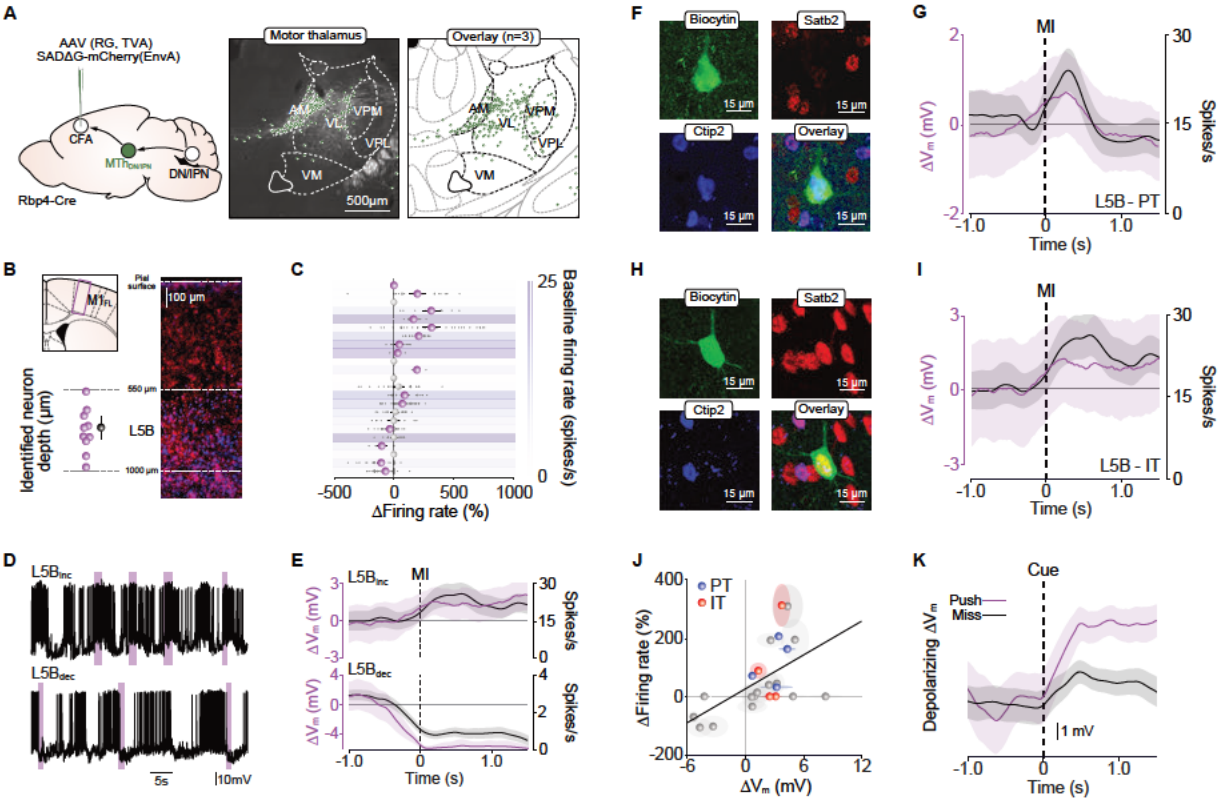

Figure S3. Membrane potential dynamics and projection class identity of CFA L5B neurons, related to Figure 3.
(A) *Left*, Monosynaptic rabies tracing strategy: injection of AAV2/1-CAG-FLEX-mTagBFP2-2A-TVA & SADΔG-mCherry(EnvA) into caudal forelimb motor area (CFA) of an Rbp4-Cre mouse. *Centre & Right*, CFA-projecting neurons in ventral motor thalamus. AM, anteromedial; VL, ventrolateral; VPM, ventral posteromedial; VPL, ventral posterolateral; VM, ventromedial thalamic nuclei. (B) *Top left*: Schematic coronal brain slice showing location of CFA. Purple rectangle depicts the expanded view shown on the right. *Right:* Distribution of PT-type (blue, Ctip2 staining) and IT-type (red, Satb2 staining) projection neurons in layer 5B of CFA. *Bottom left:* depth of recovered layer 5B neurons as measured perpendicularly from the pial surface (n = 11/23 neurons identified, black symbol represents mean ± 95% CI). (C) Average firing rate change ± 95% CI as a function of baseline firing rate. Gray dots represent individual trials, purple symbols represent significant changes in firing rate, gray symbols represent non-significant changes, defined by comparing 95% bootstrapped confidence intervals. (D) Voltage traces from a (*top*) depolarizing and (*bottom*) hyperpolarizing layer 5B neuron across multiple trials. Filled purple bars depict push trials. (E) Average subthreshold ΔV_m (purple) and firing rate (FR, black) trajectories for the layer 5B neurons shown in *(B)* aligned to movement initiation (MI). Thick lines represent the mean ± 95% CI. (F) Biocytin staining (green) and post-hoc immunohistochemical staining for Satb2 (red) and Ctip2 (blue) confirmed the PT-type projection class identity of an individually recorded layer 5B pyramidal neuron. (G) Mean subthreshold V_m and firing rate of the layer 5B PT-type projection neuron depicted in *(F)*. (H) Biocytin staining (green) and post-hoc immunohistochemical staining for Satb2 (red) and Ctip2 (blue) confirmed the IT-type projection class identity of an individually recorded L5B pyramidal neuron. (I) Mean subthreshold V_m and firing rate of the L5B IT-type projection neuron depicted in *(H)*. (J) Correlation between movement-related subthreshold ΔV_m and firing rate changes. Blue/red symbols represent means ± 95% CI from individual PT-/IT-type neurons respectively, black line is a linear fit to the data. Gray symbols represent means ± 95% CI from neurons where projection class identity was not determined (N = 23 neurons from 23 mice). (K) Example cue aligned push-trial mean ΔVm (purple) vs miss-trial mean ΔVm (black) trajectories from a representative layer 5B neuron in CFA.

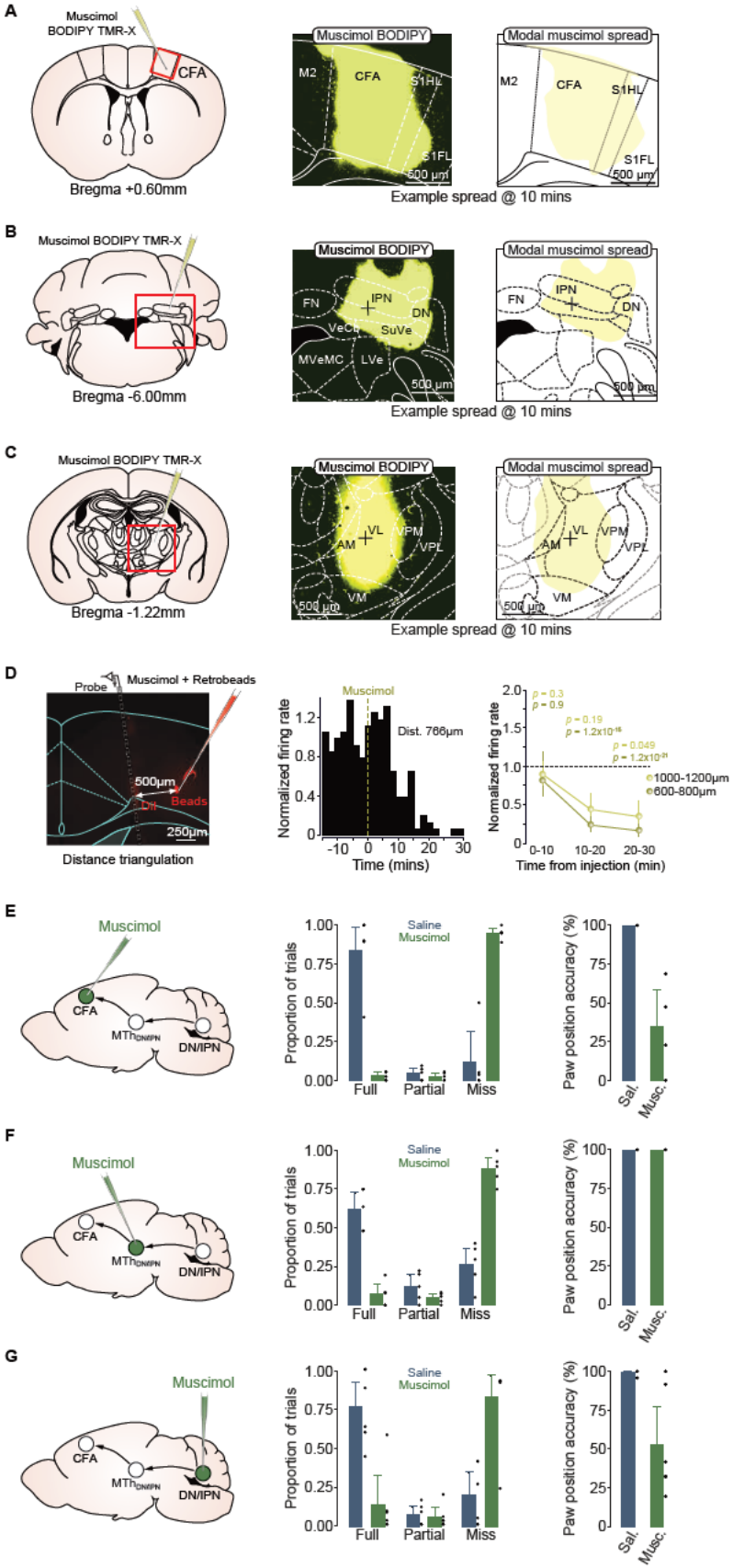

Figure S4. Diffusional spread and behavioral effects of muscimol in CFA, cerebellar nuclei and ventral thalamus, related to Figure 4.
(A) *Left*, injection of muscimol BODIPY TMR-X into CFA. *Middle*, example image of fluorescent muscimol spread in CFA at 10 mins post injection. *Right*, Modal spread of fluorescent muscimol in CFA (i.e., area in which fluorescence is present across all mice) (N = 3 mice). M2, secondary motor cortex; CFA, caudal forelimb area; S1HL, primary hindlimb somatosensory cortex. (B) *Left*, injection of muscimol BODIPY TMR-X targeted to dentate and interpositus cerebellar nuclei. *Middle*, example image of fluorescent muscimol spread across cerebellar nuclei at 10 mins post injection. *Right*, Example of diffusional spread outline used to calculate the modal spread shown in in Figure 4B. DN, dentate nucleus; IPN, interpositus nucleus; FN, fastigial nucleus, VN, vestibular nuclei including: VeCb, vestibulocerebellar nuclei; SuVe, superior vestibular nucleus; MVeMC, medial vestibular nucleus magnocellar part; LVe, lateral vestibular nucleus. The cross represents the median point of injection located using fluorescent retrobeads (N = 4 mice). (C) *Left*, injection of muscimol BODIPY TMR-X targeted to $MTh_{DN/IPN}$. *Middle*, example image of fluorescent muscimol spread in ventral thalamus at 10 mins post injection. *Right*, Example of diffusional spread outline used to calculate the modal spread shown in in Figure 4C. AM, anteromedial; VL, ventrolateral; VPM, ventral posteromedial; VPL, ventral posterolateral; VM, ventromedial thalamic nuclei. The cross represents the median point of injection located using fluorescent retrobeads (N = 4 mice). (D) *Left*, example silicon probe tract through cortex visualized using DiI and muscimol injection site visualized using red fluorescent retrobeads. The distance between the centre of the bead injection and the electrode position of each recorded unit was used to group neurons (600-800 µm or 1000-1200µm). *Middle*, normalized firing rate as a function of time from muscimol injection in an example CFA neuron. *Right*, normalized suppression of firing rate in CFA neurons as a function of time and distance. Group: 600-800 µm, n = 43 neurons; 1000-1200 µm, n = 25 neurons, one-way t-test for significant differences from baseline at each time point. (E) *Left*, Muscimol injection into CFA. *Middle*, Proportion of full / partial lever pushes and miss trials 10 minutes after saline (blue) or muscimol (green) injection into CFA. Black dots represent data from individual mice, bars represent population means ± 95% CI. *Right*, Paw position accuracy at the point of cue presentation and 10 mins after saline (Sal., blue) or muscimol (Musc., green) injection into CFA (N = 5 and 5 mice). (F) Same as *(E)* but with injections targeted to $MTh_{DN/IPN}$. (N = 5 and 5). (G) Same as *(E)* but with injections targeted to DN/IPN (N = 5 and 5 mice).

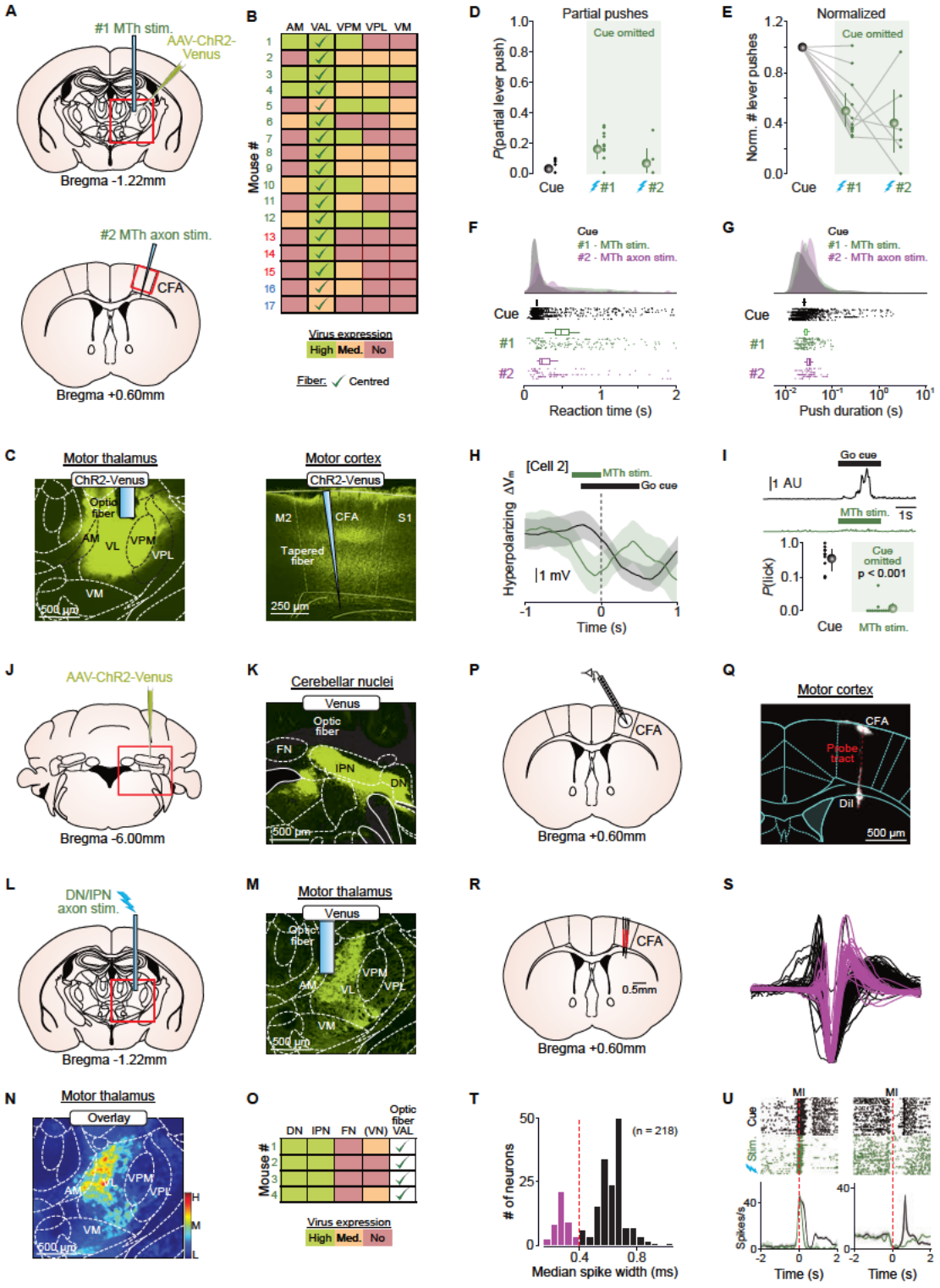

Figure S5. Photoactivation of the cerebello thalamocortical pathway, related to Figure 5.
(A) Injection of AAV-Venus-ChR2 targeted to $MTh_{DN/IPN}$ with optic fiber chronically implanted directly above thalamus (*top, #1*) or a tapered optic fiber acutely implanted into CFA (*bottom, #2*). (B) Quantification of viral expression in ventral motor thalamus (red/no = <5 %, orange/medium = 5-50 % & green/high = 50-100 % expression within each nuclei, green ticks represent correct fiber placement above ventral anterolateral thalamus). Data from mice 1-12 are included in Figure 5B, mice 13-15 displayed no behavioral effects upon photoactivation, mice 16-17 were transduced with AAV-mCherry as controls. (C) Expression of ChR2-Venus and fiber placement in (*left*) ventrolateral thalamus and (*right*) CFA. AM, anteromedial; VL, ventrolateral; VPM, ventral posteromedial; VPL, ventral posterolateral; VM, ventromedial thalamic nuclei. M2, secondary motor cortex; CFA caudal forelimb area; S1, primary sensory cortex. (D) Probability of partial lever push movements evoked by an auditory go cue (black) or photoactivation of $MTh_{DN/IPN}$ (#1) or $MTh_{DN/IPN}$ axons in CFA (#2) in the absence of a go cue (green). Colored dots represent data from individual mice, colored circles represent mean ± 95% CI. For Cue, #1 and #2, N = 12, 12 and 6 mice, respectively. (E) Normalized number of lever pushes evoked by an auditory go cue (black) or photoactivation of $MTh_{DN/IPN}$ (#1) or $MTh_{DN/IPN}$ axons in CFA (#2) in the absence of a go cue (green). Colored dots represent data from individual mice, colored circles represent mean ± 95% CI. For Cue, #1 and #2, N = 12, 12 and 6 mice, respectively. (F-G) Raincloud plots showing the distributions of *(F)* reaction times and *(G)* push durations of cue-evoked (black) and photoactivation (#1 & #2) push trials. Box-and-whisker plots represent bootstrapped estimates of median statistics. (H) Example hyperpolarizing subthreshold V_m change ± 95% CI in a layer 5B projection neuron in response to the cue (black) or photoactivation of $MTh_{DN/IPN}$ (green) in the absence of a cue. Dashed line indicates movement initiation. (I) *Top traces*, average across-trial motion index from an ROI covering the tongue (i.e. licking). Black, cue-evoked licking; green, $MTh_{DN/IPN}$ photoactivation-evoked licking. *Bottom*, probability of licking evoked by an auditory go cue (black) or photoactivation of $MTh_{DN/IPN}$ in the absence of a go cue (green). Colored dots represent data from individual mice, colored circles represent mean ± 95% CI (N = 12 mice). (J) Injection of AAV-Venus-ChR2 targeted to DN/IPN. (K) Expression of ChR2-Venus in DN/IPN. FN, fastigial nucleus; IPN, interpositus nucleus ; DN, dentate nucleus. (L) Photoactivation of DN/IPN axon terminals in $MTh_{DN/IPN}$. (M) Anterograde labelling of DN/IPN axons in motor thalamus and optic fiber placement. (N) Average density of DN/IPN axons across motor thalamic nuclei (N = 4 slices from 4 mice). Scale bar, H - high, M - medium, L - low-level expression. AM, anteromedial; VL, ventrolateral; VPM, ventral posteromedial; VPL, ventral posterolateral; VM, ventromedial thalamic nuclei. (O) Quantification of viral expression (red/no = <5 %, orange/medium = 5-50 % & green/high = 50-100 % expression within each nuclei, green ticks represent correct fiber placement above ventral anterolateral thalamus) (N = 4 mice). FN, fastigial nucleus; IPN, interpositus nucleus ; DN, dentate nucleus. (P) Silicone probe recordings in deep layers of CFA. (Q) Example probe tract in CFA visualized using DiI. (R) Overlay of probe tracts in CFA (N = 4 mice). (S) Overlaid mean spike waveforms for putative interneurons (purple) and pyramidal cells (black). (T) Histogram of spike durations (see methods). (U) Rasters and peri-stimulus time histograms of activity in 2 example deep layer CFA neurons aligned to movement initiation (red dashed line). Black represents cue trials, green represents photoactivation trials.

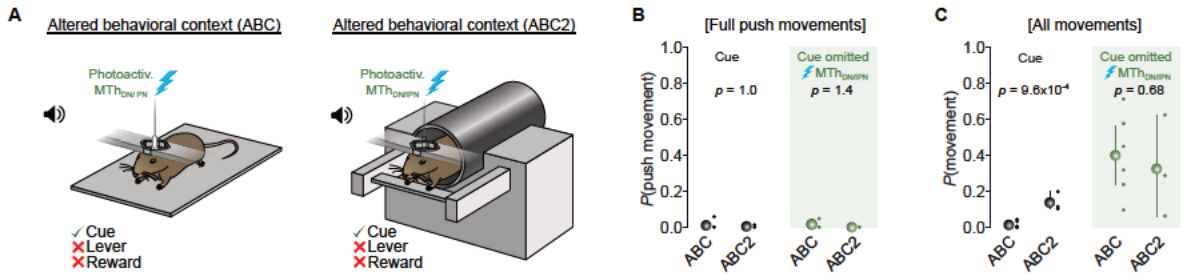

Figure S6. Comparison of photoactivated forelimb movements in two altered behavioral contexts, related to Figure 6.
(A) Photoactivation of $MTh_{DN/PN}$ in (*left*) an altered behavioral context with flat baseplate (ABC) and (*right*) altered behavioral context that recapitulates LBC mouse posture (ABC2, i.e. horizontal bar positioned at the height of the LBC movable lever - see Figure 6A). (B) Probability of push-like movements evoked by an auditory go cue (black) or photoactivation of $MTh_{DN/PN}$ in the absence of a go cue (green). Colored dots represent data from individual mice, colored circles represent mean ± 95% CI. ABC, N = 6 mice, ABC2 N = 3 mice. (C) Probability of any forelimb movement evoked by an auditory go cue (black) or photoactivation of $MTh_{DN/PN}$ in the absence of a go cue (green) in ABC (N = 6 mice) or ABC2 (N = 3 mice).

Table S1. Contributions Matrix

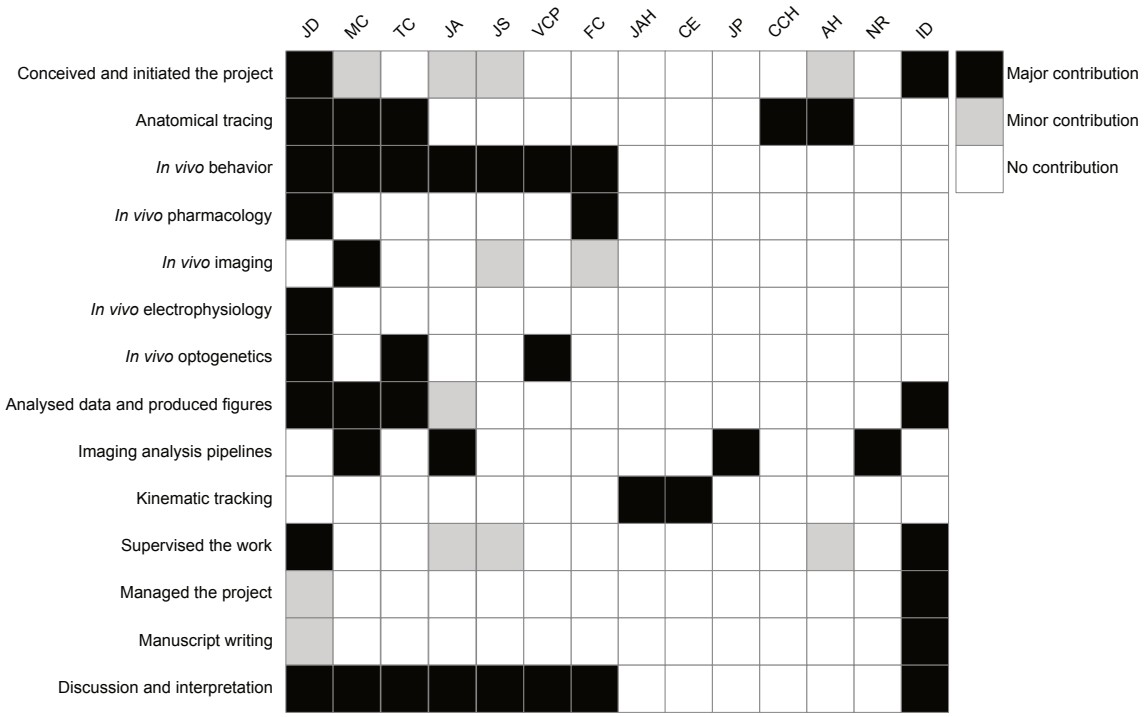

trials, demonstrating that this projection can initiate movement. If the pathway conveys a movement timing signal, as suggested by the $MTh_{DN/IPN}$ recordings, then CFA activity during photoactivation-evoked movements should be similar to CFA activity during cued movements. Motivated by this reasoning, Dr Joshua Dacre recorded the activity of CFA neurons in the same mice using high-density Neuropixels probes. Using the `pixels` pipeline described in Chapter 3, I processed and analysed data from 4 mice to identify putative pyramidal cells (216 units) in layer 5B and examined how their firing patterns related to cued pushes and pushes triggered by DN/IPN terminal stimulation (Figures 5e-h, S5s-u). By testing for significant firing rate changes between a pre-cue baseline period and a peri-movement onset period, I identified 47/216 units that were recruited during cued movements. Next, I tested these units for significant firing changes during photoactivation trials and found that 30/47 (64%) were similarly recruited during these trials, irrespective of the direction of firing rate changes. These results suggest that photoactivation of DN/IPN input to $MTh_{DN/IPN}$ could mimic cue-evoked activity patterns in CFA.

These experiments, in combination with experiments performed by others demonstrating that inactivation of $MTh_{DN/IPN}$ blocks movement initiation and photoactivation of $MTh_{DN/IPN}$ axon terminals in CFA can trigger movement, revealed an influential role for the DN/IPN-thalamocortical pathway in movement initiation.

Appendix B: Movement-specific signaling is differentially distributed across motor cortex layer 5 projection neuron classes

Currie, S.P., Ammer, J.J., Premchand, B., Dacre, J., Wu, Y., Eleftheriou, C., Colligan, M., Clarke, T., Mitchell, L., Faisal, A.A., Hennig, M.H., Duguid, I., 2022. Cell reports (Cambridge) 39, 110801-110801. https://doi.org/10.1016/j.celrep.2022.110801

Primary motor cortex generates movement commands and outputs them via layer 5B projection neurons to the brain stem and spinal cord. While a majority of motor cortex layer 5 projection neurons have been shown to display movement-related activity in rodents, whether this activity encodes information about the type of movement being executed remained unclear. To investigate movement-specific signalling output from motor cortex, we examined activity patterns in layer 5B of the caudal forelimb area of motor cortex (CFA) in mice performing a cued forelimb push/pull task. We found that population dynamics were dominated by movement-invariant activity, and that movement-specific activity was displayed differentially by small subpopulations of pyramidal tract (PT) and intratelencephalic (IT) neuron populations (see attached paper).

First, we sought to understand how activity in CFA layer 5B related to the execution of push and pull movements. In behaving mice, Dr Stephen Currie performed two-photon calcium imaging in CFA at depths corresponding to layer 5B, which were determined in separate experiments in which PT neurons were labelled by retrograde tracer injected into the pons. While a majority of neurons (468/653, 73.5%) displayed movement-related activity, only a small minority (181/653, 27.7%) displayed activity that distinguished between the two movement types. This technique provides an indirect readout of neural activity that depends on calcium indicators that report changes in calcium ion concentration via changes in fluorescence. A limitation of this technique is that calcium indicators report a low-pass filtered, delayed, and transformed version of firing rates (Wei et al., 2020). Therefore, we sought to confirm that the relatively low level of movement-specific activity was not the result of using calcium indicators, which may have masked subtle changes in firing rate. To validate the imaging results with a higher

Cell Reports

Article

Movement-specific signaling is differentially distributed across motor cortex layer 5 projection neuron classes

Graphical abstract

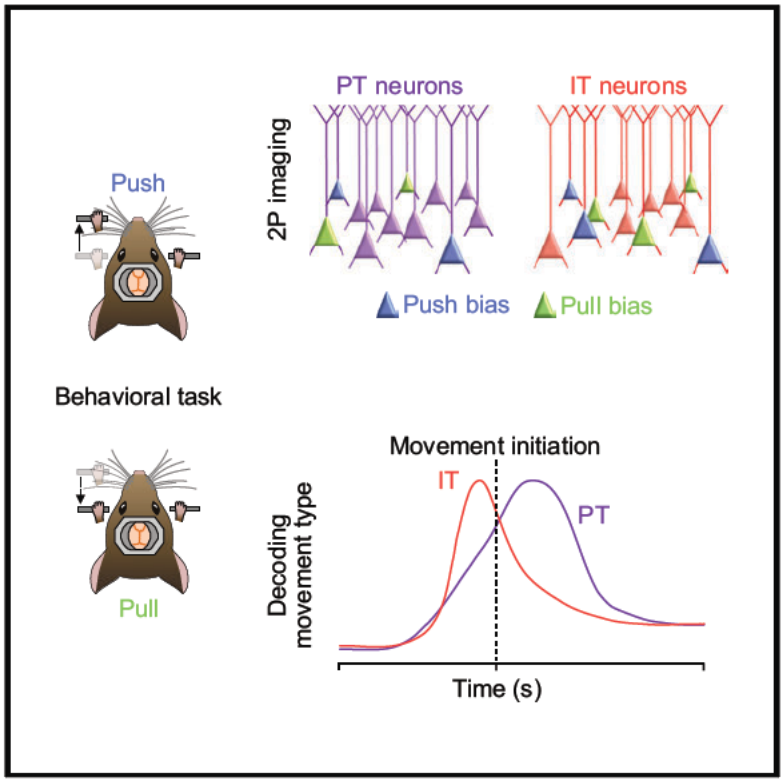

Authors

Stephen P. Currie, Julian J. Ammer, Brian Premchand, ..., A. Aldo Faisal, Matthias H. Hennig, Ian Duguid

Correspondence

In brief

Currie et al. show that movement-type-specific information is routed through relatively small, distributed subpopulations of motor cortical layer 5B projection neurons. Using 2-photon population calcium imaging, they demonstrate that movement-invariant signaling dominates layer 5B population dynamics, whereas movement-specific signaling is differentially distributed across projection neuron classes.

Highlights

- Movement-invariant responses dominate layer 5B population dynamics
- Small proportions of layer 5B projection neurons display movement-specific activity
- Movement specificity is differentially distributed across projection neuron classes
- IT neurons encode movement type before and PT neurons after movement initiation

Currie et al., 2022, Cell Reports 39, 110801
May 10, 2022
https://doi.org/10.1016/j.celrep.2022.110801

CellPress

Cell Reports

CellPress
OPEN ACCESS

Article

Movement-specific signaling is differentially distributed across motor cortex layer 5 projection neuron classes

Stephen P. Currie,[1,9] Julian J. Ammer,[1,7,9] Brian Premchand,[1,8,9] Joshua Dacre,[1,9] Yufei Wu,[3] Constantinos Eleftheriou,[1,2] Matt Colligan,[1] Thomas Clarke,[1] Leah Mitchell,[1] A. Aldo Faisal,[3,4,5] Matthias H. Hennig,[6] and Ian Duguid[1,2,10,*]

[1]Centre for Discovery Brain Sciences and Patrick Wild Centre, Edinburgh Medical School: Biomedical Sciences, University of Edinburgh, Hugh Robson Building, George Square, Edinburgh EH8 9XD, UK
[2]Simons Initiative for the Developing Brain, Edinburgh Medical School: Biomedical Sciences, University of Edinburgh, Edinburgh EH8 9XD, UK
[3]Department of Bioengineering, Imperial College London, London SW7 2AZ, UK
[4]Department of Computing, Imperial College London, London SW7 2AZ, UK
[5]MRC London Institute of Medical Sciences, London W12 0NN, UK
[6]Institute for Adaptive and Neural Computation, School of Informatics, University of Edinburgh, Edinburgh EH8 9AB, UK
[7]Present address: Optophysiology, Faculty of Biology, University of Freiburg, 79100 Freiburg, Germany
[8]Present address: Infocomm Research, A*STAR, 1 Fusionopolis Way, #21-01 Connexis (South Tower), Singapore 138632, Singapore
[9]These authors contributed equally
[10]Lead contact
*Correspondence:
https://doi.org/10.1016/j.celrep.2022.110801

SUMMARY

Motor cortex generates descending output necessary for executing a wide range of limb movements. Although movement-related activity has been described throughout motor cortex, the spatiotemporal organization of movement-specific signaling in deep layers remains largely unknown. Here we record layer 5B population dynamics in the caudal forelimb area of motor cortex while mice perform a forelimb push/pull task and find that most neurons show movement-invariant responses, with a minority displaying movement specificity. Using cell-type-specific imaging, we identify that invariant responses dominate pyramidal tract (PT) neuron activity, with a small subpopulation representing movement type, whereas a larger proportion of intratelencephalic (IT) neurons display movement-type-specific signaling. The proportion of IT neurons decoding movement-type peaks prior to movement initiation, whereas for PT neurons, this occurs during movement execution. Our data suggest that layer 5B population dynamics largely reflect movement-invariant signaling, with information related to movement-type being routed through relatively small, distributed subpopulations of projection neurons.

INTRODUCTION

In mammals, descending cortical output is necessary for the learning and execution of voluntary movements (Guo et al., 2015; Hwang et al., 2019, 2021; Kawai et al., 2015; Lawrence and Kuypers, 1968; Martin and Ghez, 1991). Deep-layer projections from primary motor cortex form multiple descending pathways innervating cortical, subcortical, brain stem, and spinal cord circuits necessary for triggering and controlling movement (for reviews, see Lemon, 2008; Ruder and Arber, 2019; Shepherd, 2013). Individual layer 5 projection neurons display complex firing patterns that correlate with various aspects of limb trajectories, such as joint angle, direction, and speed (Georgopoulos et al., 1982; Moran and Schwartz, 1999; Paninski et al., 2004; Thach, 1978), and during single-action tasks in rodents, most layer 5 projection neurons (>70%) display movement-related activity in the form of bidirectional changes in firing rate (Dacre et al., 2021; Estebanez et al., 2017; Levy et al., 2020; Park et al., 2022; Sauerbrei et al., 2019; Wang et al., 2017), suggesting widespread encoding of movement. However, in non-human primates, the largest components of motor cortex population responses during a delayed-multi-direction reach task have been shown to be "condition invariant," meaning the population response magnitude and time course were similarly irrespective of reach direction (Kaufman et al., 2016). Condition-invariant responses are tightly linked to the onset of movement, likely reflecting movement timing rather than movement type, similar to condition-invariant population transitions observed in recurrent neural networks trained to recapitulate complex muscle patterns in reaching primates (Sussillo et al., 2015). Deciphering how condition-invariant (which we call "movement-invariant") and movement-specific signaling is spatiotemporally organized in the output layers of motor cortex and how they map onto specific projection classes would be an important step toward understanding descending cortical control of movement.

In rodents, descending information from the main output layer of motor cortex, layer 5B, is routed via two molecularly and anatomically defined projection pathways. Pyramidal tract (PT) neurons innervate multiple targets, including the thalamus, subthalamic nucleus, superior colliculus, ipsilateral striatum, brain stem, and spinal cord, but not the cortex or contralateral striatum (Economo et al., 2018; Kita and Kita, 2012; Muñoz-Castañeda et al., 2021; Ueta et al., 2014; Winnubst et al., 2019), whereas intratelencephalic (IT) neurons target cortex and the striatum bilaterally but not other subcortical targets (Levesque et al., 1996; Muñoz-Castañeda et al., 2021; Wilson, 1987; Winnubst et al., 2019). Although layer 5B neurons are reciprocally connected (Kiritani et al., 2012; Morishima and Kawaguchi, 2006; Morishima et al., 2011), connectivity is essentially unidirectional from IT to PT neurons (Kiritani et al., 2012). This form of asymmetric across-projection class connectivity appears to be a common cortical motif necessary for sensorimotor processing (Brown and Hestrin, 2009; Kiritani et al., 2012; Molyneaux et al., 2007; Reiner et al., 2010). From a descending control perspective, asymmetric connectivity coupled with differential PT and IT intrinsic excitability, sensitivity to neuromodulation and local- and long-range inputs (for reviews, see Baker et al., 2018; Shepherd, 2013) provides a mechanism for flexible routing of information via distinct output channels depending on behavioral state and task requirements. Accumulating evidence suggests that PT neurons provide an essential source of descending control for execution of voluntary limb movements (Economo et al., 2018; Nelson et al., 2021; Peters et al., 2017; Soma et al., 2017; Wang et al., 2017), whereas IT neurons provide input to cortical and striatal circuits contributing to movement preparation and specification (Panigrahi et al., 2015; Park et al., 2022; Yttri and Dudman, 2016), but how movement-specific information is spatiotemporally organized across the two output channels remains unclear.

Here we performed 2-photon calcium imaging in deep layers of the caudal forelimb area (CFA) of mice trained to perform two diametrically opposing forelimb movements (i.e., an alternating push/pull lever task). By combining population imaging with neural classifiers and dimensionality reduction, we show that the majority of layer 5B neurons display movement-invariant signaling (i.e., the same magnitude of response for push and pull movements), correlated with movement timing rather than movement type, whereas small subpopulations of PT and IT neurons convey movement-specific information. Decoding movement type was most prevalent prior to movement initiation in IT neurons and during movement execution in PT neurons, with neurons with high decoding accuracy from both projection classes being temporally uncorrelated and distributed across layer 5B. These findings provide evidence that movement-invariant signaling dominates layer 5B activity, whereas movement-specific information is spatially and temporally distributed across projection neuron classes.

RESULTS

CFA is required for execution of a push/pull lever task for mice

To explore how layer 5B signaling relates to execution of different movements, we first developed a cued linear push/pull lever task for mice. The task design required mice to push or pull a horizontal lever during presentation of a 2-s 6 kHz auditory cue to receive a water reward. After a 4- to 6-s inter-trial interval (ITI), mice had to push the lever 4 mm forward from an initial starting position. The lever would then be locked, and a servo-controlled lick spout would deliver a 5-μL reward following a 1-s delay. The lever then unlocked, and a second ITI commenced, where mice would be expected to pull the lever backward 4 mm to the original starting position after presentation of the same 6-kHz auditory cue. Missed trials or spontaneous movement during the ITI resulted in a lever reset and restarting of the ITI (Figure 1A). Individual mice displayed idiosyncratic strategies to engage with the lever but showed reproducible trial-to-trial forelimb trajectories (Figure 1B). In general, mice reoriented their forelimb and paw upon cue presentation (lift and rotate backward for pushes, lift and rotate forward for pulls) (Video S1) prior to initiation of the push or pull action. Mice rapidly learned the task (mean, 10.5 days; [4] inter-quartile range (IQR); N = 24 mice), displaying fast reaction times and movement durations that reflect the combination of paw reorientation and lever manipulation (Figure 1C). "Expert" mice completed 44.5 [9.5] IQR successful push and 45.0 [8.5] IQR successful pull trials during each 30-min behavioral session, equating to ~71% task success (push median 68.0%, [35.9] IQR; pull median 74.5%, [43.4] IQR; N = 24 mice) (Figures 1D and 1E).

To confirm that CFA is required for execution of push and pull movements, we focally injected the Gamma aminobutyric acid type A ($GABA_A$) receptor agonist muscimol (1.6 mm lateral and 0.6 mm rostral of bregma; STAR Methods; Dacre et al., 2021; Schiemann et al., 2015). By applying muscimol during behavior, we could assess the immediate effects of CFA inactivation within the first 10 min after drug injection (Figure 1F), where drug diffusion remained in the targeted region (Figures S1A–S1C). Muscimol rapidly blocked initiation of both actions, reducing the number of successful trials in the first 10 min by ~65% (push Pre 13.9 [11.1 17.1] 95% CI trials, push Post 5.0 [3.3 6.8] 95% CI trials, N = 10 mice; pull Pre 14.0 [10.9 17.2] 95% CI trials, pull Post 5.3 [3.2 7.4] 95% confidence interval [CI] trials, N = 10 mice) (Figure 1G). Sham injections of saline into CFA or muscimol injections into hindlimb motor cortex had no effect on behavior (Figures S1D–1G). Blocking CFA activity resulted in an inability to initiate push or pull movements and monoparesis of the contralateral forelimb (i.e., localized weakness without complete loss of function), as evidenced by a significant reduction in paw position accuracy (i.e., the forepaw was not positioned on the lever at cue presentation) (Figures 1H and S1H–1J; Video S2). The effect of muscimol inactivation was most pronounced in mice that displayed the highest number of successful trials, confirming that task execution is CFA dependent even in expert mice (Hwang et al., 2019, 2021; Kawai et al., 2015; Figure S1K).

Movement-invariant signaling dominates layer 5B activity patterns

To examine how output from CFA relates to execution of push and pull movements, we restricted imaging of behavior-related population activity to cortical depths corresponding to layer 5B, the upper boundary of which was identified by the presence of

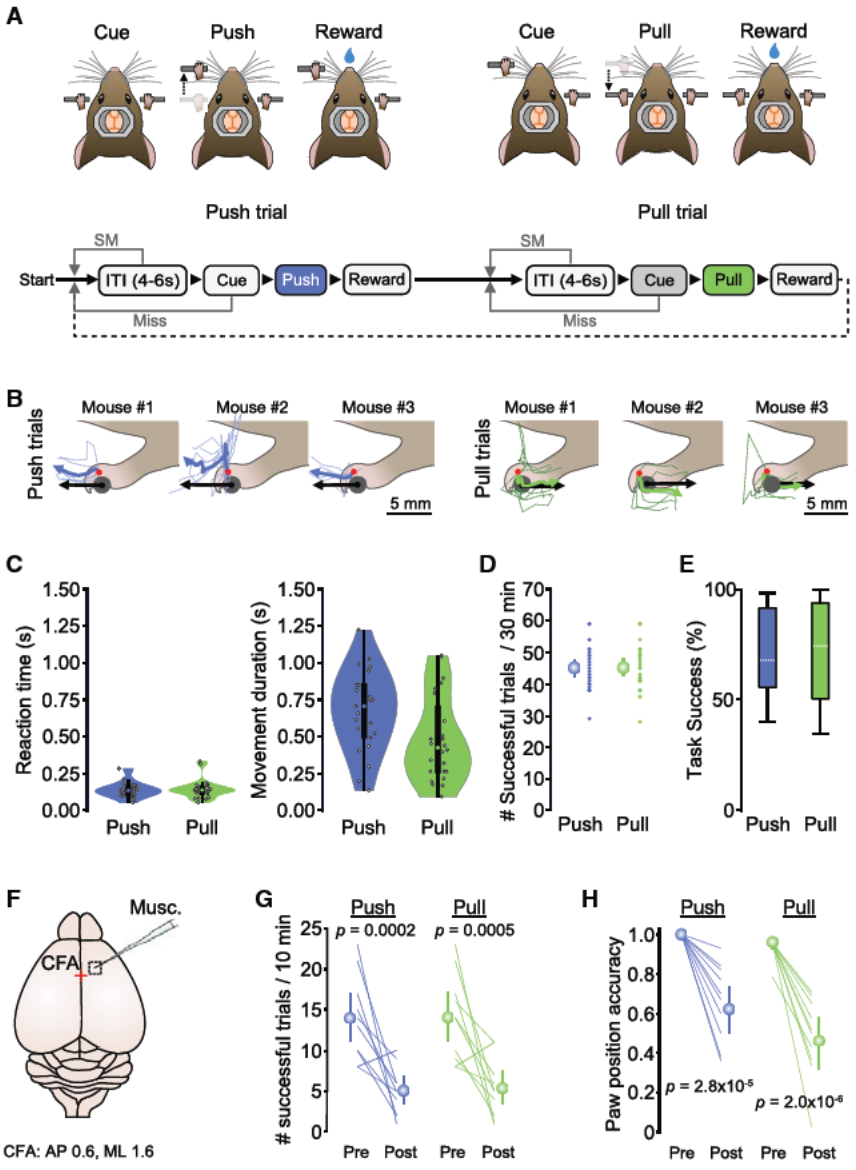

Figure 1. CFA is necessary for executing cued push and pull movements

(A) Top: cued alternating push/pull task for head-restrained mice. Bottom: behavioral task structure. ITI, inter-trial interval; SM, spontaneous movement.

(B) Paw and lever movement trajectories from 3 mice relative to position at movement initiation. Single trials (dashed lines) and mean paw trajectories (solid lines) during push (left, blue) and pull (right, green) trials are shown alongside the average movement vector of the lever (black arrow). Red dots depict approximate tracked positions on the paw.

(C) Violin plots showing median, IQR, and range of reaction times (left) and movement durations (right) during push (blue) and pull (green) trials. Circles represent data from individual mice (N = 24 mice).

(D) Number of successful trials per 30-min training session (small symbols, data from individual mice; large symbols, mean ± 95% CI; N = 24 mice).

(E) Box-and-whisker plots showing median, IQR, and range of task success across mice (N = 24 mice).

(F) Focal muscimol inactivation of CFA, centered 0.6 mm anterior and 1.6 mm medial of bregma (red cross).

(G) Number of successful push (blue) and pull (green) trials in a 10-min period before (Pre) and after (Post) injection of muscimol (N = 10 mice); paired t test. Colored lines, individual mice. Symbols, population means ± 95% CI.

(H) Paw position accuracy at the point of cue presentation before (Pre) and 10 min after (Post) muscimol injection into CFA (N = 10 mice); paired t test. Colored lines, individual mice. Symbols, population means ± 95% CI.

PT neurons in separate tracing experiments (CFA upper boundary ≥500 μm from the pial surface) (Schiemann et al., 2015; Figures 2A, 2B, and S2A). Cell density estimates suggested that we imaged the majority of layer 5B neurons at depths up to 650 μm from the pial surface (Figures S2A–2C). A large proportion of layer 5B neurons displayed movement-related activity (468 of 653 neurons, mean = 73.5% [54.7 81.8] 95% CI per field of view [FOV], N = 12 FOVs from 6 mice), defined as $\Delta F/F_0$ changes occurring within a peri-movement window spanning 150 ms prior to movement initiation to 40 ms after median movement completion. The remaining neurons were classified as non-responsive or reward-related when changes in $\Delta F/F_0$ occurred after the peri-movement window (Figures 2C and 2D). The trial-to-trial similarity in population responses of movement-related neurons strongly correlated with the similarity in forelimb movement magnitude (i.e., motion index; STAR Methods), suggesting that $\Delta F/F_0$ changes reflected movement of the forelimb (Figure 2E). By comparing push and pull trials, we found that most layer 5B neurons displayed movement-related activity that was indistinguishable between trial types (median = 59.8% [31.4] IQR of neurons, N = 6 mice), termed "movement-invariant" signaling, manifested as increased (85%) or decreased (15%) activity around movement onset. Movement-invariant neurons appeared to reflect the timing of movement (i.e., transition from a resting posture to push/pull) rather than movement type and were spatially distributed across each FOV (Figures 2F–2H). In contrast, only a small fraction of neurons displayed movement-specific signaling, where $\Delta F/F_0$ changes were significantly different between push and pull trials (termed movement bias; push bias, median = 14.3% [15.9] IQR; pull bias, median = 11.8% [19.5] IQR, N = 6 mice) (Figure 2M). Responses of movement bias neurons were classified into four different types, including positive and negative changes in $\Delta F/F_0$, consistent with bidirectional movement-specific tuning of neural activity (Georgopoulos et al., 1982). Most movement-bias neurons were classified as type 1 (136/181 neurons, 75.1%, N = 6 mice), showing increased $\Delta F/F_0$ during

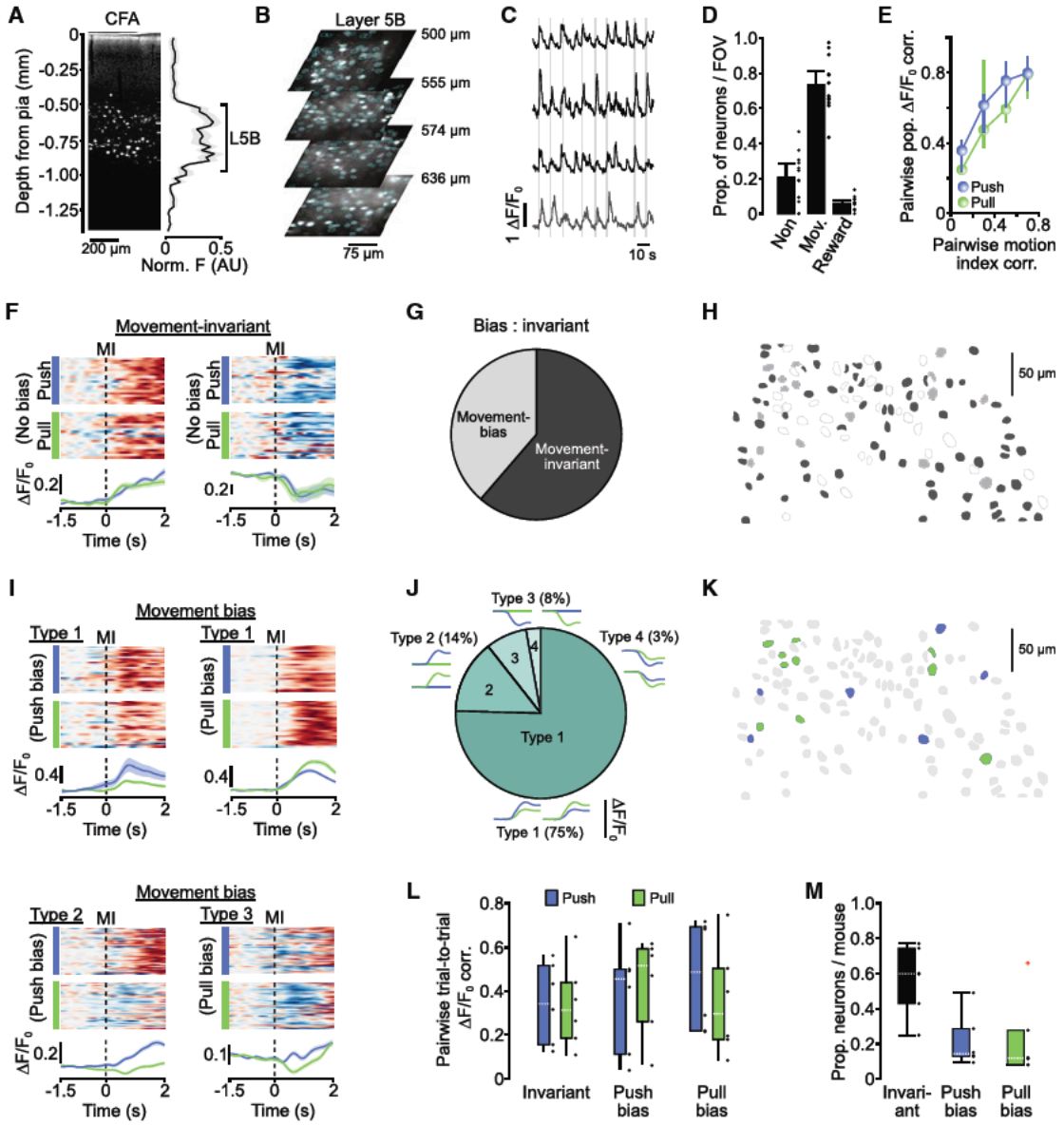

Figure 2. Movement-invariant and movement-specific signaling in layer 5B of CFA

(A) Depth profile of pyramidal tract (PT) neurons in CFA. Left: Retrobead labeling of PT neurons after injection into the pons. Right: normalized fluorescence ± SEM as a function of depth from the pial surface (N = 3 mice). A black line indicates the upper and lower boundary of layer 5B across mice.

(B) Representative 2-photon imaging fields of view (FOVs) from layer 5B in CFA (N = 4 mice). Cyan circles depict regions of interest.

(C) $\Delta F/F_0$ traces from four example layer 5B neurons during task execution (gray vertical bars). Black traces depict neurons with movement-related activity. Gray trace depicts a neuron with reward-related activity.

(D) Proportion of non-responsive, movement-related, or reward-related neurons per FOV (N = 12 FOVs from 6 mice). Black dots represent individual FOVs, and bars represent mean ± 95% CI.

(E) Pairwise trial-to-trial correlation of population $\Delta F/F_0$ during push (blue) or pull (green) trials as a function of the pairwise trial-to-trial correlation of the corresponding motion index (N = 12 FOV from 6 mice).

(F) Activity of two example movement-invariant neurons. Top: raster showing normalized $\Delta F/F_0$ across successive push (blue) or pull (green) trials. Bottom: mean $\Delta F/F_0$ ± 95% CI for push and pull trials. Dashed lines, movement initiation (MI).

(G) Summary of movement-invariant and movement-bias neuron classification in layer 5B of CFA (n = 468 neurons, N = 6 mice).

(H) 2 overlapping FOVs from a single mouse, showing movement-invariant (dark gray), movement bias (light gray), and non-responsive neurons (white).

(I) Activity of movement bias neurons split by type. Top: example type 1 neurons with push (left) or pull (right) bias. Bottom left: example type 2 neuron with push bias. Bottom right: example type 3 neuron with pull bias. Dashed lines, MI.

(J) Summary of movement bias classification in the layer 5B CFA (n = 181 neurons, N = 6 mice). Insets: model examples of type 1–4 $\Delta F/F_0$ changes.

(legend continued on next page)

push and pull trials, whereas smaller proportions of type 2 neurons (25/181 neurons, 13.8%, N = 6 mice) and type 3 (15/181 neurons, 8.3%, N = 6 mice) displayed movement selectivity (i.e., a significant change in $\Delta F/F_0$ for one movement with no response during the opposing movement). Finally, a small minority of cells displayed reduced activity during push and pull trials, classified as type 4 neurons (5 of 181 neurons, 2.8%; N = 6 mice) (Figures 2I and 2J). In terms of spatial organization, movement bias neurons were found in all FOVs and were spatially intermingled with movement-invariant neurons (Figures 2H and 2K). Although there was a high degree of variability in $\Delta F/F_0$ changes trial to trial, no consistent differences in mean pairwise trial to trial $\Delta F/F_0$ correlations were found between movement-invariant and movement-bias neurons across trial types (Figure 2L). A small proportion of bias neurons displayed differences in baseline $\Delta F/F_0$ between push and pull trials, which could reflect postural differences (i.e., different trial to trial start positions for push and pull trials) or differential preparatory activity (Li et al., 2015; Figures S2D–S2F). However, baseline differences were, on average, smaller than those observed during the peri-movement epoch (data not shown) and, thus, unlikely to be the main driver of movement-specific signaling. Given that $\Delta F/F_0$ changes provide an indirect readout of neural activity, we sought to confirm the proportions of movement-invariant and movement-bias neurons in layer 5B using high-density silicone probe recordings. Putative layer 5B projection neurons were identified using spike-width thresholding and electrode depth profiling based on retrograde labeling from the pons (Figures S2G–S2I). We found similar proportions of movement-invariant and push/pull bias neurons when comparing both recording methods (Figures 2M and S2J–S2L), confirming that movement-invariant signaling dominated layer 5B responses, whereas a small proportion of neurons conveyed movement-specific information.

Movement-specific signaling is more prevalent in superficial layers

Excitatory networks in primary motor cortex display a top-down laminar organization, where output from layer 2/3 provides strong excitatory input to upper layer 5B projection neurons (Anderson et al., 2010; Weiler et al., 2008). Thus, movement bias in layer 5B neurons could be inherited from top-down input. To explore this possibility, we imaged behavior-related activity in layer 2/3 of CFA and found that, in contrast to layer 5B, movement-specific signaling dominated, with ~60% of neurons displaying push or pull bias (movement bias, 216 of 375 neurons, 57.6%; movement-invariant, 159 of 375, 42.4%; N = 5 mice). The vast majority of movement bias neurons were classified as type 1 (200 of 216 neurons, 93.0%), showing increased $\Delta F/F_0$ during push and pull trials (Figures S3A–S3G). The difference in lamina-specific activity profiles could indicate a top-down convergence of movement-specific information where widespread movement bias signaling in layer 2/3 converges on specific subpopulations of downstream layer 5B neurons.

A small proportion of layer 5B neurons decode movement type

Next we investigated how reliably movement type could be decoded from layer 5B single-neuron and population changes in $\Delta F/F_0$ using a Gaussian naive Bayes classifier and logistic regression, respectively (STAR Methods). Approximately 37% of neurons (172 of 468 neurons) displayed decoding accuracy scores above chance (Figure 3A), similar to but slightly higher than the combined proportion of identified push and pull bias neurons (see Figure 2M), likely reflecting subtle differences in the sensitivity of both approaches (see also layer 2/3 decoding accuracy scores for comparison; Figure S3H). Given the trial-to-trial variability in $\Delta F/F_0$ and resultant moderate decoding scores (Figures 2I and 3A), we reasoned that population responses could provide a more robust movement-related signal that would enhance decoding of movement type. By applying logistic regression, population decoding was found to be consistently more accurate (single-cell median decoding accuracy = 0.61, [0.07] IQR; population median decoding accuracy 0.75, [0.16] IQR; N = 6 mice, $p = 2.8 \times 10^{-2}$, Wilcoxon signed rank test) (Figure 3B). However, this increase was driven almost entirely by a small proportion of neurons with high decoding accuracy. Removing the top ~20% of neurons ordered by decoding accuracy score abolished movement type classification (median prop. removed = 0.21, [0.50] IQR, N = 6 mice), whereas sequential removal of randomly selected neurons resulted in a significantly larger proportion of neurons having to be removed before decoding accuracy reduced to chance (median prop. removed = 0.64, [0.57] IQR, N = 6 mice, $p = 2.8 \times 10^{-2}$, Wilcoxon signed rank test) (Figure 3D–3F). This dependency on neurons with high decoding accuracy suggests that movement-specific information is routed through a selected subset of layer 5B neurons.

To further explore the underlying structure of layer 5B population activity, we employed principal-component analysis (Churchland et al., 2010, 2012; Cunningham and Yu, 2014; Kaufman et al., 2014; Stopfer et al., 2003). For the leading 16 principal components, we compared the difference between push and pull trials to compute a discrimination index (d') (Figure S4A). Leading principal components tended to be more similar across actions, whereas movement type was often better represented by higher components (Figure S4B). Despite correlating with population decoding scores, high d' values were not preferentially associated with the leading principal components of the population activity (Figures S4C–4E), suggesting that movement type is not a dominant signal in the population response (Kaufman et al., 2016).

(K) 2 overlapping FOVs from a single mouse, showing neurons with push (blue) or pull (green) bias. Gray, movement-invariant, non-responsive, or reward-phase neurons.

(L) Mean pairwise trial-to-trial $\Delta F/F_0$ correlation for push (blue) and pull (green) trials in invariant and push- and pull-biased neurons (n = 468 neurons from 12 FOVs, N = 6 mice). Black dots represent individual mice.

(M) Proportion of invariant and push- and pull-biased neurons per mouse (n = 468 neurons from 12 FOVs, N = 6 mice). Black dots represent individual mice. A red cross marks an identified outlier.

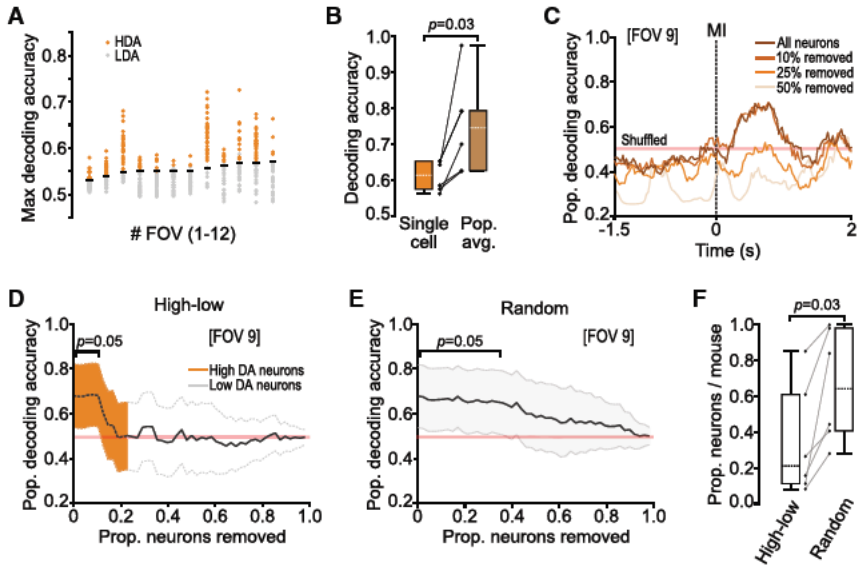

Figure 3. Population decoding relies on a small proportion of neurons with high decoding accuracy

(A) Maximum decoding accuracy during peri-movement epochs generated using a Gaussian naive Bayes classifier. Circles represent individual neurons; black horizontal lines indicate significance threshold. HDA, high decoding accuracy (orange); LDA, low decoding accuracy (gray).

(B) Box-and-whisker plots showing median, IQR, and range of single-cell (naive Bayes classifier, orange) and population (logistic regression, brown) decoding accuracy (N = 12 FOVs from 6 mice, $p = 2.8 \times 10^{-2}$, Wilcoxon signed-rank test). Black dots represent individual mice.

(C) Mean population decoding accuracy for all neurons from a representative FOV (all neurons) or after removal of 10%–50% of neurons in order from high to low single-cell decoding accuracy (A). Red shaded line, 95% CI based on shuffled data. Dashed line, MI.

(D) Change in population decoding accuracy for an example FOV after sequential removal of neurons in order from high (orange) to low (gray) single-cell decoding accuracy (A). Line, mean ± 95% CI. Red line, 95% CI based on shuffled data.

(E) Change in population decoding accuracy for an example FOV after random removal of individual neurons. Line, mean ± 95% CI. Red line, 95% CI based on shuffled data.

(F) Box-and-whisker plots showing the median, IQR, and range for ordered (HDA to LDA) versus random removal of neurons (N = 12 FOVs from 6 mice, $p = 2.8 \times 10^{-2}$, Wilcoxon signed-rank test). Black dots represent individual mice.

IT and PT neurons display temporal differences in encoding of movement type

Layer 5B contains two broad classes of projection neurons: IT neurons form striatal and cortico-cortical connections (Levesque et al., 1996; Muñoz-Castañeda et al., 2021; Wilson, 1987; Winnubst et al., 2019), whereas PT neurons target multiple subcortical, brain stem, and spinal cord areas (Economo et al., 2018; Kita and Kita, 2012; Muñoz-Castañeda et al., 2021; Ueta et al., 2014; Winnubst et al., 2019) (Figure 4A). We next sought to understand whether movement-specific and movement-invariant signaling was dependent on projection class identity. To perform population imaging from identified cell types, we used an intersectional retrograde viral approach targeting the ipsilateral brain stem (pons, PT) and contralateral CFA (IT) using a retrograde adeno-associated virus (r-AAV-retro cre) and conditional expression of GCaMP6s in ipsilateral CFA (Figures 4B and 4C). Using a bicistronic viral vector expressing GCaMP6s (flex) and mRuby, we confirmed that we recorded from the majority of PT and IT neurons per FOV at depths of up to 700 μm from the pial surface (Figure S5), consistent with our previous estimates (Figures S2A–2C). Comparing push and pull trials, most PT neurons displayed movement-invariant activity (75.0% [21.1] IQR), with a small number of neurons displaying push or pull bias (push bias = 10.3% [19.9] IQR, pull bias = 13.8% [11.3] IQR, N = 5 mice), mainly consisting of type 1 (78.2%) and type 2 neurons (16.9%) (Figures 4D and 4E). In contrast, similar proportions of IT neurons displayed movement-specific and movement-invariant signaling (movement bias = 48.8% [11.6] IQR), movement-invariant = 51.2% [11.6] IQR) with type 1 and type 2 neurons again being the most abundant (Figures 4F and 4G). Single-cell decoding accuracy scores were highly consistent across mice, and, as expected, population decoding accuracy increased when averaging the activity of all high-decoding-accuracy neurons per FOV (Figures 4H and 4I). Although trial type could only be decoded in approximately one-third of projection neurons during the peri-movement window, the proportion of IT neurons with decoding accuracy above chance was highest prior to movement initiation, whereas for PT neurons, this occurred during movement execution (IT peak proportion of neurons, 0.19 at −192 ms; PT peak proportion of neurons, 0.21 at +544 ms, N = 6 and 5 FOVs from 5 and 4 mice, respectively), suggesting differential roles for IT and PT populations in movement initiation and execution, respectively. Importantly, at no time during the peri-movement window was the proportion of neurons with high decoding accuracy above 21% for either cell type (Figure 4J), consistent with a small proportion of projection neurons conveying time-dependent, movement-specific information.

Movement-specific signaling is distributed across layer 5B

To explore whether high decoding accuracy PT and IT neurons form functional clusters, we first detected the onset of movement-related $\Delta F/F_0$ changes. Within each FOV, activity changes occurred ~300 ms prior to movement, consistent with a role in preparation/initiation (Dacre et al., 2021; Estebanez et al., 2017; Isomura et al., 2009; Li et al., 2015), and tiled the peri-movement window. Neurons displaying a range of $\Delta F/F_0$ onsets were spatially distributed across each FOV (Figures 5A and 5B). To explore correlations in peri-movement activity patterns, we split PT and IT neurons based on their decoding accuracy scores (high, low, and all) and compared pairwise activity during push

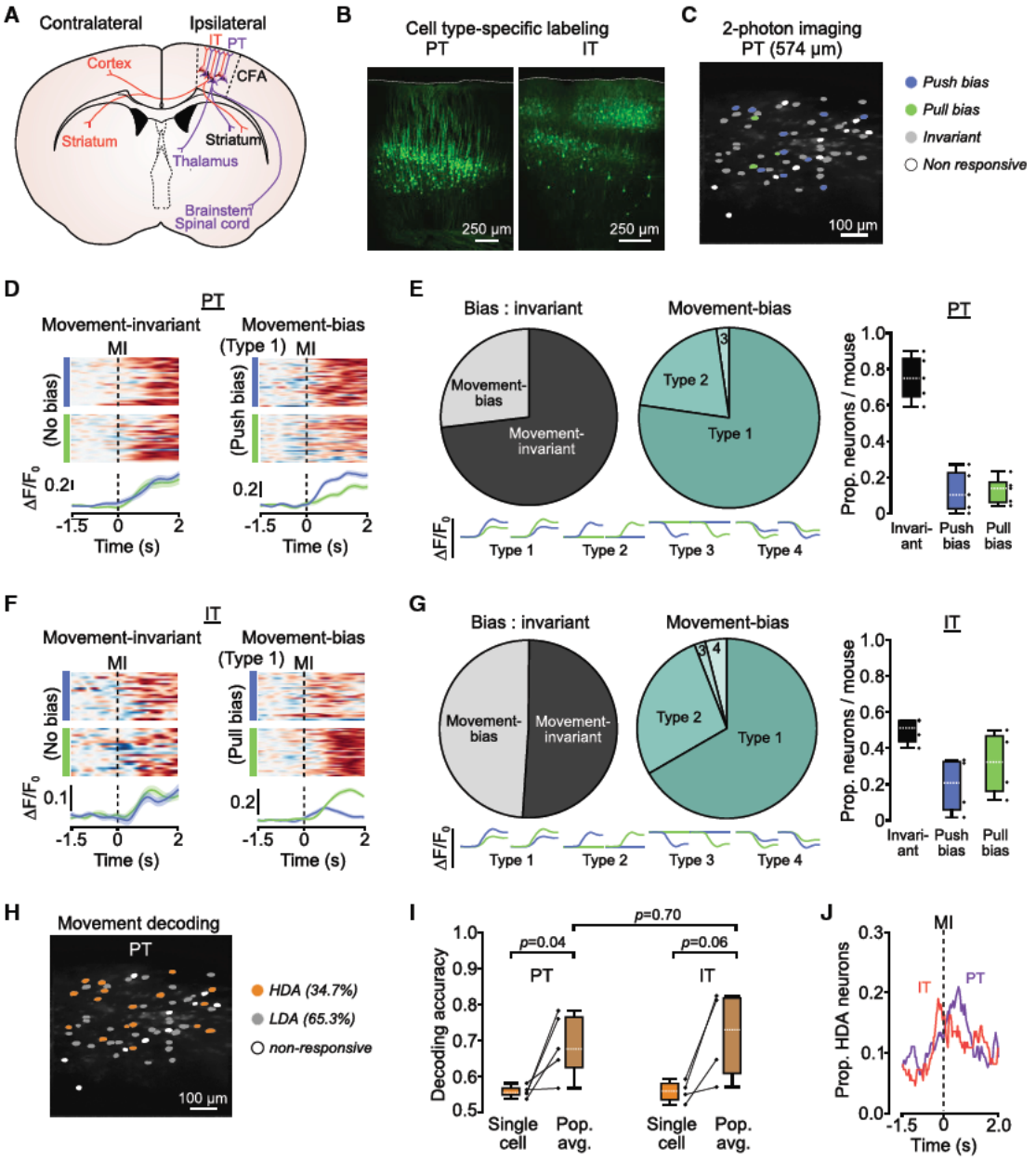

Figure 4. Movement-invariant and movement-specific signaling in identified layer 5B projection neurons

(A) Schematic showing brain-wide projections of layer 5B PT (purple) and IT (red) neurons. Contra- and ipsilateral relate to the site of 2-photon imaging.

(B) Histology from two imaged mice showing retrograde cell-type-specific labeling of PT (left) and IT (right) neurons in CFA.

(C) Example FOV showing PT neurons with push (blue) or pull (green) bias. Gray, movement invariant; white, non-responsive neurons.

(D) Activity of two example PT neurons: movement-invariant (left) and movement bias, type 1 (right). Top: raster showing normalized $\Delta F/F_0$ across successive push (blue) or pull (green) trials. Bottom: mean $\Delta F/F_0 \pm 95\%$ CI for push and pull trials. Dashed lines, MI.

(E) Left: summary of movement-invariant and movement bias PT neuron classification (n = 125 versus 46 neurons, N = 5 mice). Center: summary of movement bias classification in PT neurons (n = 46 neurons, N = 5 mice). Right: proportion of invariant, push- and pull-biased PT neurons per mouse (n = 171 neurons from 6 FOVs, N = 5 mice). Black dots represent individual mice. Bottom: model examples of $\Delta F/F_0$ changes classified as type 1–4.

(F) Activity of two example IT neurons: movement-invariant (left) and movement bias, type 1 (right). Top: raster showing normalized $\Delta F/F_0$ across successive push (blue) or pull (green) trials. Bottom: mean $\Delta F/F_0 \pm 95\%$ CI for push and pull trials. Dashed lines, MI.

(G) Left: summary of movement-invariant and movement bias IT neuron classification (n = 56 versus 54 neurons, N = 4 mice). Center: summary of movement bias classification in layer 5B IT neurons (n = 54 neurons, N = 4 mice). Right: proportion of invariant, push- and pull-biased layer 5B IT neurons per mouse (n = 110 neurons from 5 FOVs, N = 4 mice). Black dots represent individual mice. Bottom: model examples of $\Delta F/F_0$ changes classified as type 1–4.

(H) Example FOV showing HDA (orange), LDA (gray), and non-responsive (white) PT neurons.

(legend continued on next page)

and pull trials. We found weak correlations within and across groups irrespective of cell type identity (Figures 5C, 5D, and S6). Moreover, comparing the activities of PT and IT neurons as a function of their pairwise distance suggested that neighboring neurons did not show correlated activity or spatiotemporal clustering (Figures 5E–5G). Thus, our data suggest a model where movement-specific information is routed through small, distributed subpopulations of layer 5B projection neurons, whereas most neurons convey movement-invariant information related to the timing of movement execution (Figure 5H).

DISCUSSION

Here we have shown that layer 5B neuronal signaling is mostly movement-invariant, with similar activity patterns generated during execution of two diametrically opposing movements. Changes in activity were tightly locked to the peri-movement period, indicative of a generic motor signal relating to movement timing but not movement type. Movement- or condition-invariant signaling also dominates in primate motor cortex, thought to trigger state-dependent switching from stable neural dynamics during rest toward oscillatory dynamics underpinning movement execution (Churchland et al., 2010, 2012; Kaufman et al., 2014, 2016; Kurtzer et al., 2005), and is an emergent property of recurrent neural networks trained to recapitulate complex muscle patterns during reaching (Sussillo et al., 2015). In contrast to primate motor cortex, we found widespread movement-invariant responses at the single-neuron level (Kaufman et al., 2016). This is unlikely to reflect differences in recording sensitivity, given that our imaging and electrophysiology approaches identified similar proportions of movement-invariant neurons across layer 5B (Wei et al., 2020; Zhou and Tin, 2021), or the limited number of movements in our task because movement-invariant responses have been shown in relatively simple tasks requiring few actions (Evarts, 1968; Hocherman and Wise, 1991; Messier and Kalaska, 2000; Riehle et al., 1994; Weinrich et al., 1984) and in complex tasks involving more than 20 separate actions (Kaufman et al., 2016). Instead, this might reflect evolutionary differences in how motor cortex recruits and controls muscle activation during the transition from rest to movement execution. Cell-type-specific imaging identified that movement-invariant signaling dominated PT neuron activity, suggesting that a large proportion of the output conveyed to subcortical, brain stem, and spinal cord areas relates to execution of movement without necessarily specifying movement type, whereas equal proportions of IT neurons displayed movement-invariant versus movement-specific signaling. If movement-invariant signaling relates to the execution of movement and dominates deep-layer motor cortex activity, then what drives the change in neural activity, and what purpose might it serve? Long-range inputs from the thalamus, basal ganglia, secondary motor cortex, and cerebellum are possible sources (Hooks et al., 2013, 2018; Nelson et al., 2021), providing an external trigger to transform motor cortical dynamics necessary for postural maintenance at rest to a neural state required for movement execution. This switch in neural dynamics would signify the intention to move, but not which movement will be executed (Elsayed et al., 2016; Kaufman et al., 2016). An important next step will be to develop methods to identify and selectively manipulate neurons displaying movement-invariant signaling to demonstrate their causal contribution to postural control and timing of movement execution.

We reasoned that execution of two diametrically opposing movements should, in principle, generate distinct patterns of cortical output dynamics, given differences in starting posture, direction of movement, and temporal sequence of muscle activation (Isomura et al., 2009; Miri et al., 2017). Although we found that the majority of layer 5B neuron signaling was movement invariant, a relatively small proportion of neurons displayed response bias toward push or pull movements. The relatively low level of movement-specific signaling is unlikely to be due to masking of subtle changes in spike rate when using calcium reporters (Wei et al., 2020; Zhou and Tin, 2021) because we observed similar proportions of movement-specific signaling when performing high-density extracellular recordings of putative layer 5B projection neurons. The firing rates of individual neurons in motor cortex reflect a complex combination of signals that correlate with joint angle, direction, and speed (Georgopoulos et al., 1982; Moran and Schwartz, 1999; Paninski et al., 2004; Thach, 1978), whereas population dynamics reflect time-varying changes in neural state during the transition from rest to movement execution (Churchland et al., 2010, 2012; Kaufman et al., 2014, 2016; Kurtzer et al., 2005; Sauerbrei et al., 2019). In mice, individual layer 5B neurons displayed moderate decoding accuracy scores, likely because of relatively high trial-to-trial variability, whereas the population average was consistently higher across mice. We found that only a small proportion ($\sim$20%) of neurons contributed to high population decoding accuracy scores, with their combined effects accurately decoding three-quarters of all trials. Removing only a handful of neurons per FOV was sufficient to abolish decoding, confirming that a minority of neurons convey the majority of information regarding movement type. This dependency on only a few neurons has important implications for understanding how movement-specific information is encoded in primary motor cortex, given that recording of neural dynamics during execution of a single movement task will likely uncover widespread movement-invariant signaling, which relates to limb movement, but not the specific movement being executed.

In mouse cortex, projection neurons display connectivity patterns within and across classes that suggest general organizing principles (Brown and Hestrin, 2009; Kiritani et al., 2012; Maruoka et al., 2017; Morishima et al., 2011). IT neurons in motor cortex are strongly recurrently connected, whereas inter-class connectivity is largely directional from IT to PT but not vice versa, generating a hierarchical organization with unidirectional signaling from higher-order to lower-order output neurons

(I) Box-and-whisker plots showing median, IQR, and range of single-cell (naive Bayes classifier, orange) and population (logistic regression, brown) decoding accuracy of PT (left) and IT (right) neurons. Comparisons were made with a two sample t test. Black dots represent individual mice.
(J) Proportion of neurons with decoding accuracy above chance (i.e., HDA) across time. PT, purple; n = 58/171 neurons from 6 FOVs, N = 5 mice. IT, red; n = 43/110 neurons from 5 FOVs, N = 4 mice. Dashed line, MI.

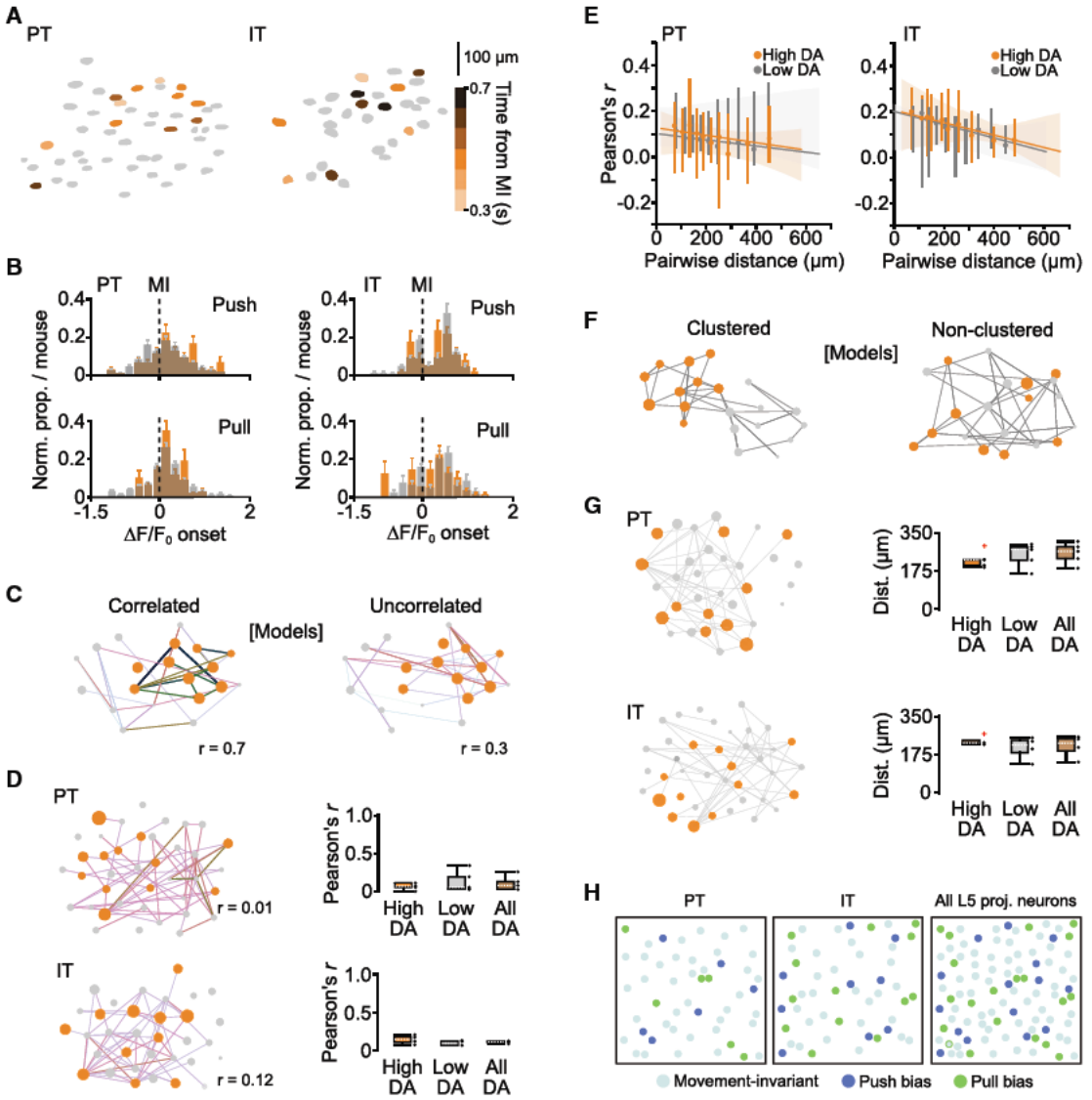

Figure 5. Cell-type-specific spatiotemporal organization of HDA neurons in layer 5B

(A) Example FOVs showing spatial distribution of $\Delta F/F_0$ onset for HDA PT (left) and IT (right) neurons during push trials. Colors represent 200-ms bins tiling the peri-movement epoch: −300 ms (light orange) to +700 ms (dark brown).

(B) Histograms of $\Delta F/F_0$ onset for HDA (orange) and LDA (gray) PT (left) and IT (right) neurons during push (top) and pull (bottom) trials (n = 6 and 5 FOVs, N = 5 and 4 mice, respectively).

(C) Modeled functional networks depicting HDA (orange) and LDA (gray) neurons with correlated (left) or uncorrelated (right) activity. Each node, represented by a circle, corresponds to a neuron, whereas the connections represent the strength of activity correlation between neurons.

(D) Left top and bottom: functional networks constructed from the pairwise activity correlations from a representative PT (top) and IT (bottom) FOV. Line color (light to dark) and width correspond to increasing values of Pearson's r. Neurons are plotted as nodes in Euclidean space, with color and size relating to increasing decoding accuracy. Right top and bottom, box-and-whisker plots showing the median, IQR, and range of correlation coefficients across mice for HDA (orange), LDA (gray), and all (brown) PT (top) and IT (bottom) neurons. Black dots represent individual mice.

(E) Median pairwise correlation coefficient with 95% CI as a function of pairwise distance for HDA (orange) and LDA (gray) PT (left) and IT (right) neurons. Horizontal lines denote linear regression model fit, with shaded regions representing the bootstrapped 95% CI (PT: p = 0.87 [(HDA], p = 1.0 [LDA], n = 3,024 observations, N = 5 mice; IT: p = 0.6 [HDA], p = 1.0 [LDA], n = 1,562 observations, N = 4 mice).

(F) Modeled functional networks depicting clustered (left) and non-clustered (right) HDA neurons. Each node, represented by a circle, corresponds to a neuron, whereas the connections represent the pairwise distances between neurons.

(G) Left top and bottom: functional networks constructed from the pairwise distances between neurons in a representative PT (top) and IT (bottom) FOV. Right top and bottom: box-and- whisker plots showing the median, IQR, and range of median pairwise distances across mice for HDA (orange), LDA (gray), and all (brown) PT (top) and IT (bottom) neurons. Black dots represent pairwise distances for individual mice, and red crosses mark identified outliers.

(H) Models depicting cell-type- and movement-specific layer 5B signaling in caudal forelimb area of motor cortex (CFA). Colored circles represent movement-invariant (cyan), push bias (blue), and pull bias (green) neurons.

(Kiritani et al., 2012). Asymmetric projection-class connectivity as well as differences in input structure and intrinsic excitability (Anderson et al., 2010; Hooks et al., 2013; Kiritani et al., 2012; Oswald et al., 2013) provide a mechanism to flexibly route movement-specific information via two independent output channels depending on behavioral requirements. Our cell-type-specific imaging identified that only a small proportion of PT neurons conveyed movement-specific information. In contrast, almost half of IT neurons displayed movement specificity, with similar proportions of push and pull bias. Although PT and IT activity onsets occurred prior to and throughout movement, consistent with both pathways contributing to movement initiation and execution (Chen et al., 2017; Economo et al., 2018; Li et al., 2015; Park et al., 2022; Wang et al., 2017), the proportion of IT neurons with high decoding accuracy was highest prior to movement initiation, whereas for PT neurons, this occurred during movement execution. This suggests that information relating to movement type is first conveyed by IT neurons, which project to the cortex and bilaterally to the striatum but not other subcortical structures (Levesque et al., 1996; Muñoz-Castañeda et al., 2021; Wilson, 1987; Winnubst et al., 2019), before PT neurons then propagate information to subcortical, brain stem, and spinal cord circuits necessary for online control of forelimb movement (Economo et al., 2018; Kita and Kita, 2012; Muñoz-Castañeda et al., 2021; Ueta et al., 2014; Winnubst et al., 2019). Importantly, the proportions of PT or IT neurons decoding movement type at any time never exceeded 25%, consistent with movement-specific signaling being confined to a relatively small subpopulation of layer 5B projection neurons. What is unclear is the extent to which movement-specific signaling in PT and IT neurons is organized by the projection target, as seen in anterolateral motor cortex during directional licking (Chen et al., 2017; Economo et al., 2018; Li et al., 2015). Targeting neurons based on molecular expression profiles and projection specificity (Muñoz-Castañeda et al., 2021; Winnubst et al., 2019) will provide a finer-grained understanding of how movement-specific information is routed via molecularly distinct projection pathways.

We also found that PT and IT neurons displaying high decoding accuracy were distributed across FOVs. This lack of functional clustering differs from the proposed modular organization of directionally tuned cells in primate motor cortex, where neurons with a similar preferred direction tend to cluster into vertically oriented minicolumns approximately 50–100 μm wide, repeated every 250 μm (Amirikian and Georgopoulos, 2003; Cheney et al., 1985; Georgopoulos et al., 2007; Jones and Wise, 1977), but consistent with the distributed spatial organization of direction-specific layer 5B projection neurons in mouse anterolateral motor cortex during execution of a whisker-based object location discrimination task (Li et al., 2015). The apparent lack of spatial clustering in CFA is unlikely to be due to reduced sensitivity of our analysis methods because 95% confidence intervals provide a lower bound indication of cluster size so that spatial clusters based on decoding accuracy would have to be less than ~50 μm. Similarly, we found no evidence of temporal clustering in neurons with high (movement-specific) or low (movement-invariant) decoding accuracy, as expected, given that the onset of PT and IT neuron activity changes occurred ~300 ms prior to movement and tiled the peri-movement period.

Our work extends previous findings in superficial layers of motor cortex showing that neurons with task-related response properties are spatially intermingled (Galiñanes et al., 2018; Huber et al., 2012), supporting a model where movement-specific signaling in layer 5B is distributed across small but distinct subpopulations of projection neurons. The flexible routing of information through distributed descending projection pathways could, in principle, provide a mechanism for differentially controlling movement variables necessary for executing a wide repertoire of limb movements.

Limitations of the study

In the present study, we suggest that layer 5B population dynamics largely reflect movement-invariant signaling, whereas relatively small subpopulations of projection neurons convey movement-specific information. However, our task design was limited to two diametrically opposing movements along a single axis, where the starting posture for push and pull movements differed. A fuller understanding of how movement-specific signaling is organized across mouse layer 5 projection neurons would require implementation of a task that incorporates multiple movement trajectories initiated from the same start position (e.g., a center-out multi-direction joystick or reaching task) or a task in which mice learn to perform multiple distinct actions (e.g., lever push and reach to grab). Another limitation of our study is that we only sampled the activity of identified projection neurons in upper layer 5B. Given the known depth dependence of top-down and long-range inputs in layer 5 (Anderson et al., 2010; Weiler et al., 2008; Hooks et al., 2013) and laminar organization of output neurons based on projection targets (Economo et al., 2018), encoding of movement specificity is likely to differ depending on cortical depth. This could be addressed using methods to image deeper within the cortex (e.g., using a glass prism or 3-photon microscopy) or high-density silicone probe recordings with optogenetic identification of projection neuron class.

STAR★METHODS

Detailed methods are provided in the online version of this paper and include the following:

- KEY RESOURCES TABLE
- RESOURCE AVAILABILITY
  - Lead contact
  - Materials availability
  - Data and code availability
- EXPERIMENTAL MODEL AND SUBJECT DETAILS
- METHOD DETAILS
  - General surgery
  - Behavioral training
  - Forelimb kinematic tracking
  - *In vivo* pharmacology
  - Quantifying muscimol diffusion
  - Retrograde tracing
  - Immunohistochemistry
  - 2-photon imaging
  - Trial-to-trial correlations

- Extracellular recording and spike sorting
- Neural decoding
- Dimensionality reduction
- Spatiotemporal mapping

- QUANTIFICATION AND STATISTICAL ANALYSIS

SUPPLEMENTAL INFORMATION

Supplemental information can be found online at https://doi.org/10.1016/j.celrep.2022.110801.

ACKNOWLEDGMENTS

We are grateful to Gülsen Sürmeli, Matt Nolan, and members of the Nolan, Duguid, and Sürmeli labs for experimental discussions and comments on the manuscript; Nick Steinmetz for the suggested design of the author contribution matrix; and Tiago Branco and Kostas Betsios for Mantis64. AAV-GCaMP6s was a gift from Douglas Kim and the GENIE Project (Addgene 100844-AAV1). AAV-pgk-Cre was a gift from Patrick Aebischer (Addgene viral prep 24593-AAVrg). pAAV-CAG-Flex-mRuby2-GSG-P2A-GCaMP6s-WPRE-pA was a gift from Tobias Bonhoeffer, Mark Huebener, and Tobias Rose (Addgene viral prep 68717-AAV1). Confocal microscopy was performed in the IMPACT Imaging Facility at the University of Edinburgh. Research was supported by grants from the Biotechnology and Biological Sciences Research Council (BB/R018537/1 to I.D.), the DFG fellowship program (AM 443/1-1 to J.J.A.), the Shirley Foundation, a Simons Initiative for the Developing Brain (SIDB) PhD studentship (to C.E.), an A*STAR PhD studentship (to B.P.), and a Wellcome Senior Research Fellowship (110131/Z/15/Z to I.D.).

AUTHOR CONTRIBUTIONS

Conceptualization, B.P., J.J.A., and I.D.; methodology & investigation, S.P.C., J.J.A., B.P., J.D., Y.W., C.E., M.C., T.C., L.M., M.H.H., and I.D.; resources, J.J.A., Y.W., M.C., A.A.F., and M.H.H.; review & editing, all authors.

DECLARATION OF INTEREST

The authors declare no competing interests.

Received: November 20, 2020
Revised: November 15, 2021
Accepted: April 18, 2022
Published: May 10, 2022

REFERENCES

Amirikian, B., and Georgopoulos, A.P. (2003). Modular organization of directionally tuned cells in the motor cortex: is there a short-range order? Proc. Natl. Acad. Sci. U S A *100*, 12474–12479. https://doi.org/10.1073/pnas.2037719100.

Anderson, C.T., Sheets, P.L., Kiritani, T., and Shepherd, G.M.G. (2010). Sublayer-specific microcircuits of corticospinal and corticostriatal neurons in motor cortex. Nat. Neurosci. *13*, 739–744. https://doi.org/10.1038/nn.2538.

Baker, A., Kalmbach, B., Morishima, M., Kim, J., Juavinett, A., Li, N., and Dembrow, N. (2018). Specialized subpopulations of deep-layer pyramidal neurons in the neocortex: bridging cellular properties to functional consequences. J. Neurosci. *38*, 5441–5455. https://doi.org/10.1523/jneurosci.0150-18.2018.

Bartlett, M.S., and Fowler, R.H. (1937). Properties of sufficiency and statistical tests. Proc. R. Soc. Lond. Ser. A Math. Phys. Sci. *160*, 268–282.

Brown, S.P., and Hestrin, S. (2009). Intracortical circuits of pyramidal neurons reflect their long-range axonal targets. Nature *457*, 1133–1136. https://doi.org/10.1038/nature07658.

Chen, T.-W., Li, N., Daie, K., and Svoboda, K. (2017). A map of anticipatory activity in mouse motor cortex. Neuron *94*, 866–879.e4. https://doi.org/10.1016/j.neuron.2017.05.005.

Cheney, P.D., Fetz, E.E., and Palmer, S.S. (1985). Patterns of facilitation and suppression of antagonist forelimb muscles from motor cortex sites in the awake monkey. J. Neurophysiol. *53*, 805–820. https://doi.org/10.1152/jn.1985.53.3.805.

Churchland, M.M., Cunningham, J.P., Kaufman, M.T., Foster, J.D., Nuyujukian, P., Ryu, S.I., and Shenoy, K.V. (2012). Neural population dynamics during reaching. Nature *487*, 51–56. https://doi.org/10.1038/nature11129.

Churchland, M.M., Cunningham, J.P., Kaufman, M.T., Ryu, S.I., and Shenoy, K.V. (2010). Cortical preparatory activity: representation of movement or first cog in a dynamical machine? Neuron *68*, 387–400. https://doi.org/10.1016/j.neuron.2010.09.015.

Cunningham, J.P., and Yu, B.M. (2014). Dimensionality reduction for large-scale neural recordings. Nat. Neurosci. *17*, 1500–1509. https://doi.org/10.1038/nn.3776.

Dacre, J., Colligan, M., Clarke, T., Ammer, J.J., Schiemann, J., Chamosa-Pino, V., Claudi, F., Harston, J.A., Eleftheriou, C., Pakan, J.M.P., et al. (2021). A cerebellar-thalamocortical pathway drives behavioral context-dependent movement initiation. Neuron *109*, 2326–2338. https://doi.org/10.1016/j.neuron.2021.05.016.

Economo, M.N., Viswanathan, S., Tasic, B., Bas, E., Winnubst, J., Menon, V., Graybuck, L.T., Nguyen, T.N., Smith, K.A., Yao, Z., et al. (2018). Distinct descending motor cortex pathways and their roles in movement. Nature *563*, 79–84. https://doi.org/10.1038/s41586-018-0642-9.

Elsayed, G.F., Lara, A.H., Kaufman, M.T., Churchland, M.M., and Cunningham, J.P. (2016). Reorganization between preparatory and movement population responses in motor cortex. Nat. Commun. *7*, 13239. https://doi.org/10.1038/ncomms13239.

Estebanez, L., Hoffmann, D., Voigt, B.C., and Poulet, J.F.A. (2017). Parvalbumin-expressing GABAergic neurons in primary motor cortex signal reaching. Cell Rep. *20*, 308–318. https://doi.org/10.1016/j.celrep.2017.06.044.

Evarts, E.V. (1968). Relation of pyramidal tract activity to force exerted during voluntary movement. J. Neurophysiol. *31*, 14–27. https://doi.org/10.1152/jn.1968.31.1.14.

Galiñanes, G.L., Bonardi, C., and Huber, D. (2018). Directional reaching for water as a cortex-dependent behavioral framework for mice. Cell Rep. *22*, 2767–2783. https://doi.org/10.1016/j.celrep.2018.02.042.

Georgopoulos, A.P., Kalaska, J.F., Caminiti, R., and Massey, J.T. (1982). On the relations between the direction of two-dimensional arm movements and cell discharge in primate motor cortex. J. Neurosci. *2*, 1527–1537. https://doi.org/10.1523/jneurosci.02-11-01527.1982.

Georgopoulos, A.P., Merchant, H., Naselaris, T., and Amirikian, B. (2007). Mapping of the preferred direction in the motor cortex. Proc. Natl. Acad. Sci. U S A *104*, 11068–11072. https://doi.org/10.1073/pnas.0611597104.

Guo, J.-Z., Graves, A.R., Guo, W.W., Zheng, J., Lee, A., Rodríguez-González, J., Li, N., Macklin, J.J., Phillips, J.W., Mensh, B.D., et al. (2015). Cortex commands the performance of skilled movement. Elife *4*, e10774. https://doi.org/10.7554/elife.10774.

Hocherman, S., and Wise, S.P. (1991). Effects of hand movement path on motor cortical activity in awake, behaving rhesus monkeys. Exp. Brain Res. *83*, 285–302. https://doi.org/10.1007/bf00231153.

Hooks, B.M., Mao, T., Gutnisky, D.A., Yamawaki, N., Svoboda, K., and Shepherd, G.M.G. (2013). Organization of cortical and thalamic input to pyramidal neurons in mouse motor cortex. J. Neurosci. *33*, 748–760. https://doi.org/10.1523/jneurosci.4338-12.2013.

Hooks, B.M., Papale, A.E., Paletzki, R.F., Feroze, M.W., Eastwood, B.S., Couey, J.J., Winnubst, J., Chandrashekar, J., and Gerfen, C.R. (2018). Topographic precision in sensory and motor corticostriatal projections varies across cell type and cortical area. Nat. Commun. *9*, 3549. https://doi.org/10.1038/s41467-018-05780-7.

Huber, D., Gutnisky, D.A., Peron, S., O'Connor, D.H., Wiegert, J.S., Tian, L., Oertner, T.G., Looger, L.L., and Svoboda, K. (2012). Multiple dynamic representations in the motor cortex during sensorimotor learning. Nature *484*, 473–478. https://doi.org/10.1038/nature11039.

Hwang, E.J., Dahlen, J.E., Hu, Y.Y., Aguilar, K., Yu, B., Mukundan, M., Mitani, A., and Komiyama, T. (2019). Disengagement of motor cortex from movement control during long-term learning. Sci. Adv. *5*, eaay0001. https://doi.org/10.1126/sciadv.aay0001.

Hwang, E.J., Dahlen, J.E., Mukundan, M., and Komiyama, T. (2021). Disengagement of motor cortex during long-term learning tracks the performance level of learned movements. J. Neurosci. *41*, 7029–7047. https://doi.org/10.1523/jneurosci.3049-20.2021.

Isomura, Y., Harukuni, R., Takekawa, T., Aizawa, H., and Fukai, T. (2009). Microcircuitry coordination of cortical motor information in self-initiation of voluntary movements. Nat. Neurosci. *12*, 1586–1593. https://doi.org/10.1038/nn.2431.

Jones, E.G., and Wise, S.P. (1977). Size, laminar and columnar distribution of efferent cells in the sensory-motor cortex of monkeys. J. Comp. Neurol. *175*, 391–437. https://doi.org/10.1002/cne.901750403.

Jun, J.J., Steinmetz, N.A., Siegle, J.H., Denman, D.J., Bauza, M., Barbarits, B., Lee, A.K., Anastassiou, C.A., Andrei, A., Aydın, Ç., et al. (2017). Fully integrated silicon probes for high-density recording of neural activity. Nature *551*, 232–236. https://doi.org/10.1038/nature24636.

Kaifosh, P., Zaremba, J.D., Danielson, N.B., and Losonczy, A. (2014). SIMA: Python software for analysis of dynamic fluorescence imaging data. Front. Neuroinform. *8*, 80. https://doi.org/10.3389/fninf.2014.00080.

Kaufman, M.T., Churchland, M.M., Ryu, S.I., and Shenoy, K.V. (2014). Cortical activity in the null space: permitting preparation without movement. Nat. Neurosci. *17*, 440–448. https://doi.org/10.1038/nn.3643.

Kaufman, M.T., Seely, J.S., Sussillo, D., Ryu, S.I., Shenoy, K.V., and Churchland, M.M. (2016). The largest response component in the motor cortex reflects movement timing but not movement type. eNeuro *3*, ENEURO.0085-16.2016. https://doi.org/10.1523/eneuro.0085-16.2016.

Kawai, R., Markman, T., Poddar, R., Ko, R., Fantana, A.L., Dhawale, A.K., Kampff, A.R., and Ölveczky, B.P. (2015). Motor cortex is required for learning but not for executing a motor skill. Neuron *86*, 800–812. https://doi.org/10.1016/j.neuron.2015.03.024.

Keemink, S.W., Lowe, S.C., Pakan, J.M.P., Dylda, E., van Rossum, M.C.W., and Rochefort, N.L. (2018). FISSA: a neuropil decontamination toolbox for calcium imaging signals. Sci. Rep. *8*, 3493. https://doi.org/10.1038/s41598-018-21640-2.

Kiritani, T., Wickersham, I.R., Sebastian Seung, H., and Shepherd, G.M.G. (2012). Hierarchical connectivity and connection-specific dynamics in the corticospinal–corticostriatal microcircuit in mouse motor cortex. J. Neurosci. *32*, 4992–5001. https://doi.org/10.1523/jneurosci.4759-11.2012.

Kita, T., and Kita, H. (2012). The subthalamic nucleus is one of multiple innervation sites for long-range corticofugal axons: a single-axon tracing study in the rat. J. Neurosci. *32*, 5990–5999. https://doi.org/10.1523/jneurosci.5717-11.2012.

Kurtzer, I., Herter, T.M., and Scott, S.H. (2005). Random change in cortical load representation suggests distinct control of posture and movement. Nat. Neurosci. *8*, 498–504. https://doi.org/10.1038/nn1420.

Lawrence, D.G., and Kuypers, H.G. (1968). The functional organization of the motor system in the monkey. I. The effects of bilateral pyramidal lesions. Brain *91*, 1–14. https://doi.org/10.1093/brain/91.1.1.

Lemon, R.N. (2008). Descending pathways in motor control. Annu. Rev. Neurosci. *31*, 195–218. https://doi.org/10.1146/annurev.neuro.31.060407.125547.

Levesque, M., Charara, A., Gagnon, S., Parent, A., and Deschenes, M. (1996). Corticostriatal projections from layer V cells in rat are collaterals of long-range corticofugal axons. Brain Res. *709*, 311–315. https://doi.org/10.1016/0006-8993(95)01333-4.

Levy, S., Lavzin, M., Benisty, H., Ghanayim, A., Dubin, U., Achvat, S., Brosh, Z., Aeed, F., Mensh, B.D., Schiller, Y., et al. (2020). Cell-type-specific outcome representation in the primary motor cortex. Neuron *107*, 954–971.e9. https://doi.org/10.1016/j.neuron.2020.06.006.

Li, N., Chen, T.-W., Guo, Z.V., Gerfen, C.R., and Svoboda, K. (2015). A motor cortex circuit for motor planning and movement. Nature *519*, 51–56. https://doi.org/10.1038/nature14178.

Martin, J.H., and Ghez, C. (1991). Impairments in reaching during reversible inactivation of the distal forelimb representation of the motor cortex in the cat. Neurosci. Lett. *133*, 61–64. https://doi.org/10.1016/0304-3940(91)90057-z.

Maruoka, H., Nakagawa, N., Tsuruno, S., Sakai, S., Yoneda, T., and Hosoya, T. (2017). Lattice system of functionally distinct cell types in the neocortex. Science *358*, 610–615. https://doi.org/10.1126/science.aam6125.

Mathis, A., Mamidanna, P., Cury, K.M., Abe, T., Murthy, V.N., Mathis, M.W., and Bethge, M. (2018). DeepLabCut: markerless pose estimation of user-defined body parts with deep learning. Nat. Neurosci. *21*, 1281–1289. https://doi.org/10.1038/s41593-018-0209-y.

Messier, J., and Kalaska, J.F. (2000). Covariation of primate dorsal premotor cell activity with direction and amplitude during a memorized-delay reaching task. J. Neurophysiol. *84*, 152–165. https://doi.org/10.1152/jn.2000.84.1.152.

Miri, A., Warriner, C.L., Seely, J.S., Elsayed, G.F., Cunningham, J.P., Churchland, M.M., and Jessell, T.M. (2017). Behaviorally selective engagement of short-latency effector pathways by motor cortex. Neuron *95*, 683–696.e11. https://doi.org/10.1016/j.neuron.2017.06.042.

Molyneaux, B.J., Arlotta, P., Menezes, J.R.L., and Macklis, J.D. (2007). Neuronal subtype specification in the cerebral cortex. Nat. Rev. Neurosci. *8*, 427–437. https://doi.org/10.1038/nrn2151.

Moran, D.W., and Schwartz, A.B. (1999). Motor cortical representation of speed and direction during reaching. J. Neurophysiol. *82*, 2676–2692. https://doi.org/10.1152/jn.1999.82.5.2676.

Morishima, M., and Kawaguchi, Y. (2006). Recurrent connection patterns of corticostriatal pyramidal cells in frontal cortex. J. Neurosci. *26*, 4394–4405. https://doi.org/10.1523/jneurosci.0252-06.2006.

Morishima, M., Morita, K., Kubota, Y., and Kawaguchi, Y. (2011). Highly differentiated projection-specific cortical subnetworks. J. Neurosci. *31*, 10380–10391. https://doi.org/10.1523/jneurosci.0772-11.2011.

Muñoz-Castañeda, R., Zingg, B., Matho, K.S., Chen, X., Wang, Q., Foster, N.N., Li, A., Narasimhan, A., Hirokawa, K.E., Huo, B., et al. (2021). Cellular anatomy of the mouse primary motor cortex. Nature *598*, 159–166. https://doi.org/10.1038/s41586-021-03970-w.

Nelson, A., Abdelmesih, B., and Costa, R.M. (2021). Corticospinal populations broadcast complex motor signals to coordinated spinal and striatal circuits. Nat. Neurosci. *24*, 1721–1732. https://doi.org/10.1038/s41593-021-00939-w.

Oswald, M.J., Tantirigama, M.L.S., Sonntag, I., Hughes, S.M., and Empson, R.M. (2013). Diversity of layer 5 projection neurons in the mouse motor cortex. Front. Cell Neurosci. *7*, 174. https://doi.org/10.3389/fncel.2013.00174.

Pachitariu, M., Steinmetz, N., Kadir, S., and Carandini, M. (2016). Kilosort: real-time spike-sorting for extracellular electrophysiology with hundreds of channels. Preprint at bioRxiv. https://doi.org/10.1101/061481.

Panigrahi, B., Martin, K.A., Li, Y., Graves, A.R., Vollmer, A., Olson, L., Mensh, B.D., Karpova, A.Y., and Dudman, J.T. (2015). Dopamine is required for the neural representation and control of movement vigor. Cell *162*, 1418–1430. https://doi.org/10.1016/j.cell.2015.08.014.

Paninski, L., Fellows, M.R., Hatsopoulos, N.G., and Donoghue, J.P. (2004). Spatiotemporal tuning of motor cortical neurons for hand position and velocity. J. Neurophysiol. *91*, 515–532. https://doi.org/10.1152/jn.00587.2002.

Park, J., Phillips, J.W., Guo, J.Z., Martin, K.A., Hantman, A.W., and Dudman, J.T. (2022). Motor cortical output for skilled forelimb movement is selectively distributed across projection neuron classes. Sci. Adv. *8*, 1–11. https://doi.org/10.1126/sciadv.abj5167.

Paxinos, G., and Franklin, K. (2008). The mouse brain in stereotaxic coordinates. In Compact: The Coronal Plates and Diagrams, 3rd edition (Elsevier Science Publishing/Academic Press).

Peters, A.J., Lee, J., Hedrick, N.G., O'Neil, K., and Komiyama, T. (2017). Reorganization of corticospinal output during motor learning. Nat. Neurosci. *20*, 1133–1141. https://doi.org/10.1038/nn.4596.

Podgorski, K., and Ranganathan, G. (2016). Brain heating induced by near-infrared lasers during multiphoton microscopy. J. Neurophysiol. *116*, 1012–1023. https://doi.org/10.1152/jn.00275.2016.

Reiner, A., Hart, N.M., Lei, W., and Deng, Y. (2010). Corticostriatal projection neurons - dichotomous types and dichotomous functions. Front. Neuroanat. *4*, 142. https://doi.org/10.3389/fnana.2010.00142.

Riehle, A., Kornblum, S., and Requin, J. (1994). Neuronal coding of stimulus-response association rules in the motor cortex. Neuroreport *5*, 2462–2464. https://doi.org/10.1097/00001756-199412000-00014.

Ruder, L., and Arber, S. (2019). Brainstem circuits controlling action diversification. Annu. Rev. Neurosci. *42*, 485–504. https://doi.org/10.1146/annurev-neuro-070918-050201.

Rueden, C.T., Schindelin, J., Hiner, M.C., DeZonia, B.E., Walter, A.E., Arena, E.T., and Eliceiri, K.W. (2017). ImageJ2: ImageJ for the next generation of scientific image data. BMC Bioinf. *18*, 529. https://doi.org/10.1186/s12859-017-1934-z.

Sauerbrei, B.A., Guo, J.-Z., Cohen, J.D., Mischiati, M., Guo, W., Kabra, M., Verma, N., Mensh, B., Branson, K., and Hantman, A.W. (2019). Cortical pattern generation during dexterous movement is input-driven. Nature *577*, 386–391. https://doi.org/10.1038/s41586-019-1869-9.

Schiemann, J., Puggioni, P., Dacre, J., Pelko, M., Domanski, A., van Rossum, M.C.W., and Duguid, I. (2015). Cellular mechanisms underlying behavioral state-dependent bidirectional modulation of motor cortex output. Cell Rep. *11*, 1319–1330. https://doi.org/10.1016/j.celrep.2015.04.042.

Schindelin, J., Arganda-Carreras, I., Frise, E., Kaynig, V., Longair, M., Pietzsch, T., Preibisch, S., Rueden, C., Saalfeld, S., Schmid, B., et al. (2012). Fiji: an open-source platform for biological-image analysis. Nat. Methods *9*, 676–682. https://doi.org/10.1038/nmeth.2019.

Seabold, S., and Perktold, J. (2010). Statsmodels: econometric and statistical modeling with python. Paper presented at: Proceedings of the 9th Python in Science Conference (Austin, TX).

Shepherd, G.M.G. (2013). Corticostriatal connectivity and its role in disease. Nat. Rev. Neurosci. *14*, 278–291. https://doi.org/10.1038/nrn3469.

Soma, S., Saiki, A., Yoshida, J., Ríos, A., Kawabata, M., Sakai, Y., and Isomura, Y. (2017). Distinct laterality in forelimb-movement representations of rat primary and secondary motor cortical neurons with intratelencephalic and pyramidal tract projections. J. Neurosci. *37*, 10904–10916. https://doi.org/10.1523/jneurosci.1188-17.2017.

Stopfer, M., Jayaraman, V., and Laurent, G. (2003). Intensity versus identity coding in an olfactory system. Neuron *39*, 991–1004. https://doi.org/10.1016/j.neuron.2003.08.011.

Sussillo, D., Churchland, M.M., Kaufman, M.T., and Shenoy, K.V. (2015). A neural network that finds a naturalistic solution for the production of muscle activity. Nat. Neurosci. *18*, 1025–1033. https://doi.org/10.1038/nn.4042.

Thach, W.T. (1978). Correlation of neural discharge with pattern and force of muscular activity, joint position, and direction of intended next movement in motor cortex and cerebellum. J. Neurophysiol. *41*, 654–676. https://doi.org/10.1152/jn.1978.41.3.654.

Ueta, Y., Otsuka, T., Morishima, M., Ushimaru, M., and Kawaguchi, Y. (2014). Multiple layer 5 pyramidal cell subtypes relay cortical feedback from secondary to primary motor areas in rats. Cereb. Cortex *24*, 2362–2376. https://doi.org/10.1093/cercor/bht088.

Wang, X., Liu, Y., Li, X., Zhang, Z., Yang, H., Zhang, Y., Williams, P.R., Alwahab, N.S.A., Kapur, K., Yu, B., et al. (2017). Deconstruction of corticospinal circuits for goal-directed motor skills. Cell *171*, 440–455.e14. https://doi.org/10.1016/j.cell.2017.08.014.

Wei, Z., Lin, B.-J., Chen, T.-W., Daie, K., Svoboda, K., and Druckmann, S. (2020). A comparison of neuronal population dynamics measured with calcium imaging and electrophysiology. PLoS Comput. Biol. *16*, e1008198. https://doi.org/10.1371/journal.pcbi.1008198.

Weiler, N., Wood, L., Yu, J., Solla, S.A., and Shepherd, G.M.G. (2008). Top-down laminar organization of the excitatory network in motor cortex. Nat. Neurosci. *11*, 360–366. https://doi.org/10.1038/nn2049.

Weinrich, M., Wise, S.P., and Mauritz, K.H. (1984). A neurophysiological study of the premotor cortex in the rhesus monkey. Brain *107*, 385–414. https://doi.org/10.1093/brain/107.2.385.

Wilson, C.J. (1987). Morphology and synaptic connections of crossed corticostriatal neurons in the rat. J. Comp. Neurol. *263*, 567–580. https://doi.org/10.1002/cne.902630408.

Winnubst, J., Bas, E., Ferreira, T.A., Wu, Z., Economo, M.N., Edson, P., Arthur, B.J., Bruns, C., Rokicki, K., Schauder, D., et al. (2019). Reconstruction of 1,000 projection neurons reveals new cell types and organization of long-range connectivity in the mouse brain. Cell *179*, 268–281.e13. https://doi.org/10.1016/j.cell.2019.07.042.

Yttri, E.A., and Dudman, J.T. (2016). Opponent and bidirectional control of movement velocity in the basal ganglia. Nature *533*, 402–406. https://doi.org/10.1038/nature17639.

Zhou, Z., and Tin, C. (2021). Effective and efficient neural networks for spike inference from *in vivo* calcium imaging. Preprint at bioRxiv. https://doi.org/10.1101/2021.08.30.458217.

Zong, W., Heldt, T., Moody, G.B., and Mark, R.G. (2003). An open-source algorithm to detect onset of arterial blood pressure pulses. In Computers in Cardiology, 2003 (IEEE), pp. 259–262. ieeexplore.ieee.org.

STAR★METHODS

KEY RESOURCES TABLE

REAGENT or RESOURCE	SOURCE	IDENTIFIER
Antibodies		
AlexaFluor-568 goat anti-mouse	Invitrogen	CAT#: A-21124; AB_2535766
Anti-NeuN Antibody, clone A60	Sigma Aldrich	Cat#: MAB377
Bacterial and virus strains		
AAV1-Syn-GCaMP6s	Penn Vector Core	#100844-AAV1
AAV-pkg-Cre	Addgene	#24593-AAVrg
pAAV-CAG-Flex-mRuby2-GSG-P2A-GCaMP6s-WPREpA	Addgene	#68717-AAV1
Chemicals, peptides, and recombinant proteins		
Muscimol hydrobromide	Sigma-Aldrich, Missouri, USA	Cat#: G019-5MG
Muscimol, BODIPY TMR-X Conjugate	Thermo Fisher Scientific	Cat#: M23400
Red Retrobeads™	Lumaflor	N/A
Green Retrobeads™	Lumaflor	N/A
Fast Blue	Polysciences	Cat#: 17740
Vybrant DiI Cell-Labeling	Thermo Fisher Scientific	Cat#: V22885
Experimental models: Organisms/strains		
Mouse: C57BL/6J	The Jackson Laboratory	RRID: IMSR_JAX:000664
Software and algorithms		
MATLAB	MathWorks (https://www.mathworks.com/)	RRID: SCR_001622
Python 3	Python (https://www.python.org/)	RRID: SCR_008394
Streampix 7.0	Norpix (https://www.norpix.com/products/streampix/streampix.php)	RRID:SCR_015773
SpikeGLX	(http://billkarsh.github.io/SpikeGLX/)	N/A
Mantis64	https://www.mantis64.com/	N/A
Kilosort3	https://github.com/MouseLand/Kilosort	N/A
Phy	Jun et al., 2017 (https://github.com/cortex-lab/phy)	N/A
FIJI	Schindelin et al., 2012 (https://github.com/fiji)	RRID:SCR_002285
Deeplabcut	Adaptive Motor Control Lab (https://github.com/DeepLabCut/DeepLabCut)	N/A
FISSA	Keemink et al., 2018	N/A
SIMA 1.3.2	Kaifosh et al., 2014	
Onset detection algorithm	Zong et al., 2003	N/A
Arduino IDE 1.6.5	Arduino (https://www.arduino.cc/en/software)	N/A
NIS-Elements	Nikon (https://www.microscope.healthcare.nikon.com/products/software)	RRID:SCR_014329
LotosScan	LabVIEW version 8.2; National Instruments	N/A

(*Continued on next page*)

Continued

REAGENT or RESOURCE	SOURCE	IDENTIFIER
SciScan	Scientifica (https://www.scientifica.uk.com/products/scientifica-sciscan)	N/A
Other		
Neuropixels probes	IMEC	Neuropixels 1.0
Laser, Ti:Sapphire pulsed	Coherent	Chameleon Vision-S
Arduino UNO	Arduino (https://www.arduino.cc/en/Guide/ArduinoUno/)	RRID:SCR_017284

RESOURCE AVAILABILITY

Lead contact

Further information and requests for resources and reagents should be directed to and will be fulfilled by the Lead Contact, Ian Duguid ( ).

Materials availability

This study did not generate new unique reagents.

Data and code availability

Data reported in this paper will be shared by the lead contact upon request. All original code has been deposited at https://github.com/DuguidLab and is publicly available as of the date of publication. Any additional information required to reanalyze the data reported in this paper is available from the lead contact upon request.

EXPERIMENTAL MODEL AND SUBJECT DETAILS

Male adult C57BL/6J wild-type mice (5-12 weeks old, 20-30 g, 1-4 animals per cage) were maintained on a reversed 12:12 hour light:-dark cycle and provided *ad libitum* access to food and water as well as environmental enrichment (e.g., cardboard tubes, plastic domes, chewing sticks, and rope ladders). All experiments and procedures were approved by the University of Edinburgh local ethical review committee and performed under license from the UK Home Office in accordance with the Animal (Scientific Procedures) Act 1986.

METHOD DETAILS

General surgery

Surgical procedures were performed under ~1.5% isoflurane anaesthesia and each animal received fluid replacement therapy (0.5 ml sterile Ringer's solution), buprenorphine (0.05 mg/kg) and either carprofen (4 mg/kg) or dexamethasone (2 mg/kg) for pain relief and to reduce inflammation. At 24 and 48 hours, carprofen (4 mg/kg) was administered for post-operative pain relief. Craniotomies were performed in a stereotactic frame (David Kopf Instruments, CA, USA) using a hand-held dentist drill with 0.5 mm burr. A small lightweight headplate (0.5 g) was implanted on the surface of the skull using cyanoacrylate glue and dental cement (Lang Dental, IL, USA) and mice were left for at least 48 hours to recover.

Behavioral training

After recovery from head plate surgery, mice were handled extensively before being head restrained and habituated to a custom forelimb lever push / pull behavioral setup. Mice were trained to perform two diametrically opposing movements (4 mm push or pull) in response to a 6 kHz auditory cue to obtain a 5 μl water reward. Mice rested their right forepaw on a stationary lever while making push or pull movements with their left forepaw. Upon completion of a successful push or pull (determined by the status of IR beams at either end of the lever travel), the moveable lever was locked in place for the duration of the reward period (3 s) and the water reward was delivered by an automated spout - both locking mechanism and spout were controlled by micro servo motors (HXT900, HexTronik). To increase task engagement, mice were placed on a water control paradigm (1 ml/day) and weighed daily to ensure body weight remained above 85% of baseline. Mice were trained once per day for 30 mins and advanced through different phases of the task once they achieved > 50 rewards in two consecutive sessions or > 70 rewards in a single session. Initially, mice were required to perform uncued push and pull movements to obtain rewards (phase 1). Next, an auditory cue was introduced with pseudo-random inter-trial-interval (ITI) of 4-6 s and a response window of 10 s (phase 2). During the ITI, mice had to hold the move-

able lever still as spontaneous movements of the lever within the ITI triggered a reset and the lever was locked in the original position for 1 s. The response window was gradually reduced to 5 (phase 3) and then 2 s (phase 4) across training sessions. Mice were deemed "expert" after achieving > 70 rewards on two consecutive days of training with a response window of 2 s. During 2-photon imaging experiments (see below), a 1 s delay between completion of a successful movement and reward delivery was introduced to temporally separate movement- and reward-related activity.

Forelimb kinematic tracking

Behavior was recorded using a high-speed camera (60 fps Prosilica GC780C, Allied Vision, Germany or 100 - 300 fps Mako U U-029, Allied Vision - cell-type specific calcium imaging and *in vivo* pharmacology) and acquired using Streampix 7 (Norpix, Canada) or Mantis64 (https://www.mantis64.com/). To measure gross forelimb movement, a region of interest (ROI) was manually drawn around the left forelimb and the frame-to-frame difference in pixel intensity was calculated using the formula: $MI_f = \sum_i^N {}_1(c_{f+1,i} - c_{f,i})^2$, where $c_{f,i}$ is the grayscale level of pixel i in frame f. The resulting motion index was smoothed with a 1 s LOESS filter then aligned to behaviorally relevant time points (lever displacement, cue presentation etc.), with videos and behavior resampled to a common sampling rate. Motion index onsets were calculated by aligning the motion index to the lever movement and identifying the first point prior to movement where mean motion index was > threshold (mean upper bound of 95% confidence interval during baseline). Directional tracking of the forelimb and lever movement was performed using Deep Lab Cut (Mathis et al., 2018). Tracking data were aligned to cue presentation, baselined to mean xy position during the 100 ms prior to cue and then cropped between movement initiation and movement completion. For presentation, trials of different durations were resampled to a fixed length to enable a mean trajectory to be plotted across multiple trials.

In vivo pharmacology

To assess the behavioral effects of caudal forelimb area (CFA; N = 10) or hind limb motor cortex ($M1_{hl}$; N = 5) inactivation, 'expert' mice had a small burr hole drilled directly above the target area (CFA: 1.6 mm lateral, 0.6 mm rostral to bregma; $M1_{hl}$: 1.25 mm lateral, 1.25 caudal to bregma) before being left to recover for > 90 mins. After 10 mins of baseline behavior, the lever was locked and a small volume of the $GABA_A$ receptor agonist muscimol (200 nl, 2 mM) dissolved in external saline solution (containing 150 mM NaCl, 2.5 mM KCl, 10 mM HEPES, 1.5 mM $CaCl_2$ and 1 mM $MgCl_2$, adjusted to pH 7.3) was injected into the target area. Each injection site was at a depth of 0.7 mm below the cortical surface. To confirm the anatomical location of drug injection, 1% w/v of retrobeads (red, Lumaflor Inc.) was included in the injected solution. A subset of mice (N = 5/10) also had saline injected into CFA (vehicle only; injection was perfromed on a different day). In these experiments, mice were randomly assigned to drug or control groups (each mouse received one injection of muscimol and one injection of saline) and experiments were blinded. After each experiment, mice were transcardially perfused and coronal (60 μm) or sagittal (100 μm) sections were cut with a vibratome (Leica VT1000S), mounted with Vectashield mounting medium (H-1000, Vector Laboratories), imaged using a fluorescence microscope (Leica DMR, 5x objective) and manually referenced to the Paxinos and Franklin Mouse Brain Atlas (Paxinos and Franklin, 2008). Behavioral metrics were analyzed by comparing videos of 10 mins pre and post injection. Behavioral video data for all pharmacology experiments was captured using a high-speed camera (Mako U U-029, Allied Vision), and paw position accuracy was calculated as the proportion of trials in which mice were holding the moveable lever at time of cue presentation.

Quantifying muscimol diffusion

To measure muscimol diffusion, a small volume of muscimol-BODIPY TMR-X Conjugate (ThermoFisher Scientific; dissolved in 0.1 PBS w/1% dimethyl sulfoxide) was injected into CFA (200 nl of 2 mM at 4 sites centered on 1.6 mm lateral, 0.6 mm rostral to bregma at a depth of 0.7 mm below the cortical surface). To mark the center of the injection site, pipettes were backfilled with a small volume (~20 nl) of green retrobeads (Lumafluor Inc.) prior to filling with muscimol-BODIPY. Following injection, animals were transcardially perfused and brains snap-frozen on dry ice 10 minutes after completion of the muscimol injection. Brains were stored on dry ice, coronal sections (60 μm) collected with a cryostat (Leica) at -20°C and imaged with a light microscope (Leica DMR, 5x objective). We assumed maximum fluorescence ≈ maximum injected concentration and that grayscale pixel intensity was proportional to muscimol-BODIPY concentration. Therefore, pixel values were thresholded at the equivalent pixel value of an EC_{20} concentration of muscimol and fluorescence outlines were drawn to generate a 'spread profile'. Green retrobeads were used to mark the center of each injection, and images were aligned to the injection center of gravity. From the aligned profiles, a modal spread profile (i.e., pixels with positive grayscale values across all mice) was generated and aligned to the Paxinos and Franklin Mouse Brain Atlas (Paxinos and Franklin, 2008).

Retrograde tracing

To selectively label pyramidal tract (PT) neurons in layer 5B of CFA, red retrobeads (Lumafluor, USA) were injected into the pons (4.0 mm caudal and 0.4 mm lateral to bregma ipsilateral to the target CFA), delivered via pulled glass pipettes (5μl, Drummond Scientific, PA, USA; 10–20 nl/min) using an automated injection system (Model Picospritzer iii, Parker, NH, USA). Injections were made at 4 sites (100 nl per site) located 200, 400, 600 and 800 μm dorsal from the cranial floor. After > 14 days post-injection, mice were terminally anaesthetized using an intraperitoneal injection of a ketamine/domitor mixture (75 mg/kg ketamine, 1 mg/kg domitor) and transcardially perfused with 30 ml of phosphate-buffered saline (PBS) followed by 30 ml of 4% paraformaldehyde (PFA, Sigma-Aldrich,

MO, USA), dissolved in PBS and adjusted to pH 7.4. Brains were post-fixed at 4°C for 1–3 days in 4% PFA solution, then transferred to PBS solution. Individual brains were cut into coronal sections (60 μm) using a vibrating microtome (Leica VT1200S, Leica Microsystems (UK) Ltd.) and mounted with Vectashield Antifade Mounting Medium (Vector Laboratories, CA, USA). Images were acquired with a Leica DM R epifluorescence microscope and image analysis was performed using ImageJ (Rueden et al., 2017) and MATLAB (MathWorks, MA, USA). To obtain estimates of the depth of layer 5B in CFA, 3 coronal sections from each brain were imaged (0.54 mm, 0.6 mm and 0.66 mm rostral to bregma). Brightness/contrast adjustments and background subtraction (rolling ball, 30 pixels wide at 1.28 μm/pixel; Fiji (Schindelin et al., 2012)) functions were performed to reduce the contribution of background autofluorescence. Each ROI was then divided into 25 μm deep bins that were normalized to a value between 0 and 1, with 0 being the darkest bin and 1 being the brightest bin and all bins were compared to baseline. To obtain a depth profile of layer 5B within CFA, the depth of the dorsal-most retrogradely labeled neurons were recorded at 100 μm intervals from 1.3 - 1.9 mm lateral to bregma and repeated in 5 sequential coronal sections from 0.36 - 0.84 mm rostral to bregma. For each mouse, the depth of layer 5B at the center of CFA (1.6 mm lateral, 0.6 mm rostral to bregma) was taken as the reference depth and the depths of other locations reported relative to this value.

Immunohistochemistry

Mice expressing GCaMP6s were transcardially perfused and horizontal sections (30 μm) were cut parallel to the surface of CFA. Sections were rinsed in PBS overnight, incubated with a blocking solution (PBS, with 0.5% Triton X-100 (Sigma-Aldrich) and 10% goat serum (Sigma-Aldrich)) for 2 hrs and rinsed with PBS. Sections were incubated overnight with mouse anti-NeuN (MAB377 Anti-NeuN Antibody, clone A60, Sigma-Aldrich) diluted 1:1500 in carrier solution (PBS, with 0.5% Triton X-100 and 1% goat serum), then rinsed with PBS. For secondary antibody binding, sections were incubated overnight with goat anti-mouse Alexa Fluor 568 (Invitrogen, MA, USA) diluted 1:750 in carrier solution then rinsed with PBS. Sections were mounted onto glass slides, briefly air-dried, covered with Vectashield Antifade Mounting Medium (Vector Laboratories), and sealed with a glass coverslip. Images of CFA were acquired using a Nikon A1R FLIM confocal microscope (20X objective lens, 0.8 NA, Plan Apo VC, Nikon, Europe). Three images were taken at imaging planes corresponding to layer 5B (550 μm from the cortical surface). The number of cells in each image was manually counted and divided by the area to obtain a measure of neuron density. For most FOVs recorded during calcium imaging, neurons were not visible in all portions of the frame due to occlusion by blood vessels. Polygons were manually drawn around visible neurons in each field-of-view to provide a realistic estimate of the imaging area.

2-photon imaging

To perform population calcium imaging in layer 5B (12 FOVs, N = 6 mice), 200 nl of the adeno-associated virus (AAV) AAV1-SynGCaMP6s (diluted to $2.9x10^{12}$ GC/ml, Addgene 100844-AAV1) was injected into CFA (1.6 mm lateral, 0.6 mm rostral to bregma and 0.6 mm from the cortical surface) using a pulled glass pipette (5 μl, Drummond Scientific; 10–20 nl/min) and automated injection system (Model Picospritzer iii, Parker), before sealing the craniotomy with silicone (Body Double; Smooth-On, PA, USA) and implanting a lightweight headplate. For imaging, a cranial window (glass coverslip #0; Menzel-Gläser, Germany fixed with cyanoacrylate glue), was implanted above the virus injection site. 2-photon calcium imaging was performed using a custom-built resonant scanning 2-photon microscope (320 x 320 μm FOV; 600 x 600 pixels) with a Ti:Sapphire pulsed laser (Chameleon Vision-S, Coherent, CA, USA; < 75 fs pulse width, 80 MHz repetition rate) tuned to 920 nm wavelength. Images were acquired at 40 Hz with a 40x objective lens (0.8 NA; Nikon) and custom-programmed LabVIEW-based software (LotoScan).

For cell type specific imaging, AAV-pkg-Cre (Addgene 24593-AAVrg; $1.7x10^{13}$ GC/ml) was injected into either the ipsilateral (right) pons (PT; 0.4 mm lateral, 0.4 mm rostral to lambda and 0.2, 0.4 and 0.6 mm dorsal from the cranial floor) or contralateral (left) CFA (IT; 4 injections centered on 1.6 mm lateral, 0.6 mm rostral relative to bregma at 0.7 and 0.35 mm from the cortical surface) followed by an injection of pAAV-CAG-Flex-mRuby2-GSG-P2A-GCaMP6s-WPRE-pA (Addgene 68717-AAV1; $1.8x10^{13}$ GC/ml) into right CFA (1.6 mm lateral, 0.6 mm rostral to bregma and 0.6 mm from the cortical surface). 2-photon calcium imaging was performed using an 8 kHz resonant scanning microscope (HyperScope, Scientifica, UK; 690 x 690 μm FOV; 512 x 512 pixels) with a Ti:Sapphire pulsed laser (Chameleon Vision-S, Coherent, CA, USA; < 75 fs pulse width, 80 MHz repetition rate) tuned to 920 nm. Images were acquired at ~30 Hz with a 16x objective lens (0.8 NA; Nikon) using SciScan image software (Scientifica) and synchronized with external high-speed videos and behavioral data using Mantis64. To facilitate reliable imaging at depths > 500 μm, all imaging was performed 24 hrs post-surgery. Laser power was between 91 – 173 mW (mean = 143 mW) across all imaging sessions, well below the damage thresholds of 250 – 300 mW outlined in Podgorski and Ranganathan (2016). The combination of low pixel dwell time and systematic blanking of FOV edges, where the dwell time is higher, and the addition of room temperature artificial cerebrospinal fluid on the surface of the skull reduced the risk of thermal effects (as discussed in Podgorski and Ranganathan 2016).

Motion artifacts in the raw fluorescence videos were corrected using discrete Fourier 2-dimensional-based image alignment (SIMA 1.3.2; (Kaifosh et al., 2014)). ROIs were drawn manually in Fiji and pixel intensity within each ROI averaged to produce a raw fluorescence time series (F). To remove fluorescence originating from neuropil and neighboring neurons, fluorescence signals were decontaminated and extracted using nonnegative matrix factorization, as implemented in FISSA (Keemink et al., 2018). Normalized fluorescence was calculated as $\Delta F/F_0$, where F_0 was calculated as the 5^{th} percentile of the 1 Hz low-pass filtered raw fluorescence signal and $\Delta F = F-F_0$. All further analyses were performed in custom written scripts in MATLAB or Python 3.

To identify movement-related neurons, we defined a baseline (-500 ms to -150 ms relative to motion index onset) and peri-movement (-150 ms relative to motion index onset to 40 ms after median movement completion) epoch. Next, we used two independent methods: 1) a bootstrapped distribution (10,000 samples) of baseline-to-peak values (mean of the 100 ms centered on the largest deviation from baseline within the peri-movement epoch - mean of baseline epoch) was used to test whether 95% confidence intervals were different from 0; 2) bootstrapped distributions of mean $\Delta F/F_0$ in 250 ms bins within the peri-movement epoch were compared to bootstrapped distributions of mean $\Delta F/F_0$ within the baseline epoch. If either method identified significant differences the neuron was classified as movement-related. Neurons with no differences between baseline and movement epochs were classified as non-responsive and excluded from further analysis. Neurons with a median onset occurring after median movement completion (plus a small correction factor of 40 ms, to account for the rise time of GCaMP6s) were defined as 'reward phase' neurons and excluded from further analysis. The median onset time of each cell was calculated by employing a previously published onset detection algorithm using a slope sum function (SSF; Zong et al., 2003; Dacre et al., 2021) with the decision rule and window of the SSF adapted to the calcium imaging data (threshold 10% of peak, SSF window 375 ms, smoothed with a Savitzky Golay filter across 27 frames with order 2 and reported as the median of 10,000 bootstrapped samples to reduce the influence of noisy individual trials). Prior to extracting $\Delta F/F_0$ onsets, we verified this algorithm with simulated data thereby accounting for any bias in the onset detection potentially introduced by filtering and/or the decision rule. To simulate the rising phase of the movement related calcium events in our data we used linear ramps with defined onset times and a rise time of 0.5 s mimicking GCaMP6s kinetics. We then calibrated the onset detection algorithm on the simulated data (100 simulated cells with 30 simulated trials per cell and artificially added noise in each trial matching the noise level in the imaging data) and updated it by a small correction factor. Neurons with movement bias were detected using the same classification criteria described above but across movements (i.e. significant differences in bootstrapped $\Delta F/F_0$ baseline-to-peak or 250 ms peri-movement bins).

Trial-to-trial correlations

To assess the similarity of trial-to-trial activity, the average pairwise trial-to-trial correlation coefficients (Pearson's r) of the peri-movement $\Delta F/F_0$, smoothed with a 1 s LOESS filter, were computed for each neuron. Data are presented as bootstrapped medians per animal for each movement bias classification (10,000 repetitions, 50 samples). To investigate the relationship between trial-to-trial similarity of movement and population $\Delta F/F_0$, pairwise trial-to-trial correlation coefficients (Pearson's r) of peri-movement motion index and pairwise trial-to-trial correlation coefficients (Pearson's r) of the peri-movement population $\Delta F/F_0$ of the same trials were compared. Population $\Delta F/F_0$ was the sum of all movement-related neurons in each FOV. Data were binned according to the pairwise trial-to-trial correlation coefficients of their motion index and are presented as the bootstrapped median (10,000 repetitions, 50 samples) within each bin.

Extracellular recording and spike sorting

To compare neural activity during the task, extracellular unit recordings in CFA were performed using acutely implanted silicone probes (Neuropixels 1.0 probes, IMEC). Data were acquired from the 384 channels closest to the probe tip (bank 0) with SpikeGLX software at 30 KHz, an amplifier gain of 500 for each channel and high-pass filtered with a cutoff frequency of 300 Hz. Spike data were synchronized with external high-speed videos and behavioral data (cue presentation, lever movement, and reward delivery) using Mantis64. Spike sorting was performed using Kilosort3 to automatically cluster units from raw data (Pachitariu et al., 2016). The resulting spike clusters were manually curated using Phy (https://github.com/cortex-lab/phy), and any unit with sufficient refractory period violations, inconsistent waveform amplitude across the duration of the recording, or clipped amplitude distribution was excluded from analyses. Probe location was confirmed via DiI (Thermofisher) reconstruction of the recording track and compared to retrogradely labeled PT neurons (FastBlue (Polysciences) injected into the pons) in each animal to limit analysis to units within layer 5B (upper boundary, 500-680 μm; lower boundary, 900-1080 μm; N = 5 mice). Spike widths were calculated as the duration from trough to following maxima of the spike waveform. Putative pyramidal neurons were identified as units with median spike widths greater than 0.4 ms.

To classify units as responsive to push or pull movements, firing rates were calculated by convolving motion index-aligned spike times with a 50 ms Gaussian kernel and mean changes in firing rate were calculated by subtracting the mean firing rate during a baseline period (1 s period before cue presentation) from the mean firing rates in 250 ms bins tiling a response period extending back from *max*(*pX ushcompletion*,*pX* u*llcompletion*)) to include motion index onset. Briefly, motion index onsets were calculated as the first point after cue where the motion index was > threshold (threshold = mean motion index in a baseline window from the 1.5 s before cue plus 2 SD). Trials where the motion index onset was prior to cue presentation were excluded from analysis. Significant responses were identified by comparing bootstrapped 95% confidence intervals of mean changes in firing rates to 0; if at least one bin differed from 0, that unit is considered movement-responsive. Movement-responsive units were classified as having a push or pull bias if confidence intervals did not overlap.

Neural decoding

To decode movement type in single neurons we employed a naïve Bayes classifier, where distributions of features are assumed to be Gaussian. Movement-aligned $\Delta F/F_0$ data were assessed within a 5 s peri-movement window to produce a time series for the decoding accuracy. At each time point, leaving one trial out (test trial), the likelihood of determining a push or pull was esti-

mated based on the remaining trials (training set). The leave-one-out procedure was then repeated for all trials to calculate a mean decoding accuracy time series for each neuron. The resulting time series were analyzed within the peri-movement epoch - the peri-movement epoch began at -0.15 s relative to motion index onset and ended based on the peak $\Delta F/F_0$ response of each neuron; the position of the median peak was calculated for each movement type and the later of these time points used as the cut off. To identify neurons with decoding performance above chance, the bootstrapped distributions of decoding accuracy scores were compared against a threshold value for each session. Only neurons with at least 1 bin significantly higher than threshold were defined as high decoding accuracy. The threshold for each session was calculated based on modeled data composed of random samples from a Gaussian distribution with the same number of trials as the experimental data. For each session, modeled data accuracy was calculated 1000 times, assuming a prior probability of 50:50, and the mean + 2 SD was used as the threshold for significance. For population level classification of movement type, we employed logistic regression. As above, the decoding accuracy of the time series for each population was generated via leave-one-out design looped over all the trials in a given session. Population decoding accuracy was defined as the maximum decoding accuracy in any 250 ms bin within the peri-movement epoch. Population decoding was also performed on subsets of the entire population. Neurons were removed from the population one at a time, either in order from highest to lowest decoding accuracy score or randomly, with the network retrained for each iteration. The process was repeated 25 times in the random condition and the median of all responses used as the representative example for comparison with the ordered removal condition. Subpopulations of neurons decoding significantly above chance were determined by comparing decoding scores with a shuffled dataset (sampled randomly from 1000 time points with the trial labels (push or pull) randomized for each sample). If confidence intervals from the population data did not overlap with those of the shuffled data, population scores were deemed to be above chance. In 3/12 FOVs the number of high decoding accuracy neurons and/or trial number were low and were excluded from further comparison.

Dimensionality reduction

Raw fluorescence traces for all trials with successful movements in a 7.5 s peri-movement window were concatenated, filtered with a three frame (75 ms) wide boxcar kernel, whitened, and transformed with principal component analysis. The principal components (PCs) corresponding to the 16 highest eigenvalues, which corresponded to an average 83% (range [77 94]) cumulative explained variance, were analyzed. To compute trajectories in PC space, PC projections for all trials were averaged (separately for push or pull) and the variance and 95% confidence intervals for each time point estimated via 100-fold bootstrapping. The separability of the trajectories for push or pull was computed in each PC separately as $d'(t) = |mpush(t) - m_{pull}(t)| / \sqrt{0.5(v_{push}(t) + v_{pull}(t))}$, where $m_{push}(t)$ and $m_{pull}(t)$ are the mean trajectories for push and pull, and $v_{push}(t)$ and $v_{pull}(t)$ the corresponding variances, estimated from trials. The separability $d'(t)$ was bootstrapped from 400 samples, and variance and 95% confidence intervals estimated from this sample. $d'(t)$ was computed for all frames from movement onset to completion, where the latter was the longest movement duration recorded in each session. PCs were considered separable if the difference between d'(t) and $d_{shuffle}'(t)$ (obtained in the same way from trial-shuffled data) was within the 95% confidence interval, which was estimated from the sum of the relevant bootstrapped variances. For each FOV, the largest significant $d'(t)$ was used; in 1/12 FOVs no PCs showed significant separability and was excluded.

Spatiotemporal mapping

To assess the functional (temporal) organization of simultaneously recorded populations of neurons, pairwise correlation coefficients (Pearson's r) from the smoothed (1 s LOESS filter) and motion index-aligned $\Delta F/F_0$ within the peri-movement epoch were compared. Data were split based on their decoding accuracy scores and the bootstrapped median difference between high decoding accuracy neurons and those of the population were subtracted and a median difference calculated per sample. This process was repeated 10,000 times to generate a distribution for high decoding neurons versus the entire population and the same sampling procedure was used to investigate the correlations within low decoding accuracy neurons. To investigate spatial clustering, bootstrapped median differences between high decoding accuracy neurons and the population using pairwise distances (defined as the Euclidean distance between the centroids of manually drawn ROIs from 2-photon imaging processing) were compared. A Generalized Linear Mixed-Effects Model:

$$r \sim distance_{pairwise} \times accuracy_{decoder} + movement_{type} + animal$$

was used to model the pairwise correlation coefficient as a function of pairwise distance (continuous), decoding accuracy and movement type. Pairwise distance and decoding accuracy were modeled as interacting fixed terms, while movement type and animal were modeled as random intercepts to account for the dependency of the measurements on observations from the same animal and across the different movement types. The model was estimated using the restricted maximum likelihood, or REML, method (Bartlett and Fowler, 1937). Model assumptions were verified by comparing residual versus fitted values for each covariate in the model against each covariate removed from the model.

QUANTIFICATION AND STATISTICAL ANALYSIS

Data analysis was performed using custom-written scripts in MATLAB or Python3 and code will be made available on request. All statistical details of experiments can be found in the figure legends or main text, including description of the specific test used and sample sizes. Data are reported as mean ± 95% bootstrapped confidence interval, 10,000 bootstrap samples, unless otherwise indicated. Where multiple measurements were made from a single animal, suitable weights were used to evaluate summary population statistics. Statistical significance was considered when $p < 0.05$ unless otherwise stated. Data were tested for normality and parametric/non-parametric tests were used as appropriate and as detailed in the text. The GLMM was designed in Python using the statsmodels library (Seabold and Perktold, 2010).

Cell Reports, Volume *39*

Supplemental information

Movement-specific signaling is differentially distributed across motor cortex layer 5 projection neuron classes

Stephen P. Currie, Julian J. Ammer, Brian Premchand, Joshua Dacre, Yufei Wu, Constantinos Eleftheriou, Matt Colligan, Thomas Clarke, Leah Mitchell, A. Aldo Faisal, Matthias H. Hennig, and Ian Duguid

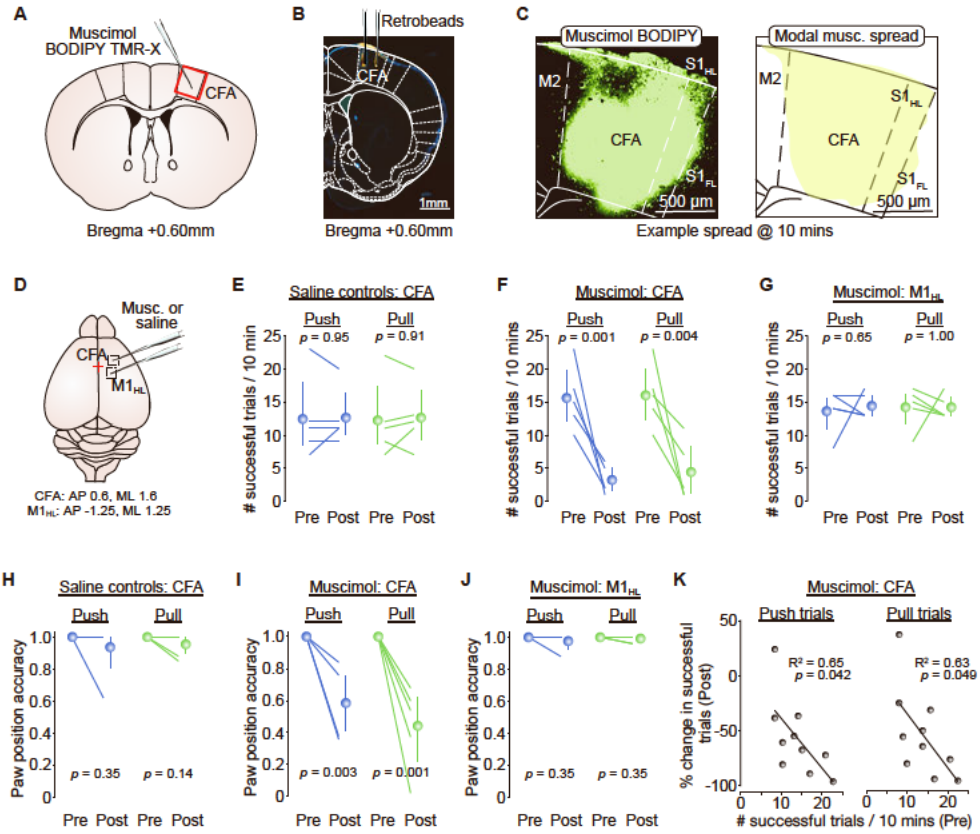

Figure S1 - Muscimol inactivation of CFA affects forelimb posture and task success. Related to Figure 1.

(A) Injection of muscimol BODIPY TMR-X into caudal forelimb area (CFA).
(B) Muscimol injection sites visualized using fluorescent retrobeads.
(C) *Left*, example image of fluorescent muscimol spread in CFA at 10 mins post injection. *Right*, modal spread of fluorescent muscimol in CFA (i.e., area in which fluorescence is present across all mice) (N = 3 mice). M2, secondary motor cortex; $S1_{HL}$, hindlimb primary somatosensory cortex; $S1_{FL}$, forelimb primary somatosensory cortex.
(D) Focal muscimol inactivation of CFA or hindlimb motor cortex ($M1_{HL}$), 0.6 mm anterior, 1.6 mm lateral of bregma and 1.25 mm posterior, 1.25 mm lateral of bregma, respectively. Red cross denotes bregma.
(E-G) Number of successful push (blue) and pull (green) trials in a 10 min period before (Pre) and after (Post) injection of (E) saline into CFA, (F) muscimol into CFA or (G) muscimol into $M1_{HL}$ (N = 5 mice), paired t-test. Colored lines, individual mice. Symbols, population means ± 95% CI.
(H-J) Paw position accuracy at the point of cue presentation before (Pre) and 10 mins after (Post) (H) saline into CFA, (I) muscimol into CFA or (J) muscimol into $M1_{HL}$ (N = 5 mice), paired t-test. Colored lines, individual mice. Symbols, population means ± 95% CI.
(K) Correlation between the number of successful push (left) and pull (right) trials before (Pre) and the % change in successful trials after (Post) muscimol injection (N = 10 mice). Symbols, individual animals, Black line, linear fit to the data (Pearson's *r*).

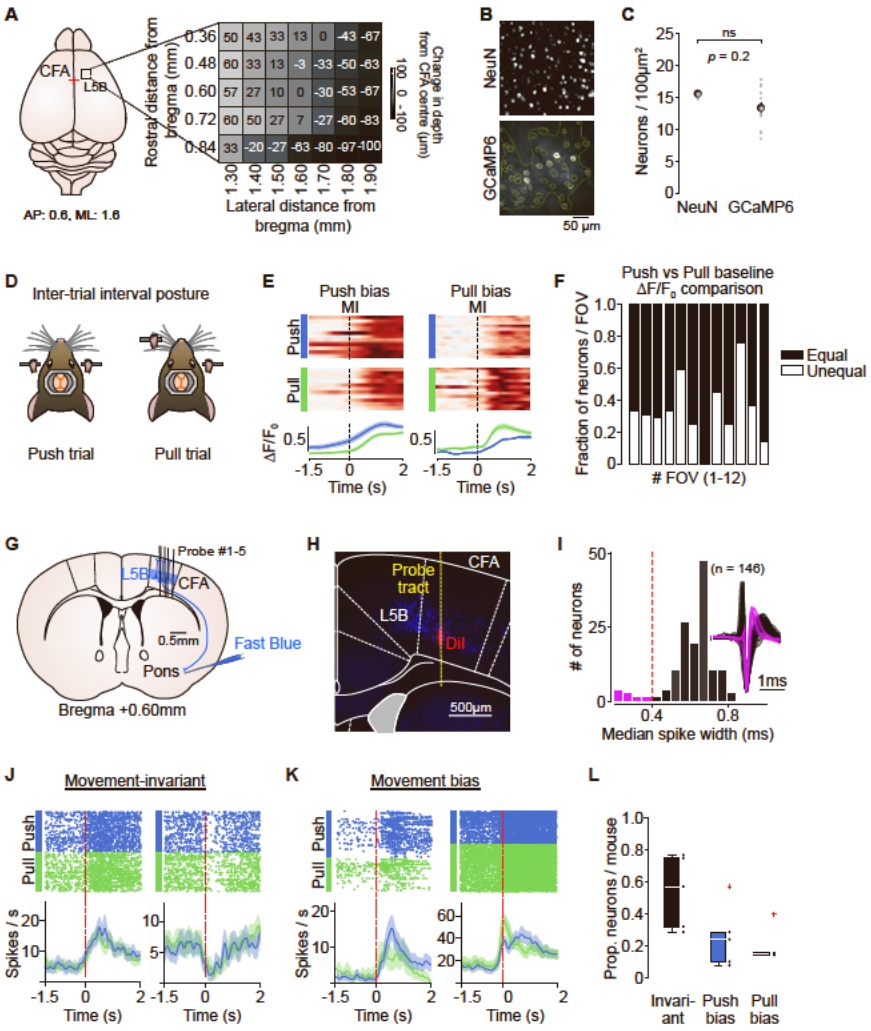

Figure S2 - Cell density and movement-type classification in layer 5B of CFA. Related to Figure 2.

(A) *Left*, schematic showing mapped region of caudal forelimb area (CFA) centred on 0.6 mm anterior, 1.6 mm medial of bregma. Red cross denotes bregma; *Right*, heatmap indicating changes in layer 5B depth across a range of cortical coordinates. Values represent the mean depth in µm of the upper boundary of Layer 5B (N = 3 mice).
(B) *Top*, representative image of NeuN stained layer 5B neurons; *Bottom*, representative two-photon FOV of L5B neurons expressing GCaMP6s. Small circles depict regions-of-interest (yellow) drawn around individual neurons within a larger bounded area excluding blood vessels.
(C) Average number of NeuN versus GCaMP6s expressing neurons / 100µm² in layer 5B of CFA. Gray dots represent individual slices, bars depict s.e.m. (NeuN, n = 3 slices, N = 1 mouse; GCaMP6s, n = 15 slices, N = 7 mice; two-sample t-test).
(D) Schematic depicting inter-trial posture for push (left) and pull (right) trials.
(E) Activity of two neurons with differences in inter-trial baseline $\Delta F/F_0$. *Left*, example neuron with push bias. *Right*, example neuron with pull bias. *Top*, raster showing normalized $\Delta F/F_0$ across successive push (blue) or pull (green) trials; *Bottom*, mean $\Delta F/F_0$ ± 95% CI for push and pull trials. Dashed lines, movement initiation (MI).
(F) Proportion of neurons per field-of-view (FOV) with equal (black) or unequal (white) inter-trial $\Delta F/F_0$ baselines (n = 486 neurons from 12 FOVs, N = 6 mice).
(G) Silicone probe recordings of putative layer 5B (L5B) neurons in CFA. Approximate position of probes within CFA are shown. The upper and lower boundaries of layer 5B are defined based on retrograde labeling of pyramidal tract (PT) neurons after FastBlue injection into the pons (N = 5 mice).
(H) Retrograde labeling of pons-projecting PT neurons within CFA (blue) with silicon probe tract visualized using DiI (red). Dashed line, overlay of probe tract.
(I) Histogram of spike durations, highlighting putative interneurons (purple) and pyramidal neurons (black). Inset, trough-aligned mean spike waveforms, normalized based on peak-to-trough height (n = 148 units, N = 5 mice).
(J) Activity of two example movement-invariant layer 5 CFA neurons. *Top*, Spike rasters during push (blue) and pull (green) trials. Dots represent individual spikes. *Bottom*, peri-stimulus time histograms depicting mean ± s.e.m. firing rate during push (blue) and pull (green) trials. Red dashed lines, movement initiation (MI).
(K) Activity of two example layer 5 CFA neurons with push (left) and pull (right) bias. *Top*, Spike rasters during push (blue) and pull (green) trials. Dots represent individual spikes. *Bottom*, peri-stimulus time histograms depicting mean ± s.e.m. firing rate during push (blue) and pull (green) trials. Red dashed lines, movement initiation (MI).
(L) Proportion of invariant, push- and pull-bias neurons per mouse (n = 71 neurons, N = 5 mice). Black dots represent individual mice. Red crosses, identified outliers.

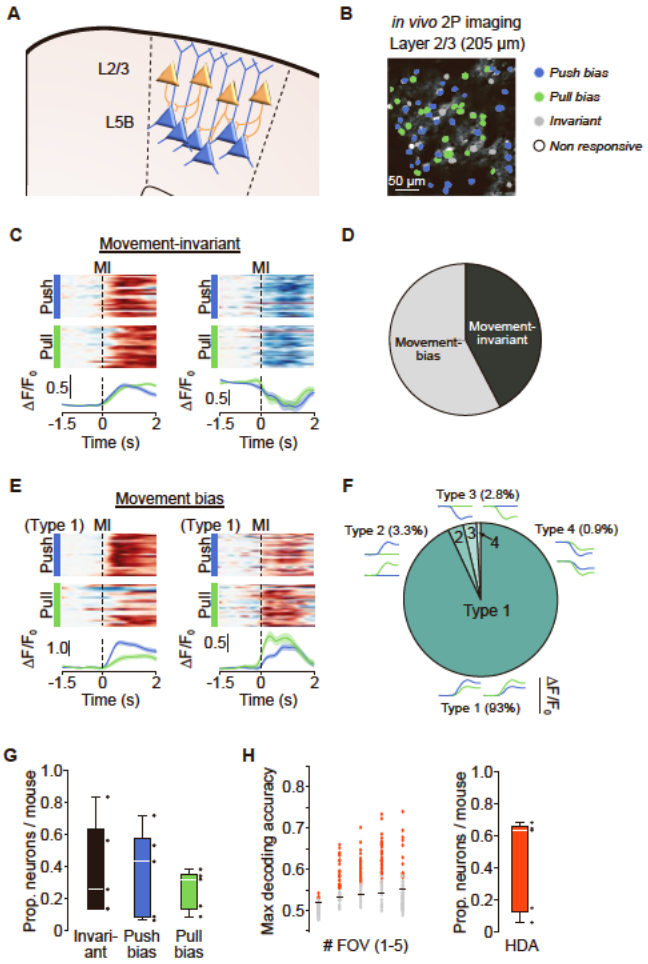

Figure S3 - Movement-specific signalling is more prevalent in Layer 2/3 neurons. Related to Figure 2 and Figure 3.

(A) Schematic showing top-down laminar inter-connectivity between layer 2/3 and layer 5B of CFA.
(B) Example FOV showing layer 2/3 CFA neurons with push (blue) or pull (green) bias. Gray, movement-invariant; white, non-responsive neurons.
(C) Activity of two example movement-invariant neurons. *Top*, raster showing normalised $\Delta F/F_0$ across successive push (blue) or pull (green) trials; *Bottom*, mean $\Delta F/F_0 \pm 95\%$ CI for push and pull trials. Dashed lines, movement initiation (MI).
(D) Summary of movement-invariant and movement-bias neuron classification in CFA layer 2/3 neurons (n = 215 vs 160 neurons, N = 5 mice).
(E) Activity of two example Type 1 movement-bias neurons. *Top*, raster showing normalised $\Delta F/F_0$ across successive push (blue) or pull (green) trials; *Bottom*, mean $\Delta F/F_0 \pm 95\%$ CI for push and pull trials. Dashed lines, movement initiation (MI).
(F) Summary of movement-bias classification in CFA layer 2/3 neurons (n = 215 neurons, N = 5 mice). *Insets*, model examples of $\Delta F/F_0$ changes classified as Type 1 - 4.
(G) Proportion of invariant, push- and pull-bias neurons per mouse (n = 375 neurons from 5 FOVs, N = 5 mice). Black dots represent individual mice.
(H) *Left*, maximum decoding accuracy during peri-movement epochs generated using a naïve Bayes classifier. Circles represent individual neurons; black horizontal lines indicate significance threshold. *Right*, box-and-whisker plot showing the proportion of high decoding accuracy (HDA) neurons across mice (n = 375 neurons from 5 FOVs, N = 5 mice).

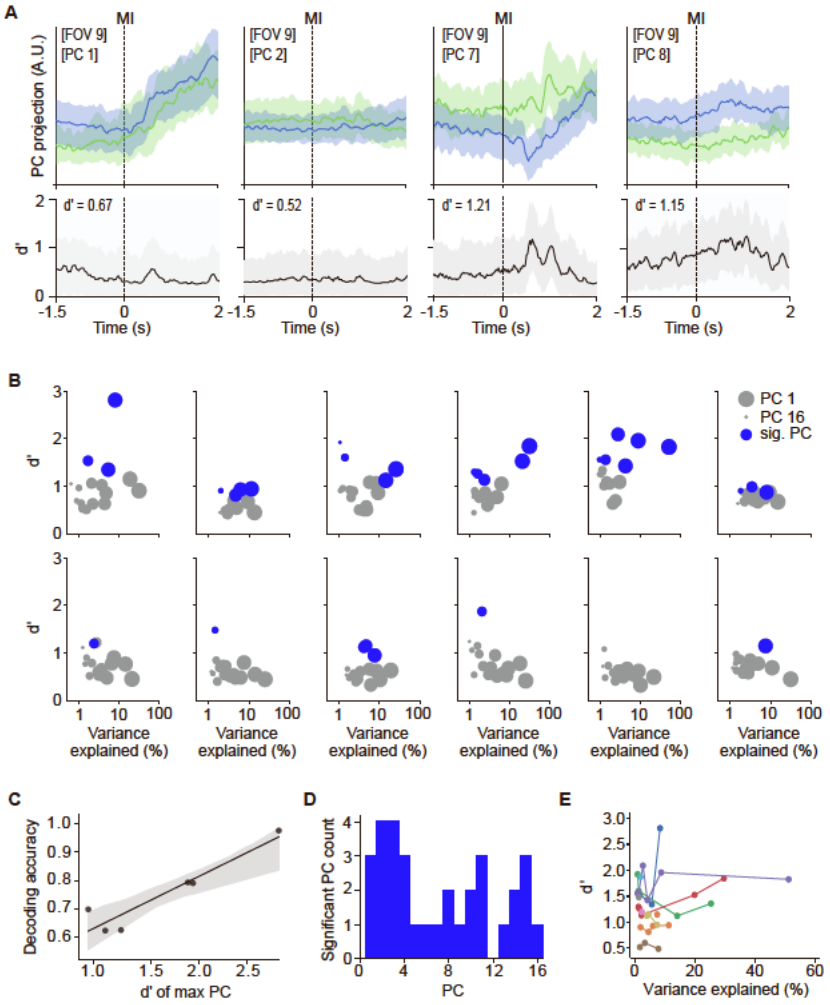

Figure S4 - Movement type is represented in both leading and higher principal components. Related to Figure 3.

(A) *Top*, example trajectories of 4 principal components (PC) from a representative field-of-view (FOV) during push (blue) and pull (green trials). *Bottom*, discrimination index (d') calculated from the corresponding PCs. Inset, maximum d' of each PC. Thick lines, mean ± 95% CI. Dashed lines, movement initiation (MI).
(B) Variance explained as a function of discrimination index (d') for all PCs in each FOV. *Top*, FOVs 1-6. *Bottom*, FOVs 7-12. Dot size (large to small) represents PC rank (1-16). Blue dots are significant PCs.
(C) Discrimination index (d') of the highest significant PC vs population decoding accuracy (Figure 3) for each mouse (N = 6 mice). Black line, linear regression fit ± 95% CI.
(D) Histogram of significant PCs across all 12 FOVs.
(E) Significance explained as a function of discrimination index (d') for all significant PCs. Dots represent individual PCs. Lines and colours link PCs from the same FOV.

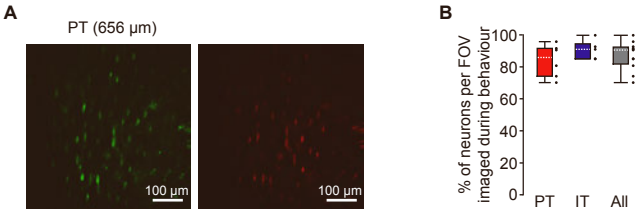

Figure S5 - Quantifying proportions of imaged neurons per field-of-view. Related to Figure 4.

(A) Example field-of-view (FOV) showing PT neurons expressing GCaMP6s (left; green) and mRuby (right; red).
(B) Percentage of mRuby positive PT and IT neurons per FOV imaged ($\Delta F/F_0$) during behaviour. Box-and-whisker plots showing median, interquartile range and range. PT (red), IT (purple) and all neurons (gray). Black dots represent individual FOVs. N = 6, 5 and 11, respectively.

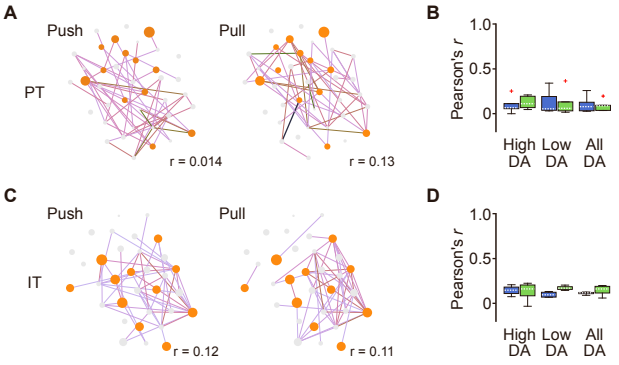

Figure S6 - Temporal organization of high decoding accuracy neurons in layer 5B during push and pull movements. Related to Figure 5.

(A) *Left & right*, functional networks constructed from the pairwise activity correlations from a representative PT field-of-view (FOV) for push (left) or pull (right) trials. Line color (light to dark) and width correspond to increasing values of Pearson's *r*. Neurons are plotted as nodes in Euclidean space with color and size relating to increasing decoding accuracy.
(B) Box-and-whisker plots showing the median, interquartile range and range of correlation coefficients across mice for high decoding accuracy (HDA), low decoding accuracy (LDA) and all neurons. Data are shown for both push (blue) and pull (green) trials. Red crosses, identified outliers.
(C) *Left & right*, functional networks constructed from the pairwise activity correlations from a representative IT FOV for push (left) or pull (right) trials. Line color (light to dark) and width correspond to increasing values of Pearson's *r*. Neurons are plotted as nodes in Euclidean space with color and size relating to increasing decoding accuracy.
(D) Box-and-whisker plots showing the median, interquartile range and range of correlation coefficients across mice for high decoding accuracy (HDA), low decoding accuracy (LDA) and all neurons. Data are shown for both push (blue) and pull (green) trials.

Table S1 - Contributions Matrix. Related to Figures 1-5 and Figures S1-S6.

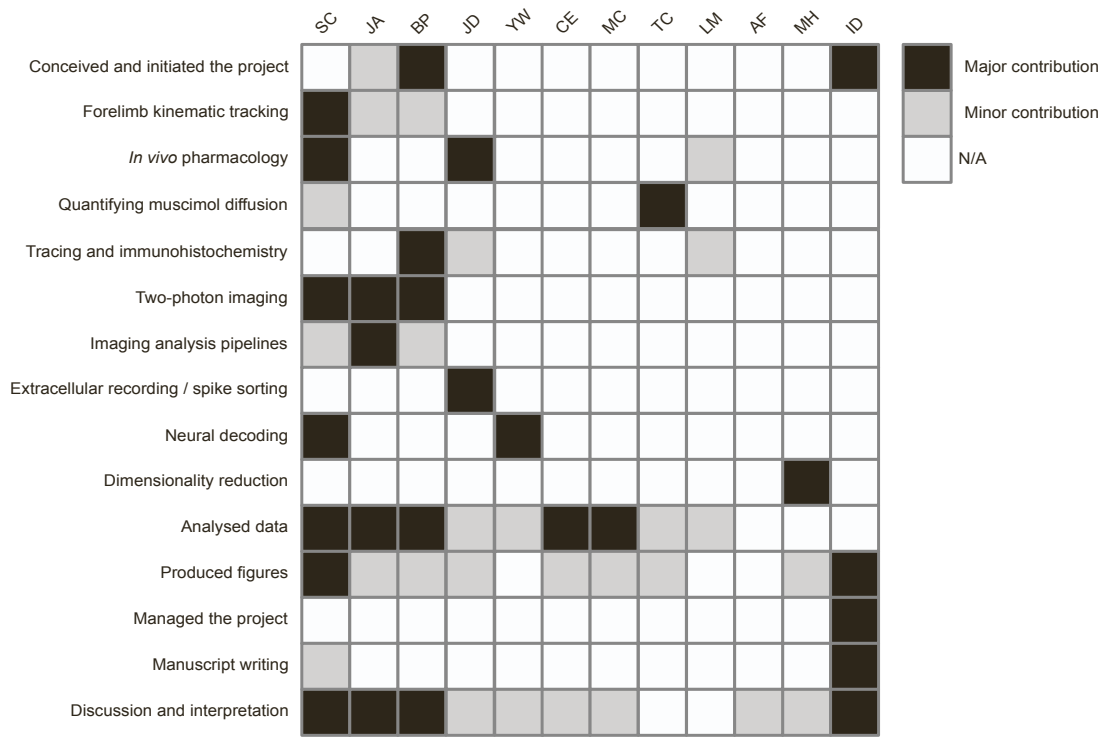

Table S2, statistical details, related to Figures 1-5 and Figures S1-S6.

$\bar{X}$ = mean $\tilde{X}$ = median SD = standard deviation IQR = interquartile range
fov = fields-of-view H / LDA = high / low decoding accuracy GLMM = generalised linear mixed-effects model

Figure	Description	Sample size	Result	Variance	Confidence intervals (95%)	Statistical test result
1C-E	Training time (days)	N = 24	$\tilde{X}$ = 10.5	IQR = 4		
1C	Reaction time (s; push / pull)	N = 24	$\tilde{X}$ = 0.132 / 0.135	IQR = 0.058 / 0.043		
	Movement duration (s; push / pull)	N = 24	$\tilde{X}$ = 706 / 422	IQR = 352 / 438		
1D	Successful trials / session (push / pull)	N = 24	$\tilde{X}$ = 44.5 / 45	IQR = 9.5 / 8.5		
1E	Task success (%; push / pull)	N = 24	$\tilde{X}$ = 68.0 / 74.5	IQR = 35.9 / 43.4		
1G	Successful trials / 10min (push muscimol CFA pre / post)	N = 10	$\bar{X}$ = 13.9 / 5	SD = 5.22 / 2.94	[11.1 17.1] / [3.3 6.8]	t(18) = 4.70, P = 1.79×10^{-4}, paired t-test
	Successful trials / 10min (pull muscimol CFA pre / post)	N = 10	$\bar{X}$ = 14.0 / 5.3	SD = 5.33 / 3.62	[10.9 17.2] / [3.2 7.4]	t(18) = 4.27, P = 4.64×10^{-4}, paired t-test
1H	Paw position accuracy (push muscimol CFA pre / post)	N = 10	$\bar{X}$ = 1 / 0.66	SD = 0 / 0.2	[1 1] / [0.54 0.77]	t(18) = 5.56, P = 2.79×10^{-5}, paired t-test
	Paw position accuracy (pull muscimol CFA pre / post)	N = 10	$\bar{X}$ = 0.98 / 0.50	SD = 0.06 / 0.21	[0.95 1] / [0.36 0.62]	t(18) = 6.85, P = 2.07×10^{-6}, paired t-test
S1. E	Successful trials / 10min (push saline CFA pre / post)	N = 5	$\bar{X}$ = 12.4 / 12.6	SD = 6.23 / 4.28	[8.6 18] / [10 16.4]	t(8) = -0.06, P = 0.95, paired t-test
	Successful trials / 10min (pull saline CFA pre / post)	N = 5	$\bar{X}$ = 12.2 / 12.6	SD = 5.81 / 4.72	[8.6 17.4] / [9 16.6]	t(8) = -0.12, P = 0.91, paired t-test

S1. F	Successful trials / 10min (push muscimol CFA pre / post)	N = 5	$\bar{X}$ = 15.6 / 3.2	SD = 4.88 / 2.17	[12.0 19.8] / [1.6 4.8]	t(8) = 5.19, $P = 8.29 \times 10^{-4}$, paired t-test
	Successful trials / 10min (pull muscimol CFA pre / post)	N = 5	$\bar{X}$ = 16.0 / 4.4	SD = 4.74 / 4.45	[12.4 20.0] / [1.2 8.2]	t(8) = 3.99, $P = 4.0 \times 10^{-3}$, paired t-test
S1. G	Successful trials / 10min (push muscimol $M1_{HL}$ pre / post)	N = 5	$\bar{X}$ = 13.6 / 14.4	SD = 3.29 / 1.95	[10.8 15.6] / [13.0 16.0]	t(8) = -0.47, $P = 0.65$, paired t-test
	Successful trials / 10min (pull muscimol $M1_{HL}$ pre / post)	N = 5	$\bar{X}$ = 14.2 / 14.2	SD = 3.11 / 1.79	[11.4 16.2] / [13.0 15.8]	t(8) = 0, $P = 1.0$, paired t-test
S1. H	Paw position accuracy (push saline CFA pre / post)	N = 5	$\bar{X}$ = 1 / 0.92	SD = 0 / 0.17	[1 1] / [0.77 1]	t(8) = 1.0, $P = 0.35$, paired t-test
	Paw position accuracy (pull saline CFA pre / post)	N = 5	$\bar{X}$ = 1 / 0.95	SD = 0 / 0.07	[1 1] / [0.89 1]	t(8) = 1.62, $P = 0.15$, paired t-test
S1. I	Paw position accuracy (push muscimol CFA pre / post)	N = 5	$\bar{X}$ = 1 / 0.59	SD = 0 / 0.22	[1 1] / [0.41 0.76]	t(8) = 4.27, $P = 2.7 \times 10^{-3}$, paired t-test
	Paw position accuracy (pull muscimol CFA pre / post)	N = 5	$\bar{X}$ = 1 / 0.44	SD = 0 / 0.26	[1 1] / [0.23 0.62]	t(8) = 4.79, $P = 1.4 \times 10^{-3}$, paired t-test
S1. J	Paw position accuracy (push muscimol $M1_{HL}$ pre / post)	N = 5	$\bar{X}$ = 1 / 0.98	SD = 0 / 0.05	[1 1] / [0.93 1]	1(8) = 1.0, $P = 0.35$, paired t-test
	Paw position accuracy (pull muscimol $M1_{HL}$ pre / post)	N = 5	$\bar{X}$ = 1 / 0.99	SD = 0 / 0.02	[1 1] / [0.98 1]	1(8) = 1.0, $P = 0.35$, paired t-test
S1. K	Successful trial vs % change in successful trials (push / pull)	N = 10				$r^2 = -0.65$ $P = 0.042$ / $r^2 = -0.63$, $P = 0.049$
2D	Prop. of responsive neurons (non / movement / reward)	N = 6 fov = 12 cell = 653	$\bar{X}$ = 20.9 / 73.5 / 5.7	SD = 15.1 / 16.0 / 3.7	[12.8 29.1] / [64.7 81.8] / [3.7 7.7]	

2E	Trial-trial correlation - ΔF/F0 vs motion index for push trials (motion index correlation 0.1 / 0.3 / 0.5 0.7)	N = 6 fov = 12 trials = 2931	$\tilde{X}$ = 0.36 / 0.62 / 0.75 / 0.80		[0.24 0.40] / [0.46 0.68] / [0.60 0.86] / [0.65 0.89]	
	Trial-trial correlation - ΔF/F0 vs motion index for pull trials (motion index correlation 0.1 / 0.3 / 0.5 0.7)	N = 6 fov = 12 trials = 2931	$\tilde{X}$ = 0.25 / 0.47 / 0.59 / 0.79		[0.23 0.27] / [0.37 0.87] / [0.52 0.68] / [0.65 0.89]	
2G	# of movement-responsive neurons (%; bias / invariant)	N = 6 fov = 12 Cell = 468	181 (38.7) / 287 (61.3)			
2J	# of movement bias neurons (%; type 1 / 2 / 3 / 4)	N = 6 fov = 12 Cell = 181	136 (75.1) / 25 (13.8) / 15 (8.3) / 5 (2.8)			
2L	Average ΔF/F0 trial-trial correlation for push trials (non / push / push)	N = 6 fov = 12 cell = 468	$\tilde{X}$ = 0.37 / 0.49 / 0.45	IQR = 0.37 / 0.47 / 0.39	[0.12 0.56] / [0.21 0.72] / [0.04 0.70]	
	Average ΔF/F0 trial-trial correlation for pull trials (non / push / push)	N = 6 fov = 12 cell = 468	$\tilde{X}$ = 0.31 / 0.30 / 0.53	IQR = 0.25 / 0.32 / 0.33	[0.10 0.65] / [0.08 0.75] / [0.06 0.61]	
2M	Prop. of movement-responsive neurons (non / push / pull)	N = 6 fov = 12 cell = 468	$\tilde{X}$ = 59.8 / 14.3 / 11.8	IQR = 31.4 / 15.9 / 19.5		
S2. C	Neurons / 100 μm^2 (NeuN / GCaMP6s)	N = 1 / 7 fov = 3 / 15	$\bar{X}$ = 15.6 / 13.3	SD = 0.9 / 2.7		t(16) = 1.75, P = 0.2, Student's t-test
S2. E-F	Prop. of biased neurons (equal / unequal baseline)	N = 6 fov = 12 cell = 181	$\tilde{X}$ = 69.5 / 30.5	IQR = 8.2 / 8.2		
S2. G-L	# units (%; pyramidal / interneurons)	N = 5 n = 146	137 (93.8) / 9 (6.2)			

	# units (%; non / move / reward)	N = 5 n = 137	61 (45.2) / 72 (52.6) / 4 (2.9)			
S2. L	Prop. of movement-responsive neurons (non / push / pull)	N = 5 n = 72	$\tilde{X}$ = 0.57 / 0.15 / 0.24	IQR = 0.43 / 0.01 / 0.19		
S3. D	# of movement-responsive neurons L2-3 (%; bias / invariant)	N = 5 fov = 5 cell = 375	216 (57.6) / 159 (42.4)			
S3. F	# of movement bias neurons L2-3 (%; type 1 / 2 / 3 / 4)	N = 5 fov = 5 cell = 216	200 (93.0) / 7 (3.3) / 6 (2.8) / 2 (0.9)			
S3. G	Prop. of movement-responsive neurons L2-3 (non / push / pull)	N = 5 fov = 5 cell = 375	$\tilde{X}$ = 0.25 / 0.43 / 0.32	IQR = 0.50 / 0.50 / 0.22		
S3. H	Prop. of movement-responsive neurons L2-3	N = 5 fov = 5 cell = 375	$\tilde{X}$ = 0.64	IQR = 0.53		
3A	Prop. of movement-responsive neurons (LDA / HDA)	N = 6 fov = 12 cell = 468	0.63 / 0.37			
3B	Decoding accuracy (single cell / population)	N = 6 fov = 12	$\tilde{X}$ = 0.61 / 0.75	IQR = 0.07 / 0.16		W = 1, Z = -2.20, P = 2.8×10^{-2}, Wilcoxon signed rank test
3F	Prop. neurons removed (high-low / random)	N = 6 fov = 9	$\tilde{X}$ = 0.21 / 0.64	IQR = 0.5 / 0.57		W = 1, Z = -2.20, P = 2.8×10^{-2}, Wilcoxon signed rank test
S4. C	Population decoding vs max d’	N = 6 fov = 10				r^2 =0.88, F(1,5) = 29.95, P = 5.4×10^{-3}

4E	# of movement-responsive neurons PT (%; bias / invariant)	N = 5 fov = 6 cell = 171	46 (26.9) / 125 (73.1)			
	# of movement bias neurons PT (%; type 1 / 2 / 3 / 4)	N = 5 fov = 6 cell = 46	36 (78.2) / 9 (19.6) / 1 (2.2) / 0 (0)			
	Prop. of movement-responsive neurons PT (non / push / pull)	N = 5 fov = 6 cell = 171	$\tilde{X}$ = 0.75 / 0.10 / 0.14	IQR = 0.21 / 0.19 / 0.11		
4G	# of movement-responsive neurons IT (%; bias / invariant)	N = 4 fov = 5 cell = 110	54 (49.1) / 56 (50.9)			
	# of movement bias neurons IT (%; type 1 / 2 / 3 / 4)	N = 4 fov = 5 cell = 54	34 (62.9) / 15 (27.8) / 2 (3.7) / 3 (5.6)			
	Prop. of movement-responsive neurons IT (non / push / pull)	N = 4 fov = 5 cell = 110	$\tilde{X}$ = 0.51 / 0.21 / 0.32	IQR = 0.11 / 0.26 / 0.31		
4I	Decoding accuracy PT (single / population) (HDA only)	N = 5 fov = 6 cell = 58	$\tilde{X}$ = 0.55 / 0.68	IQR = 0.02 / 0.14		t(4) = -3.04, P = 0.04
	Decoding accuracy IT (single / population) (HDA only)	N = 4 fov = 5 cell = 43	$\tilde{X}$ = 0.56 / 0.73	IQR = 0.04 / 0.21		t(3) = -2.95, P = 0.06
	Decoding accuracy population (PT / IT) (HDA only)	N = 5 / 4 fov = 6 / 5 cell = 58 / 43	$\tilde{X}$ = 0.68 / 0.73	IQR = 0.14 / 0.21		t(7) = 0.40, P = 0.70
S5. B	% of all neurons per FOV imaged during behaviour (PT / IT / All)	N = 5 / 4 / 9	$\tilde{X}$ = 85.8 / 91.2 / 90.7	IQR = 17.4 / 9.3 / 10.7		

		fov = 6 / 5 / 11				
5B	Norm. prop. $\Delta F/F_0$ onsets push PT (ms; HDA / LDA). ANOVA [animal:cell type: onset time]	N = 5 fov = 6 cell = 238	$\tilde{X}$ = 210 / 113	IQR = 709 / 662		F(4) = 0, P = 1 / F(1) = 0, P = 1 / F(17) = 5.12, $P = 8.32 \times 10^{-9}$
	Norm. prop. $\Delta F/F_0$ onsets pull PT (ms; HDA / LDA). ANOVA [animal:cell type: onset time]	N = 5 fov = 6 cell = 238	$\tilde{X}$ = 145 / 177	IQR = 226 / 500		F(3) = 0, P = 1 / F(1) = 0, P = 1 / F(17) = 8.57, $P = 3.35 \times 10^{-15}$
	Norm. prop. $\Delta F/F_0$ onsets push IT (ms; HDA / LDA). ANOVA [animal:cell type: onset time]	N = 4 fov = 5 cell = 137	$\tilde{X}$ = 500 / 339	IQR = 524 / 677		F(3) = 1.1×10^{-14}, P = 1 / F(1) = 0, P = 1 / F(17) = 7.31, $P = 4.85 \times 10^{-12}$
	Norm. prop. $\Delta F/F_0$ onsets pull IT (ms; HDA / LDA). ANOVA [animal:cell type: onset time]	N = 4 fov = 5 cell = 137	$\tilde{X}$ = 403 / 468	IQR = 444 / 710		F(3) = 0, P = 1 / F(1) = 0, P = 1 / F(17) = 3.81, $P = 6.85 \times 10^{-6}$
5D	Pairwise correlation coefficient PT (r; push; HDA vs ALL / LDA vs ALL)	N = 5 fov = 6 cell = 171	HDA $\tilde{X}$ = 0.07 LDA $\tilde{X}$ = 0.06 ALL $\tilde{X}$ = 0.08	HDA IQR = 0.05 LDA IQR = 0.16 ALL IQR = 0.10	[-0.103 0.087] / [-0.085 0.094]	P = 0.84 / 1.0
	Pairwise correlation coefficient IT (r; push; HDA vs ALL / LDA vs ALL)	N = 4 fov = 5 cell = 110	HDA $\tilde{X}$ = 0.15 LDA $\tilde{X}$ = 0.09 ALL $\tilde{X}$ = 0.12	HDA IQR = 0.07 LDA IQR = 0.05 ALL IQR = 0.01	[-0.093 0.081] / [-0.073 0.076]	P = 1.0 / 0.96
5E	Pairwise corr. Vs distance PT (HDA / LDA)	N = 5 fov = 6 cell = 171	Spearman r = -0.1 / 0.0			P = 0.87 / 1.0
	GLMM PT r distance pairwise accuracydecoder + movementtype+animal	N = 5, n = 3024 observations				P = 0.33
	Pairwise corr. Vs distance IT (HDA / LDA)	N = 4 fov = 5	Spearman r = -0.40 / 0.0			P = 0.6 / 1.0

		cell = 110				
	GLMM IT r distance pairwise accuracydecoder + movementtype+animal	N = 5, n = 1562 observations				*P* = 0.49
5G	Pairwise distance PT (µm; HDA vs ALL / LDA vs ALL)	N = 5 fov = 6 cell = 171	HDA $\tilde{X}$ = 226 LDA $\tilde{X}$ = 273 ALL $\tilde{X}$ = 264	HDA IQR = 26 LDA IQR = 60 ALL IQR = 53	[-69 102] / [-62 69]	*P* = 1.0 / 1.0
	Pairwise distance IT (µm; HDA vs ALL / LDA vs ALL)	N = 4 fov = 5 cell = 110	HDA $\tilde{X}$ = 228 LDA $\tilde{X}$ = 220 ALL $\tilde{X}$ = 229	HDA IQR = 14 LDA IQR = 56 ALL IQR = 58	[-82 67] / [-63 68]	*P* = 0.88 / 1.0
S6. B	Pairwise correlation coefficient PT (r; pull; HDA vs ALL / LDA vs ALL)	N = 5 fov = 6 cell = 171	HDA $\tilde{X}$ = 0.11 LDA $\tilde{X}$ = 0.06 ALL $\tilde{X}$ = 0.09	HDA IQR = 0.12 LDA IQR = 0.10 ALL IQR = 0.06	[-0.1 0.15] / [-0.1 0.09]	*P* = 1.17 / 0.79
S6. D	Pairwise correlation coefficient IT (r; pull; HDA vs ALL / LDA vs ALL)	N = 4 fov = 5 cell = 110	HDA $\tilde{X}$ = 0.16 LDA $\tilde{X}$ = 0.17 ALL $\tilde{X}$ = 0.16	HDA IQR = 0.12 LDA IQR = 0.03 ALL IQR = 0.08	[-0.08 0.07] / [-0.07 0.1]	*P* = 0.89 / 1.28

temporal resolution assay of neural activity, Dr Joshua Dacre performed high-density Neuropixels recordings in CFA. For this experiment, I applied the `pixels` data processing and analysis pipeline described in Chapter 3 to identify putative projection neurons in layer 5B and assess how their firing rate patterns related to movement type (Figures S2i-l). I compared unit firing rates between a pre-cue baseline period and 250 ms bins spanning the response period to identify units that displayed reproducible firing rate changes as mice performed pushes or pulls. Movement-invariant signalling dominated layer 5B activity, while a small proportion of units exhibited movement-specific firing rate changes, corroborating the imaging results.

These experiments, in combination with cell-type specific calcium imaging experiments targeting PT and IT neuron populations, suggest that CFA layer 5B population dynamics primarily reflect movement-invariant signalling, while relatively small populations of PT and IT neurons differentially encode movement type as mice perform two distinct movements.

Bibliography

Allen Institute for Brain Science, 2012. Allen mouse brain altas.

Anaconda software distribution, 2020. Anaconda Documentation.

Andermann, M.L., Kerlin, A.M., Reid, R.C., 2010. Chronic cellular imaging of mouse visual cortex during operant behavior and passive viewing. Frontiers in cellular neuroscience 4, 3–3.

Anderson, M.E., Turner, R.S., 1991. Activity of neurons in cerebellar-receiving and pallidal-receiving areas of the thalamus of the behaving monkey. Journal of neurophysiology 66, 879–893.

Archambault, P.S., Ferrari-Toniolo, S., Battaglia-Mayer, A., 2011. Online control of hand trajectory and evolution of motor intention in the parietofrontal system. The Journal of neuroscience 31, 742–752.

Archambault, P.S., Ferrari-Toniolo, S., Caminiti, R., Battaglia-Mayer, A., 2015. Visually-guided correction of hand reaching movements: The neurophysiological bases in the cerebral cortex. Vision Research 110, 244–256.

Asanuma, C., Thach, W.T., Jones, E.G., 1983. Brainstem and spinal projections of the deep cerebellar nuclei in the monkey, with observations on the brainstem projections of the dorsal column nuclei. Brain Research Reviews 5, 299–322.

Averbeck, B.B., Battaglia-Mayer, A., Guglielmo, C., Caminiti, R., 2009. Statistical analysis of parieto-frontal cognitive-motor networks. Journal of Neurophysiology 102, 1911–1920.

Azim, E., Jiang, J., Alstermark, B., Jessell, T.M., 2014. Skilled reaching relies on a V2a propriospinal internal copy circuit. Nature (London) 508, 357–363.

Baird, A.L., Meldrum, A., Dunnett, S.B., 2001. The staircase test of skilled reaching in mice. Brain research bulletin 54, 243–250.

Bakola, S., Passarelli, L., Gamberini, M., Fattori, P., Galletti, C., 2013. Cortical connectivity suggests a role in limb coordination for macaque area PE of the superior parietal cortex. The Journal of neuroscience : the official journal of the Society for Neuroscience 33.

Balleine, B.W., O'Doherty, J.P., 2010. Human and rodent homologies in action control: Corticostriatal determinants of goal-directed and habitual action. Neuropsychopharmacology (New York, N.Y.) 35, 48–69.

Barthas, F., Kwan, A.C., 2017. Secondary motor cortex: Where 'sensory' meets 'motor' in the rodent frontal cortex. Trends in Neurosciences 40, 181–193.

Battaglia-Mayer, A., Buiatti, T., Caminiti, R., Ferraina, S., Lacquaniti, F., Shallice, T., 2014. Correction and suppression of reaching movements in the cerebral cortex: Physiological and neuropsychological aspects. Neuroscience and Biobehavioral Reviews 42, 232–251.

Battaglia-Mayer, A., Ferrari-Toniolo, S., Visco-Comandini, F., Archambault, P.S., Saberi-Moghadam, S., Caminiti, R., 2013. Impairment of online control of hand and eye movements in a monkey model of optic ataxia. Cerebral cortex (New York, N.Y. 1991) 23, 2644–2656.

Becker, M.I., Person, A.L., 2019. Cerebellar control of reach kinematics for endpoint precision. Neuron (Cambridge, Mass.) 103, 335–348.e5.

Berg, L., Gerdey, J., Masseck, O.A., 2020. Optogenetic manipulation of neuronal activity to modulate behavior in freely moving mice. Journal of Visualized Experiments.

Berke, J.D., Okatan, M., Skurski, J., Eichenbaum, H.B., 2004. Oscillatory entrainment of striatal neurons in freely moving rats. Neuron (Cambridge, Mass.) 43, 883–896.

Bhalla, U.S., Bower, J.M., 1997. Multiday recordings from olfactory bulb neurons in awake freely moving rats: Spatially and temporally organized variability in odorant response properties. Journal of computational neuroscience 4, 221–256.

Binkofski, F., Dohle, C., Posse, S., Stephan, K.M., Hefter, H., Seitz, R.J., Freund, H.-J., 1998. Human anterior intraparietal area subserves prehension: A combined lesion and functional MRI activation study. Neurology 50, 1253–1259.

Blatow, M., Caputi, A., Monyer, H., 2005. Molecular diversity of neocortical GABAergic interneurones: Molecular diversity of interneurones. The Journal of physiology 562, 99–105.

Bolkan, S.S., Stone, I.R., Pinto, L., Ashwood, Z.C., Iravedra Garcia, J.M., Herman, A.L., Singh, P., Bandi, A., Cox, J., Zimmerman, C.A., Cho, J.R., Engelhard, B., Pillow, J.W., Witten, I.B., 2022. Opponent control of behavior by dorsomedial striatal pathways depends on task demands and internal state. Nature neuroscience 25, 345–357.

Bonazzi, L., Viaro, R., Lodi, E., Canto, R., Bonifazzi, C., Franchi, G., 2013. Complex movement topography and extrinsic space representation in the rat forelimb motor cortex as defined by long-duration intracortical microstimulation. The Journal of neuroscience 33, 2097–2107.

Bonnefoi-Kyriacou, B., Legallet, E., Lee, R.G., Trouche, E., 1998. Spatio-temporal and kinematic analysis of pointing movements performed by cerebellar patients with limb ataxia. Experimental brain research 119, 460–466.

Bosch-Bouju, C., Hyland, B., Parr-Brownlie, L., 2013. Motor thalamus integration of cortical, cerebellar and basal ganglia information: Implications for normal and parkinsonian conditions. Frontiers in Computational Neuroscience 7.

Boussaoud, D., Wise, S., 1993. Primate frontal cortex: Neuronal activity following attentional versus intentional cues. Experimental Brain Research 95, 15–27.

Bragin, A., Hetke, J., Wilson, C.L., Anderson, D.J., Engel, J., Buzsáki, G., 2000. Multiple site silicon-based probes for chronic recordings in freely moving rats: Implantation, recording and histological verification. Journal of neuroscience methods 98, 77–82.

Brochier, T., Boudreau, M.-J., Paré, M., Smith, A.M., 1999. The effects of muscimol inactivation of small regions of motor and somatosensory cortex on independent finger movements and force control in the precision grip. Experimental brain research 128, 31–40.

Brown, A.R., Teskey, G.C., 2014. Motor cortex is functionally organized as a set of spatially distinct representations for complex movements. The Journal of neuroscience 34, 13574–13585.

Buccino, A.P., Hurwitz, C.L., Garcia, S., Magland, J., Siegle, J.H., Hurwitz, R., Hennig, M.H., 2020. SpikeInterface, a unified framework for spike sorting.

Buneo, C.A., Andersen, R.A., 2006. The posterior parietal cortex: Sensorimotor interface for the planning and online control of visually guided movements. Neuropsychologia 44, 2594–2606.

Butler, E.G., Finkelstein, D.I., Harvey, M.C., Churchward, P.R., Forlano, L.M., Horne, M.K., 1996. The relationship between monkey ventrolateral thalamic nucleus activity and kinematic parameters of wrist movement. Brain research 736, 146–159.

Butler, E.G., Horne, M.K., Hawkins, N.J., 1992. The activity of monkey thalamic and motor cortical neurones in a skilled, ballistic movement. The Journal of physiology 445, 25–48.

Caminiti, R., Borra, E., Visco-Comandini, F., Battaglia-Mayer, A., Averbeck, B.B., Luppino, G., 2017. Computational architecture of the parieto-frontal network underlying cognitive-motor control in monkeys. eNeuro 4, ENEURO.0306-16.2017-.

Caminiti, R., Ferraina, S., Johnson, P.B., 1996. The sources of visual information to the primate frontal lobe: A novel role for the superior parietal lobule. Cerebral cortex (New York, N.Y. 1991) 6, 319–328.

Casabona, A., Bosco, G., Perciavalle, V., Valle, M.S., 2010. Processing of limb kinematics in the interpositus nucleus. Cerebellum (London, England) 9, 103–110.

Chen, I.-W., Papagiakoumou, E., Emiliani, V., 2018. Towards circuit optogenetics. Current opinion in neurobiology 50, 179–189.

Chiba, S., Numakawa, T., Ninomiya, M., Richards, M.C., Wakabayashi, C., Kunugi, H., 2012. Chronic restraint stress causes anxiety- and depression-like behaviors, downregulates glucocorticoid receptor expression, and attenuates glutamate release induced by brain-derived neurotrophic factor in the prefrontal cortex. Progress in neuro-psychopharmacology & biological psychiatry 39, 112–119.

Churchland, M.M., Santhanam, G., Shenoy, K.V., 2006. Preparatory activity in premotor and motor cortex reflects the speed of the upcoming reach. Journal of Neurophysiology 96, 3130–3146.

Cisek, P., Kalaska, J.F., 2005. Neural correlates of reaching decisions in dorsal premotor cortex: Specification of multiple direction choices and final selection of action. Neuron (Cambridge, Mass.) 45, 801–814.

Cooke, D.F., Stepniewska, I., Miller, D.J., Kaas, J.H., Krubitzer, L., 2015. Reversible deactivation of motor cortex reveals functional connectivity with posterior parietal cortex in the prosimian galago (otolemur garnettii). The Journal of neuroscience 35, 14406–14422.

Cui, H., Andersen, R.A., 2011. Different representations of potential and selected motor plans by distinct parietal areas. The Journal of neuroscience 31, 18130–18136.

Currie, S.P., Ammer, J.J., Premchand, B., Dacre, J., Wu, Y., Eleftheriou, C., Colligan, M., Clarke, T., Mitchell, L., Faisal, A.A., Hennig, M.H., Duguid, I., 2022. Movement-specific signaling is differentially distributed across motor cortex layer 5 projection neuron classes. Cell reports (Cambridge) 39, 110801–110801. https://doi.org/10.1016/j.celrep.2022.110801

Dacre, J., Colligan, M., Clarke, T., Ammer, J.J., Schiemann, J., Chamosa-Pino, V., Claudi, F., Harston, J.A., Eleftheriou, C., Pakan, J.M.P., Huang, C.-C., Hantman, A.W., Rochefort, N.L., Duguid, I., 2021. A cerebellar-thalamocortical pathway drives behavioral context-dependent movement initiation. Neuron 109, 2326–2338.e8. https://doi.org/10.1016/j.neuron.2021.05.016

Davare, M., Kraskov, A., Rothwell, J.C., Lemon, R.N., 2011. Interactions between areas of the cortical grasping network. Current Opinion in Neurobiology 21.

Della-Maggiore, V., Malfait, N., Ostry, D.J., Paus, T., 2004. Stimulation of the posterior parietal cortex interferes with arm trajectory adjustments during the learning of new dynamics. The Journal of neuroscience 24, 9971–9976.

Desmurget, M., Epstein, C.M., Turner, R.S., Prablanc, C., Alexander, G.E., Grafton, S.T., 1999. Role of the posterior parietal cortex in updating reaching movements to a visual target. Nature Neuroscience 2, 563.

Dhawale, A.K., Poddar, R., Wolff, S.B., Normand, V.A., Kopelowitz, E., Ölveczky, B.P., 2017. Automated long-term recording and analysis of neural activity in behaving animals. eLife 6.

Dhawale, A.K., Wolff, S.B.E., Ko, R., Olveczky, B.P., 2021. The basal ganglia control the detailed kinematics of learned motor skills. Nature neuroscience 24, 1256–1269.

Dickey, A.S., Amit, Y., Hatsopoulos, N.G., 2013. Heterogeneous neural coding of corrective movements in motor cortex. Frontiers in neural circuits 7, 51–51.

Diep, A.A., Hunsaker, M.R., Kwock, R., Kim, K., Willemsen, R., Berman, R.F., 2012. Female CGG knock-in mice modeling the fragile x premutation are impaired on a skilled forelimb reaching task. Neurobiology of learning and memory 97, 229–234.

Donkelaar, P. van, Stein, J.F., Passingham, R.E., Miall, R.C., 2000. Temporary inactivation in the primate motor thalamus during visually triggered and internally generated limb movements. Journal of Neurophysiology 83, 2780–2790.

Dudman, J.T., Krakauer, J.W., 2016. The basal ganglia: From motor commands to the control of vigor. Current opinion in neurobiology 37, 158–166.

Dum, R.P., Strick, P.L., 2002. Motor areas in the frontal lobe of the primate. Physiology & behavior 77, 677–682.

Erlich, J.c., Bialek, M., Brody, C.d., 2011. A cortical substrate for memory-guided orienting in the rat. Neuron 72, 330–343.

Esposito, M.S., Capelli, P., Arber, S., 2014. Brainstem nucleus MdV mediates skilled forelimb motor tasks. Nature (London) 508, 351–356.

Estebanez, L., Hoffmann, D., Voigt, B.C., Poulet, J.F.A., 2017. Parvalbumin-expressing GABAergic neurons in primary motor cortex signal reaching. Cell reports (Cambridge) 20, 308–318.

Evarts, E.V., 1968. Relation of pyramidal tract activity to force exerted during voluntary movement. Journal of neurophysiology 31, 14–27.

Fattori, P., Breveglieri, R., Bosco, A., Gamberini, M., Galletti, C., 2017. Vision for prehension in the medial parietal cortex. Cerebral cortex (New York, N.Y. 1991) 27, 1149–1163.

Fattori, P., Raos, V., Breveglieri, R., Bosco, A., Marzocchi, N., Galletti, C., 2010. The dorsomedial pathway is not just for reaching: Grasping neurons in the medial

parieto-occipital cortex of the macaque monkey. The Journal of neuroscience 30, 342–349.

Felleman, D.J., Van Essen, D.C., 1991. Distributed hierarchical processing in the primate cerebral cortex. Cerebral cortex (New York, N.Y. 1991) 1, 1–47.

Filimon, F., 2010. Human cortical control of hand movements: Parietofrontal networks for reaching, grasping, and pointing. The Neuroscientist 16, 388–407.

Flindall, J., Gonzalez, C.L.R., 2019. On the neurocircuitry of grasping: The influence of action intent on kinematic asymmetries in reach-to-grasp actions. Attention, perception & psychophysics 81, 2217–2236.

Fogassi, L., Gallese, V., Buccino, G., Craighero, L., Fadiga, L., Rizzolatti, G., 2001. Cortical mechanism for the visual guidance of hand grasping movements in the monkey: A reversible inactivation study. Brain 124, 571–586.

Fortier, P.A., Kalaska, J.F., Smith, A.M., 1989. Cerebellar neuronal activity related to whole-arm reaching movements in the monkey. Journal of neurophysiology 62, 198–211.

Frey, M., Tanni, S., Perrodin, C., O'leary, A., Nau, M., Kelly, J., Banino, A., Bendor, D., Lefort, J., Doeller, C.F., Barry, C., 2021. Interpreting wide-band neural activity using convolutional neural networks. eLife 10.

Gabriel, D.A., 1997. Shoulder and elbow muscle activity in goal-directed arm movements. Experimental brain research 116, 359–366.

Gage, G.J., Stoetzner, C.R., Wiltschko, A.B., Berke, J.D., 2010. Selective activation of striatal fast-spiking interneurons during choice execution. Neuron (Cambridge, Mass.) 67, 466–479.

Galea, M., Dariansmith, I., 1994. Multiple corticospinal neuron populations in the macaque monkey are specified by their unique cortical origins, spinal terminations, and connections. Cerebral Cortex 4, 166–194.

Galiñanes, G.L., Bonardi, C., Huber, D., 2018. Directional reaching for water as a cortex-dependent behavioral framework for mice. Cell Reports 22, 2767–2783.

Gamberini, M., Passarelli, L., Filippini, M., Fattori, P., Galletti, C., 2021. Vision for action: Thalamic and cortical inputs to the macaque superior parietal lobule. Brain Structure and Function 226, 2951–2966.

Gao, P., Hattox, A.M., Jones, L.M., Keller, A., Zeigler, H.P., 2003. Whisker motor cortex ablation and whisker movement patterns. Somatosensory & motor research 20, 191–198.

Gerbella, M., Belmalih, A., Borra, E., Rozzi, S., Luppino, G., 2011. Cortical connections of the anterior (F5a) subdivision of the macaque ventral premotor area F5. Brain Structure and Function 216, 43–65.

Gernert, M., Hamann, M., Bennay, M., Loscher, W., Richter, A., 2000. Deficit of striatal parvalbumin-reactive GABAergic interneurons and decreased basal ganglia output in a genetic rodent model of idiopathic paroxysmal dystonia. The Journal of neuroscience 20, 7052–7058.

Geyer, S., Matelli, M., Luppino, G., Zilles, K., 2000. Functional neuroanatomy of the primate isocortical motor system. Anatomy and embryology 202, 443–474.

Gharbawie, O.A., Stepniewska, I., Burish, M.J., Kaas, J.H., 2010. Thalamocortical connections of functional zones in posterior parietal cortex and frontal cortex motor regions in new world monkeys. Cerebral Cortex 20, 2391–2410.

Gharbawie, O.A., Stepniewska, I., Kaas, J.H., 2011. Cortical connections of functional zones in posterior parietal cortex and frontal cortex motor regions in new world monkeys. Cerebral Cortex 21, 1981–2002.

Ghodrati, M., Khaligh-Razavi, S.-M., Lehky, S.R., 2017. Towards building a more complex view of the lateral geniculate nucleus: Recent advances in understanding its role. Progress in neurobiology 156, 214–255.

Gielen, C.C.A.M., Heuvel, P.J.M. van den, Denier van der Gon, J.J., 1984. Modification of muscle activation patterns during fast goal-directed arm movements. Journal of motor behavior 16, 2–19.

Goard, M.J., Pho, G.N., Woodson, J., Sur, M., 2016. Distinct roles of visual, parietal, and frontal motor cortices in memory-guided sensorimotor decisions. eLife 5.

Goodale, M.A., 2011. Transforming vision into action. Vision research (Oxford) 51, 1567–1587.

Goodkin, H.P., Thach, W.T., 2003. Cerebellar control of constrained and unconstrained movements. I. Nuclear inactivation. Journal of Neurophysiology 89, 884–895.

Graziano, M., 2006. The organization of behavioral repertoire in motor cortex. Annual Review of Neuroscience, Annual review of neuroscience 29, 105–134.

Graziano, M.S.A., Aflalo, T.N.S., Cooke, D.F., 2005. Arm movements evoked by electrical stimulation in the motor cortex of monkeys. Journal of Neurophysiology 94, 4209–4223.

Gréa, H., Pisella, L., Rossetti, Y., Desmurget, M., Tilikete, C., Grafton, S., Prablanc, C., Vighetto, A., 2002. A lesion of the posterior parietal cortex disrupts on-line adjustments during aiming movements. Neuropsychologia 40, 2471–2480.

Gregoriou, G.G., Luppino, G., Matelli, M., Savaki, H.E., 2005. Frontal cortical areas of the monkey brain engaged in reaching behavior: A 14C-deoxyglucose imaging study. NeuroImage (Orlando, Fla.) 27, 442–464.

Gremel, C.M., Costa, R.M., 2013a. Premotor cortex is critical for goal-directed actions. Frontiers in computational neuroscience 7, 110–110.

Gremel, C.M., Costa, R.M., 2013b. Orbitofrontal and striatal circuits dynamically encode the shift between goal-directed and habitual actions. Nature communications 4, 2264–2264.

Grol, M.J., Majdandzic, J., Stephan, K.E., Verhagen, L., Dijkerman, H.C., Bekkering, H., Verstraten, F.A.J., Toni, I., 2007. Parieto-frontal connectivity during visually guided grasping. The Journal of neuroscience 27, 11877–11887.

Guo, J.-Z., Graves, A.R., Guo, W.W., Zheng, J., Lee, A., Rodriguez-Gonzalez, J., Li, N., Macklin, J.J., Phillips, J.W., Mensh, B.D., Branson, K., Hantman, A.W., 2015. Cortex commands the performance of skilled movement.(report). eLife 4.

Guo, Z.V., Hires, S.A., Li, N., O'Connor, D.H., Komiyama, T., Ophir, E., Huber, D., Bonardi, C., Morandell, K., Gutnisky, D., Peron, S., Xu, N.-L., Cox, J., Svoboda, K., 2014a.

Procedures for behavioral experiments in head-fixed mice. PloS one 9, e88678–e88678.

Guo, Z.V., Li, N., Huber, D., Ophir, E., Gutnisky, D., Ting, J.T., Feng, G., Svoboda, K., 2014b. Flow of cortical activity underlying a tactile decision in mice. Neuron 81, 179–194.

Gupta, A., Wang, Y., Markram, H., 2000. Organizing principles for a diversity of GABAergic interneurons and synapses in the neocortex. Science (American Association for the Advancement of Science) 287, 273–278.

Harris, C.R., Millman, K.J., Walt, S.J. van der, Gommers, R., Virtanen, P., Cournapeau, D., Wieser, E., Taylor, J., Berg, S., Smith, N.J., Kern, R., Picus, M., Hoyer, S., Kerkwijk, M.H. van, Brett, M., Haldane, A., Río, J.F. del, Wiebe, M., Peterson, P., Gérard-Marchant, P., Sheppard, K., Reddy, T., Weckesser, W., Abbasi, H., Gohlke, C., Oliphant, T.E., 2020. Array programming with NumPy. Nature 585, 357–362. https://doi.org/10.1038/s41586-020-2649-2

Harris, K.D., Mrsic-Flogel, T.D., 2013. Cortical connectivity and sensory coding. Nature (London) 503, 51–58.

Harris, K., Shepherd, G., 2015. The neocortical circuit: Themes and variations. Nature Neuroscience 18.

Hart, G., Leung, B.K., Balleine, B.W., 2014. Dorsal and ventral streams: The distinct role of striatal subregions in the acquisition and performance of goal-directed actions. Neurobiology of learning and memory 108, 104–118.

Harvey, C.D., Coen, P., Tank, D.W., 2012. Choice-specific sequences in parietal cortex during a virtual-navigation decision task. Nature 484.

Harvey, C.D., Collman, F., Dombeck, D.A., Tank, D.W., 2009. Intracellular dynamics of hippocampal place cells during virtual navigation. Nature (London) 461, 941–946.

Hasegawa, M., Majima, K., Itokazu, T., Maki, T., Albrecht, U.-R., Castner, N., Izumo, M., Sohya, K., Sato, T.K., Kamitani, Y., Sato, T.R., 2017. Selective suppression of local circuits during movement preparation in the mouse motor cortex. Cell reports (Cambridge) 18, 2676–2686.

Hennig, C., 2015. Clustering strategy and method selection. https://doi.org/10.48550/ARXIV.1503.02059

Himmelbach, M., Linzenbold, W., Ilg, U.J., 2013. Dissociation of reach-related and visual signals in the human superior colliculus. NeuroImage (Orlando, Fla.) 82, 61–67.

Hintiryan, H., Foster, N.N., Bowman, I., Bay, M., Song, M.Y., Gou, L., Yamashita, S., Bienkowski, M.S., Zingg, B., Zhu, M., Yang, X.W., Shih, J.C., Toga, A.W., Dong, H.-W., 2016. The mouse cortico-striatal projectome. Nature neuroscience 19, 1100–1114.

Hooks, B.M., Mao, T., Gutnisky, D.A., Yamawaki, N., Svoboda, K., Shepherd, G.M.G., 2013. Organization of cortical and thalamic input to pyramidal neurons in mouse motor cortex. The Journal of neuroscience 33, 748–760.

Hovde, K., Gianatti, M., Witter, M.P., Whitlock, J.R., 2018. Architecture and organization of mouse posterior parietal cortex relative to extrastriate areas. bioRxiv. https://doi.org/10.1101/361832

Hoy, J.L., Yavorska, I., Wehr, M., Niell, C.M., 2016. Vision drives accurate approach behavior during prey capture in laboratory mice. Current biology. 26.

Huff, T., Mahabadi, N., Tadi, P., 2022. Neuroanatomy, visual cortex. Treasure Island (FL): StatPearls Publishing.

Humphries, M.D., Gurney, K.N., 2002. The role of intra-thalamic and thalamocortical circuits in action selection. Network (Bristol) 13, 131–156.

Hunnicutt, B.J., Long, B.R., Kusefoglu, D., Gertz, K.J., Zhong, H., Mao, T., 2014. A comprehensive thalamocortical projection map at the mesoscopic level.(RESOURCE) (report). Nature Neuroscience 17.

Hunter, J.D., 2007. Matplotlib: A 2D graphics environment. Computing in Science & Engineering 9, 90–95. https://doi.org/10.1109/MCSE.2007.55

Hurd, C., Weishaupt, N., Fouad, K., 2013. Anatomical correlates of recovery in single pellet reaching in spinal cord injured rats. Experimental Neurology 247, 605–614. https://doi.org/10.1016/j.expneurol.2013.02.013

Hwang, E. jung, Hauschild, M., Wilke, M., Andersen, R.a., 2012. Inactivation of the parietal reach region causes optic ataxia, impairing reaches but not saccades. Neuron 76, 1021–1029.

Hwang, E.J., Dahlen, J., Mukundan, M., Komiyama, T., 2017. History-based action selection bias in posterior parietal cortex. Nat Commun 8, 1242–1242.

Hwang, E.J., Link, T.D., Hu, Y.Y., Lu, S., Wang, E.H.-J., Lilascharoen, V., Aronson, S., O'Neil, K., Lim, B.K., Komiyama, T., 2019. Corticostriatal flow of action selection bias. Neuron (Cambridge, Mass.) 104, 1126–1140.e6.

Ilinsky, I.A., Kultas-Ilinsky, K., 2002. Motor thalamic circuits in primates with emphasis on the area targeted in treatment of movement disorders. Movement disorders 17, S9–S14.

Ison, M.J., Mormann, F., Cerf, M., Koch, C., Fried, I., Quiroga, R.Q., 2011. Selectivity of pyramidal cells and interneurons in the human medial temporal lobe. Journal of neurophysiology 106, 1713–1721.

Itokazu, T., Hasegawa, M., Kimura, R., Osaki, H., Albrecht, U.-R., Sohya, K., Chakrabarti, S., Itoh, H., Ito, T., Sato, T.K., Sato, T.R., 2018. Streamlined sensory motor communication through cortical reciprocal connectivity in a visually guided eye movement task. Nature communications 9, 338–14.

Jeannerod, M., 1984. The timing of natural prehension movements. Journal of motor behavior 16, 235–254.

Ji, X.-Y., Zingg, B., Mesik, L., Xiao, Z., Zhang, L.I., Tao, H.W., 2016. Thalamocortical innervation pattern in mouse auditory and visual cortex: Laminar and cell-type specificity. Cerebral cortex (New York, N.Y. 1991) 26, 2612–2625.

Jia, X., Siegle, J.H., Bennett, C., Gale, S.D., Denman, D.J., Koch, C., Olsen, S.R., 2019. High-density extracellular probes reveal dendritic backpropagation and facilitate neuron classification. Journal of neurophysiology 121, 1831–1847.

Jiang, X., Shen, S., Cadwell, C.R., Berens, P., Sinz, F., Ecker, A.S., Patel, S., Tolias, A.S., 2015. Principles of connectivity among morphologically defined cell types in adult neocortex. Science (American Association for the Advancement of Science) 350, 1055–1055.

Johnson, P.B., Ferraina, S., Bianchi, L., Caminiti, R., 1996. Cortical networks for visual reaching: Physiological and anatomical organization of frontal and parietal lobe arm regions. Cerebral cortex (New York, N.Y. 1991) 6, 102–119.

Jolles, J.W., 2021. Broad-scale applications of the raspberry pi: A review and guide for biologists. Methods in Ecology and Evolution 12, 1562–1579. https://doi.org/10.1111/2041-210X.13652

Juavinett, A.L., Bekheet, G., Churchland, A.K., 2019. Chronically implanted neuropixels probes enable high-yield recordings in freely moving mice. eLife 8.

Juczewski, K., Koussa, J.A., Kesner, A.J., Lee, J.O., Lovinger, D.M., 2020. Stress and behavioral correlates in the head-fixed method: Stress measurements, habituation dynamics, locomotion, and motor-skill learning in mice. Scientific reports 10, 12245–12245.

Jun, J.J., Steinmetz, N.A., Siegle, J.H., Denman, D.J., Bauza, M., Barbarits, B., Lee, A.K., Anastassiou, C.A., Andrei, A., Aydin, Ç., Barbic, M., Blanche, T.J., Bonin, V., Couto, J., Dutta, B., Gratiy, S.L., Gutnisky, D.A., Häusser, M., Karsh, B., Ledochowitsch, P., Lopez, C.M., Mitelut, C., Musa, S., Okun, M., Pachitariu, M., Putzeys, J., Rich, P.D., Rossant, C., Sun, W.-L., Svoboda, K., Carandini, M., Harris, K.D., Koch, C., O'Keefe, J., Harris, T.D., 2017. Fully integrated silicon probes for high-density recording of neural activity. Nature (London) 551, 232–236.

Kaas, J.H., Gharbawie, O.A., Stepniewska, I., 2013. Cortical networks for ethologically relevant behaviors in primates: Cortical networks and behavior. American journal of primatology 75, 407–414.

Kaas, J.H., Stepniewska, I., 2016. Evolution of posterior parietal cortex and parietal-frontal networks for specific actions in primates. Journal of Comparative Neurology 524, 595–608.

Kaneko, T., 2013. Local connections of excitatory neurons in motor-associated cortical areas of the rat. Frontiers in neural circuits 7, 75–75.

Karl, J.M., Whishaw, I.Q., 2013. Different evolutionary origins for the reach and the grasp: An explanation for dual visuomotor channels in primate parietofrontal cortex. Frontiers in neurology 4, 208–208.

Kasahara, K., DaSalla, C.S., Honda, M., Hanakawa, T., 2022. Basal ganglia-cortical connectivity underlies self-regulation of brain oscillations in humans. Communications biology 5, 712–712.

Kawai, R., Markman, T., Poddar, R., Ko, R., Fantana, A.L., Dhawale, A.K., Kampff, A.R., Ölveczky, B.P., 2015. Motor cortex is required for learning but not for executing a motor skill. Neuron (Cambridge, Mass.) 86, 800–812.

Keller, C.J., Chen, C., Lado, F.A., Khodakhah, K., 2016. The limited utility of multiunit data in differentiating neuronal population activity. PloS one 11, e0153154–e0153154.

Khastkhodaei, Z., Jurjut, O., Katzner, S., Busse, L., 2016. Mice can use second-order, contrast-modulated stimuli to guide visual perception. The journal of neuroscience : the official journal of the Society for Neuroscience. 36.

Kim, J.-H., Ma, D.-H., Jung, E., Choi, I., Lee, S.-H., 2021. Gated feedforward inhibition in the frontal cortex releases goal-directed action. Nature neuroscience 24, 1452–1464.

Klaus, A., Alves da Silva, J., Costa, R.M., 2019. What, if, and when to move: Basal ganglia circuits and self-paced action initiation. Annual review of neuroscience, Annual review of neuroscience 42, 459–483.

Klein, A., Sacrey, L.-A.R., Whishaw, I.Q., Dunnett, S.B., 2012. The use of rodent skilled reaching as a translational model for investigating brain damage and disease. Neuroscience and biobehavioral reviews 36, 1030–1042.

Klioutchnikov, A., Wallace, D.J., Sawinski, J., Voit, K.-M., Groemping, Y., Kerr, J.N.D., 2023. A three-photon head-mounted microscope for imaging all layers of visual cortex in freely moving mice. Nature methods 20, 610–616.

Kravitz, A.V., Tye, L.D., Kreitzer, A.C., 2012. Distinct roles for direct and indirect pathway striatal neurons in reinforcement. Nature neuroscience 15, 816–818.

Kuramoto, E., Furuta, T., Nakamura, K.C., Unzai, T., Hioki, H., Kaneko, T., 2009. Two types of thalamocortical projections from the motor thalamic nuclei of the rat: A single neuron-tracing study using viral vectors. Cerebral Cortex 19, 2065–2077.

Lara, A.H., Elsayed, G.F., Zimnik, A.J., Cunningham, J.P., Churchland, M.M., 2018. Conservation of preparatory neural events in monkey motor cortex regardless of how movement is initiated. eLife 7.

Lee, J.-H., Donkelaar, P. van, 2006. The human dorsal premotor cortex generates on-line error corrections during sensorimotor adaptation. The Journal of neuroscience 26, 3330–3334.

Lee, K., Holley, S.M., Shobe, J.L., Chong, N.C., Cepeda, C., Levine, M.S., Masmanidis, S.C., 2018. Parvalbumin interneurons modulate striatal output and enhance performance during associative learning. Neuron (Cambridge, Mass.) 99, 239–239.

Lee, S.-H., Kwan, A.C., Zhang, S., Phoumthipphavong, V., Flannery, J.G., Masmanidis, S.C., Taniguchi, H., Huang, Z.J., Zhang, F., Boyden, E.S., Deisseroth, K., Dan, Y., 2012. Activation of specific interneurons improves V1 feature selectivity and visual perception. Nature (London) 488, 379–383.

Leinweber, M., Ward, D.R., Sobczak, J.M., Attinger, A., Keller, G.B., 2017. A sensorimotor circuit in mouse cortex for visual flow predictions. Neuron (Cambridge, Mass.) 96, 1204–1204.

Levi, A., Spivak, L., Sloin, H.E., Someck, S., Stark, E., 2022. Error correction and improved precision of spike timing in converging cortical networks. Cell reports (Cambridge) 40, 111383–111383.

Levy, S., Lavzin, M., Benisty, H., Ghanayim, A., Dubin, U., Achvat, S., Brosh, Z., Aeed, F., Mensh, B.D., Schiller, Y., Meir, R., Barak, O., Talmon, R., Hantman, A.W., Schiller, J., 2020. Cell-type-specific outcome representation in the primary motor cortex. Neuron (Cambridge, Mass.) 107, 954–971.e9.

Li, Y., Hollis, E., 2021. Basal forebrain cholinergic neurons selectively drive coordinated motor learning in mice. The Journal of neuroscience 41, 10148–10160.

Liang, H., Paxinos, G., Watson, C., 2011. Projections from the brain to the spinal cord in the mouse. Brain Structure and Function 215, 159–186.

Licata, A.M., Kaufman, M.T., Raposo, D., Ryan, M.B., Sheppard, J.P., Churchland, A.K., 2017. Posterior parietal cortex guides visual decisions in rats. The Journal of neuroscience : the official journal of the Society for Neuroscience 37.

Lima, S.Q., Hromádka, T., Znamenskiy, P., Zador, A.M., 2009. PINP: A new method of tagging neuronal populations for identification during in vivo electrophysiological recording. PloS one 4, e6099–e6099.

Lin, H.-M., Kuang, J.-X., Sun, P., Li, N., Lv, X., Zhang, Y.-H., 2018. Reconstruction of intratelencephalic neurons in the mouse secondary motor cortex reveals the diverse projection patterns of single neurons. Frontiers in neuroanatomy 12, 86–86.

Low, A.Y.T., Thanawalla, A.R., Yip, A.K.K., Kim, J., Wong, K.L.L., Tantra, M., Augustine, G.J., Chen, A.I., 2018. Precision of discrete and rhythmic forelimb movements requires a distinct neuronal subpopulation in the interposed anterior nucleus. Cell reports (Cambridge) 22, 2322–2333.

Luo, L., Callaway, E.M., Svoboda, K., 2008. Genetic dissection of neural circuits. Neuron (Cambridge, Mass.) 57, 634–660.

Luo, P., Li, A., Zheng, Y., Han, Y., Tian, J., Xu, Z., Gong, H., Li, X., 2019. Whole brain mapping of long-range direct input to glutamatergic and GABAergic neurons in motor cortex. Frontiers in neuroanatomy 13, 44–44.

Makino, H., Ren, C., Liu, H., Kim, A.N., Kondapaneni, N., Liu, X., Kuzum, D., Komiyama, T., 2017. Transformation of cortex-wide emergent properties during motor learning. Neuron 94, 880–890.e8.

Mallet, N., Le Moine, C., Charpier, S., Gonon, F., 2005. Feedforward inhibition of projection neurons by fast-spiking GABA interneurons in the rat striatum in vivo. The Journal of neuroscience 25, 3857–3869.

Manita, S., Ikezoe, K., Kitamura, K., 2022. A novel device of reaching, grasping, and retrieving task for head-fixed mice. Frontiers in neural circuits 16.

Mao, T., Kusefoglu, D., Hooks, B.M., Huber, D., Petreanu, L., Svoboda, K., 2011. Long-range neuronal circuits underlying the interaction between sensory and motor cortex. Neuron (Cambridge, Mass.) 72, 111–123.

Marconi, B., Genovesio, A., Battaglia-Mayer, A., Ferraina, S., Squatrito, S., Molinari, M., Lacquaniti, F., Caminiti, R., 2001. Eye-hand coordination during reaching. I. Anatomical relationships between parietal and frontal cortex. Cerebral Cortex 11, 513–527.

Markram, H., Toledo-Rodriguez, M., Wang, Y., Gupta, A., Silberberg, G., Wu, C., 2004. Interneurons of the neocortical inhibitory system. Nature reviews. Neuroscience 5, 793–807.

Mason, C.R., Miller, L.E., Baker, J.F., Houk, J.C., 1998. Organization of reaching and grasping movements in the primate cerebellar nuclei as revealed by focal muscimol inactivations. Journal of neurophysiology 79, 537–554.

Mathis, A., Mamidanna, P., Cury, K.M., Abe, T., Murthy, V.N., Mathis, M.W., Bethge, M., 2018. DeepLabCut: Markerless pose estimation of user-defined body parts with deep learning. Nature neuroscience 21, 1281–1289.

McGuire, L.M.M., Sabes, P.N., 2011. Heterogeneous representations in the superior parietal lobule are common across reaches to visual and proprioceptive targets. The Journal of neuroscience 31, 6661–6673.

Metz, G.A.S., Whishaw, I.Q., 2000. Skilled reaching an action pattern: Stability in rat (rattus norvegicus) grasping movements as a function of changing food pellet size. Behavioural brain research 116, 111–122.

Mink, J.W., 2003. The basal ganglia and involuntary movements: Impaired inhibition of competing motor patterns. Archives of neurology (Chicago) 60, 1365–1368.

Mink, J.W., 1996. The basal ganglia: Focused selection and inhibition of competing motor programs. Progress in neurobiology 50, 381–425.

Mirza Agha, B., Akbary, R., Ghasroddashti, A., Nazari-Ahangarkolaee, M., Whishaw, I.Q., Mohajerani, M.H., 2021. Cholinergic upregulation by optogenetic stimulation of nucleus basalis after photothrombotic stroke in forelimb somatosensory cortex improves endpoint and motor but not sensory control of skilled reaching in mice. Journal of cerebral blood flow and metabolism 41, 1608–1622.

Mitchell, J.F., Sundberg, K.A., Reynolds, J.H., 2007. Differential attention-dependent response modulation across cell classes in macaque visual area V4. Neuron (Cambridge, Mass.) 55, 131–141.

Montoya, C.P., Campbell-Hope, L.J., Pemberton, K.D., Dunnett, S.B., 1991. The 'staircase test': A measure of independent forelimb reaching and grasping abilities in rats. Journal of neuroscience methods 36, 219–228.

Monzee, J., Drew, T., Smith, A.M., 2004. Effects of muscimol inactivation of the cerebellar nuclei on precision grip. Journal of Neurophysiology 91, 1240–1249.

Moulin, T.C., 2021. Chronic optogenetic stimulation in freely moving rodents. Channelrhodopsin, Methods in molecular biology 2191, 391–401.

Mountcastle, V.B., Lynch, J.C., Georgopoulos, A., Sakata, H., Acuna, C., 1975. Posterior parietal association cortex of the monkey: Command functions for operations within extrapersonal space. Journal of neurophysiology 38, 871–908.

Müllner, D., 2011. Modern hierarchical, agglomerative clustering algorithms. https://doi.org/10.48550/ARXIV.1109.2378

Muñoz-Castañeda, R., Zingg, B., Matho, K.S., Chen, X., Wang, Q., Foster, N.N., Li, A., Narasimhan, A., Hirokawa, K.E., Huo, B., Bannerjee, S., Korobkova, L., Park, C.S., Park, Y.-G., Bienkowski, M.S., Chon, U., Wheeler, D.W., Li, X., Wang, Y., Naeemi, M., Xie, P., Liu, L., Kelly, K., An, X., Attili, S.M., Bowman, I., Bludova, A., Cetin, A., Ding, L., Drewes, R., D'Orazi, F., Elowsky, C., Fischer, S., Galbavy, W., Gao, L., Gillis, J., Groblewski, P.A., Gou, L., Hahn, J.D., Hatfield, J.T., Hintiryan, H., Huang, J.J., Kondo, H., Kuang, X., Lesnar, P., Li, X., Li, Y., Lin, M., Lo, D., Mizrachi, J., Mok, S., Nicovich, P.R., Palaniswamy, R., Palmer, J., Qi, X., Shen, E., Sun, Y.-C., Tao, H.W., Wakemen, W., Wang, Y., Yao, S., Yuan, J., Zhan, H., Zhu, M., Ng, L., Zhang, L.I., Lim, B.K., Hawrylycz, M., Gong, H., Gee, J.C., Kim, Y., Chung, K., Yang, X.W., Peng, H., Luo, Q., Mitra, P.P., Zador, A.M., Zeng, H., Ascoli, G.A., Josh Huang, Z., Osten, P., Harris, J.A., Dong, H.-W., 2021. Cellular anatomy of the mouse primary motor cortex. Nature (London) 598, 159–166.

Murata, A., Fadiga, L., Fogassi, L., Gallese, V., Raos, V., Rizzolatti, G., 1997. Object representation in the ventral premotor cortex (area F5) of the monkey. Journal of neurophysiology 78.

Murata, A., Gallese, V., Luppino, G., Kaseda, M., Sakata, H., 2000. Selectivity for the shape, size, and orientation of objects for grasping in neurons of monkey parietal area AIP. Journal of neurophysiology 83.

Mushiake, H., Strick, P.L., 1993. Preferential activity of dentate neurons during limb movements guided by vision. Journal of neurophysiology 70, 2660–2664.

Nashef, A., Cohen, O., Harel, R., Israel, Z., Prut, Y., 2019. Reversible block of cerebellar outflow reveals cortical circuitry for motor coordination. Cell reports (Cambridge) 27, 2608–2619.e4.

Nashef, A., Cohen, O., Perlmutter, S., Prut, Y., 2022. A cerebellar origin of feedforward inhibition to the motor cortex in non-human primates. Cell reports (Cambridge) 39, 110803–110803.

Navabpour, S., Kwapis, J.L., Jarome, T.J., 2020. A neuroscientist's guide to transgenic mice and other genetic tools. Neuroscience and biobehavioral reviews 108, 732–748.

Nicola, F. do C., Hua, I., Levine, A.J., 2022. Intersectional genetic tools to study skilled reaching in mice. Experimental neurology 347, 113879–113879.

Okun, M., Lak, A., Carandini, M., Harris, K.D., 2016. Long term recordings with immobile silicon probes in the mouse cortex. PloS one 11, e0151180–e0151180.

Olsen, G.M., Hovde, K., Kondo, H., Sakshaug, T., Sømme, H.H., Whitlock, J.R., Witter, M.P., 2019. Organization of posterior parietal-frontal connections in the rat. Frontiers in systems neuroscience 13, 38–38.

Ölveczky, B.P., 2011. Motoring ahead with rodents. Current opinion in neurobiology 21, 571–578.

Osanai, H., Kitamura, T., Yamamoto, J., 2019. Hybrid microdrive system with recoverable opto-silicon probe and tetrode for dual-site high density recording in freely moving mice. Journal of Visualized Experiments.

Ota, Y., Ago, Y., Tanaka, T., Hasebe, S., Toratani, Y., Onaka, Y., Hashimoto, H., Takuma, K., Matsuda, T., 2015. Anxiolytic-like effects of restraint during the dark cycle in adolescent mice. Behavioural brain research 284, 103–111.

Pan, W.X., Mao, T., Dudman, J.T., 2010. Inputs to the dorsal striatum of the mouse reflect the parallel circuit architecture of the forebrain. Frontiers in neuroanatomy 4, 147–147.

Pandarinath, C., O'Shea, D.J., Collins, J., Jozefowicz, R., Stavisky, S.D., Kao, J.C., Trautmann, E.M., Kaufman, M.T., Ryu, S.I., Hochberg, L.R., Henderson, J.M., Shenoy, K.V., Abbott,

L.F., Sussillo, D., 2017. Inferring single-trial neural population dynamics using sequential auto-encoders. bioRxiv. https://doi.org/10.1101/152884

Parker, P.R.L., Abe, E.T.T., Leonard, E.S.P., Martins, D.M., Niell, C.M., 2022. Joint coding of visual input and eye/head position in V1 of freely moving mice. Neuron (Cambridge, Mass.) 110, 3897–3906.e5.

Parker, P.R.L., Brown, M.A., Smear, M.C., Niell, C.M., 2020. Movement-related signals in sensory areas: Roles in natural behavior. Trends in neurosciences (Regular ed.) 43, 581–595.

Parthasarathy, H.B., Graybiel, A.M., 1997. Cortically driven immediate-early gene expression reflects modular influence of sensorimotor cortex on identified striatal neurons in the squirrel monkey. The Journal of neuroscience 17, 2477–2491.

Paxinos, G., 2001. The mouse brain in stereotaxic coordinates / george paxinos, keith b.j. franklin., Second edition. ed. Academic Press, San Diego, Calif., London.

Peron, S., Chen, T.-W., Svoboda, K., 2015. Comprehensive imaging of cortical networks. Current opinion in neurobiology 32, 115–123.

Peters, A.J., Lee, J., Hedrick, N.G., O'neil, K., Komiyama, T., 2017. Reorganization of corticospinal output during motor learning. Nature neuroscience 20, 1133–1141.

Petrof, I., Viaene, A.N., Sherman, S.M., 2015. Properties of the primary somatosensory cortex projection to the primary motor cortex in the mouse. Journal of neurophysiology 113, 2400–2407.

Pisella, L., Gréa, H., Tilikete, C., Vighetto, A., Desmurget, M., Rode, G., Boisson, D., Rossetti, Y., 2000. An 'automatic pilot' for the hand in human posterior parietal cortex: Toward reinterpreting optic ataxia. Nature Neuroscience 3.

Planert, H., Berger, T.K., Silberberg, G., 2013. Membrane properties of striatal direct and indirect pathway neurons in mouse and rat slices and their modulation by dopamine. PloS one 8, e57054–e57054.

Quallo, M.M., Kraskov, A., Lemon, R.N., 2012. The activity of primary motor cortex corticospinal neurons during tool use by macaque monkeys. The Journal of neuroscience 32, 17351–17364.

Ramanathan, D., Conner, J.M., Tuszynski, M.H., 2006. A form of motor cortical plasticity that correlates with recovery of function after brain injury. Proceedings of the National Academy of Sciences - PNAS 103, 11370–11375.

Ravel, S., Sardo, P., Legallet, E., Apicella, P., 2006. Influence of spatial information on responses of tonically active neurons in the monkey striatum. Journal of Neurophysiology 95, 2975–2986.

Resulaj, A., 2021. Projections of the mouse primary visual cortex. Frontiers in neural circuits 15, 751331–751331.

Sacrey, L.-A.R., Alaverdashvili, M., Whishaw, I.Q., 2009. Similar hand shaping in reaching-for-food (skilled reaching) in rats and humans provides evidence of homology in release, collection, and manipulation movements. Behavioural brain research 204, 153–161.

Sadler, A.M., Bailey, S.J., 2016. Repeated daily restraint stress induces adaptive behavioural changes in both adult and juvenile mice. Physiology & behavior 167, 313–323.

Sakata, H., Taira, M., Murata, A., Mine, S., 1995. Neural mechanisms of visual guidance of hand action in the parietal cortex of the monkey. Cerebral cortex (New York, N.Y. : 1991) 5.

Sani, O.G., Abbaspourazad, H., Wong, Y.T., Pesaran, B., Shanechi, M.M., 2021. Modeling behaviorally relevant neural dynamics enabled by preferential subspace identification. Nature neuroscience 24, 140–149.

Sauerbrei, B.A., Guo, J.-Z., Cohen, J.D., Mischiati, M., Guo, W., Kabra, M., Verma, N., Mensh, B., Branson, K., Hantman, A.W., 2020. Cortical pattern generation during dexterous movement is input-driven. Nature (London) 577, 386–391.

Savidan, J., Kaeser, M., Belhaj-Saïf, A., Schmidlin, E., Rouiller, E.M., 2017. Role of primary motor cortex in the control of manual dexterity assessed via sequential bilateral lesion in the adult macaque monkey: A case study. Neuroscience 357, 303–324.

Schäfer, C., Gao, Z., Zeeuw, C. de, Hoebeek, F., 2021. Temporal dynamics of the cerebello-cortical convergence in ventro-lateral motor thalamus. The Journal of physiology 599, 2055–2073.

Schaffelhofer, S., Scherberger, H., 2016. Object vision to hand action in macaque parietal, premotor, and motor cortices.(report). eLife 5.

Schwartz, A., Kettner, R., Georgopoulos, A., 1988. Primate motor cortex and free arm movements to visual targets in three- dimensional space. I. Relations between single cell discharge and direction of movement. The Journal of neuroscience 8, 2913–2927.

Schwarz, C., Hentschke, H., Butovas, S., Haiss, F., Stüttgen, M.C., Gerdjikov, T.V., Bergner, C.G., Waiblinger, C., 2010. The head-fixed behaving rat-procedures and pitfalls. Somatosensory & motor research 27, 131–148.

Soma, S., Saiki, A., Yoshida, J., Ríos, A., Kawabata, M., Sakai, Y., Isomura, Y., 2017. Distinct laterality in forelimb-movement representations of rat primary and secondary motor cortical neurons with intratelencephalic and pyramidal tract projections. The Journal of neuroscience 37, 10904–10916.

Soma, S., Yoshida, J., Kato, S., Takahashi, Y., Nonomura, S., Sugimura, Y.K., Ríos, A., Kawabata, M., Kobayashi, K., Kato, F., Sakai, Y., Isomura, Y., 2019. Ipsilateral-dominant control of limb movements in rodent posterior parietal cortex. The Journal of neuroscience 39, 485–502.

Spidalieri, G., Busby, L., Lamarre, Y., 1983. Fast ballistic arm movements triggered by visual, auditory, and somesthetic stimuli in the monkey. II. Effects of unilateral dentate lesion on discharge of precentral cortical neurons and reaction time. Journal of neurophysiology 50, 1359–1379.

Stalnaker, T.A., Calhoon, G.G., Ogawa, M., Roesch, M.R., Schoenbaum, G., 2012. Reward prediction error signaling in posterior dorsomedial striatum is action specific. The Journal of neuroscience 32, 10296–10305.

Steinmetz, N.A., Aydin, C., Lebedeva, A., Okun, M., Pachitariu, M., Bauza, M., Beau, M., Bhagat, J., Bohm, C., Broux, M., Chen, S., Colonell, J., Gardner, R.J., Karsh, B., Kloosterman, F., Kostadinov, D., Mora-Lopez, C., O'Callaghan, J., Park, J., Putzeys, J., Sauerbrei, B., Daal, R.J.J. van, Vollan, A.Z., Wang, S., Welkenhuysen, M., Ye, Z., Dudman, J.T., Dutta, B., Hantman, A.W., Harris, K.D., Lee, A.K., Moser, E., O'Keefe, J., Renart, A., Svoboda, K., Hausser, M., Haesler, S., Carandini, M., Harris, T.D., 2021. Neuropixels 2.0: A miniaturized high-density probe for stable, long-term brain

recordings. Science (American Association for the Advancement of Science) 372, 258–.

Stepniewska, I., Fang, P.-C.Y., Kaas, J.H., 2009. Organization of the posterior parietal cortex in galagos: I. Functional zones identified by microstimulation. Journal of comparative neurology (1911) 517, 765–782.

Stepniewska, I., Gharbawie, O.A., Burish, M.J., Kaas, J.H., 2014. Effects of muscimol inactivations of functional domains in motor, premotor, and posterior parietal cortex on complex movements evoked by electrical stimulation. Journal of neurophysiology 111, 1100–1119.

Stirman, J.N., Townsend, L.B., Smith, S.L., 2016. A touchscreen based global motion perception task for mice. Vision research. 127.

Stoltz, S., Humm, J.L., Schallert, T., 1999. Cortical injury impairs contralateral forelimb immobility during swimming: A simple test for loss of inhibitory motor control. Behavioural brain research 106, 127–132.

Sul, J., Jo, S., Lee, D., Jung, M., 2011. Role of rodent secondary motor cortex in value-based action selection. Nature Neuroscience 14.

Swets, J.A., 1988. Signal detection theory and psychophysics, Reprint ed. ed. Peninsula Publishing, Los Altos (Calif.).

Takei, T., Lomber, S.G., Cook, D.J., Scott, S.H., 2021. Transient deactivation of dorsal premotor cortex or parietal area 5 impairs feedback control of the limb in macaques. Current biology 31, 1476–1487.e5.

Tennant, K.A., Adkins, D.L., Donlan, N.A., Asay, A.L., Thomas, N., Kleim, J.A., Jones, T.A., 2011. The organization of the forelimb representation of the C57BL/6 mouse motor cortex as defined by intracortical microstimulation and cytoarchitecture. Cerebral cortex (New York, N.Y. 1991) 21, 865–876.

Terra, H., Bruinsma, B., Kloet, S.F. de, Roest, M. van der, Pattij, T., Mansvelder, H.D., 2020. Prefrontal cortical projection neurons targeting dorsomedial striatum control behavioral inhibition. Current biology 30, 4188–4200.e5.

Teune, T.M., Burg, J. van der, Moer, J. van der, Voogd, J., Ruigrok, T.J.H., 2000. Topography of cerebellar nuclear projections to the brain stem in the rat. CEREBELLAR MODULES: MOLECULES, MORPHOLOGY, AND FUNCTION, PERSPECTIVES IN ANALYTICAL PHILOSOPHY 124, 141–172.

The pandas development team, 2020. Pandas-dev/pandas: pandas. Zenodo. https://doi.org/10.5281/zenodo.3509134

Thorn, C.A., Atallah, H., Howe, M., Graybiel, A.M., 2010. Differential dynamics of activity changes in dorsolateral and dorsomedial striatal loops during learning. Neuron (Cambridge, Mass.) 66, 781–795.

Umilta, M.A., Brochier, T., Spinks, R.L., Lemon, R.N., 2007. Simultaneous recording of macaque premotor and primary motor cortex neuronal populations reveals different functional contributions to visuomotor grasp. Journal of neurophysiology 98.

Usrey, W.M., Alitto, H.J., 2015. Visual functions of the thalamus. Annual review of vision science, Annual review of vision science 1, 351–371.

Vaidya, M., Kording, K., Saleh, M., Takahashi, K., Hatsopoulos, N.G., 2015. Neural coordination during reach-to-grasp. Journal of neurophysiology 114, 1827–1836.

Valero, M., English, D.F., 2019. Head-mounted approaches for targeting single-cells in freely moving animals. Journal of neuroscience methods 326, 108397–108397.

Vallat, R., 2018. Pingouin: Statistics in python. The Journal of Open Source Software 3, 1026.

Vandaele, Y., Mahajan, N.R., Ottenheimer, D.J., Richard, J.M., Mysore, S.P., Janak, P.H., 2019. Distinct recruitment of dorsomedial and dorsolateral striatum erodes with extended training. eLife 8.

Vandamme, T., 2014. Use of rodents as models of human diseases. Journal of pharmacy & bioallied science 6, 2–9.

Virtanen, P., Gommers, R., Oliphant, T.E., Haberland, M., Reddy, T., Cournapeau, D., Burovski, E., Peterson, P., Weckesser, W., Bright, J., van der Walt, S.J., Brett, M., Wilson, J., Millman, K.J., Mayorov, N., Nelson, A.R.J., Jones, E., Kern, R., Larson, E., Carey, C.J., Polat, İ., Feng, Y., Moore, E.W., VanderPlas, J., Laxalde, D., Perktold, J., Cimrman, R.,

Henriksen, I., Quintero, E.A., Harris, C.R., Archibald, A.M., Ribeiro, A.H., Pedregosa, F., van Mulbregt, P., SciPy 1.0 Contributors, 2020. SciPy 1.0: Fundamental Algorithms for Scientific Computing in Python. Nature Methods 17, 261–272. https://doi.org/10.1038/s41592-019-0686-2

Voroslakos, M., Petersen, P.C., Voroslakos, B., Buzsaki, G., 2021. Metal microdrive and head cap system for silicon probe recovery in freely moving rodent. eLife 10.

Wall, N.R., De La Parra, M., Callaway, E.M., Kreitzer, A.C., 2013. Differential innervation of direct- and indirect-pathway striatal projection neurons. Neuron (Cambridge, Mass.) 79, 347–360.

Wang, A.Y., Miura, K., Uchida, N., 2013. The dorsomedial striatum encodes net expected return, critical for energizing performance vigor. Nature neuroscience 16, 639–647.

Wang, Q., Sporns, O., Burkhalter, A., 2012. Network analysis of corticocortical connections reveals ventral and dorsal processing streams in mouse visual cortex. The Journal of neuroscience 32, 4386–4399.

Wang, X., Liu, Y., Li, X., Zhang, Z., Yang, H., Zhang, Y., Williams, P.R., Alwahab, N.S.A., Kapur, K., Yu, B., Zhang, Y., Chen, M., Ding, H., Gerfen, C.R., Wang, K.H., He, Z., 2017. Deconstruction of corticospinal circuits for goal-directed motor skills. Cell 171, 440–455.e14.

Waskom, M.L., 2021. Seaborn: Statistical data visualization. Journal of Open Source Software 6, 3021. https://doi.org/10.21105/joss.03021

Wei, Z., Lin, B.-J., Chen, T.-W., Daie, K., Svoboda, K., Druckmann, S., 2020. A comparison of neuronal population dynamics measured with calcium imaging and electrophysiology. PLoS computational biology 16, e1008198–e1008198.

Weiler, N., Wood, L., Yu, J., Solla, S.A., Shepherd, G.M.G., 2008. Top-down laminar organization of the excitatory network in motor cortex. Nature neuroscience 11, 360–366.

Whishaw, I.Q., Faraji, J., Kuntz, J., Mirza Agha, B., Patel, M., Metz, G.A.S., Mohajerani, M.H., 2017. Organization of the reach and grasp in head-fixed vs freely-moving mice provides support for multiple motor channel theory of neocortical organization. Experimental brain research 235, 1919–1932.

Whishaw, I.Q., Tomie, J.-A., 1989. Olfaction directs skilled forelimb reaching in the rat. Behavioural brain research 32, 11–21.

Wise, S.P., Boussaoud, D., Johnson, P.B., Caminiti, R., 1997. Premotor and parietal cortex: Corticocortical connectivity and combinatorial computations. Annual review of neuroscience 20, 25–42.

W.J, W., J.J, D., Geuze, R., C.R, M., 1979. Control of fast goal-directed arm movements. Journal of Human Movement Studies 5, 3–17.

Yamawaki, N., Borges, K., Suter, B.A., Harris, K.D., Shepherd, G.M.G., 2014. A genuine layer 4 in motor cortex with prototypical synaptic circuit connectivity. eLife 3, e05422–e05422.

Yamawaki, N., Shepherd, G.M.G., 2015. Synaptic circuit organization of motor corticothalamic neurons. The Journal of neuroscience 35, 2293–2307.

Yin, H.H., Ostlund, S.B., Knowlton, B.J., Balleine, B.W., 2005. The role of the dorsomedial striatum in instrumental conditioning. The European journal of neuroscience 22, 513–523.

Zagha, E., Ge, X., McCormick, D.A., 2015. Competing neural ensembles in motor cortex gate goal-directed motor output. Neuron (Cambridge, Mass.) 88, 565–577.

Zatka-Haas, P., Steinmetz, N.A., Carandini, M., Harris, K.D., 2021. Sensory coding and the causal impact of mouse cortex in a visual decision. eLife 10.

Zhang, F., Aravanis, A.M., Adamantidis, A., Lecea, L. de, Deisseroth, K., 2007. Circuit-breakers: Optical technologies for probing neural signals and systems. Nature reviews. Neuroscience 8, 732–732.

Zhang, J., Zhang, K.-Y., Zhang, L.-B., Zhang, W.-W., Feng, H., Yao, Z.-X., Hu, B., Chen, H., 2019. A method for combining multiple-units readout of optogenetic control with natural stimulation-evoked eyeblink conditioning in freely-moving mice. Scientific reports 9, 1857–1857.

Zingg, B., Hintiryan, H., Gou, L., Song, M.y., Bay, M., Bienkowski, M.s., Foster, N.n., Yamashita, S., Bowman, I., Toga, A.w., Dong, H.-W., 2014. Neural networks of the mouse neocortex. Cell 156, 1096–1111.

Zong, W., Obenhaus, H.A., Skytøen, E.R., Eneqvist, H., Jong, N.L. de, Vale, R., Jorge, M.R., Moser, M.-B., Moser, E.I., 2022. Large-scale two-photon calcium imaging in freely moving mice. Cell 185, 1240–1256.e30.